Feasibility of using Basalt Fiber Reinforced Polymer (BFRP) bars as internal reinforcement in bridge decks

Final Report
August 31, 2022

Principal Investigator
Mohsen A. Issa, Ph.D., PE, SE, F.ASCE, F.ACI
Department of Civil, Material, and Environmental Engineering
University of Illinois at Chicago

Author
Mohsen A. Issa

Sponsored by
Illinois State Toll Highway Authority
A report of the finding of
Tollway #19-03
Feasibility of using Basalt Fiber Reinforced Polymer (BFRP) bars as internal reinforcement in bridge decks

A report from
The University of Illinois at Chicago
Department of Civil, Material and Environmental Engineering
Room 2095 ERF, 842 West Taylor Street, Chicago, Illinois, 60607
Phone: 312-996 3432 / Email: missa@uic.edu

ACKNOWLEDGMENT, DISCLAIMER, MANUFACTURERS' NAMES

This publication is based on the results of Illinois Tollway #19-03 Feasibility of using Basalt Fiber Reinforced Polymer (BFRP) bars as internal reinforcement in bridge decks. Illinois Tollway #19-03 was conducted in cooperation with the Illinois State Toll Highway Authority.

The Illinois State Toll Highway Authority sponsored this study. The researchers would like to thank the Technical Review Panel (TRP) for their valuable inputs and organizational capabilities that facilitated the completion of this research and the preparation of the final report for this project. In particular, TRP Chair Michael Brink greatly facilitated the research project. The author would like to express his gratitude and sincere appreciation to the Illinois Tollway for the financial and technical support for this research project. Special thanks to OZINGA for providing the concrete and PULTRALL for providing the BFRP bars for the bridge decks. A great appreciation to the Ph.D. students Mohammad Mahdi, Mohammad Abandah, Mounir Kassem, Alain Saroufim, Ahmad Elrefae, and the undergraduate student Matthew Gasienica for the help provided for fulfilling this research. Also, the author would like to thank the UIC technicians Jaimy Juliano, Kassem Saad, Todd Taylor, and Douglas Perzan for their help and support. We also want to thank the members of the TRP and interested participants for their support and many review comments:

- Michael Brink, Illinois State Toll Highway Authority
- Cynthia Williams, Illinois State Toll Highway Authority
- Daniel Gancarz, Illinois State Toll Highway Authority
- Elias Ajami, Illinois State Toll Highway Authority
- Mohammad Faraj, Illinois State Toll Highway Authority
- Ahmad Hammad, WSP
- Mark Schaffer, IDOT Bureau of Bridges and Structures
- Dan Brydl, Federal Highway Administration

Executive Summary

Corrosion is the most common structural deterioration source in any structural element exposed to environmental conditions, particularly in severe weather conditions where deicing salt is used. Basalt fiber-reinforced polymer (BFRP) bars have been gaining the attention of researchers due to their high tensile strength, lightweight, and environmentally friendly compared to conventional steel reinforcement. Thus, the Illinois Tollway is interested in reevaluating its current construction specification for the feasibility of using BFRP bars as internal reinforcement in bridge decks. Basalt fibers are made from igneous basalt volcanic rocks melted at 1400 ºC utilizing a technology similar to those used to produce E-Glass and AR-Glass fibers. BFRP bars are a reinforcing material made from basalt fibers with a resin material for fiber bonding and sand coat at the surface for bonding with concrete. BFRP bar is an environmentally friendly material and has better resistance to corrosion and freeze and thaw cycles than conventional steel reinforcement, which attracts the attention to use this material in special structural applications. Per ACI 440.1R and ASTM D7957, the current specification for Glass-FRP, Aramid-FRP, and Carbon-FRP, and since Basalt-FRP has not been added to the specification yet, it can be used as a material specification for BFRP, which revealed the same tensile behavior as the other FRP material.

A thorough experimental program was conducted at the University of Illinois at Chicago to evaluate the mechanical properties and durability characteristics of the BFRP material. In bridge deck design with FRP material, the main concern is the reinforcing bar's tensile properties (maximum tensile stress, stress-strain behavior, and the modulus of elasticity). The laboratory testing program consisted of studying the tensile strength properties, shear strength, bond strength, creep behavior, the effect of freeze and thaw and alkaline solution on the bar, and full-scale bridge deck testing, as well as cost analysis and parametric study for the different parameters used in the design of bridge decks.

The tensile properties test can be summarized by applying a uniaxial load on the rebar with a strain gauge on the surface to record the stress-strain readings. Unlike steel, BFRP is weak in the lateral direction, requiring special attention for the gripping system used in this test. Moreover, the bond strength is a significant factor in introducing BFRP to bridge deck design to ensure the fixation of the embedded rebar in concrete. This test is composed of pulling the bar from a concrete cube with a specific bonded length, and the bond stress versus slippage is plotted. As an outcome of this test, the required lap length is 40x the bar diameter for BFRP bars #4, #5, and #6 with no possible splicers. These bars can be manufactured with different lengths limited by the shipment requirements. Furthermore, BFRP bars can be manufactured in different shapes and forms, allowing the bar to be used as a stirrup in concrete beams and it’s available in North America through multiple manufactures. Here lies the importance of studying the shear strength of BFRP bars which is expected to be much lower than the tensile strength.

The durability characteristics of BFRP material are still unclear since the production of BFRP bar has not been standardized yet. The resin material used in bar manufacturing plays an essential role in the bar's resistance to harsh environmental conditions, especially alkaline solutions such as deicing salt. On the other hand, the mechanical properties testing program showed high tensile strength, moderate shear

strength, sufficient bond strength, excellent resistance to freeze and thaw cycles, and good resistance to the alkaline solution for #5 and #6 BFRP bars.

It is essential to reevaluate the current construction specification to allow BFRP bars as the primary reinforcement in bridge decks. Although a BFRP bar exhibits a lower modulus of elasticity compared to mild steel reinforcement, it can be incorporated in special applications such as bridge decks where deflection is not an issue. The research study includes the following parameters: bar size and spacing, slab length, and continuity on the behavior of the bridge deck reinforced with BFRP bars. A total of six full-scale single-span and two-span continuous bridge deck slabs were cast in place, instrumented, and tested in the newly built high-bay structures laboratory at UIC. The bridge deck slabs were reinforced with #5 BFRP bars spaced at 4 and 6 inches in the transverse directions (primary reinforcement) and #5 BFRP bars at 4, 6, and 8 inches in the long direction. Due to the lower modulus of elasticity of BFRP compared to mild steel, the bridge deck slabs design calls for an over-reinforced section to control the section's serviceability at cracking. Unlike traditional concrete design, the concrete crushes in the compression zone before the BFRP bars rupture. The single-span slabs were 10-ft long, 4-ft wide, and 8-in thick, and the continuous two-span bridge deck slabs were 18-ft long, 10-ft wide, and 8-in thick. The bridge decks were subjected to static loading simulating the AASHTO LRFD loading (HL93). The structural testing up to failure accounts for the dynamic effect by multiplying the wheel loading by a factor 1.33. The bridge decks were tested and monitored for serviceability, including pre-cracking, cracking, and post-cracking up to their ultimate strength (failure). The collected test results include deflection, crack width, concrete and BFRP bars strains, ultimate flexural capacity, and compression-shear failure mode. As an outcome of this research, a design document for a span length-to-depth ratio less than 12 is developed for bridge deck slabs reinforced with BFRP bars. The tests show promising results for the feasibility of using BFRPs bar as internal reinforcement in bridge decks. Test results also indicated that the load from AASHTO LRFD service limit state combination is less than the cracking load observed during testing of the bridge deck slabs. At ultimate load, the maximum strain observed in the BFRP bars represents about 35% of the ultimate strain of the bar. Moreover, the crack widths at the ultimate design load were about 30% less than the crack width limit specified in ACI 440.1R-15. As an outcome of this research, a new empirical model was generated to evaluate the flexural shear strength of bridge decks reinforced with FRP bars.

A nonlinear finite element analysis parametric study was conducted to assess the behavior of the concrete bridge prototypes. The experimental work at UIC was simulated using ABAQUS for validating the nonlinear finite element models. As a result of the validation, the finite element modeling was extrapolated to assess the structural behavior of the BFRP reinforced concrete bridge deck slabs. The parametric study includes the following parameters: (1) slab span length, (2) transverse bar size, (3) transverse bar spacing, (4) longitudinal bar spacing, and (5) concrete compressive strength. The parametric study results showed that the cracking load is directly proportional to the span length and concrete compressive strength, while the nominal load is directly proportional to the span length, concrete compressive strength, and transverse bar amount. Also, the strain in the BFRP bars at factored design load is directly proportional to concrete compressive strength and transverse main bar amount. After the numerical evaluation of those parameters, a statistical approach will be used for deriving an empirical equation to predict the bridge deck slab behavior.

In addition, a design guide document is developed using MathCad software. The document illustrates a design procedure for designing a BFRP-reinforced concrete bridge deck slab based on AASHTO LRFD bridge design guide specifications for GFRP-Reinforced concrete (AASHTO GFRP). The design procedure is based on limit state design principles where structural components shall be proportioned to satisfy the requirements at all appropriate service, fatigue and creep rupture, strength, and extreme event limit states. The traditional design method for deck slabs is based on flexure as outlined in Article 3.7.3 in AASHTO GFRP. The traditional design method permits the approximate elastic and refined analysis methods as specified in Articles 4.6.2.1 and 4.6.3.2 of the AASHTO LRFD. Therefore, AASHTO LRFD Table A4.1 is implemented in the document for the structural analysis of slab live load. The design guide document analyzes the bridge deck structurally and checks all the limit states.

Table of Contents

List of Figures

List of Tables

Chapter 1

1 Introduction

1.1 Introduction

The Illinois Tollway and the Illinois Department of Transportation continue to implement newly inventive materials to enhance the infrastructure's sustainability and durability. Since Illinois experiences harsh freeze and thaw conditions resulting from average temperature drops in the winter below 0˚C, the snow on the highways, and the use of deicing salt, the steel reinforcement used with various infrastructural applications becomes more prone to corrosion. Due to these underlying consequences, new material applications have the capacity to mitigate the effects caused by extremely corrosive environments. Therefore, substituting more advanced materials can prevent corrosion and reduce the maintenance of the infrastructure in the long term compared to the conventional usage of steel reinforcement. Basalt fiber reinforcement polymer (BFRP) bars have a more idealistic application in Illinois due to their advantageous mechanical and material properties.

Basalt fibers are made from igneous basalt volcanic rocks melted at 1400˚C using a technology similar to those used to produce E-Glass and AR-Glass fibers. Basalt Fiber Reinforced polymer BFRP bars are a type of reinforcing material made from basalt fibers with a resin material and sand coat at the surface for bonding. Design and construction guidelines are currently available for other fiber reinforcement polymer FRP bars but not for basalt fiber reinforced polymer BFRP bars due to the lack of research studies. This report presents tensile strength, modulus of elasticity, ultimate strain, bond strength, transverse shear strength, alkaline effect, and freeze and thaw effect of BFRP bars. The experimental investigation includes three different bar sizes: bar #4, #5, and #6 for all tests.

The use of Basalt Fiber Reinforced Polymer (BFRP) composite material in concrete structures has been attributed to most Structural Engineers' and researchers' attention because of their ability to resist corrosion and harsh environmental conditions, have lightweight characteristics, and high tensile strength compared to the conventional steel reinforcement. Furthermore, BFRP can come in many forms of bar, tendon, or sheet composition with various shapes and properties. Due to its high tensile strength, good chemical resistance, and environmental friendliness, BFRP bars are very suitable for infrastructure, especially bridge decks, since engineers suffer from heavy corrosion and, consequently, frequent and costly maintenance.

1.2 Problem Statement

Recently, the usage of BFRP bars in concrete structures has been increasing in the US and worldwide with the number of manufacturers. However, there is not any standard yet for the production and design of BFRP bars. Manufacturers produce different forms of BFRP bars, each with different mechanical and physical properties, depending on the resin material, source of igneous rocks used, and the production procedure. Therefore, with the increasing infrastructure and technology, conducting a comprehensive and full study of the BFRP performance (mechanical and durability properties) for safe transition in concrete structures becomes significant to meet infrastructural demands, specifically in prominent structures, such as bridge decks. Moreover, a detailed cost analysis for substituting BFRP bars with conventional steel reinforcement and the constructability cost differences must be investigated. This study's durability and mechanical properties of BFRP bars can be standardized for implementation in bridge decks.

1.3 Research Objectives

The project objective is to perform laboratory tests on the mechanical and durability characteristics of BFRP bars. The study includes the tensile strength, modulus of elasticity, transverse shear strength, tensile creep rupture, alkali resistance, and resistance to freeze and thaw. Moreover, a detailed cost analysis using BFRP reinforced concrete bridge slabs will include the construction cost, future cost, and the

life-cycle cost analysis. After completing the laboratory tests for the mechanical and durability characteristics, single-span and two-span bridge deck full-scale prototypes, reinforced with BFRP bars will be tested to study the behavior and the mode of failure of the bridge deck under HL-93-wheel configuration. A design document for implementing BFRP bar in Tollway bridge decks is developed based on the key findings of the material and structural characteristics.

As a summary of the research objectives, the tasks can be summarized by the following:

- Perform laboratory tests on the mechanical and durability characteristics of BFRP reinforcement. This includes (1) basic mechanical properties, (2) the transverse shear strength, (3) tensile creep rupture, (4) long-term relaxation, (5) alkali resistance, and (6) resistance to Freeze/Thaw.
- Perform cost analysis on using BFRP reinforced concrete bridge deck slabs. This includes the (1) construction cost, (2) future cost, and the (3) life-cycle cost analysis.
- Perform structural laboratory testing. This program includes testing of (1) full-scale bridge deck slabs and (2) prototype bridge segments with decks reinforced with BFRP bars.
- Develop a design document for implementing BFRP bar in Illinois Tollway bridge decks: This task will be refined based on the key findings of the material and structural characterization.

Chapter 2

2 Literature Review

2.1 Background

Corrosion is the most common structural deterioration source in bridges, particularly in severe weather conditions where deicing salts are used. Epoxy-coated steel bars appeared to be a feasible solution against corrosion. However, the (ACI 440.1R-15, 2015) Committee reported that these bars will still corrode when implemented in harsh weather conditions. The Fiber Reinforced Polymer (FRP) materials offer better resistance to corrosion and chemical attacks and appear more environmentally friendly and sustainable. Carbon FRP (CFRP), Aramid FRP (AFRP), and Glass FRP (GFRP) have all been introduced for strengthening and rehabilitating structures in the last decade. Basalt FRP is made from Basalt rocks and resin material to bind fibers. Basalt is defined as an igneous rock; it is generated from the rapid cooling of basaltic lava unveiled close to its crust. The fibers are combined by imbibing them with vinyl epoxy resin and then sand coating them to enhance the bond with concrete.

Basalt FRP (BFRP) is a new addition to the FRP materials. It is a brittle elastic material with a linear stress-strain behavior to failure. In 1993, Nanni illustrated that rupturing BFRP bars at failure in the reinforced concrete is far more dangerous than concrete crushing (Nanni, 1993); in 2006, Bank had the same conclusion as Nanni (Bank, 2007). BFRP poses more advantageous characteristics than glass fibers. These include economically feasible, higher strength, more sustainable alkali resistance, adaptability across a broader range of temperatures, better insulation, and a rupture strain greater than carbon fiber. However, the essential drawback of BFRP is the low modulus of elasticity (Elgabbas et al., 2015), causing a higher deformation and lower ductility. Because of this low ductility, structures reinforced with BFRP bars can

suddenly fail without any prediction (Grace et al., 1998), one of the primary considerations for RC structural designers using BFRP.

Basalt fibers are advantageously known for their higher tensile strength and modulus, chemical resistance, extended operating temperature range, and environmental friendliness. Their behavior is ideal for extended usage involving high temperature, durability, chemical resistance, and low water absorption compared to E-glass FRP. BFRP offers enhanced material quality, exhibiting five times the strength and modulus as E-glass FRP and about one-third the density of commonly used low carbon steel bars (Wu et al., 2012). BFRP has been researched as reinforcing bars for testing and industrial applications. Due to their high mechanical and durability qualities and similar chemical nature to glass fibers, BFRP bars will stimulate application and optimize the design and cost.

2.2 Durability

Fiber-reinforced polymer (FRP) composites are being used in civil infrastructure applications. These include (1) FRP composite bridge decks; (2) FRP composites as a substitute reinforcement for steel and concrete; (3) prefabricated FRP structural components; (4) FRP composites; (5)) prestressed FRP cables and rods to reinforce concrete beams; and (6) FRP rods used as a substitute for steel in reinforced concrete (Mkarand et al., 2004). Although they have immense applications in the industry, they are still unknown to the infrastructure world. CERF closely analyzed the durability of these materials in response to civil infrastructure. The research lacked results regarding sustained performance in response to harsh, severe, and changing conditions under load (Karbhari V. M., Durability of FRP Composites for Civil Infrastructure – Myth, Mystery and Reality, 2003). Although long-term performance data was not available, some materials (resin, fiber, etc.) are of high initial cost and cause ambiguity in their use.

2.2.1 Alkali resistance

In 2005, Sim et al. inspected basalt fiber's durability, mechanical properties, and flexural strengthening characteristics (Sim et al., 2005). After testing ten specimens, the authors noticed that the basalt fiber's strength was about 30% the strength of carbon

fiber (CFRP) and 60% of glass fiber (GFRP). Three different experiments were performed to find the long-term durability of the basalt fibers: (1) alkali resistance, (2) weathering resistance, and (3) autoclave and thermal stability. The BFRP test results were compared with CFRP and GFRP characteristics under the same circumstances. Alkali-resistance experiment showed that the basalt and the glass fibers seem to have typical failure characteristics and drop strength and volumetric stability more rapidly than carbon fiber under harsh alkali conditions.

Although old research indicates that the interfacial region in basalt composites might be more exposed to environmental destruction than glass composites; the interface between basalt and resin material might also be more lasting than between glass and epoxy in tension-tension fatigue; this is because basalt composites fatigue life is longer. Huo et al. systematically inspected the chemical durability and mechanical properties of basalt fiber and the effect of dipping BFRP in an alkaline solution for three months on the bar strength and epoxy-resin composite (Huo et al., 2007). The results showed that the modulus of the BFRP was unaffected after exposure, but it experienced a reduction of 40% in the tensile strength. Li et al. investigated basalt-epoxy FRP bars' durability and fatigue performances under hydrothermal and alkaline environmental conditions (Li et al., 2012). The BFRP bars showed severe deterioration in tensile properties without resin protection because of the corrosion of the fibers' exposed environments. In contrast, BFRP bars showed better durability when exposed to the same environmental conditions.

2.2.2 Freeze and thaw resistance

Freeze and thaw deterioration are among the most significant factors affecting cracked concrete structural elements considering the permeability of concrete material. Hence, water could potentially accumulate at the interface between FRP and concrete. Schaefer B. concluded that when the temperature decreases, the water will expand, producing a force against the bond between concrete and FRP bar. Moreover, as the water crystallizes, it produces forces that break the FRP bond and concrete (Schaefer, 2002). Furthermore, the extreme variation in temperature through freeze and thaw cycles is predicted to have the same effect as changing the coefficient of thermal expansion for the glass FRP bars in the transverse direction (32–36x10--6/ºC) and

concrete (8–12x10-6/ºC), which leads to freezing water. It should be recognized that the coefficient of thermal expansion for the glass FRP bars in the longitudinal direction is similar to that of concrete (Zhang & Ou, 2007). Karbhari stated that low-temperature thermal cycling reveals more degradation effect than immersion of bar at a constant temperature below freezing due in part to interface-level degradation (Karbhari V. M., Durability of FRP Composites for Civil Infrastructure – Myth, Mystery and Reality, 2003). It's been mentioned that the absorption moisture of composite materials causes the material to be more plastic and hydrated through an attack on the ester linkage; both processes are simulated by the change in the molecular mobility, generating the degradation of composites.

Micro-cracking is caused by an increase in water absorption at higher temperatures and, resultantly, increases resin plasticization and hydrolysis processes. Due to lower temperatures, the expansion of frozen water collects in the cracks and voids, altering bonding action and inducing transverse micro-crack propagation (Rivera & Karbhari, 2002). These vicious freezes and thaw cycles cause material degradation in the matrix, fiber-matrix debonding, brittleness, and considerable damage to mechanisms monitored under ambient conditions (Lord & Dutta, 1988; Haramis, 2003; Karbhari & Pope, 1994; Karbhari et al., 2000). Freeze-thaw experiments have been previously conducted to test the effects of carbon-vinyl ester composites and E-glass/vinyl ester composites in low-temperature thermal cycling (Karbhari et al., 2002). In response, the specimens showed considerable reduction in the mechanical properties and glass-transition temperatures when submerged in saltwater. The significant reactions to this include fiber-matrix bond deterioration and matrix cracking compared to other exposure. These resin matrix-controlled FRP automotive composites are more susceptible to moisture differences than the resin matrix-controlled FRP automotive composites. Simulating the behavior included applying a sustained load during the conditioning process, further deteriorating the composite behavior's durability, and moisture absorption in both the polymers and polymer (Hollaway & Head, 2001).

Sim et al. studied the durability and performance of basalt, glass, and carbon fibers by changing the temperature (Sim et al., 2005). They concluded that a volume change and strength loss through a surface reaction would occur when basalt and glass fibers

are immersed in an alkaline solution, whereas carbon fibers did not significantly lose strength. However, basalt fibers retained about 90% of their strength at room temperature after exposure to 60°C for 2 hours. Liu et al. provided an experimental study to determine if BFRP composites were suitable, effective, and could be contributed to transportation applications (Liu et al., 2006). Their experiment concluded that the chemical formation of basalt fibers is similar to glass fibers, except that the ratio of iron oxide gives basalt fibers their brown color. Further development of BFRP bars will initiate industrial applications, possibly optimizing and creating a cost-effective design from a mechanical and durability standpoint. They found no essential differences in stiffness or strength between BFRP and GFRP.

2.3 Mechanical Properties

FRP bars are commercially available in various options of cross-sectional dimensions, composition, and surface deformation patterns. Thus, unlike steel bars, it is necessary to measure the mechanical properties of FRP bars from different producers. Its principal mechanical properties need to be determined to utilize FRP bar reinforcement, including ultimate strength, modulus of elasticity, and development length. In addition to mechanical properties measurements, shear strength perpendicular to fiber for dowel action and shear strength parallel to fibers may be measured. (Castro and Carino 1998).

2.3.1 Tensile Strength

Many researchers have covered tensile strength and the modulus of elasticity of BFRP reinforcement bars. Adhikari investigated the mechanical properties (tensile strength, rupture strain, and modulus of elasticity), bond strength of BFRP bars, and the flexural behavior of beams reinforced with BFRP bars of three different BFRP bar diameters (Adhikari, 2009). The tested bars were 3 mm (0.12 in), 5 mm (0.2 in), and 7 mm (0.28 in). The test specimens' standard deviations from the tensile strength and rupture strains fluctuated from 7 to 13.74%.

The tensile properties of FRP control the design process of the FRP reinforced concrete elements since the capacity of the section is determined using the rebar tensile strength, and the service limit state is governed by the rebar modulus of elasticity

(Elgabbas 2015). Moreover, the anisotropic properties of the FRP material, strength, and stiffness in the transverse direction are inferior compared to their longitudinal strength and stiffness; thus, traditional tensile-test methods like the universal testing method are not relevant. Castro and Carino cited that the traditional wedge-shaped frictional gripping system adopted in the tensile testing of FRP bars may cause high compressive stress in the transverse direction, which leads to regional stress concentration generated by the harsh grips resulting in crushing of the FRP bar (Castro & Carino, 1998). Progressively, the FRP bar is subject to an earlier rupture. Many gripping techniques were established to implement the anchorage for extremities in FRP bars by researchers performing the tensile test. FRP bars, in general, have a linear elastic stress-strain relationship up to the rapture. The fiber type, volume fraction, bar diameter, and manufacturing process are factors that affect the tensile properties of FRP bars (Fasa 1993).

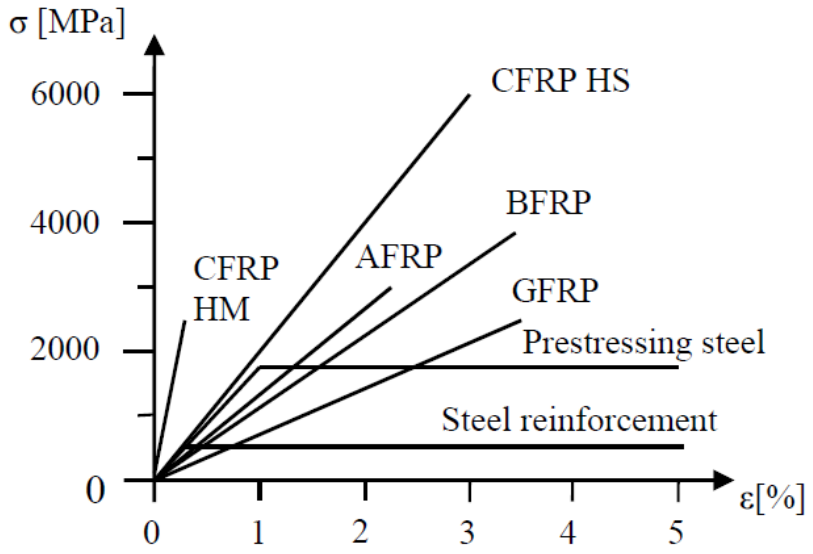

Figure 1: Stress-strain curve of steel vs. FRP.

Additionally, they mentioned commonly used gripping techniques for the anchorage of the FRP pre-stressing tendons ends have evolved in tensile testing of FRP bars by many researchers. It indicated that the ultimate tensile strength is not a built-in material property and is related to the size and geometry of the FRP specimen. This issue is due to more stress in the outer fibers than the interior bars when subjected to axial tensile, consequently reducing the bar's overall load-carrying capacity. Based on

Ehsani et al., this incident is defined as the shear lag effect (Ehsani et al., 1996; Adhikari, 2009). It indicates that the more the bar size increases, the less tensile strength obtained. Kocaoz et al. declared that the tensile strength must always be specified for the specific bar size (Kocaoz et al., 2005). However, the modulus of elasticity is not relatively affected by the cross-sectional size of the bar. The tensile test can obtain stress-strain behavior, modulus of elasticity, and rupture strain.

Ovitigala and Issa tested BFRP bars to obtain the tensile strength and elasticity modulus (Ovitigala & Issa, 2013). They tested five different bar sizes (6 mm, 10 mm, 13 mm, 16mm, and 25 mm) according to the ASTM D7205 standard and noticed that the ultimate tensile strength and modulus of elasticity of BFRP bars are more than 155 ksi and 7000 ksi, respectively.

2.3.2 Bond Strength

The main concern for accomplishing the best composite behavior in reinforced concrete is that steel or FRP reinforcement should be perfectly bonded with concrete to avoid any slippage of steel or FRP bars and collapse in the structure element under ultimate loads. Complete composite action is extremely more important than the use of high-strength and high-performance materials. For instance, the tensile strength of reinforcement bars is not fully used by the structural element when it is easily affected by loading unless the reinforcement bars are bonded to concrete. Also, the structure loses ductility, and a brittle, immature, and sudden failure will occur because the structural designers design the structure based on fully composite regardless of the mechanical properties of the element such as flexural, shear, or torsion. Structural engineers' significant concern is studying bond behavior between concrete and FRP and requiring the development length of BFRP to maintain perfect bonding with concrete in designing structures.

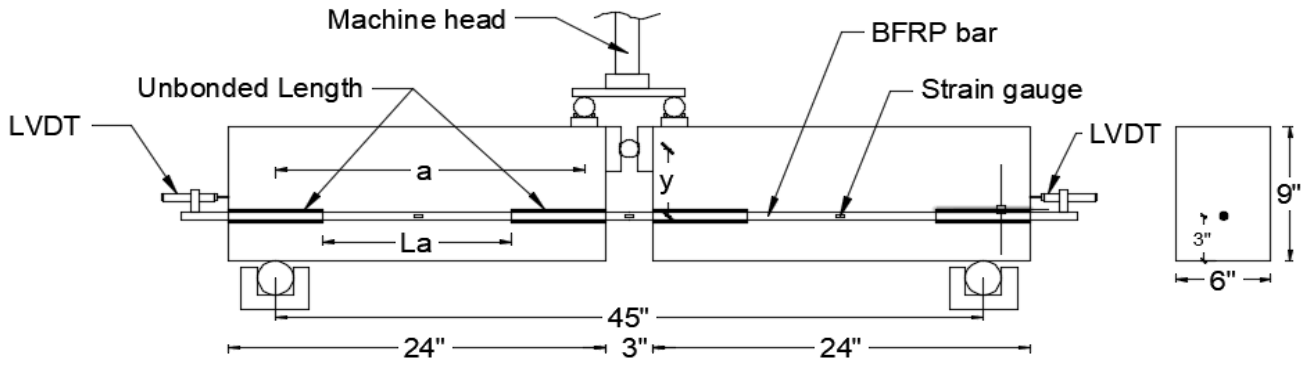

Figure 2: Hinged beam test setup.

The study of the FRP bars' bond strength with concrete is extracted from two primary methods, the pull-out, and the hinged beam test. Nonetheless, various experimental test methods quantify the bond strength experimentally in the literature. This research project will achieve the hinged beam and pull-out test analysis to study the bond strength of BFRP bars with concrete. The following researchers (de Larrard et al., 1993; Benmokrane et al., 1996; Nanni et al., 1993, Ehsani et al., 1996 and (Benmokrane et al., 1995) illustrated that beam tests could practically simulate the stress distribution behavior of a concrete structural element reinforced with FRP bars subjected to bending. The advantage of this method is that the load is not directly applied to the FRP bar, which is the optimum condition for studying the bond strength between the BFRP bar and concrete. The factors affecting bond characteristics between BFRP reinforcement and concrete are: (1) the size and type of reinforcement; (2) the concrete strength; (3) the bar's modulus of elasticity; (4) the geometry of the concrete member; (5) the position of the bar in the member section; (6) the type of loading; (7) the concrete cover; (8) surface condition of the reinforcement (smooth, deformed, and sand-coated); (9) Poisson's ratio, confinement (spiral or stirrups); and (10) the volume of fiber and matrix. The more parameters that affect any study, the harder to predict the real strength based on these parameters. Consequently, the test will not be fully accurate.

There are a variety of studies that tackle the bond strength between concrete and BFRP bars. Some mention that concrete strength affects the concrete-bar bond, while others do not acknowledge this. Achillides and Tepfers stated when the concrete

strength increases from 30 MPa (4.35 ksi) to 40 MPa (5.8 ksi), a transfer of bond shear failure from concrete into the surface layer of the FRP bar would occur because FRP bars have lower internal shear strength in resin between the fibers than steel (Achillides, 1998 and Tepfers, 2006). Hence, they concluded that bond shear resistance is not related to concrete strength.

Ovitigala and Issa investigated bond strength by testing a set of 10 hinged beam specimens and found that BRFP bond characteristics are similar to those of GFRP bars. (Ovitigala & Issa, 2013). They found that $20d_b$ bond length can be considered the development length for flexural specimens, and the more increase in the BFRP bar diameter results in more maximum average bond stress. Refai et al. (2015) investigated the bond strength of thirty-six concrete cylinders reinforced with BFRP bar and twelve concrete cylinders reinforced with GFRP rebar. After plotting the bond-slip curves for BFRP and GFRP, it is found that they follow the same trend. Also, the BFRP bar development of average bond strength equals 75% of the average bond strength developed by GFRP rebars.

Adhikari used the pull-out test method to study the bond strength of the BFRP bars (Adhikari, 2009). The bond test consisted of four pull-out cylindrical samples by changing the BFRP bar diameter: 3 mm (0.12 in), 5 mm (0.2 in), and 7 mm (0.28 in) with the same embedment length of 10 in. are used in the test. Although Brik investigated the bond strength between the modified basalt bars, the author compared the ultimate moment capacity of concrete beams reinforced with BFRP bars and calculated the ultimate moment capacities according to ACI 440 (Brik, 2003). They conclude the bond between BFRP bars and concrete was satisfactory due to multiple observations: (1) the ultimate moment was significantly higher than the first cracking moment in all the beam specimens; (2) the observed difference in deflection was easily noticeable, indicating enough ductility; and (3) the majority of the beams had principal flexural failures, and few of them had subordinate shear failures. In other words, they suggested that basalt bars are relevant for reinforced concrete structures.

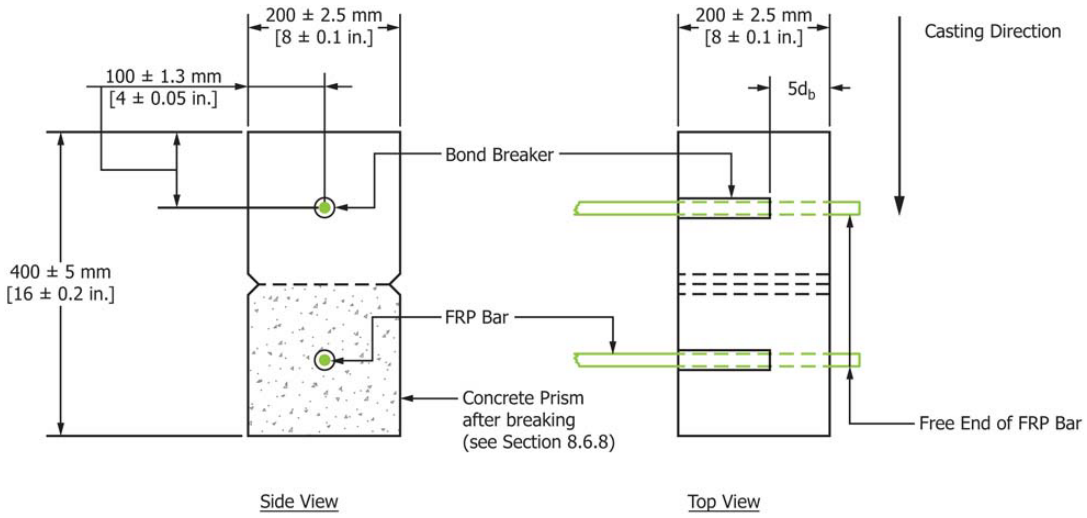

Figure 3: Pull out testing specimen.

2.3.3 Beams reinforced with BFRP bars

By definition, a beam is a structural element that primarily resists applied loads and self-weight perpendicular to the central axis of the member by internal moments and shears, with a negligible axial load. The FRP reinforced concrete element's flexural design is close to the design of the steel-reinforced concrete member. Existing ACI 440 (2015) and the studies done by Faza and GangaRao, Nanni, GangaRao, and Vijay agreed that the flexural design of FRP reinforced concrete members could be quantified based on a similar assumption to those made for members reinforced with steel bars (Faza & GangaRao, 1993; Nanni, 1993).

Ovitigala et al. tested eight beams reinforced with BFRP bars by changing the reinforcement ratio to the balanced reinforcement ratio (ρ_f/ρ_{fb}). The tested specimens have ratio ranges between 1.42 and 10.69 (Ovitigala et al., 2016). The failure in all beams was by the crushing of concrete in the compression zone, and the ultimate strain difference with the post-cracking strain of the flexural BFRP bars agrees with the ACI 440.1R. The prediction of the effective moment of inertia of the beam section using ACI.1R was conservative compared to the experimental results. Gribniak et al. tested four beams of the exact dimensions under the same conditions to failure, retrofitted them with BFRP sheets, and noticed approximately 40% recovered strength (Gribniak et al., 2015). Elgabbas et al. also tested eight BFRP concrete beams of the same dimensions up to failure and concluded that ACI 440 underestimated the deflection at

service load (Elgabbas et al., 2016). Kara et al. tested three continuously and two simply supported concrete slabs reinforced with BFRP bars and concluded that continuously supported slabs recorded wider cracks and far huge deflection than the steel-reinforced slabs due to the lower modulus of elasticity of BFRP bars (Fatih Kara et al., 2017). To limit the crack width and deflection at service loading, prestressing the BFRP bars represents an ideal solution for this issue. Twelve large-scale beams were tested by Atutis et al. by changing the degree of prestressing of the BFRP bar to enhance its behavior as a composite material (Atutiset al., 2017).

Here are basic suggestions in flexural design for steel reinforcement summarized by the following:

- No lateral displacement, out-of-plane failure, or torsion is permitted.
- The concrete and the reinforcing bar are perfectly bonded. Thus, reinforcement and concrete have the same strain at the same level.
- The stresses in concrete and the reinforcement can be computed using stress-strain curves of concrete and steel.
- Ignore the tensile strength of concrete in flexural strength calculations.
- Failure of concrete is assumed to occur when the maximum ultimate compressive stain is 0.003 (ACI 440.1R-15, 2015).

The use of FRP bars as reinforcement for concrete structures is expected to increase in the future. Many researchers have done studies investigating the performance of FRP as the main reinforcement. In contrast, few studies have been conducted to study the shear behavior of concrete elements reinforced with FRP bars with and without FRP stirrups. Limited studies examine the shear behavior of concrete beams reinforced with BFRP bars. Since shear failure is sudden and brittle, the element should be designed to ensure that the shear strength is greater than or equal to the flexural strength at all beam points.

The relative improvement of beam action, arch action, and magnitude of shear reinforcement control the nature of shear resistance of reinforced concrete beams. The concrete blocks created between flexural cracks at the shear span act as cantilevers

restricted by the beam's compression zone and specify the beam's action. Fenwick and Paulay stated that when the load creates diagonal cracking at the shear span, the beam action becomes destroyed (Fenwick & Pauley, 1968).

2.3.4 Tensile Creep Rupture

Generally, the creep behavior of any material is done by applying a constant load under a specific temperature and elongation recorded versus time. Limited research on creep behavior has shown that accelerated environmental conditioning alters creep's dominant dynamics (Scott et al., 1995). After applying a load, the embedded reinforcement in a structural element is subjected to sustainable tensile stress. Singhvi and Mirmiran concluded that environmental circumstances could decrease the FRP bars' stiffness and, therefore, lower the FRP-concrete bond, which leads to a reduction in the post-cracking stiffness of the beams (Singhvi & Mirmiran, 2002). The lower the modulus of elasticity of FRP bars, the more pivotal the overall creep characteristics.

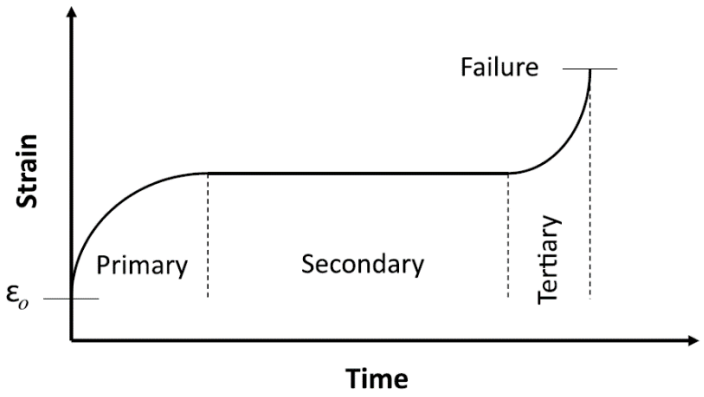

Figure 4: Typical creep strain versus time.

Far from the structural complication, it is well accepted that manufacturing parameters also govern the polymeric materials' creep behavior. Plaseied and Fatemi showed that curing conditions play an essential role in changing thermoset polymers' creep properties (Plaseied & Fatemi, 2009). Moreover, curing vinyl esters at room temperature has a higher creep effect (i.e., lower creep resistance) than the vinyl esters that are post-cured at 93°C (200°F) (Plaseied & Fatemi, 2009; Bradley et al., 1998).

Banibayar and Patnaik (2015) conducted an accelerated creep rupture test of BFRP bars. The test was held under an elevated temperature and in an alkaline

environment. Fifteen BFRP bars were subjected to a stress level between 20% and 80%. Values of 0.28 and 0.18 ultimate creep rupture coefficients are found for 5- and 50-years endurance time, respectively. They commented that the ACI 440 approach of using one creep rupture limit corresponding to 50-year service life for all structures is conservative. Wang et al. (2014) investigated the creep behavior of basalt fiber reinforced polymer tendons for prestressing application. A 52% stress level limit for prestressing applications is recommended based on 95% reliability. Shi et al. (2015) evaluated the creep behavior enhancement pretension treated BFRP tendons. They found that these tendons can sustain a 0.7 stress level for 1000h endurance time, 17% higher than the untreated BFRP tendons.

2.4 Cost Analysis

Life cycle cost analysis (LCCA) is used to compare how economic FRP composites are to conventional materials (Ehlen, 1997; Nystrom et al., 2003). These are expressed in models for estimation of life-cycle cost (LCC) in FRP composites as simulated by Hartman et al. (Hartmann et al., 2000) and Nathan and Onyemelukwe (Nathan & Onyemelukwe, 2000). Since the mentioned studies lacked historical data on costs of FRP maintenance, repair, and rehabilitation (MR&R) actions, many assumptions were considered to analyze the future MR&R costs of FRP composites. Therefore, further research must be conducted to enhance the model estimate of LLC in FRP composites.

Even though research concerning LCC issues in newly developed materials is just beginning, there is a vast amount of research relating to life-cycle management and life-cycle maintenance costs, including LCCA in conventional materials used in civil infrastructure (Estes & Frangopol, 2001; Hong et al., 2007). These studies are useful to assess the optimal LCC of FRP bridge deck panels.

2.5 Bridge Deck Prototype Testing

Concrete deck slabs deteriorate quicker than other bridge elements due to their direct exposure to harsh environmental factors, such as wet-dry cycles, freeze-thaw

cycles, deicing chemicals, traffic loads resulting, and corroded steel reinforcement. This corrosion signifies the importance of deck cracking and delamination when accounting for traffic disruptions and rehabilitation costs (Bradberry, 2001; Stone, Nanni, & Myers, 2001; Nanni & Faza, 2002; El-Salakawy, Benmokrane, & Desgagné, 2003; El-Salakawy et al., 2003; Huckelbridge & Eitel, 2003).

Because FRP rebar is more economical than steel reinforcement, it is more apparent in infrastructure usage and construction. Many concrete bridge decks have been constructed in North America with FRP composite reinforcements (Joffre Bridge in Sherbrooke, Wotton Bridge in Wotton, Magog Bridge, Cookshire-Eaton Bridge, Val-Alain Bridge, Morristown Bridge in Vermont, bridge on Pierce Street in Lima, Ohio, Salem Avenue in Dayton Ohio, Rollins Road in Rollinsford, Sierrita de la Cruz Creek in Potter County Texas, 53rf Avenue in Bettendorf Iowa, Bridge Street in Southfield Michigan, Highway 151 in Waupun Wisconsin, and Route Y in Boone County Missouri). Most of these bridges were constructed using GFRP reinforcing bars. The Canadian Highway Bridge Design Code CAN/CSA-S6-00 (Bakht et al., 2000) discusses FRP composite reinforcement as prestressed and non-prestressed reinforcement for concrete bridges (barrier walls, slabs, and girders) in Section 16. Also, various codes and design guidelines for concrete structures reinforced with FRP bars were published. Punching shear failure occurred in six tested edge-restrained concrete bridge decks reinforced with BFRP (16 mm bars at 600 mm and 300 mm) and shows the deck's behavior under concentrated load (Elgabbas et al., 2016). Results show that top reinforcement has no significant effect on the behavior of the deck and BFRP-concrete bond. It also recommended reducing the reinforcement bar size and spacing to limit the crack width and enhance the bond strength between concrete and bars. Ultimate capacity was increased by 31.9% as well, as compared with an unrestrained slab.

The behavior of steel-RC deck slab systems has been considerably studied; however, only a few studies have considered the behavior of restrained concrete deck slabs reinforced with glass-and carbon- FRP bars (Hassan & Rizkalla, 2004; El-Gamal, El-Salakawy, & Benmokrane, 2005; El-Ragaby et al., 2007; Bouguerra et al., 2011; Zheng, Yu, & Pan, 2012). These studies reported initial structural action in the slabs resisting concreted wheel loads as an internal arch action mechanism rather than the

assumed traditional flexion action. This arch action produces an internal compressive dome, resulting in a punching shear failure mode. Using FRP as reinforcement can fulfill strength serviceability and decrease the reinforcement used in deck slabs. These studies have prompted the industrial usage of FRP as the primary reinforcement in bridges (AASHTO, 2009).

University of Sherbrooke's Department of Civil Engineering conducted a large-scale research project to inspect the long-term and short-term characteristics of freshly developed BFRP bars. This was an initial step in introducing and using these new materials more broadly in pilot projects, FRP design codes, and material specifications. The project studied one type of BFRP tendon and five different types of BFRP bars. The results obtained from this project confirm the feasibility of producing new BFRP bars for structural concrete elements with physical and mechanical properties meeting ACI 440.6M and CAN/CSA S807 requirements (Vincent & Vincent, 2013; Elgabbas et al., 2013).

Eight lightweight concrete bridge decks were tested by Dr. Issa at the University of Illinois at Chicago research lab with a different reinforcement ratio. The test results indicated that the shear failure mode was dominant, and the reinforcement ratio affected the crack's width.

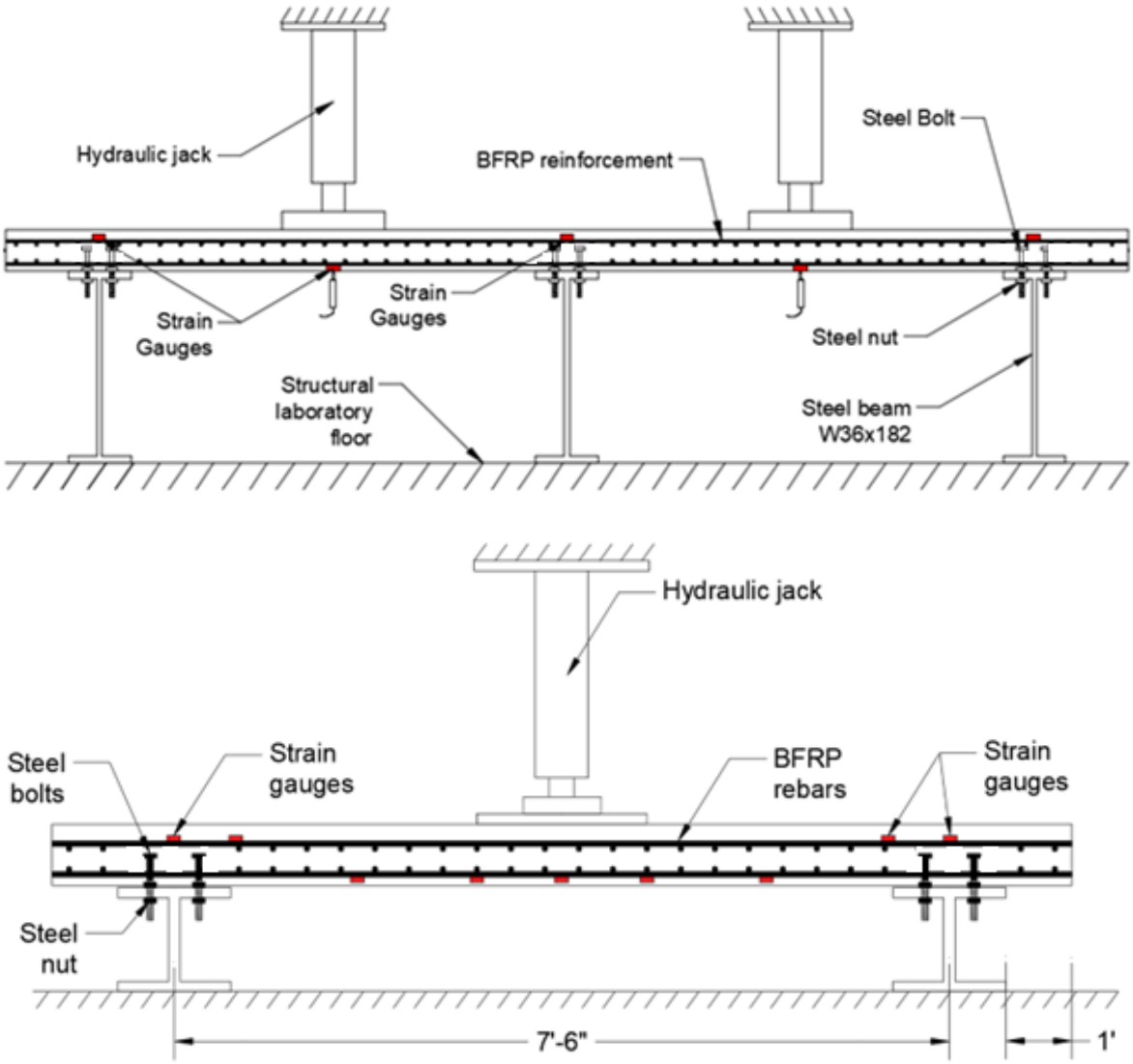

Figure 5: Bridge deck testing setup

Chapter 3

3 Experimental Program

The experimental tests were carried out on BFRP bars with a sand-coated surface with a vinyl-ester resin material to study the short- and long-term properties. This research project's findings will help standardizing this new FRP rebar into ACI 440.1R and other standards.

3.1 Tensile properties

The BFRP bars of diameters: ½ in, ⅝ in, and ¾ in (bars #4, #5, and #6) were tested to determine the mechanical properties, which include the tensile strength, rupture strain, and modulus of elasticity. The widely accepted method of anchoring FRP bars using steel tubes filled with epoxy, as stated in ASTM D7205M (2016) and ACI 440.3R (2015) guidelines, was used. The required dimensions of the tensile test specimens are presented in the ASTM D7205 (2016) standards. ASTM requirements include that the steel tube length is 15 in. for bars #4 and 18 in. for bars #5 and #6, and the free length shall not be less than 40 times the bar diameter of 15 inches. The material used for bonding between the steel pipe and the bar was expansive grout that is usually used for breaking big rocks and concrete, but it can be used for gripping. The technicians attached a strain gauge and an extensometer to each BFRP bar to measure the tensile strain, and the readings recorded from both were consistent.

The specimens were tested using a closed-loop universal testing machine of 400,000-pound capacity. The sample was mounted on the testing machine so that the longitudinal axis of the specimen coincides with the line joining the two anchorages fitted to the testing machine, so the bars need to be perfectly aligned to distribute the stress equally all over the section. A special wooden frame was made to maintain a perfect alignment during the sample preparation, as shown in Figure 6. The specimen was gradually and loaded continuously at a 35 ksi/minute rate until failure so that the sample would fail between one and ten minutes as the ASTM D7205 standard requires.

Figure 6: Tensile test sample preparation and test setup.

The curves in Figures 7, 8, 9, and 10 show the stress-strain behavior of the BFRP, which is perfectly linear until failure because of the brittleness of the BFRP bars. Figure 11 shows the mode of failure in the bars of different sizes. It was noticed that after reaching the maximum load, the bar undergoes sudden failure, indicating the brittle nature of the BFRP bars. Any structural design of any reinforced concrete element design should avoid the bar's failure.

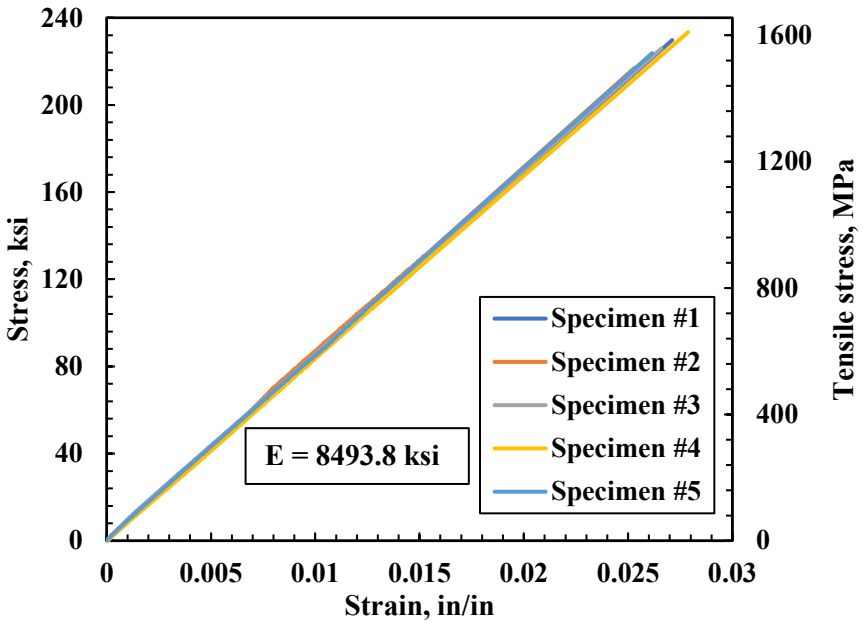

Figure 7: Stress-strain curves of tensile test of bar #4.

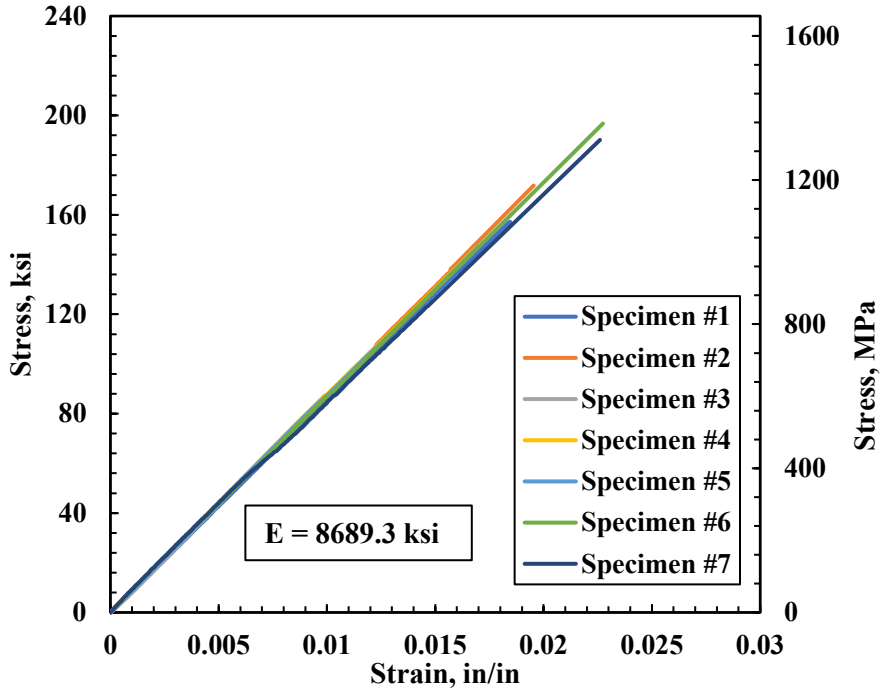

Figure 8: Stress-strain curves of tensile test of bar #5.

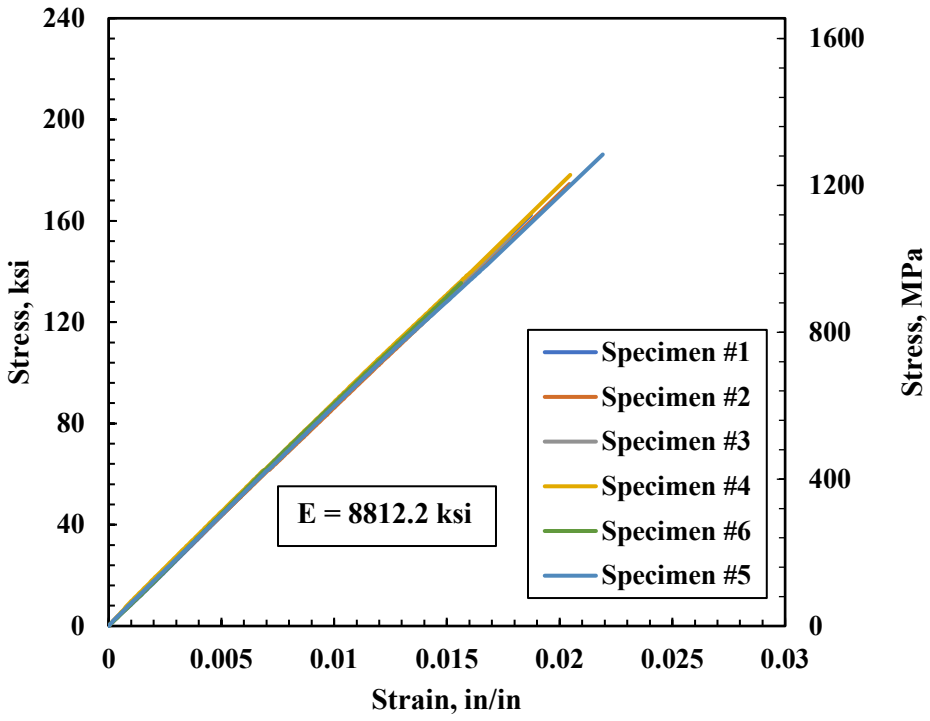

Figure 9: Stress-strain curves of tensile test of bar #6.

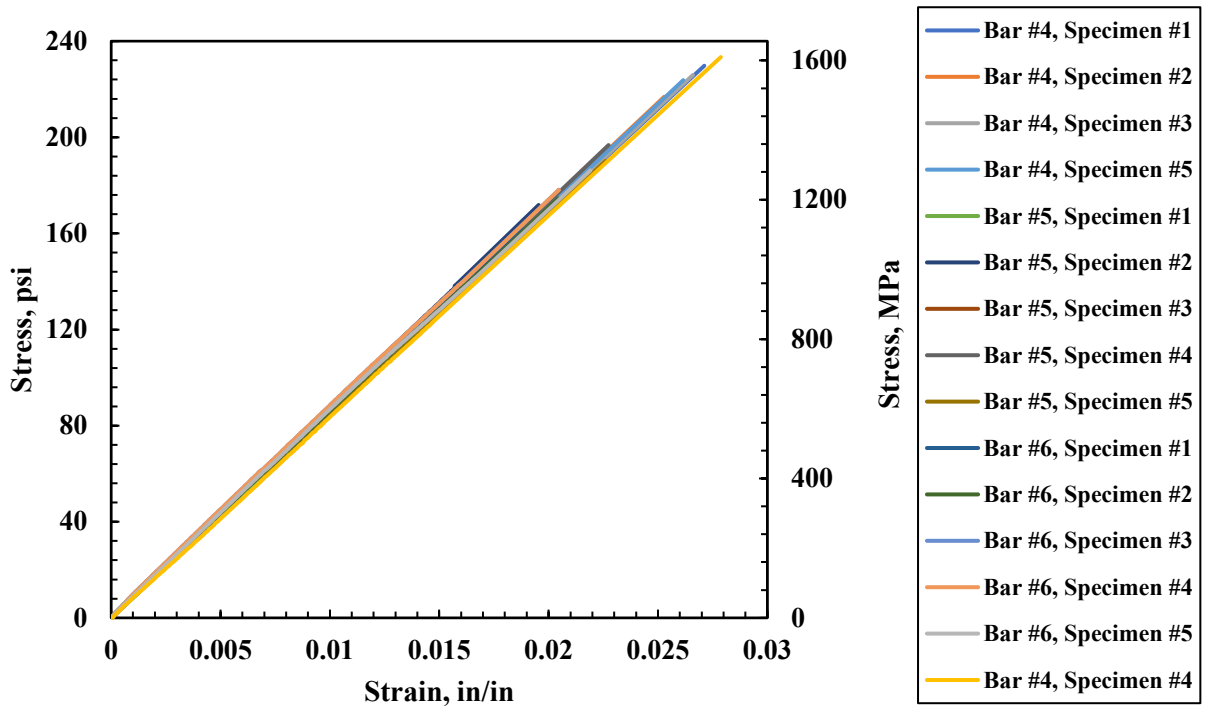

Figure 10: Stress-strain curves for tensile tests of all bar sizes.

Two of the tensile tests of #5 bar and one for #6 had a bond failure, so they won't be counted in the calculation of the ultimate stress but can be used for the modulus of elasticity calculation. The extensometer was taken off from the sample before failure to prevent any damage to it.

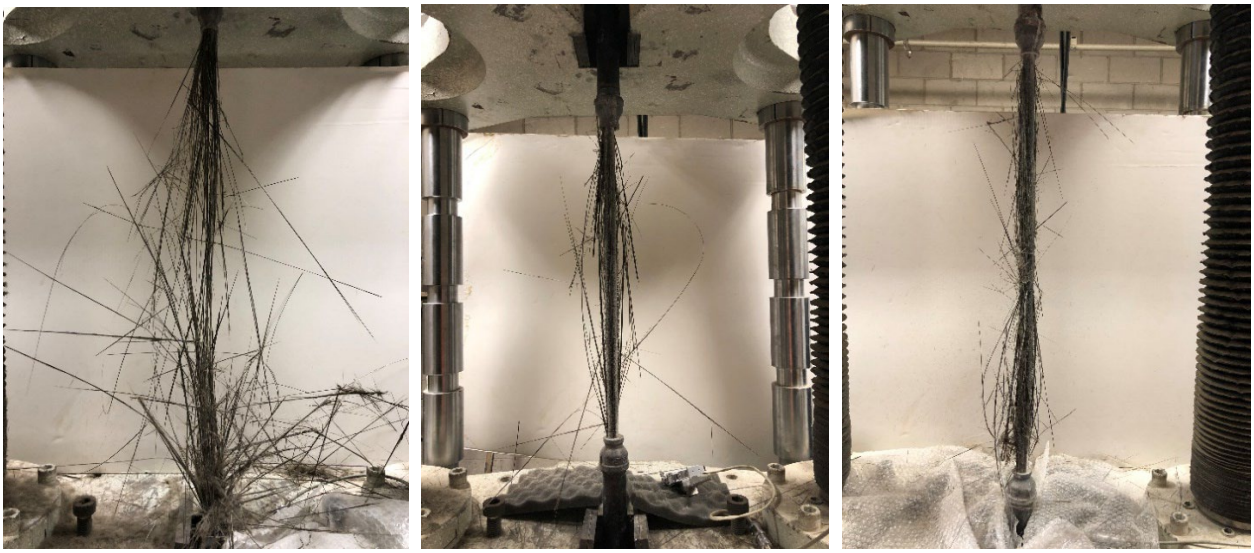

Figure 11: Modes of failure for bars #4, #5, and #6.

According to ASTM D7205, five samples of each bar size shall be tested, and the modulus of elasticity, the ultimate strength, and the ultimate strain need to be reported, as well as any anomalies noticed during testing. Table 1 shows the different bar size properties.

Table 1: Tensile test results.

Bar size	Sample #	Tensile modulus of elasticity, ksi	Average, ksi	Tensile stress, ksi	Average, ksi	Standard deviation, ksi	Ultimate strain, %	Average, %
4	Sample 1	8473		230			2.71	
4	Sample 2	8576		217			2.53	
4	Sample 3	8494	**8494**	226	**226**	**5.6**	2.66	**2.66**
4	Sample 4	8372		233			2.78	
4	Sample 5	8555		224			2.62	
5	Sample 1	8583		209			2.43	
5	Sample 2	8695		214			2.45	
5	Sample 3	8563	**8674**	203	**202**	**9.5**	2.37	**2.35**
5	Sample 4	8725		197			2.27	
5	Sample 5	8802		190			2.26	
6	Sample 1	8713		162			1.87	
6	Sample 2	8729		175			2.04	
6	Sample 3	8808	**8798**	154	**171**	**11.6**	1.78	**1.98**
6	Sample 4	8969		178			2.04	
6	Sample 5	8774		186			2.19	

As shown in the table above, the ultimate tensile strength decreases with the increase in bar size from 226 ksi to 171 ksi for bar numbers four and five, respectively. This phenomenon is due to the stress distribution in the bar section, so the bar's core will be less stressed. This phenomenon is called the shear lag. The modulus of elasticity increases with the bar size increase from 8494 ksi to 8798 ksi for bars #4 and #6, respectively. All the testing results satisfy the minimum modulus of elasticity required as per ASTM D7957 is 6500 ksi and 108, 94, and 93 ksi for bars #4, #5, and #6, respectively. Elgabbas et al. tested three different types of BFRP bars from different fiber and bar sources for tension and concluded that the maximum tensile stress is 243, 240, and 227 ksi for types A, B, and C, respectively.

According to ACI 440.1R, the design of an FRP member should be based on the guaranteed tensile strength, which is the average tensile stress minus three times the standard deviation. In this case, the guaranteed tensile strength will be 209, 160, and 136 ksi for bars #4, #5, and #6, respectively. Kampmann et al. tested five different types of BFRP bars from different fiber and bar sources and concluded that the smaller the cross-sectional area, the higher tensile stress will be obtained except for type A. The variation of the ultimate tensile stress of the tested BFRP bars as a function of bar size is shown in Figure 12.

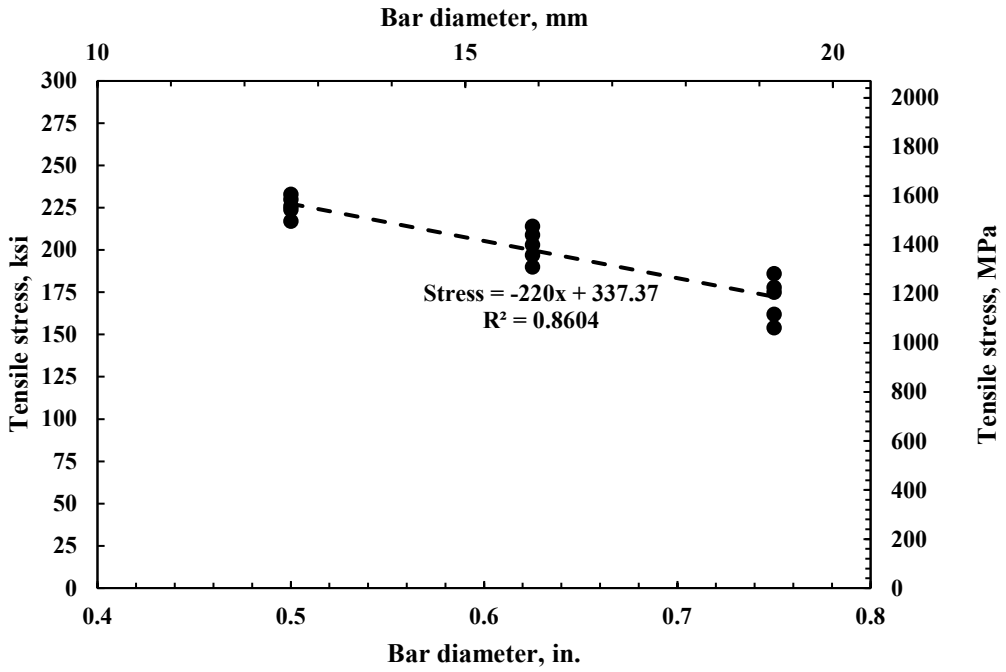

Figure 12: Tensile stress versus bar size curve.

As shown in this figure, the trendline predicts the ultimate tensile strength, which varies with the variation of the bar size. For instance, the predicted ultimate tensile strength of bar #7 is 143 ksi with a 0.86 coefficient of determination.

Acceptance criterion:

FRP bar's failure is a sudden and catastrophic failure with a linear stress-strain relationship; the difference in fiber contents and non-standardized production affect the fiber content and the bar's actual diameter for the commercially available glass and basalt

FRP bars. Any tensile test results must satisfy the acceptance criteria of tensile strength for better material production and quality. An existing acceptance criterion for tensile strength of glass FRP bars, without generalization of this criteria for basalt FRP reinforcing bars, is implemented in ACI 440.1R-15. The acceptance criterion is defined as the guaranteed tensile strength, which is the average tensile strength minus three times the standard deviations (Eq. 1), and the guaranteed tensile modulus of elasticity, which is defined as the average of the measured elastic modulus of the tested samples.

$$f_{fu}^{*} = f_{fu_{average}} - 3\sigma \qquad Equation\ (1)$$

The guaranteed tensile strength f_{fu}^{*} corresponds to the 99% of confidence (Rossini et al. 2018), so the error percentage will be less than 1%. The fiber content is a significant factor that indicates the bar's tensile strength. In concrete design, the bars need to be tested for tension for quality assurance and safe construction structures. If not, the design strength f_{fu}' should always be less than the guaranteed tensile strength of the same lot that the bar has been used for construction.

$$f_{fu}' < 0.95\ f_{fu}^{*} \qquad Equation\ (2)$$

Despite the fact that the majority of the strength values for the basalt FRP reinforcing bars tested in this study showed that they perform better with 100% above the guaranteed tensile strength, the general material behavior appeared to be similar to that of GFRP bars. That means Eq. (2) applies to calculate the guaranteed strength of basalt reinforcing bars for structural design. Accordingly, the tensile modulus of elasticity in Table 1 represents the guaranteed elastic modulus of the tested rebars according to ACI 440.1R-15. The bar chart in Figure 13 shows all the testing results with higher performance and a value greater than the guaranteed tensile strength. Kampmann et al. tested five different bar sources. They concluded that two bar sources did not match the guaranteed tensile strength requirement by ACI 440.1R. These bars are not recommended to be used for any structural purposes.

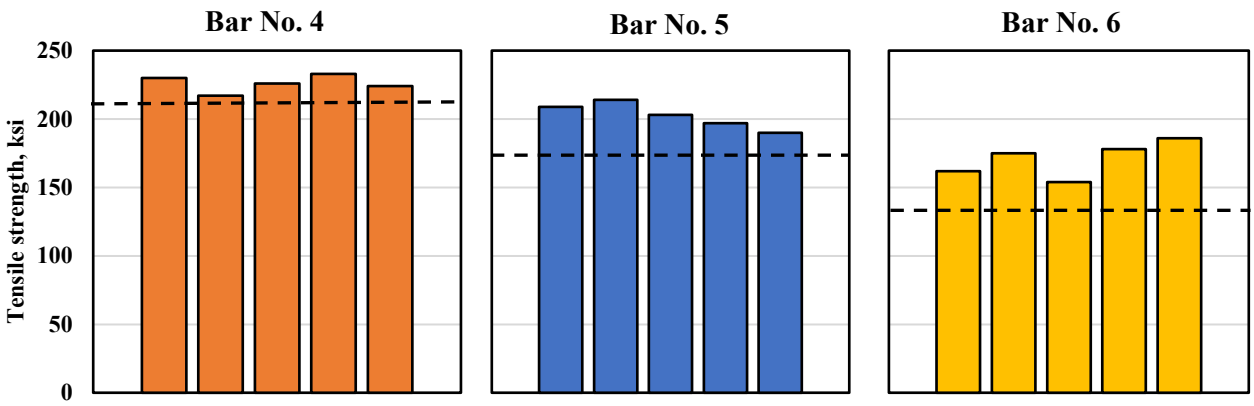

Figure 13: Tensile strength of BFRP bars #4, 5, and 6 compared with the guaranteed tensile strength.

Unlike steel reinforcement, BFRP bars as all the FRP group reinforcement has a linear stress-strain relationship with no ductility. The minimum requirements for the tensile strength in ASTM D7957 are 108, 95, and 93 ksi for bars #4, #5, and #6, respectively, while the minimum requirements for the modulus of elasticity is 6500 ksi. All the tested BFRP bars in this research matches the minimum requirements in ASTM D7957.

3.2 Bond Strength

The bond strength of the BFRP bars with concrete was assessed with the beam hinged and pull-out tests. These tests were carried out in concrete with normal strength of 4 ksi with around 8% air entrainment, which is very suitable for bridge decks in North America and for areas that reach the freezing temperature. This mix matches the Illinois Tollway mix requirements for bridge decks.

3.2.1 Hinged flexural beam test

The experimental program to determine the bond strength of BFRP bars consists of testing twelve beams. The beams are composed of two separate parts joined with the BFRP bar in the tension zone and a special fixture in the compression zone that allows rotation, as shown in Figure 14. When making these wooden forms, special attention was given to keep the spacing between the concrete blocks since space should be strictly compatible with the ball joint's measurement after casting of the specimen. This

space was also maintained with a specially made wooden block after removing the wooden forms to avoid the stresses that can be imposed.

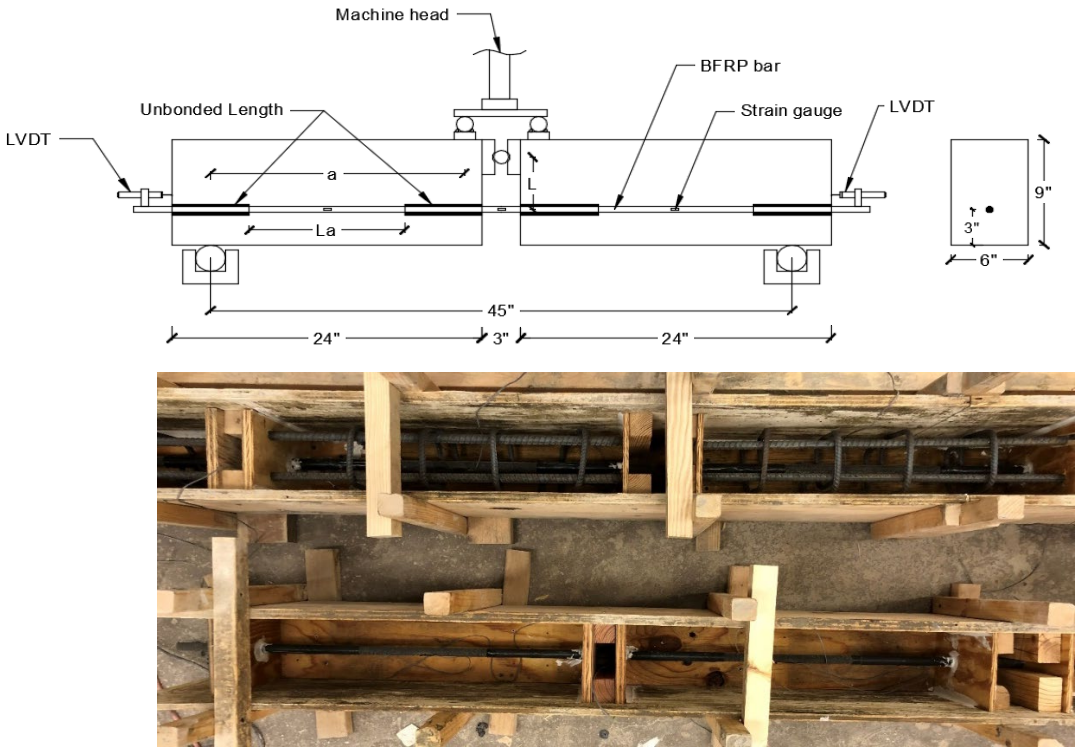

Figure 14: Hinged beam wood forms and testing setup.

The total length of the bars was kept the same. It was adjusted to have a three in. extra length on each side outside the concrete block to attach the two LVDTs (Linear variable Differential Transformer) for measuring the slippage. Figure 14 shows the specimens' details and dimensions (note: d_b = diameter of reinforcement bar, and L = bonded length). The bond lengths were 15 and 20 times the bar diameter ($15d_b$ and $20d_b$) for each bar diameter. Two identical specimens were cast for $15d_b$ specimens and the other two identical beams for $20d_b$ for each bar size. The total length of the BFRP bars was 60 in. long and placed at three in. distance above the specimens' bottom surface. The strain gauges were instrumented on each BFRP reinforcement bar to measure the bars' strains during testing. The twelve hinged beam specimens were instrumented with three strain gauges at the center and the other two at the bonded length of the BFRP bar on both sides, as shown in figure 14. The intended unbonded sections were covered with thick electric tape for more than five layers to prevent any bonding between the concrete and the BFRP bar at the specific intended unbonded

areas. Each wooden form was divided into two main sections for concrete pouring. LVDTs were attached to the extended part of the BFRP bar and mounted against the concrete end surface to measure the bond slip, as shown in Figure 15. The strain gauges, LVDTs, and the load cell were connected to the data logger to collect the strain readings, the bond slip at the end of the beam, and the loads' corresponding readings. The applied loading rate was 0.15 in/min, and it was kept constant and continued until the BFRP bar ruptured or the maximum slip measured using the LVDT was reached. Steel reinforcement was used, with two longitudinal bars in the compression zone and four stirrups added to beams of bars #6 to prevent shear failure in the concrete.

Tensile force and stress in the BFRP bar

The tensile force (*T*) exerted on the BFRP bar can be calculated by Eq. (3).

$$T = \frac{Pa}{l} \qquad Equation\ (3)$$

Where, P is the applied force in pounds.

a is the span length in inches.

l is the lever arm in inches.

Then the average bond stress (*u*) can be calculated from Eq. (4) using the tensile force (*T*) found in above Eq. (3).

$$u = \frac{T}{\pi L d_b} \qquad Equation\ (4)$$

where, L is the bonded length in inches.

d_b is the BFRP bar diameter in inches.

Figure 15: Hinged beam and test setup.

Figures 16, 17, and 18 show the bond stress versus slippage of different bar sizes for two bonded lengths ($15d_b$ and $20d_b$).

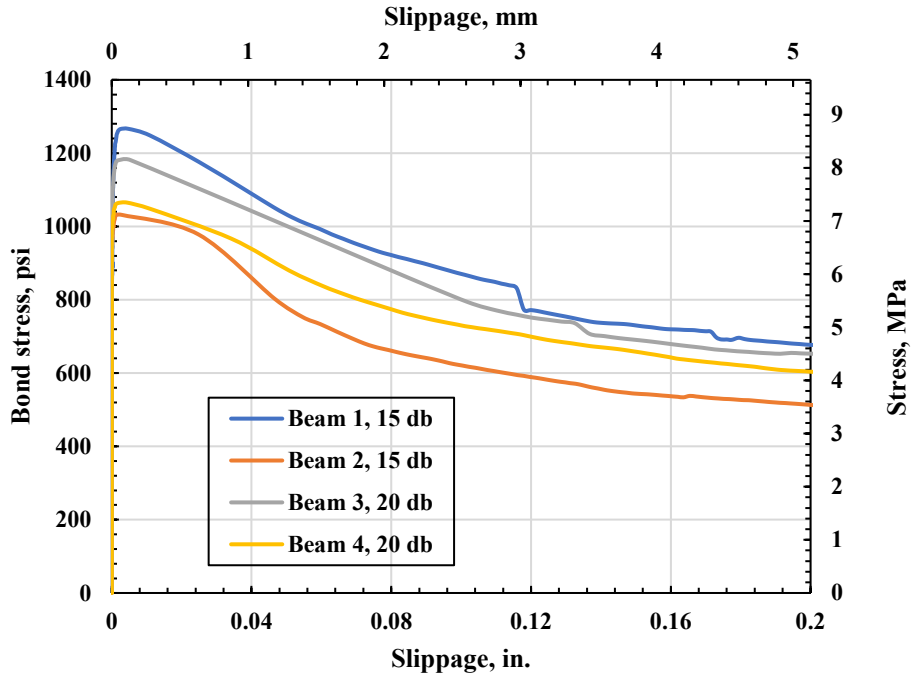

Figure 16: Bond stress versus slippage curves for bar #4.

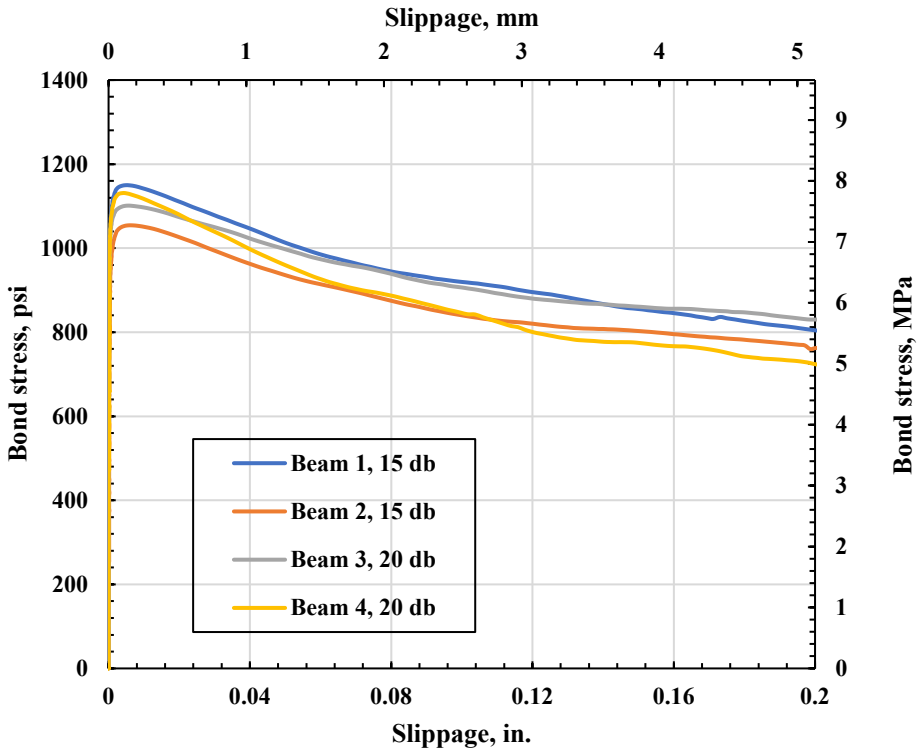

Figure 17: Bond stress versus slippage curves for bar #5.

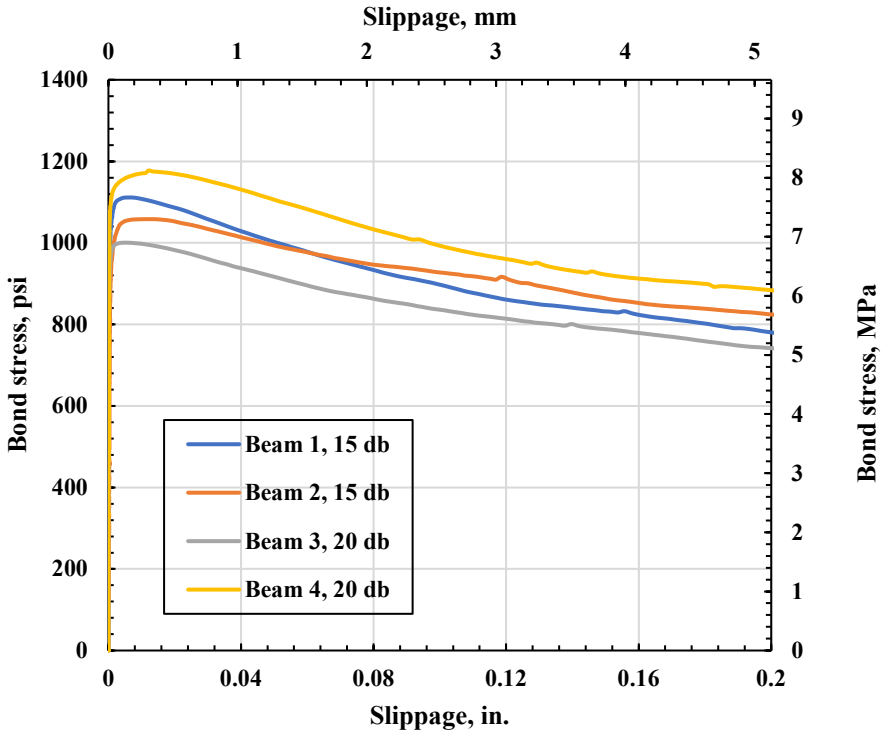

Figure 18: Bond stress versus slippage curves for bar #6.

All the tested beams had a slippage of the bar from concrete, which indicates that the minimum bond length of the BFRP bar with concrete shall be more than $20d_b$. As shown in Table 2, BFRP bars showed average bond stress of 1136, 1109, and 1086 psi for bars #4, #5, and #6, respectively. This indicates that the bond stress decreases with the increase of the bar size. Figure 19 shows the slippage of the bar from the concrete beam. Logically, the bond stress in beam testing should be less than the direct pull-out test results due to the misalignment in the beam testing caused by the deflection of the beam. This test reflects the actual behavior of BFRP bars in the real concrete beams.

Figure 19: Slippage of BFRP bar from concrete.

Table 2: Hinged beam test results.

Bar size	Sample #	Maximum tensile force, kips	Bonded area, in^2	Maximum bond stress, psi	Average bond stress, psi	Standard deviation, psi	Coefficient of variation, %
4	Sample 1	14.9	11.77	1266	**1136**	108	9.5
4	Sample 2	12.2	11.77	1032			
4	Sample 3	18.6	15.7	1181			
4	Sample 4	16.7	15.7	1065			
5	Sample 1	21.2	18.4	1150	**1109**	42	3.7
5	Sample 2	25.8	18.4	1054			
5	Sample 3	27.0	24.5	1101			
5	Sample 4	20.8	24.5	1131			
6	Sample 1	29.5	26.5	1111	**1086**	76	6.9
6	Sample 2	28.1	26.5	1054			
6	Sample 3	35.4	35.3	1000			
6	Sample 4	41.6	35.3	1178			

3.2.2 Pull-out test

The pull-out test is composed of pulling the BFRP bar from an 8 in. x 8 in. x 8 in. concrete cube with a bonded length of $5d_b$. The BFRP bar needs to be perfectly aligned and perpendicular to the concrete's surface to prevent any stress concentration in the bar sides bonded to concrete. The BFRP bar has an extra length of three inches from the concrete cylinder to attach the LVDTs for measuring the slippage at the end. The other end of the bar is embedded into a steel tube gripped to the machine, using the same bonding material as the tensile test (expansive grout).

A total of fifteen samples (five samples for each bar size) were fabricated and tested using Tinius Olsen Universal Testing Machine 400,000-pound capacity. The concrete compressive strength was tested in accordance with ASTM C39, and the results are shown in Table 3, with an average compressive strength of 4056 psi. The percentage of air entrainment in the concrete is 7%. Figure 20 shows the specimens preparation and test setup. The upper part of the machine grips the steel pipe that has been used for anchoring, and the fixed lower part holds the concrete cube while pulling the BFRP bar. The non-loaded end of the bar is connected to an LVDT to measure the BFRP bar slippage from the concrete cube.

According to ASTM D7913, the pull-out testing specimen can either be single casted (vertical or horizontal) or two FRP bars casted into one horizontal prism. The specimens in this research project were single-casted since the concern is on the effect of a single bar. The corners and the edges of the wood form were sealed with silicon to guarantee a watertight mold. Because the mold provides the embedment length, the non-bonded area had to be controlled by a bond breaker by wrapping the bar with tape at least seven times to ensure the separation of the bar from the concrete after casting. Figure 20 shows the wood mold before and after casting the concrete, the bar's non-bonded length, and the testing setup.

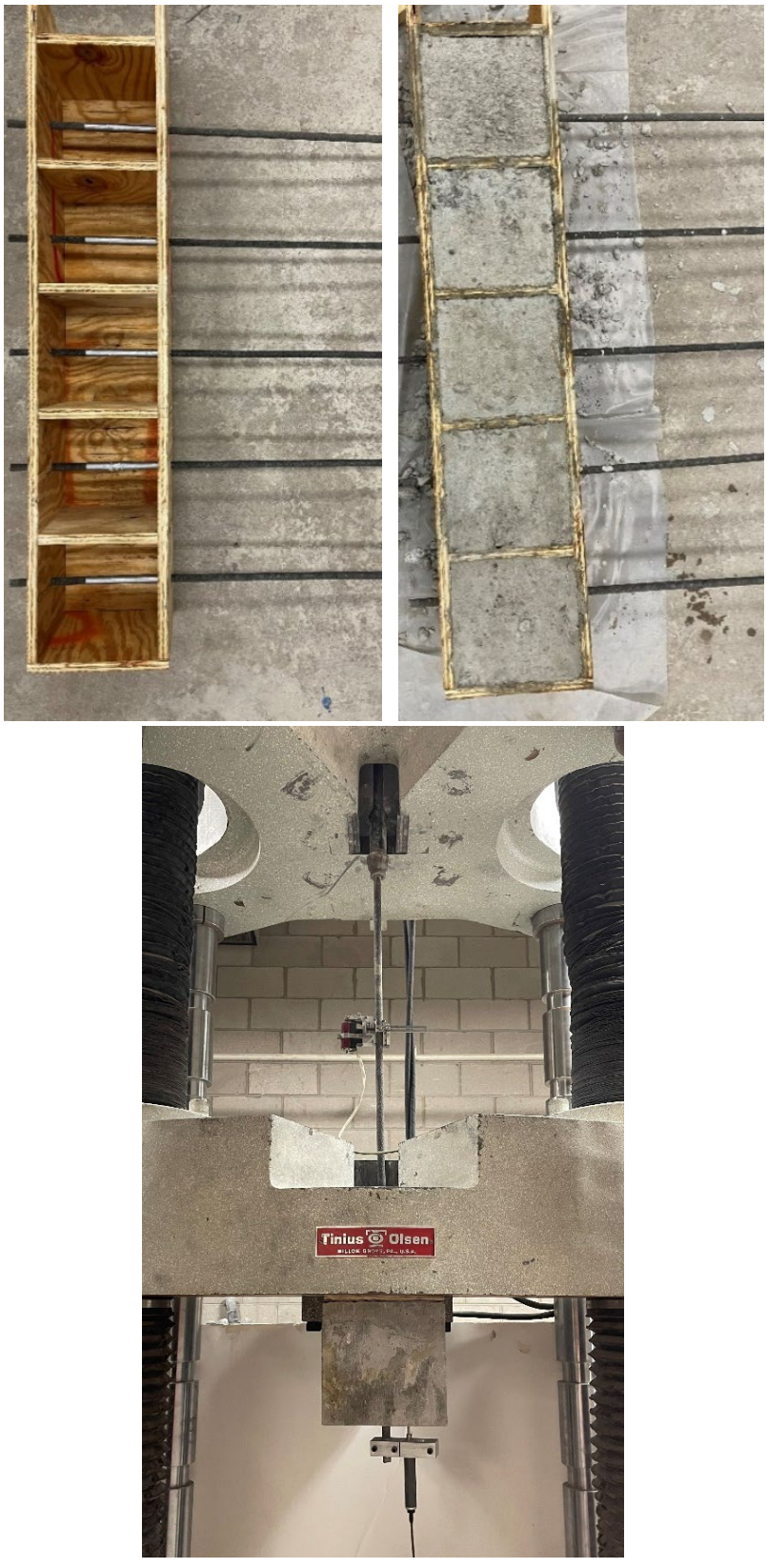

Figure 20: Sample’s preparation and testing setup.

Table 3: Concrete compressive strength.

Specimen #	Compressive strength, psi	Average Compressive strength, psi	Standard deviation, psi	Coefficient of variation, %
1	4160			
2	4070	**4056**	110	2.7
3	3940			

Figure 21 shows the bond stress versus slippage curves of BFRP bars #4, #5, and #6. Inspection of Figure 21 reveals that the bond stress increases with the increase of the applied load until a bond-slip failure of the BFRP bar occurs. The testing condition was at room temperature of 73ºF and average humidity of about 50%. The primary failure mode was the loss of bond versus slippage between the bonded bar and the concrete substrate due to pull-out from the concrete block. The bond stress is computed by dividing the applied force to the bonded area, according to Equation (5):

$$\mu = \frac{\boldsymbol{P_u}}{\boldsymbol{\pi . l_e . d_b}^2} \qquad \text{Equation (5)}$$

Where: μ: Bond stress, psi

P_u: Applied load, lb.

l_e: Bonded length, in.

d_b: BFRP bar diameter, in.

The bond stress increases with the increased applied load until a bond-slip failure results in the BFRP bar, followed by a decrease in the bond stress with an increase in bar slippage.

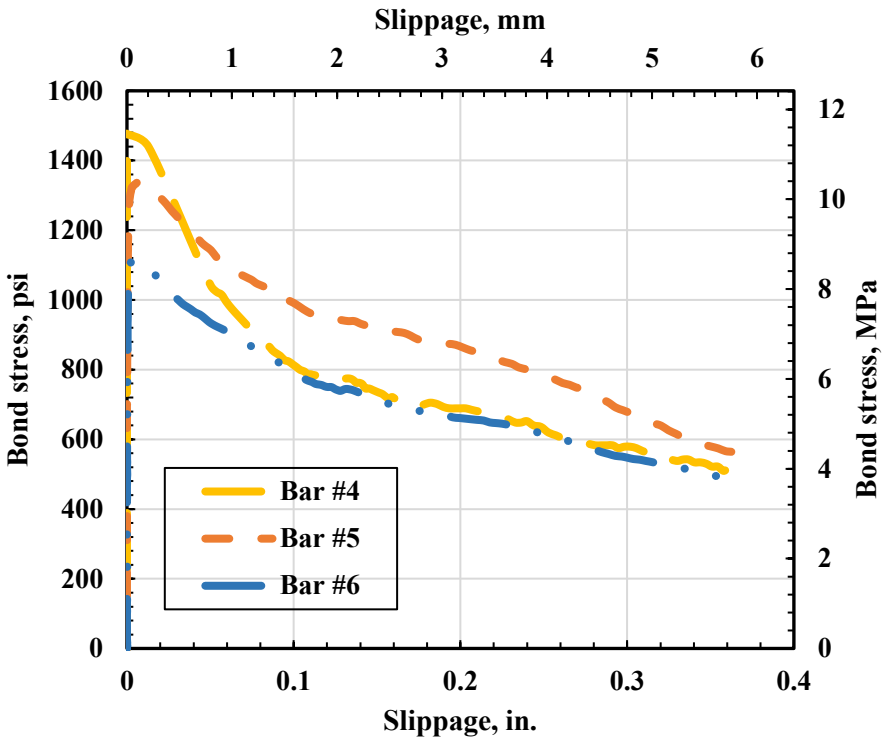

Figure 21: Bond stress versus slippage curve for three different samples for bars #4, #5, and #6.

Table 4: Pullout test results.

Bar size	Sample #	Maximum bond stress, psi	Average bond stress, psi	Standard deviation, psi	Coefficient of variation, %
4	Sample 1	1402			
4	Sample 2	1483			
4	Sample 3	1524	**1484**	181.1	12.2
4	Sample 4	1397			
4	Sample 5	1614			
5	Sample 1	1237			
5	Sample 2	1338			
5	Sample 3	1304	**1273**	101	7.9
5	Sample 4	1212			
5	Sample 5	1273			
6	Sample 1	1215			
6	Sample 2	1116			
6	Sample 3	1163	**1147**	8406	7.4
6	Sample 4	1119			
6	Sample 5	1124			

Table 4 shows that the bond stress of the BFRP bars with concrete decreases with the increase of the bar size, with average bond stress of 1484 psi, 1273 psi, and 1147 psi for bar sizes #4, #5, and #6, respectively. All the indicated bond stress results are higher than the minimum bond stress of 1.1 ksi, as required per the ASTM D7957 standard. Elgabbas et al. tested three different BFRP bar types, and the average bond stress of each bar type was 1.01, 3.68, and 3.95 ksi for types A, B, and C, respectively. Qiaowei et al., Thilan and Issa also tested the bond stress between BFRP reinforcing bars and high-strength concrete (8-9 ksi) and showed that the average bond stress decreases with the increase of the bar size.

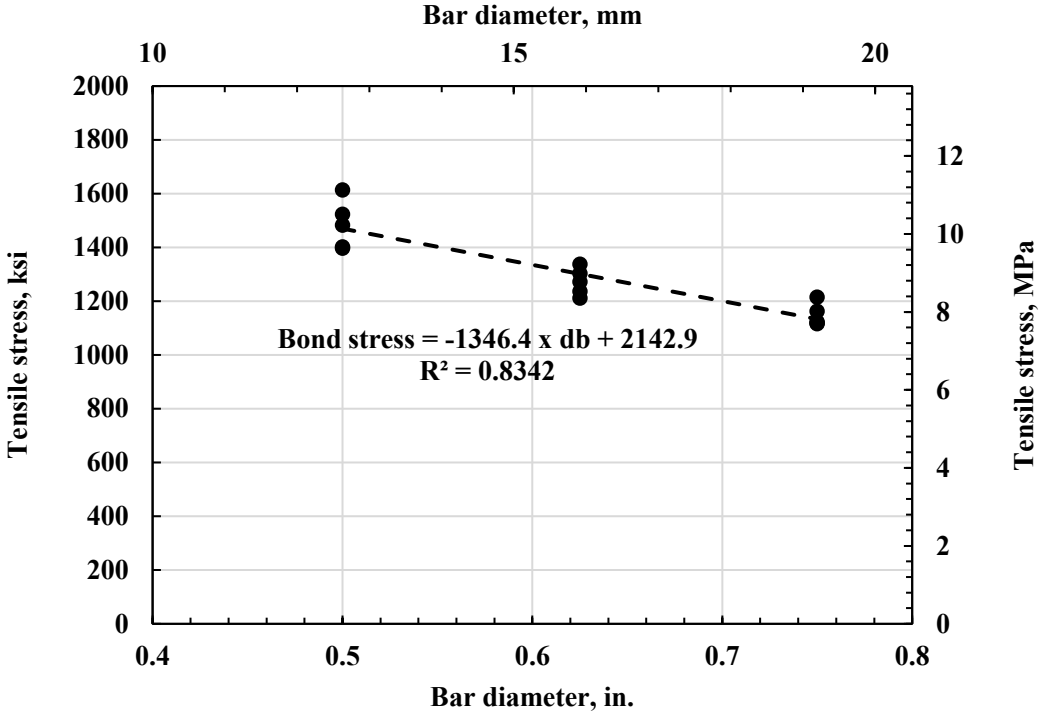

Figure 22: Bond stress versus bar size curve.

Based on the results obtained from the pull-out test, the development length can be calculated from Equation 6 (Equation 10.1a in ACI 440.1R). The equilibrium condition of an FRP bar of development length le is maintained when the resistance force is equal to the ultimate force in the bar. The minimum development length should be $39d_b$, $40d_b$, and $37d_b$ for bar sizes #4, #5, and #6, respectively. Table 5 shows the ultimate stress of BFRP bar sizes #4, #5, and #6.

$\ell_e . \pi . d_b . \mu = A_f . f_f$ Equation (6)

Where: ℓ_e: Bonded length, in.

d_b: Bar diameter, in.

μ: Bond stress, psi.

A_f: Area of the bar, in^2.

f_f: Ultimate stress of the bar, psi.

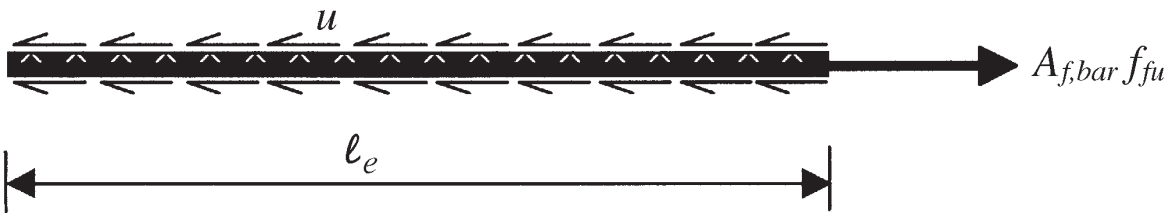

Figure 23: Pullout test schema.

Table 5: Average ultimate tensile strength of BFRP bars.

Bar size	Ultimate tensile strength, ksi
#4	**226**
#5	**202**
#6	**171**

After considering the ultimate tensile strength of the bar sizes, the bonded length of bars sizes #5 and #6 were increased to $40d_b$ and $50d_b$. Table 6 shows the results of eight tested specimens for two specimens of bonded length $40d_b$ and two specimens of bonded length $50d_b$ for bar sizes #5 and #6.

Table 6: Pull-out test results for $40d_b$ and $50d_b$ bonded length specimens.

Bar size	Bonded bar diameter	Bonded length, in	Bonded area, in^2	Maximum bond stress, psi	Mode of failure	Maximum stress in BFRP bar, ksi	Maximum force, lb
#5	$40d_b$	25	49	1066	Bar Slipped	169	8287
	$40d_b$	25	49	983	Bar Slipped	156	7641
	$50d_b$	31.25	61.4	940	BFRP failure	186	11413
	$50d_b$	31.25	61.4	809	BFRP failure	160	9830

#6	$40d_b$	30	70.7	981	BFRP failure	158	11137
	$40d_b$	30	70.7	1089	BFRP failure	175	12370
	$50d_b$	37.5	88.4	846	BFRP failure	170	15001
	$50d_b$	37.5	88.4	844	BFRP failure	169	15969

Note: Ultimate tensile strength of #5 BFRP bar is higher than #6 BFRP bar

The compressive strength of the concrete used is about 6000 psi. The maximum bond stress recorded is less than the maximum stress in the previous test because, with more development length, the maximum bond stress decreases. BFRP #5 bar with $40d_b$ embedded length exhibits a bond-slip with about 1000 psi bond strength, while $50d_b$ embedded length results in a failure in the bar, which reveals that $50d_b$ is an adequate bond length for #5 bar. On the other hand, BFRP #6 bar failed with 40 and $50d_b$, indicating that $40d_b$ is an adequate development length for #5 bar. Figure 24 shows the testing setup and the mode of failure of sample #3 (bar #5 with $50d_b$ bonded length), and Table 7 shows the concrete compressive strength results of the 6x12 in. concrete cylinders.

Table 7: Concrete compressive strength for $40d_b$ and $50d_b$ bonded length samples.

Specimen #	Compressive strength, psi	Average Compressive strength, psi	Standard deviation, psi	Coefficient of variation, %
1	5970			
2	6240	**6163**	168	2.73
3	6280			

Figure 24: Pullout testing setup of $40d_b$ and $50d_b$.

3.3 Transverse shear strength

Even though the transverse shear strength of the BFRP bar is much smaller than the tensile strength, it is still an important parameter because the bar can be used in dowel-like application stirrups or concrete applications. The transverse shear is an indication of the strength of the resin used in bar manufacturing. In concrete design, shear strength is not considered for BFRP bars, and the compressive strength of the BFRP doesn't have any effect according to ACI 440.1R.

A transverse shear test was conducted following ASTM D7617. As required in the ASTM standard, the test fixture comprises two v-block steel pieces with a bar seat and two lower blades that keep the space for the upper blade connected to the machine to apply the load on the bar, as shown in Figure 25. Five specimens of 9-inch lengths were tested under laboratory conditions with an Instron machine equipped with a 50,000-pound load cell for each bar size. The loading rate was a displacement-control of 0.08

in./min for bars #4 and 0.1 in./min for bars #5 and #6 to ensure the specimen's failure between one and ten minutes.

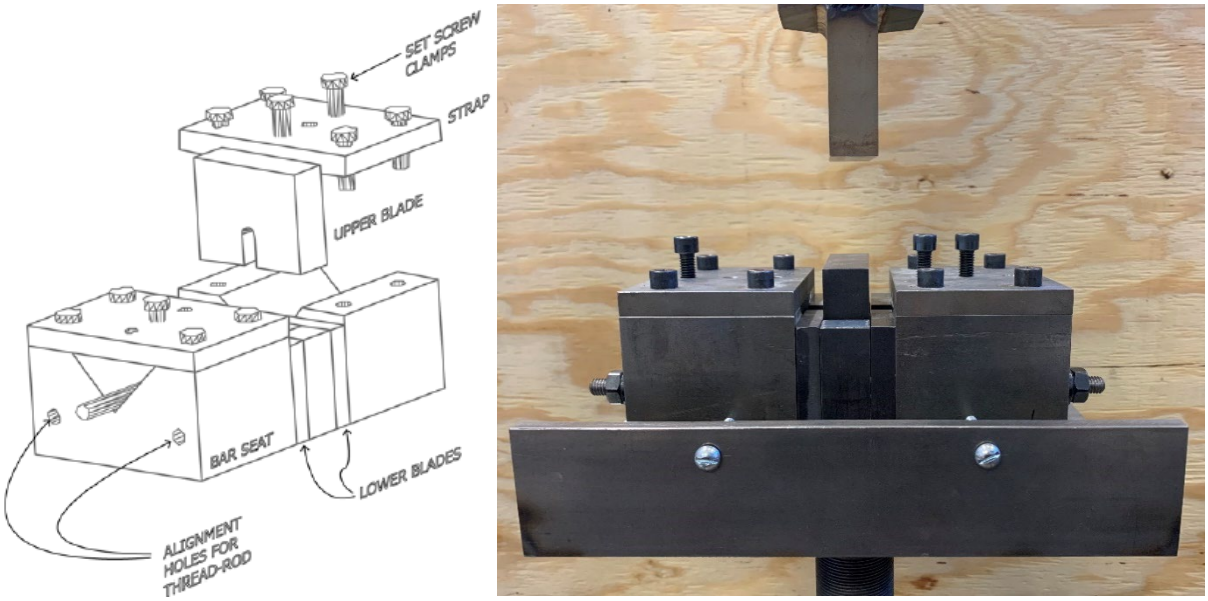

Figure 25 Test fixture and test setup

The transverse shear stress exerted on the BFRP bar can be calculated by Eq. (7).

$$\tau_u = \frac{P_s}{2A} \qquad \text{Equation (7)}$$

where: τ_u is the transverse shear stress, psi.

P_s is the applied load, lbs.

A is the area of the bar, in^2.

Figures 26, 27, and 28 show the shear stress versus displacement behavior of fifteen different specimens of five specimens from each bar size. Figure 29 shows the stress-strain curves of all tested samples of the three different bar sizes.

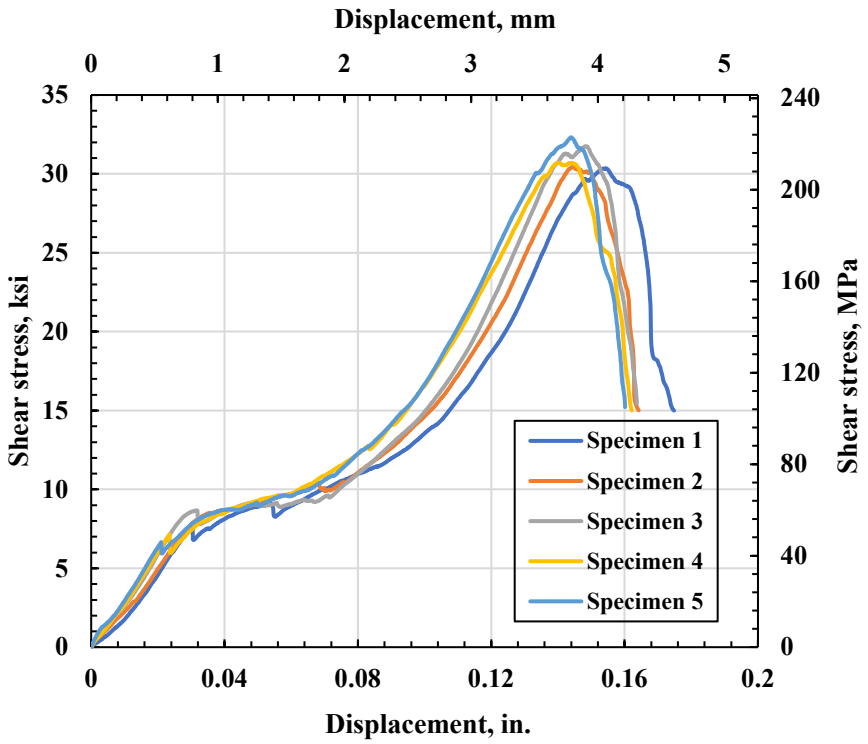

Figure 26: Shear stress versus displacement curves for #4 bar.

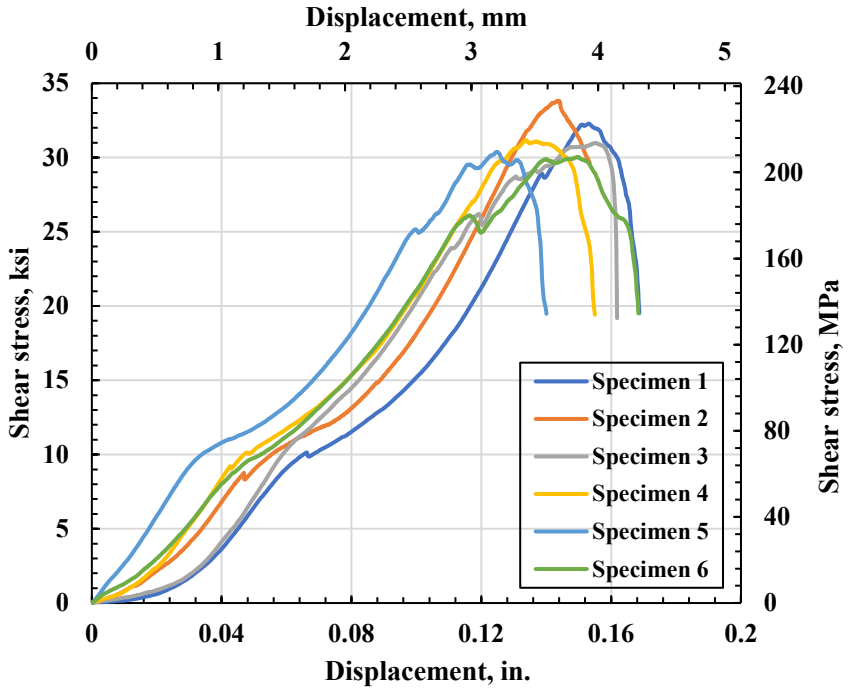

Figure 27: Shear stress versus displacement curves for #5 bar.

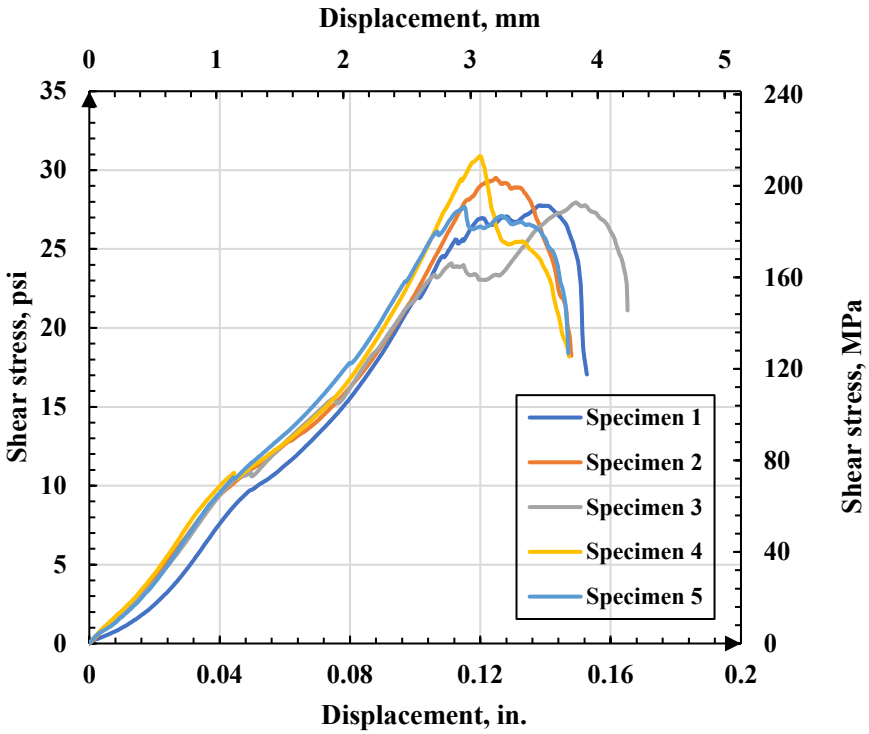

Figure 28: Shear stress versus displacement curves for #6 bar.

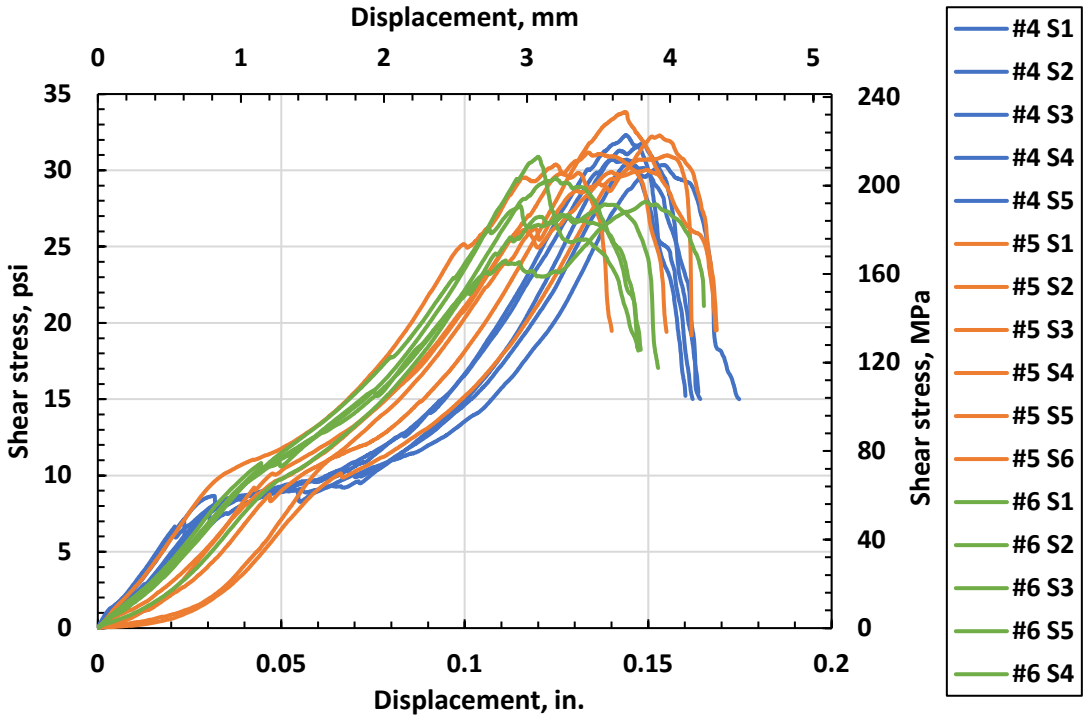

Figure 29 Shear stress versus displacement curves for #4, #5, and #6 bar sizes

The results obtained from the transverse test were presented in graphs and tables, which show the same behavior in stress versus displacement curves of the tested specimens. Figure 29 and Table 8 show that all the tests have almost the same maximum shear stress, with an average maximum transverse shear stress of 29.4 ksi, 30 ksi, and 27.6 ksi for #4, #5, and #6 BFRP bars, respectively. The average shear stress for all bar sizes is about 30 ksi, about 15% of the tensile stress.

Table 8: Shear test results.

Bar size	Sample #	Maximum applied force, kips	Shear area, in^2	Maximum shear stress, psi	Average shear stress, psi	Standard deviation, psi	Coefficient of variation, %
4	Sample 1	12.2	0.40	30,349			
4	Sample 2	12.2	0.40	30,469			
4	Sample 3	11.2	0.40	27,947	**29,465**	1528	5.1
4	Sample 4	12.4	0.40	30,888			
4	Sample 5	11.0	0.40	27,671			
5	Sample 1	20.0	0.62	32,289			
5	Sample 2	21.0	0.62	33,823			
5	Sample 3	19.2	0.62	30,982	**31,447**	1398	4.4
5	Sample 4	19.4	0.62	31,172			
5	Sample 5	18.8	0.62	30,377			
5	Sample 6	18.6	0.62	30,038			
6	Sample 1	24.4	0.88	27,771			
6	Sample 2	26.0	0.88	29,509			
6	Sample 3	24.2	0.88	27,947	**28,757**	1406	4.8
6	Sample 4	27.2	0.88	30,888			
6	Sample 5	24.4	0.88	27,671			

The specimens' failure modes are expected for three different bar sizes and are shown in Figure 30. It can be concluded that the average transverse shear strength of BFRP bars is about 30 ksi with no significant effect on the bar size. The minimum required transverse shear in ASTM D7957 is 19 ksi, so the results obtained from this test match the requirements. Elgabbas et al. tested three different types of BFRP bars in accordance with ASTM D7617 and computed the transverse shear strength as 50, 46, and 42 ksi for the three tested BFRP bar types. Moreover, Protechenko et al. tested six different BFRP bar diameters for shear. They indicated that the average transverse shear strength falls between 25 to 31 ksi, and the transverse shear strength curve

versus bar size displays a slight downward trend which indicates that the average shear strength slightly decreases with the increase of the bar size.

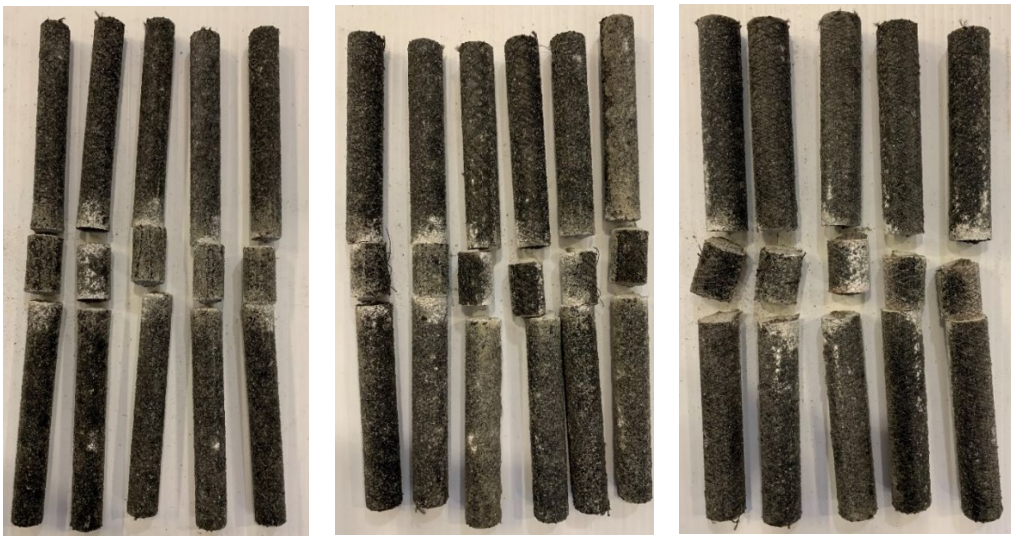

Figure 30: Mode of failure of Transverse shear strength test of bars #4, #5, and #6.

3.4 Durability tests

FRP is advantageous for its resistance to corrosion in structures exposed to harsh environmental conditions. Therefore, studying the BFRP bars' resistance to alkaline effect, exposure to deicing salt in bridge decks, and degradation due to freeze and thaw cycles is essential. This research project studies the impact of the alkaline solution exposure and the freeze and thaw cycles on the tensile strength and modulus of elasticity of BFRP bars.

3.4.1 Alkali resistance

This test aims to investigate the degradation of strength due to exposure to an alkaline solution under constant temperature. This test was conducted according to ASTM D7705, which requires conditioning the BFRP bars at a constant temperature (60 ºC) in an aqueous solution with a composition similar to the pore water inside Portland cement concrete. The solution comprises 118.5 g of $Ca(OH)_2$, 0.9 g of NaOH, and 4.2 g of KOH per 1 liter of deionized water, and the PH ranges between 12.6 and 13.0. Twenty BFRP bar samples of each bar sizes 5 and 6 were immersed for 1, 2, 3, and 6 months for five specimens of each bar size in a stainless-steel chamber with an automated controlled temperature system to ensure the temperature range between 59

ºC and 61 ºC. The stainless-steel tank was perfectly covered to prevent excessive moisture or temperature loss with the fresh air or calcium hydroxide reaction with CO_2. A water circulation system was provided to maintain the same temperature throughout the tank. The samples were weighed before and after the exposure, and Figure 32 shows the mass gain/loss versus time of exposure.

After the BFRP bars' exposure to the aqueous solution, the bars were tested according to ASTM D7205 to determine their mechanical properties. The results were compared to those of the control specimens (ten specimens of each bar size). Figure 31 shows the alkaline solution tank with circulation to maintain a constant temperature all over the tank.

Figure 31: Alkaline solution tank with circulation.

Exposed bars were dipped in epoxy at the ends to prevent any lateral effect of the alkaline solution, according to the recommendation provided in ASTM D7705, as shown in Figure 33. The mass loss shown in Figure 32 reveals more mass losses in bar #5 than in bar number 6, which is clearly, directly proportional to the loss in the ultimate tensile stress. The mass loss in the BFRP bar increases with the exposure time to the aqueous solution for three different bar sizes. The gain in the mass after one month of exposure is due to the precipitation of the non-dissolved substances on the surface of the rebar and the absorption of the material into some of the aqueous solutions.

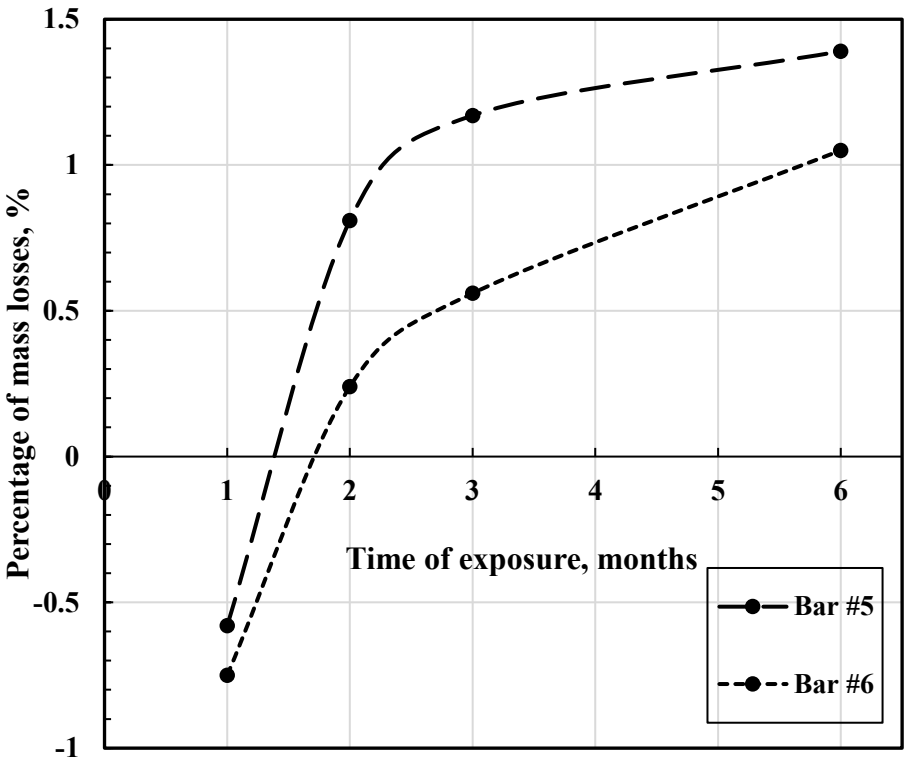

Figure 32: Mass losses versus time of exposure curve.

Figure 33: Alkaline test samples preparation.

Table 9 shows the tested samples' results after one, two, three, and six months of exposure to an aqueous solution. The tensile capacity retention is the ratio of the ultimate tensile stress after exposure to the ultimate tensile stress of the control specimens. Bar number 6 had better resistance to aqueous solution that lost 45% of the ultimate tensile strength after six months of exposure to the aqueous solution. The testing results did not show any significant loss in the modulus of elasticity.

Figures 34 and 35 show the tensile capacity retention and the tensile capacity loss of the exposed bars versus the time of exposure to aqueous solution. The tensile capacity retention and loss are calculated according to equations 8 and 9, respectively.

$$R_{et} = \frac{F_{tu1}}{F_{tu0}} \times 100 \qquad \text{Equation (8)}$$

$$R_L = \frac{F_{tu0} - F_{tu1}}{F_{tu0}} \times 100 \qquad \text{Equation (9)}$$

Where: R_{et}: tensile capacity retention, %

R_L: tensile capacity loss, %

F_{tu2}: tensile capacity before conditioning, ksi

F_{tu1}: tensile capacity after conditioning, ksi

Table 9: Tensile capacity retention (%) of the exposed bars versus exposure time

Bar size	Exposure time, months				
	0	1	2	3	6
#5	100	83.5	59.6	44	30
#6	100	89.5	87.3	64.2	54

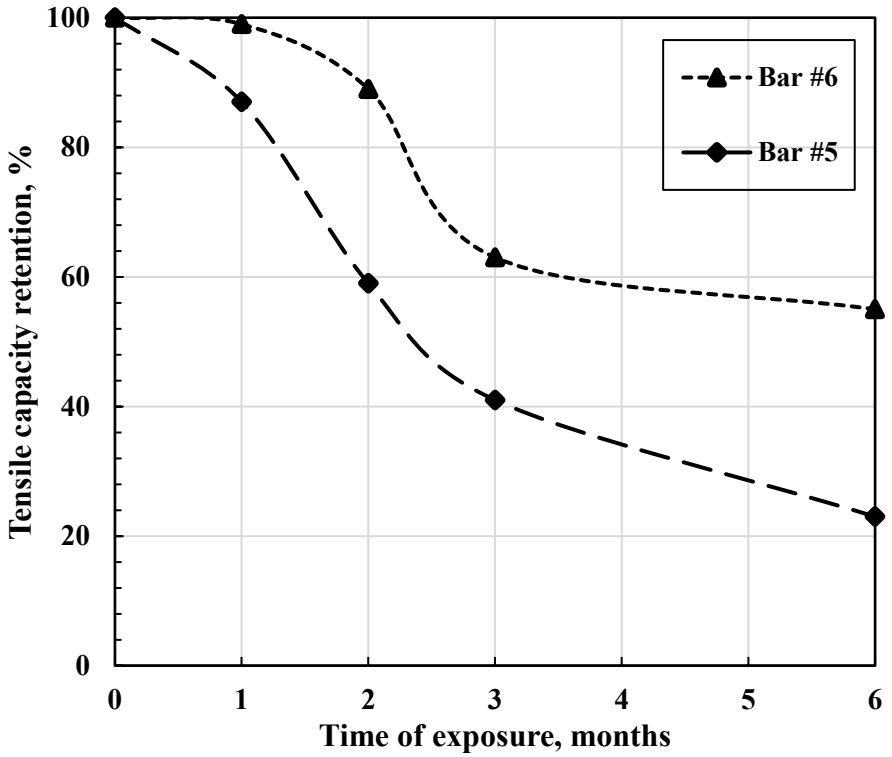

Figure 34: Tensile capacity retention curve versus time of exposure.

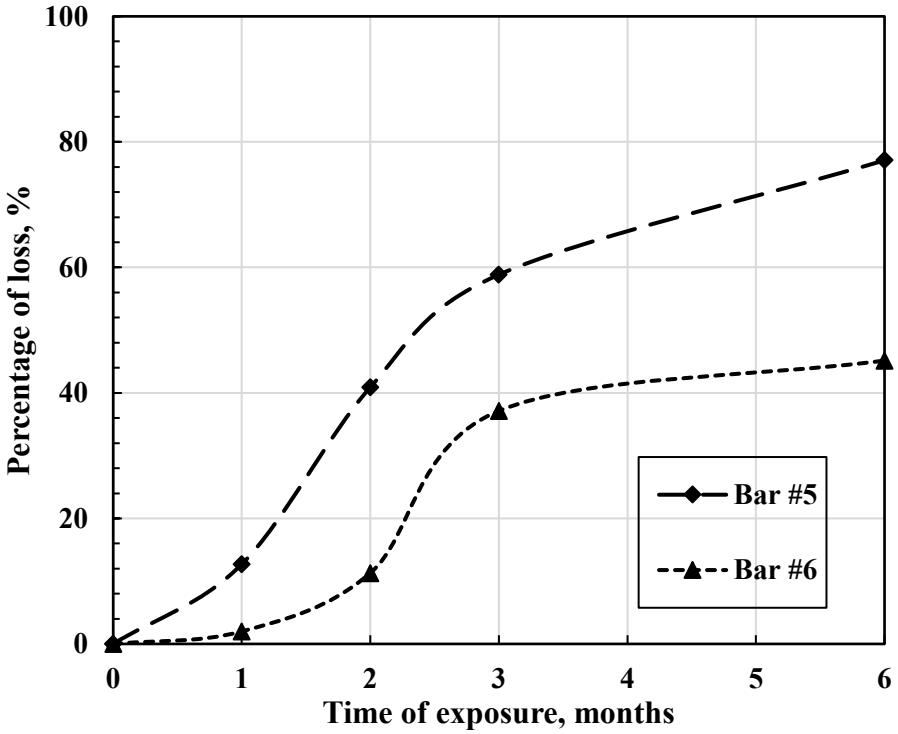

Figure 35: Tensile capacity losses versus time of exposure.

The results show that the tensile strength degradations decrease as the bar size increases for tested bars #5 and #6. As indicated in Table 9, the percent losses for bars #5 and #6 for a one-month exposure are **12.7%** and **2%**, respectively. Moreover, the tensile strength degradations for a two-month exposure have the same trend as the one-month exposure; however, since the bars are exposed for a longer duration, the percent losses will be more significant per bar size. As indicated in Table 9, the percent losses for bars #5 and #6 for a two-month exposure are **40.9%** and **11.3%**, respectively. The tensile strength degradation continues to decrease with the increase of exposure time to reach **77% and 45%** for six months of exposure for bars #5 and #6, respectively. This disparity is due to the alkaline solution's attack on the bar's surface. At about halfway through the testing, the failure began to initiate on the surface, and significant cracks were noted, indicating the aqueous solution's direct effect on the bar's surface. No significant loss in the modulus of elasticity was observed.

The mode of failure was different between the three different bar sizes. After one month of exposure, the bar surface was affected significantly by the alkaline solution exposure and the mode of failure has changed as shown in Figure 36. The mode of failure of bar #6 remains the same as the regular failure of the bar after exposure. Bar #5 had a mix between the surface's complete failure and the rebar's typical failure. The specimens with a total surface failure showed lower tensile capacity than the samples with a common failure, confirming that the BFRP bar's surface exposed to the aqueous solution will be affected more than the inner part.

In the concrete design using FRP materials as the main reinforcement, a factor C_E reduces the design tensile strength due to environmental conditions. The indication of this factor for BFRP bars requires knowledge of the strengths of the composite bar after weathering for some years in a variety of natural climates.

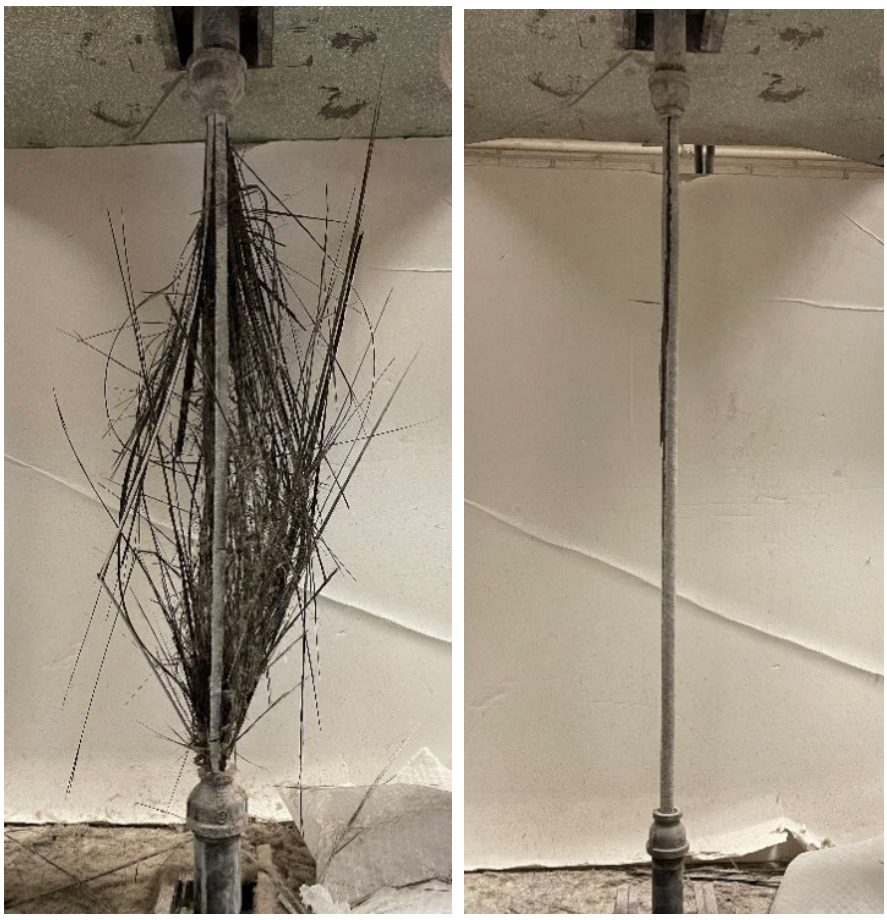

(a) #5 BFRP (b) #6 BFRP

Figure 36: Mode of failure of bars #5 and #6.

Results show that the tested bars had no significant loss in the tensile modulus of elasticity. During the testing of the conditioned bars and after reaching about 25% to 50% of the ultimate strength, major cracks were observed on the surface of the tested rebars. Ali et al. (2019) stated that the damage caused by the moisture diffusion was confined to the thin outer layer of the bar, and the fibers were not affected by the conditioning, which verifies the testing observation of the propagated cracks on the surface of the tested bars. As shown in Figure 32, the conditioned bars had a gain in mass after one month of exposure due to the absorption of the solution and the precipitation of some of the non-dissolved Calcium Hydroxide in the form of a jelly-like substance on the surface of the bar. The bar continued to lose mass after two months of exposure. The degradation rate was low for the first month, and then it increased with more exposure time. The absorption of the BFRP bar is highly affected by the exposure to the alkaline solution (Ma et al.,

2018). The more absorption of the solution, the more degradation in the bar properties. This might be the reason for the slow reduction in the strength at the beginning of the exposure time and accelerated as the absorption increased. The bar tensile strength was negligible after six months of exposure.

Bars No. 5 and 6 had a significant loss in tensile strength, and the tensile capacity retention was 23% and 55% after six months of exposure at 60 ºC, respectively. The tensile capacity retention was highest for the larger diameter, which contradicts the results obtained by Ali et al. They stated that the tensile capacity retention of bar No. 4 after three months of exposure at 60 ºC was 67% which agrees only with our testing results for bar No. 6 at three months. Serbescu et al. (2014) stated that the BFRP bars are slightly affected by the PH and highly affected by the temperature. In this research, exposed BFRP had tensile capacity retention of 64 and 56% after 1000h of exposure at a PH of 7 and 13, respectively. They are estimated to retain about 72 and 80% of their strength after 100 years of exposure to the concrete environment. The interface between the fibers and the resin material is an essential factor in the bar's resistance to alkalis (Nkurunziza et al., 2005, Benmokrane et al., 2017, Benmokrane et al., 2015). Thus, improving the interface strength enhances the bar's resistance to harsh environmental conditions.

Figure 37 shows the data of the present study in comparison with other researchers on the durability test of BFRP bars. The figure clearly shows the wide range of differences in the data in the literature. The production needs to be standardized to eliminate this difference in the durability data of BFRP.

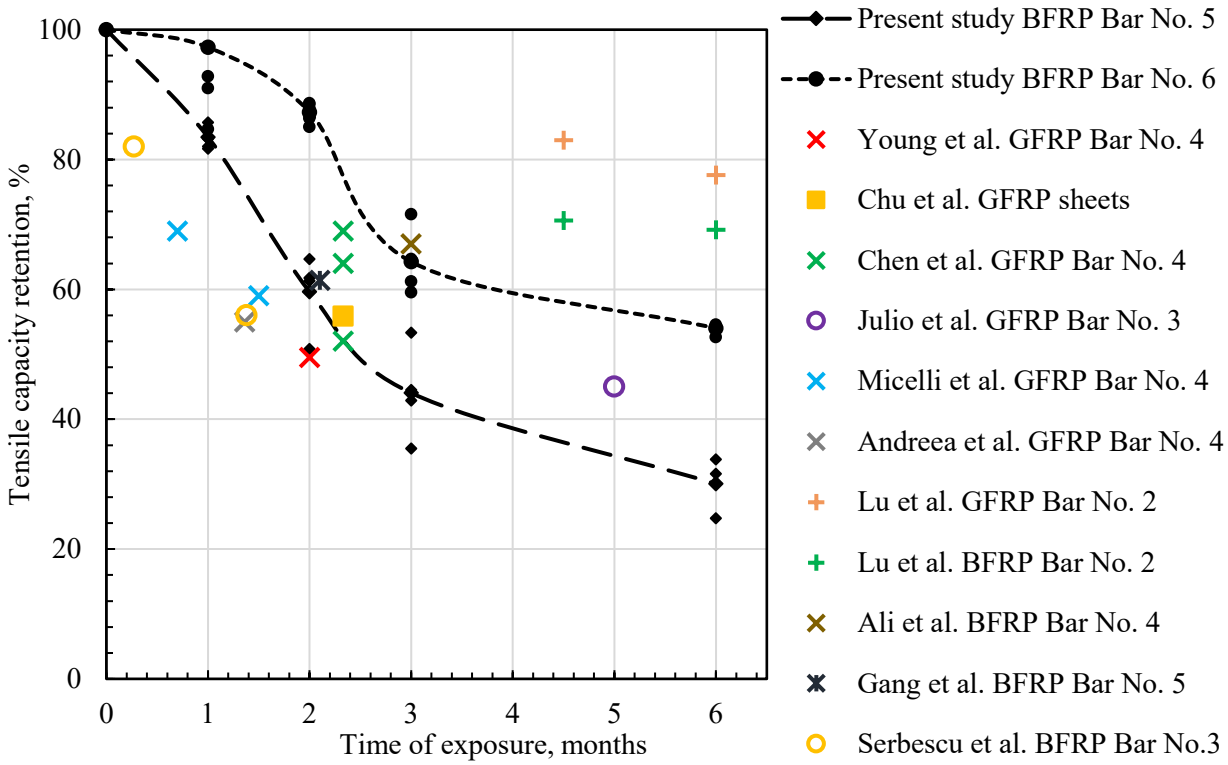

Figure 37: Comparison of the durability results of the present study to other durability tests in the literature.

Long-term predictive model of the tensile strength of BFRP bars

The prediction of the long-term tensile service life prediction of BFRP bars is one of the significant aims of this research. Several research employed the Arrhenius concept for long-term service life prediction (Ali et al., 2018). According to fib Bulletin 40, a double logarithmic scale is used to graphically represent the loss in strength as a function of time (FIB 2007). The outcome of this model is the strength reduction factor due to the alkaline effect on the BFRP bar (η_{env} in fib Bulletin 40 or C_E in ACI 440.1R). According to fib Bulletin 40 (2007), the 1000h (41 days) is sufficient for the chemical reactions to stabilize and enable long-term prediction of the tensile capacity retention. The double logarithmic scale graph for three bar sizes in Figure 38 shows the degradation versus exposure time. The line was extrapolated to predict the capacity after one million hours of exposure (114 years). The slope of the degradation line is calculated according to Eq. 10.

$$m = \frac{\log(f_0) - \log(f_{f1000h})}{\log(1) - \log(1000)}$$ Equation (10)

Where f_0 is the tensile capacity retention before exposure in %, f_{1000h} is the tensile capacity retention after 1000 hours of exposure in %. The degradation rate in this method is obtained per logarithmic decade of real exposure in the structural member. R_{10} represents the degradation in one logarithmic decade and can be calculated using Equation 11.

$$R_{10} = 100 - (10^m * 100)$$ Equation (11)

Moreover, the graph shows the factor η_{env} which considers the loss in the ultimate strength of the bar after 1,000,000 hours of exposure to the actual concrete environment. This factor can be computed using Equation 12:

$$\eta_{env} = {}^{1}/_{[(100 - R_{10})/100]^n}$$ Equation (12)

Where n is the degradation factor (after 10^n hours). The factor n account for the individual influence of moisture, temperature, time, PH level, the diameter of the tested bar I comparison with the studied bar size, degradation onset. Table 10 shows the effect of all the parameters on the factor n.

Table 10: Degradation parameters adopted in this study.

Degradation parameter	**Range**	**Value**
Moisture RH (n_{mo})	Dry (50%)	-1
	Moist (80%)	0
	Saturated (100%)	1
PH (n_{PH})	7	0
	10	0.5
	13	1
Time (n_t)	≤1,000 h	0
	≥1,000 h	Log(h/1,000)
Diameter (n_d)	≥tested	0
	~75% tested	0.5
	~50% tested	1

Temperature (n_T)	0ºC	-0.5
	10ºC	0
	20ºC	0.5
	30ºC	1
	40ºC	1.5
	50ºC	2
	60ºC	2.5
Onset (n_{on})	$f_{fk\ ref} = f_{fk0}$	-1.5
	$f_{fk\ ref} \neq f_{fk0}$	$n_{on,opt}$
While $n = n_{mo} + n_T + n_t + n_{pH} + n_d + n_{on}$		(no unit)

In this study, the tested rebars were conditioned in a saturated environment (n_{mo} = 1), pH = 13 (n_{pH} = 1), exposure time equal 1,000 h (n_t = 0), the diameter of the tested rebar for reference is equal to the conditioned rebar (n_d = 0), exposure temperature is 60ºC (n_T = 2.5), $f_{fk\ ref} = f_{fk0}$ (n_{on} = -1.5). The value of n_{on} is a function of the degradation onset in the bar (reference time). The reference environment is assumed to be PH7 and 20ºC, which considers the degradation initiation in most FRP bars suitable for laboratory testing (Serbescu et al., 2014). The value of -1.5 assumes that the degradation will start after changing this environment. By adding all these values, the factor n will be 3. This factor n represents graphically the second point (f0) position that needs to be connected to f_{f1000h}.

After the computation of all these factors, the percentage of strength retained after a desired period of time can be expressed according to Equation 13:

$$f_{f,t\%} = \left({}^{1}/_{\eta_{\boldsymbol{env}}}\right) * 100 \qquad \text{Equation (13)}$$

Where $f_{f,t\%}$ is the strength retained after a desired period of time in %.

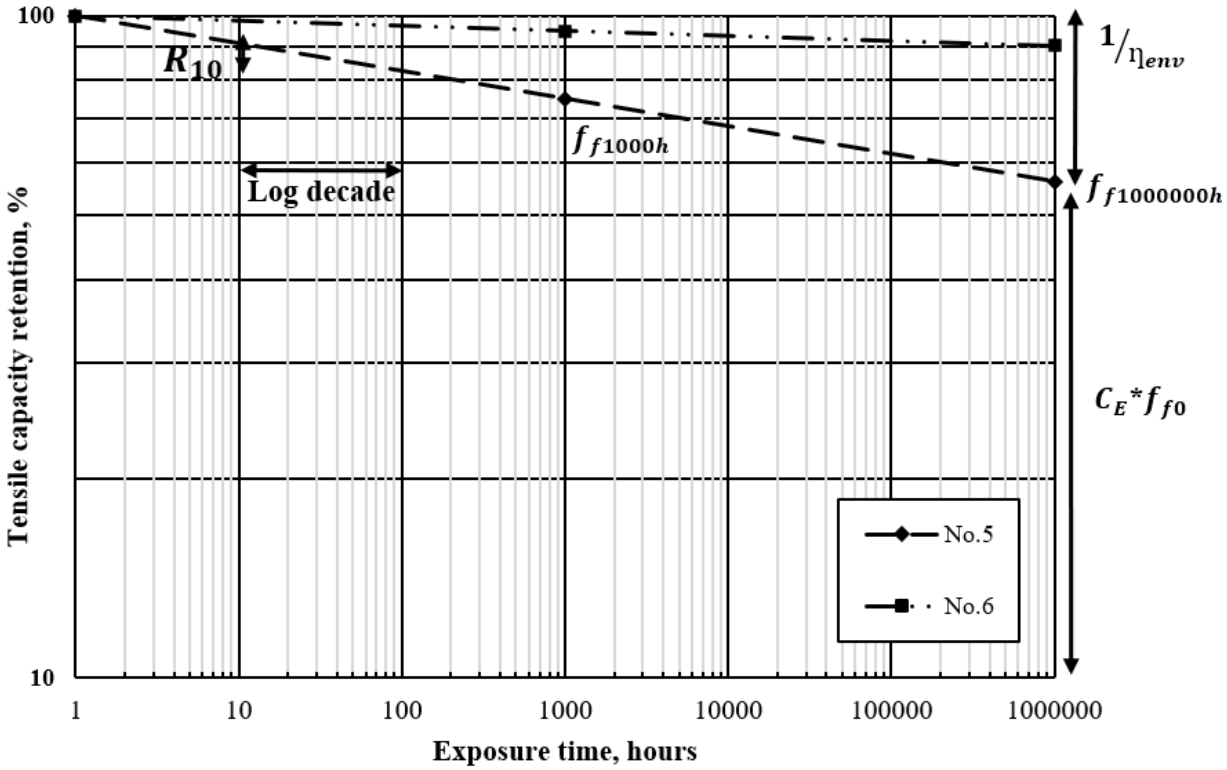

Figure 38: Double logarithmic scale of the tensile capacity retention as a function of exposure time.

The predicted tensile strength retention can be obtained for 25, 50, and 114 years and shown in Table 11. The effect of bar size on the predicted long-term service life is well demonstrated in the following section.

Table 11: Predicted tensile capacity retention for different time intervals.

Time, years	Predicted tensile capacity retention for bar No. 5, %	Predicted tensile capacity retention for bar No. 6, %
25	**57**	**89**
50	**55**	**88**
114	**53**	**87**

3.4.2 Freeze and thaw

This test aims to investigate the freeze and thaw resistance of unidirectional pultrall BFRP bars from -4 ˚F to 73 ˚F for 100 cycles by freezing in air and thawing in water. The test was conducted according to ASTM D7792, which requires the bars' exposure to freeze for three hours, followed by the thaw in water for three hours. A fully

automated environmental chamber fulfilled the test with a data acquisition system that records the temperature change during the exposure, as shown in Figure 39. A total of 10 samples from each bar size (#4, #5, and #6) were exposed and then tested according to ASTM D7205 to study the reduction in tensile strength and modulus of elasticity. A total of 30 samples were tested without any exposure under the lab environment temperature and were considered as control specimens.

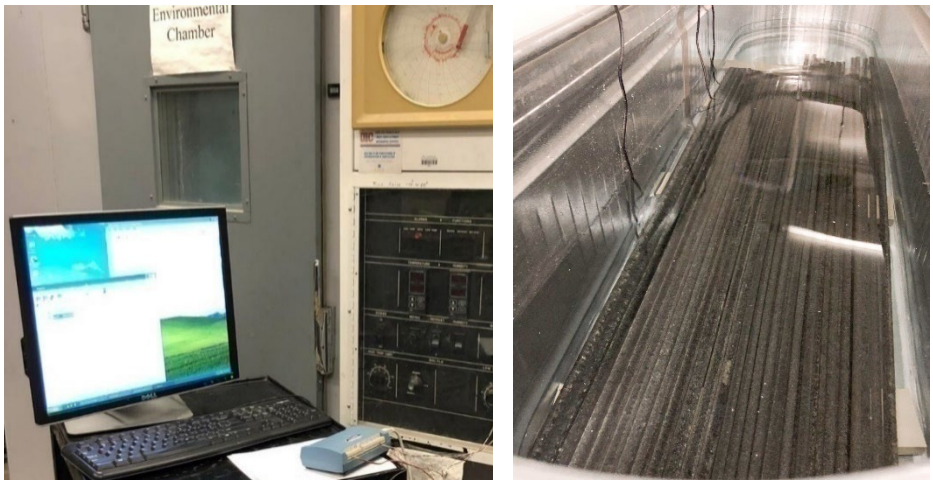

Figure 39: Environmental chamber and data acquisition system, and water tank used for freeze and thaw test.

Table 12 shows the tensile stress and the modulus of elasticity's testing results and the percentage of strength loss after exposure to 100 freeze and thaw cycles.

Table 12: Freeze and thaw data comparison.

Bar #	Control specimens		Exposed specimens		Percentage of tensile stress loss, %
	Tensile modulus of elasticity, ksi	Tensile stress, ksi	Tensile modulus of elasticity, ksi	Tensile stress, ksi	
4*	8494	226	8578	218.9	**3.1**
5*	8674	202	8481	187.1	**7.4**
6*	8798	171	8724	163.5	**4.4**

Note: *Average of 10 tested specimens

The BFRP bars had minimal losses in strength, and no significant losses in the modulus of elasticity have been recorded. The percentage of loss of bars #4, #5, and #6 is 3.1%, 7.4%, and 4.4%, with no significant mass loss. The mode of failure of the bars also stayed the same, as shown in Figure 40. Even though the gripping material was

the same as the one used in the tensile test, three tested specimens of bar #6 out of ten bars had a bond failure at the end. The test results indicated the effect of freeze and thaw cycles on the sand coating, consequently decreasing the bond strength with concrete. The freeze and thaw cycles affect the environmental factor CE used in concrete design with FRP materials. This test indicates that this factor is less than the environmental factor obtained from the alkaline exposure, and no modification in the tensile strength is needed.

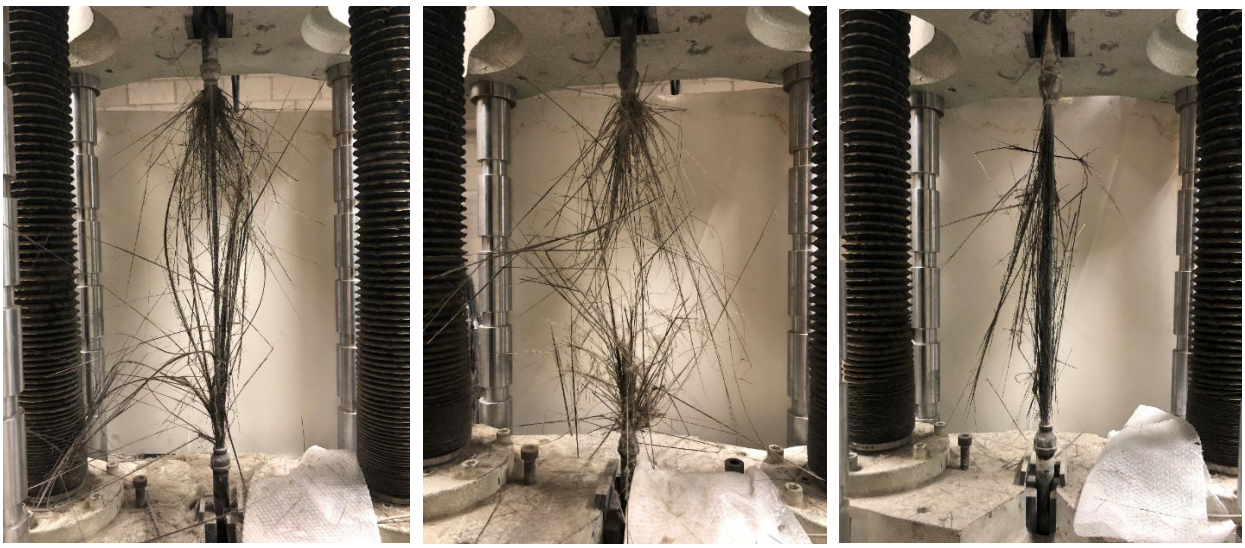

Figure 40: Mode of failure of bars samples exposed to freeze and thaw cycles.

3.5 Tensile Creep Rupture

The testing for creep properties for BRFP rebar was carried out according to ASTM D7337. The creep properties were studied for bar number 4 for four stress levels of the ultimate strength of the BFRP bars. The BFRP bars were subjected to sustained creep for four different stress levels, one of the stress levels samples was tested under the machine, and the rest will be tested as shown in Figure 41. ASTM D7337 assesses the ability of composite bars to withstand sustained loading by establishing the tensile creep-rupture capacity of the bars. The method relies on the tension testing method (D7205) for test fixtures and anchors and requires that tension testing be used to establish the baseline tensile strength of the bar. The series with the highest load level (shortest time to creep rupture failure) must contain at least four specimens whose failure time is more significant than one hour. The series with the lowest load level

(longest time to creep rupture failure) must contain at least one specimen whose failure time is greater than 8000 hours. In this way, the creep rupture times will span at least three decades. Based on test results, the method provides the calculations of the million-hour creep rupture capacity of the bar.

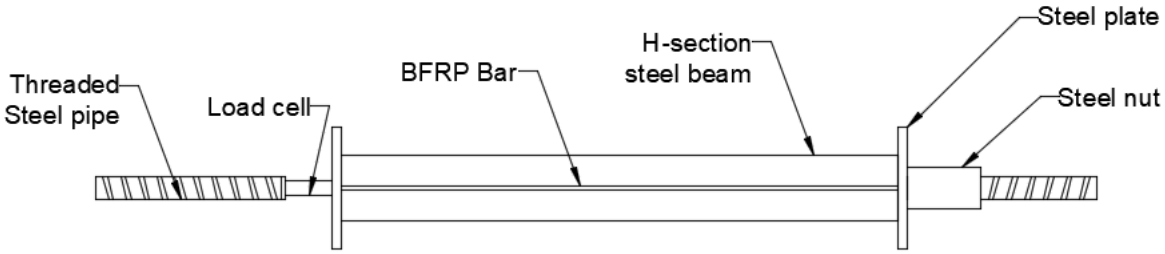

Figure 41 Testing setup for tensile creep rupture

The creep and experimental program is planned to run continuously and for a long time to determine creep effects. The limit for prestressing was decided upon due to the Ultimate Tensile strength of the bars and the bars' diameter. The applied loads are estimated to be 90%, 80%, 75%, and 70% of the ultimate tensile capacity of the BFRP bars. The temperature was kept at 25°C ±2 (77 ±4°F) so that this did not affect the samples and controlled by a constantly air-conditioned room.

The design is based on a rigid steel H section with two steel plates welded to the end capable of housing up to two bars for simultaneous testing. The technique utilizes the rigid section principle with nuts to exert the tensile load onto the threaded bars. The nut is tightened to apply the load simultaneously, preventing torque effects on the bar. Once the required load has been obtained and measured via individual load cells, an additional plate and nut are introduced to secure and act as extra resistance to the tension of the sample. The threaded bar is secured using a nut, as seen in Figure 41.

This test method measures the time to rupture a bar subjected to a constant tensile force. The method selects multiple force levels to derive a relationship between force and time-to-failure. The first stress level chosen is 90% and tested under the machine for sustaining the load. The time of failure and the strain in the specimen were recorded for three different samples, and the stress versus time curve is shown in Figure 42.

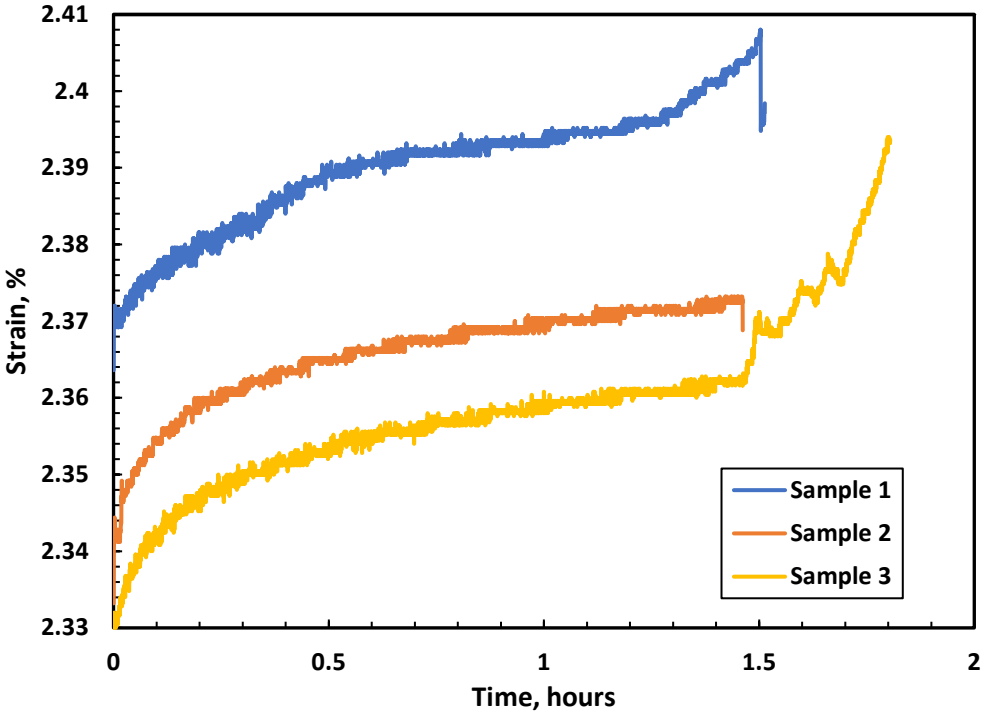

Figure 42 Strain versus time curve of the tested bars

The force ratio versus creep rupture time curve shall be plotted on a semi-logarithmic graph where the force ratio is represented on an arithmetic scale along the vertical axis and creep rupture time in hours is represented on a logarithmic scale along the horizontal axis, as shown in Figure 43. Tests resulting in no failure (run-outs) will be included in this plot but should not be included in calculating the creep rupture trend line. Run-outs should clearly be identified as such on the graph. A creep rupture trend line will be plotted from linear regression of the data by means of the least-square method according to Equation 14:

$$Y_C = a_1 - b_1 \log t \qquad \text{Equation (14)}$$

Where:

Y_c = force ratio, expressed as a percentage of quasi static tensile strength,
a_1, b_1 = empirical constants, and
t = time, hour.

The force ratio at 1 million hours, as determined from the linear extrapolation of

the trend line, will be taken as the million-hour creep-rupture force ratio. The force and stress corresponding to the million-hour creep rupture force ratio are the million-hour creep rupture capacity and the million-hour creep rupture strength, respectively. The million-hour creep rupture strength is calculated according to Equation 15, with precision to three significant digits:

$$F_r = P_r/A \qquad \text{Equation (15)}$$

where: F_r = million-hour creep rupture strength of FRP bar, MPa [psi],

P_r = million-hour creep rupture capacity, N [lbf], and

A = cross-sectional area of specimen, mm^2 [in^2]

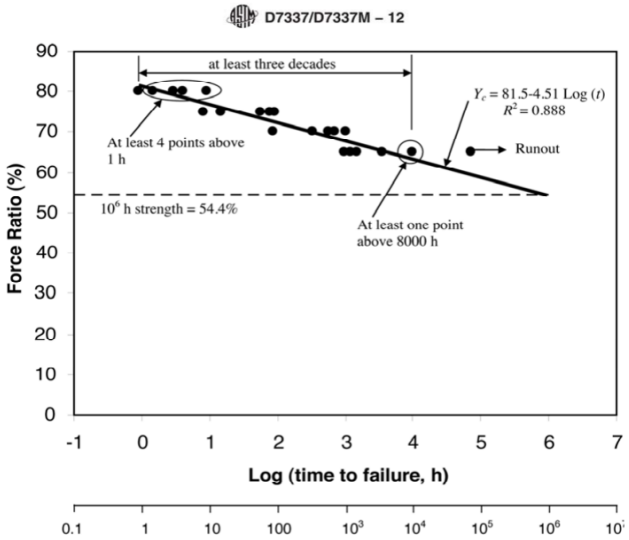

Figure 43 Example Logarithmic Time to Failure (Stress Rupture) Curve

The time of failure of the tested samples for 90% stress level are shown in Table 13. Four of the tested rebars failed after more than one hour, which validated the ASTM requirement.

Table 13 Creep test results.

Bar #	Sample #	Stress level, %	Time of failure, hours
#4	Sample 1	90	1.51
#4	Sample 2	90	1.46
#4	Sample 3	90	1.80
#4	Sample 4	90	0.23

4 Fabrication and testing of concrete bridge deck slabs

Direct exposure of bridge decks to harsh environmental conditions exhibited bridge deck deterioration faster than any other element in the bridge. Rehabilitation cost is one of the most critical factors affecting bridge maintenance decisions. A bridge deck reinforced with the BFRP material is among the solutions to reduce the maintenance cost in the long term due to its non-corrosive nature.

This research aims to study the mechanical, durability, and creep properties of the BFRP bars and examine the behavior of a bridge deck reinforced with BFRP bars. Two types of bridge decks reinforced with BFRP bar (single-span and continuous bridge decks) will be tested at UIC labs. This study aims to evaluate the effect of different bar sizes and spacing of the transverse and longitudinal reinforcement on the structural behavior of the bridge deck.

A total of six bridge deck slabs of two different BFRP bar sizes, bar spacing, and continuity conditions were constructed and tested. All the bridge deck slabs are 8 in. thick. Four slabs out of six were designed for wheel point-loading for the single-span bridge deck slabs, and two slabs are designed for tandem loading for the two-span bridge deck slabs. Table 14 shows the different slabs with different reinforcement and continuity conditions.

Table 14: Bridge deck slabs dimensions and reinforcement quantity.

Slab Prototype	Total Length, ft	Width, ft	Continuity condition	Span length, ft	Transverse bottom reinforcement	Transverse top reinforcement	Longitudinal bottom reinforcement	Longitudinal top reinforcement
SS1	10	4	SS	7	#5@4	#5@4	#5@4	#5@4
SS2	10	4	SS	7	#5@6	#5@6	#5@6	#5@6
SS3	10	4	SS	7	#6@6	#6@6	#5@6	#5@6
SS4	10	4	SS	7	#5@8	#5@8	#5@8	#5@8
TS5	18	10	TS	7.5	#5@4	#5@4	#5@4	#5@6
TS6	18	10	TS	7.5	#5@6	#5@6	#5@6	#5@8

Where the designation for the slabs is as follows:

Prototype 1 (SS1): fc5.5-Sp7-SS-T#5@4-L#5@4
Prototype 2 (SS2): fc5.5-Sp7-SS-T#5@6-L#5@6
Prototype 3 (SS3): fc5.5-Sp7-SS-T#6@6-L#5@6
Prototype 4 (SS4): fc5.5-Sp7-SS-T#5@8-L#5@8
Prototype 5 (TS5): fc5.5-Sp7.5-TS-T#5@4-L#5@4
Prototype 6 (TS6): fc5.5-Sp7.5-TS-T#5@6-L#5@6

Each specimen was labeled with four sets of codes separated by a hyphen "-" for reference. The first code denotes the concrete strength ('fc' with the compressive strength of the concrete used), followed by the span length ('sp' with the bridge deck span length). The third code indicates the continuity type ('SS' for single-span bridge deck and 'TS' for two-span bridge deck). The last two codes represent the reinforcement size and spacing for the transverse and longitudinal directions. Four single-span and two two-span bridge deck slabs were tested at the UIC structural laboratories, and the results are presented in the following paragraphs.

4.1 Single-span bridge deck slabs

4.1.1 Single-span bridge deck slab Prototype 1

The experimental program includes the fabrication and testing of four full-scale single-span bridge decks. The main experimental parameters are bar size, bar spacing, and the supported span length. Four single-span bridge deck slabs were fabricated and tested at the UIC structural and concrete research laboratory. The detailed cross-section of the deck is shown in Figures 44 and 45. Four specimens will be tested as single-span bridge deck slabs (4 ft. wide and supported span length of 7 ft.) with different reinforcement ratios. The top and bottom covers in the bridge decks are 2¼ and 1 in., respectively.

4.1.1.1 Material properties

The slabs were constructed and fabricated following the Illinois Tollway mix design for bridge deck slabs. The water-cement (w/c) ratio of 0.445 was used. The Illinois Tollway mix proportion of concrete for bridge decks is shown in Table 15. The concrete is air-entrained with 6% and a slump of 6 inches. The average concrete compressive strength used was about 7120 psi. The tensile properties of #4, #5, and #6 BFRP bars are presented in Table 16. BFRP #5 bars spaced at 4, 6 and 8 inches were used for the top and bottom mats for longitudinal and transverse directions.

Table 15: Concrete mix proportions for Prototype 1

Material	Designation	Design Qty	Required	Batched
Coarse aggregate	22CM161HR	520 lb.	1043 lb.	1030 lb.
Coarse aggregate	22CM11BLJ	1360 lb.	2774 lb.	2710 lb.
Fine aggregate	27FM01OH	1250 lb.	2557 lb.	2530 lb.
Slag	SLG-SKY	190 lb.	380 lb.	385 lb.
Cement	CEM-HCMSG	330 lb.	660 lb.	655 lb.
Water	WATER1	27.5 gal.	45.9 gal.	46.6 lb.
Air entrainment admixture	AE-DX2	2.5 oz.	5 oz.	4.5 oz.
Medium range water reducer	WRR-REC	3.5 /C	36.4 oz.	35 oz.
High range water reducer	HR-A575	2.5 /C	26 oz.	27 oz.

Table 16: Mechanical properties of BFRP bars

Bar size	Modulus of elasticity, ksi	Ultimate stress, ksi
#4	8,494	226
#5	8,674	202
#6	8,798	171

4.1.1.2 Fabrication and testing setup of bridge deck slab

The single-span bridge deck was supported on two steel sections bolted to the steel bed. The supported span of the slab is 7’-0” with 8” thickness. The slab thickness was selected to keep the ratio of supporting-beam spacing to slab thickness less than 12 and to represent the most commonly used size of the concrete bridge deck in North America. The bridge deck was cast in place to prevent defects caused by the movement and the setting of the specimens for testing. Figures 47 and 48 show the slab before and after pouring the concrete. A vibrator was used for compaction to prevent any voids in the concrete section during concrete pouring. The steel bolts shown in Figure 47 are designed to provide a full composite connection between the concrete slab and the steel section. The steel sections are fixed to the concrete floor at the bottom to prevent any displacement in the bottom flange of the steel section.

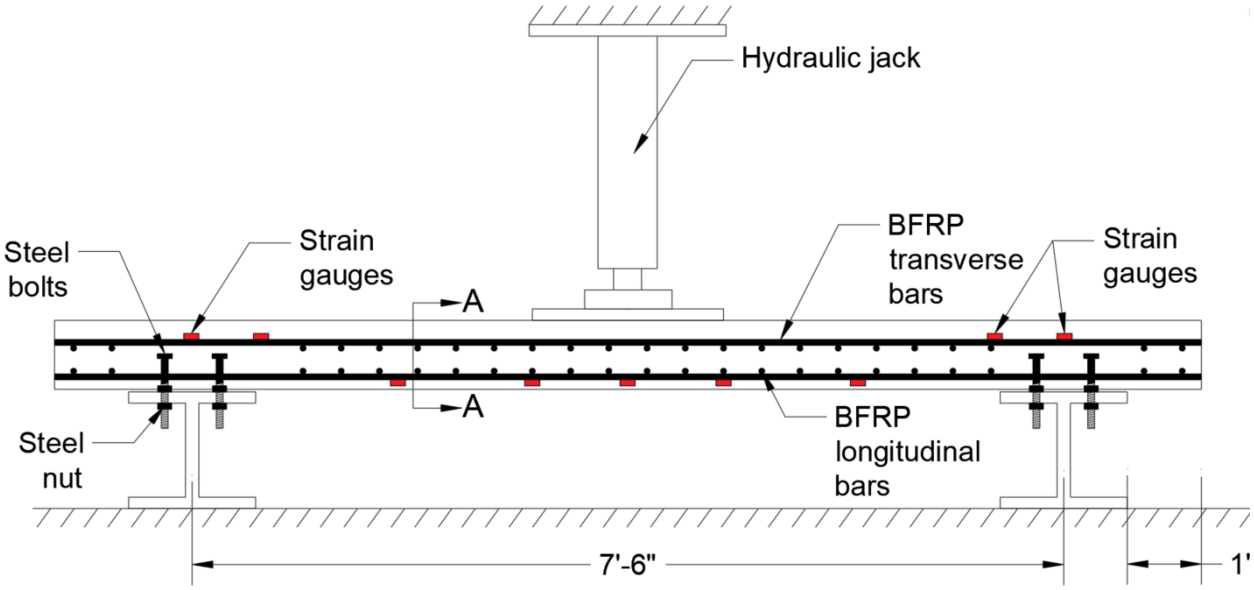

Figure 44: Single-Span Bridge Deck Testing Setup

Strain gauges were installed on the surface of the BFRP bars and the concrete surface at the critical locations. Fourteen strain gauges were installed on the surface of the BFRP bars to measure the tensile and compressive strains, six of them were installed on the top transverse bars above the support (3 on each side). Another six strain gauges were installed on the bottom transverse bars at midspan, while two strain gauges were installed on the bottom longitudinal bars at midspan. Moreover, five strain gauges were installed on the top surface of the concrete at midspan to measure the compressive strain in the concrete with a spacing of 9 inches. Three vertical LVDTs were installed at the midspan of the bridge deck slab to measure the slab's maximum vertical deflection. Four Pi-shape Displacement Transducers were attached to the bottom surface of the concrete to measure the crack openings at the bottom of the concrete surface. Figure 46 shows the location of the strain gauges on BFRP bars, strain gauges on the concrete, LVDT devices, and the Pi-shape Displacement Transducers. Figure 47 shows the vertical LVDTs and the Pi-shape Displacement Transducers in the testing setup.

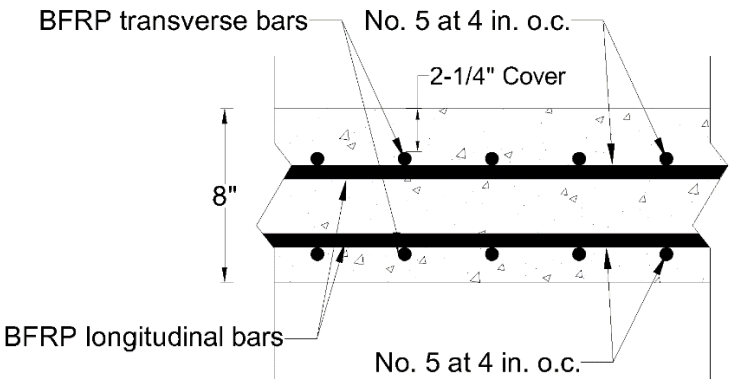

Figure 45: Slab reinforcement detailing (section A-A)

Strain gauges, LVDTs, Pi-shape Displacement Transducers, pressure gauges, and the load cell were all connected to the data acquisition system to collect the data during testing. Figure 50 shows the data acquisition system connected to the computer.

The load was applied at the mid-span of the bridge deck using a hydraulic actuator attached to a load cell, as shown in Figure 51. In addition to the reading taken from the load cell, two pressure gauges were also used to measure the value of the load applied, as shown in Figure 52. The applied load was transferred to the specimen through a 20x10 inches HDPE recycled plastic material beam, as shown in Figure 53, to represent the contact wheel load area and distribute the load evenly on the concrete surface.

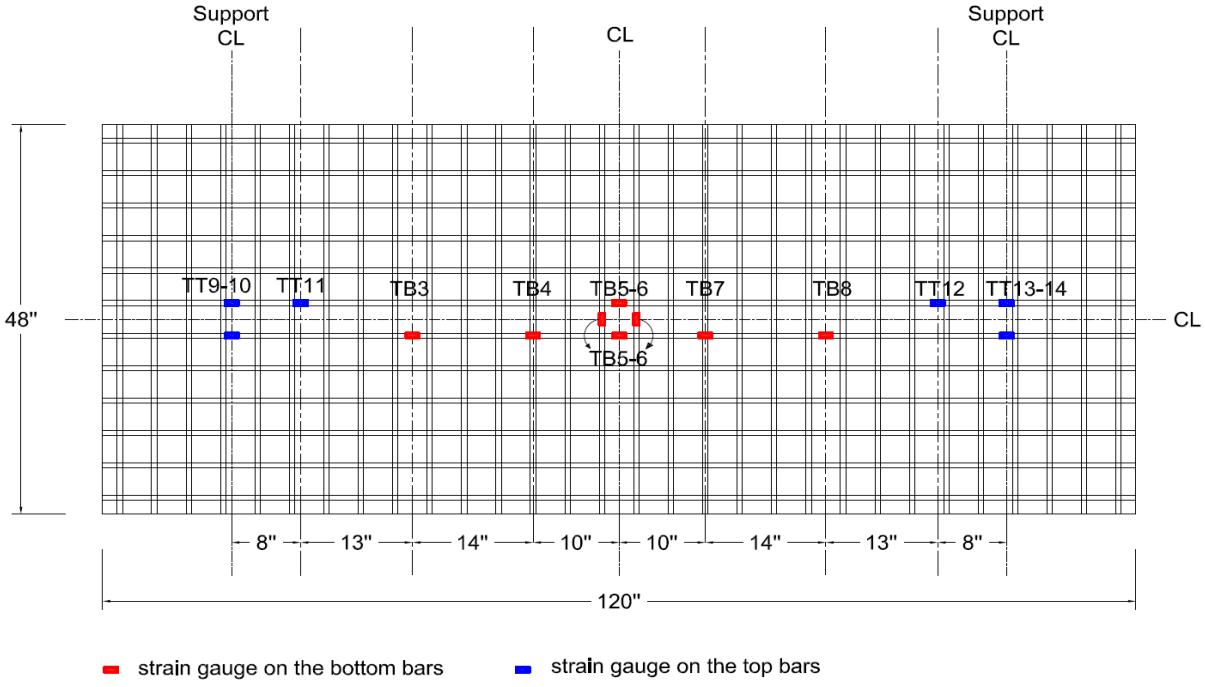

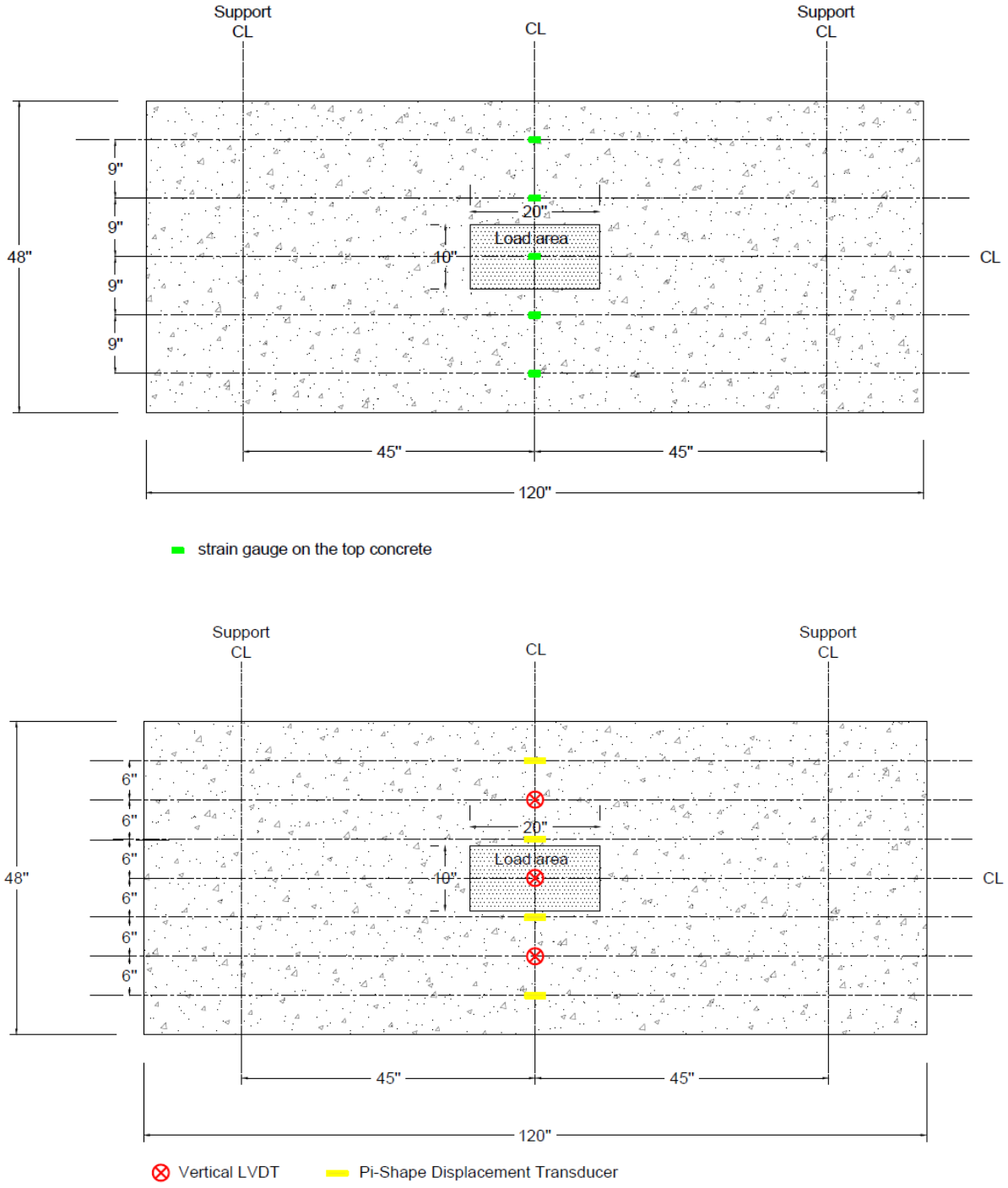

Figure 46: Slab reinforcement and location of the strain gauges.

Figure 47: Single-span bridge deck slab before pouring the concrete.

Figure 48: Cast of the first single-span bridge deck slab

Figure 49: LVDTs and the Pi-shape Displacement Transducers at the bottom midspan of the deck

Figure 50: Data acquisition system connected to the laptop

Figure 51: Load cell

Figure 52: Pressure gauges attached to the hydraulic pump

Figure 53: HDPE recycled plastic material fixture simulating wheel contact area of 20 in.x10 in.

4.1.1.3 Testing results

The research project's objective is to study the structural behavior of the system subjected to a tire contact area of a single wheel load for pre-cracking, cracking, post-cracking, and ultimate load conditions. The experimental test results, such as the cracks, deflections, strains, and failure mode, are presented in the sections below.

During testing, vertical flexural cracks were initiated at the middle region of the bridge deck (the initial crack appeared at a load of 13.5 kips). Some cracks were observed at the negative moment region with larger crack spacing than those observed in the middle region as the applied load increased. Figure 54 shows the mapping of the crack locations and loads at which the cracks occurred. The cracks presented in Figure 54 are well distributed at the bottom region of the midspan in the longitudinal direction within a transverse width of 30 inches.

Figure 54: Crack mapping of the bottom face of bridge deck Prototype 1.

The deflection was measured at the mid-span of the slab using three LVDT devices. The deflection was recorded, and the load-deflection curves were plotted as shown in Figure 55. Inspection of Figure 55 shows the bilinear curve with an elastic behavior before cracking (pre-cracking) and a smooth transition to the cracked section due to the presence of enough amount of BFRP bars that control the curvature after the section is cracked (reinforcement ratio is greater than ρ_b). More BFRP reinforcement is needed as the main reinforcement compared to mild steel due to the fact that the modulus of elasticity of mild steel is 3.4 times the modulus of elasticity of BFRP bars. The load-deflection curve continues straight after the cracking stage until failure. The maximum deflection of 0.79 inches recorded at the midspan corresponds to a failure load of 130 kips.

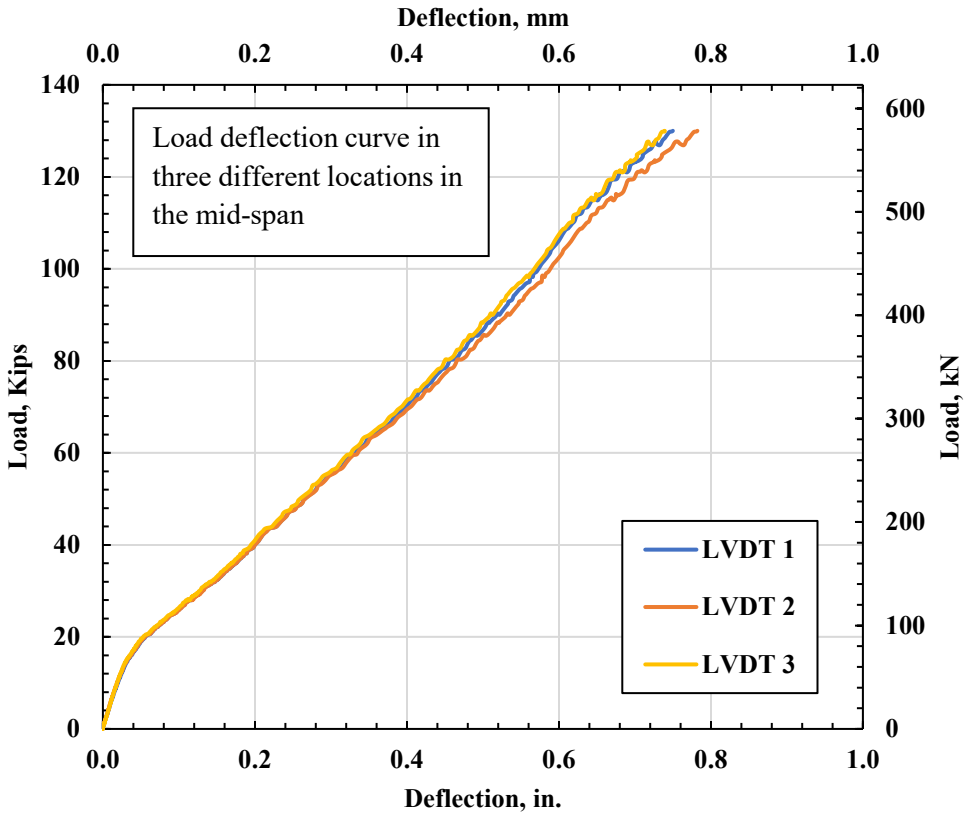

Figure 55: Load-deflection curves of bridge deck Prototype 1.

The strain readings in the transverse BFRP bars (main reinforcement) at the bottom of the span were measured using six strain gauges installed on the rebars. Strain gauges TB5 and TB6 (TB: Transverse Bottom) are at the midspan, TB4 and TB7

are at 10 inches from the midspan, and TB3 is at a distance of 24 inches from the midspan. The strain in the longitudinal BFRP bars at the bottom of the mid-span was measured using two strain gauges LB1 and LB2 (LB: Longitudinal Bottom). The strain in the transverse BFRP bars (main reinforcement) in the top mat at the support was measured using five strain gauges TT9, TT10, TT11, TT12, and TT14 (TT: Transverse Top). The strain in the BFRP bars was recorded, and the load-strain curves were plotted in Figures 56 and 57.

The maximum strain recorded by the BFRP bars before failure was 6,549 micro-strain, which is equal to 30% of the ultimate strength, based on the tensile properties of the BFRP bar. After the concrete crushing, the slab could sustain a load of 55 kips carried by the BFRP bars after the concrete crushed, as shown in Figure 58. The failure due to the concrete crushing was observed without rupturing any of the BFRP bars. The failure mode of the slab is presented in Figure 58. The bridge deck exhibited compression failure, where a significant crack initiated from the ends and extended up to the compression zone. The deflection at the midspan, strains of the concrete, and the BFRP bars strains were recorded. The load-strain curves of the BFRP bars and load-strain curves of the concrete were plotted as shown in Figures 56 and 57, respectively.

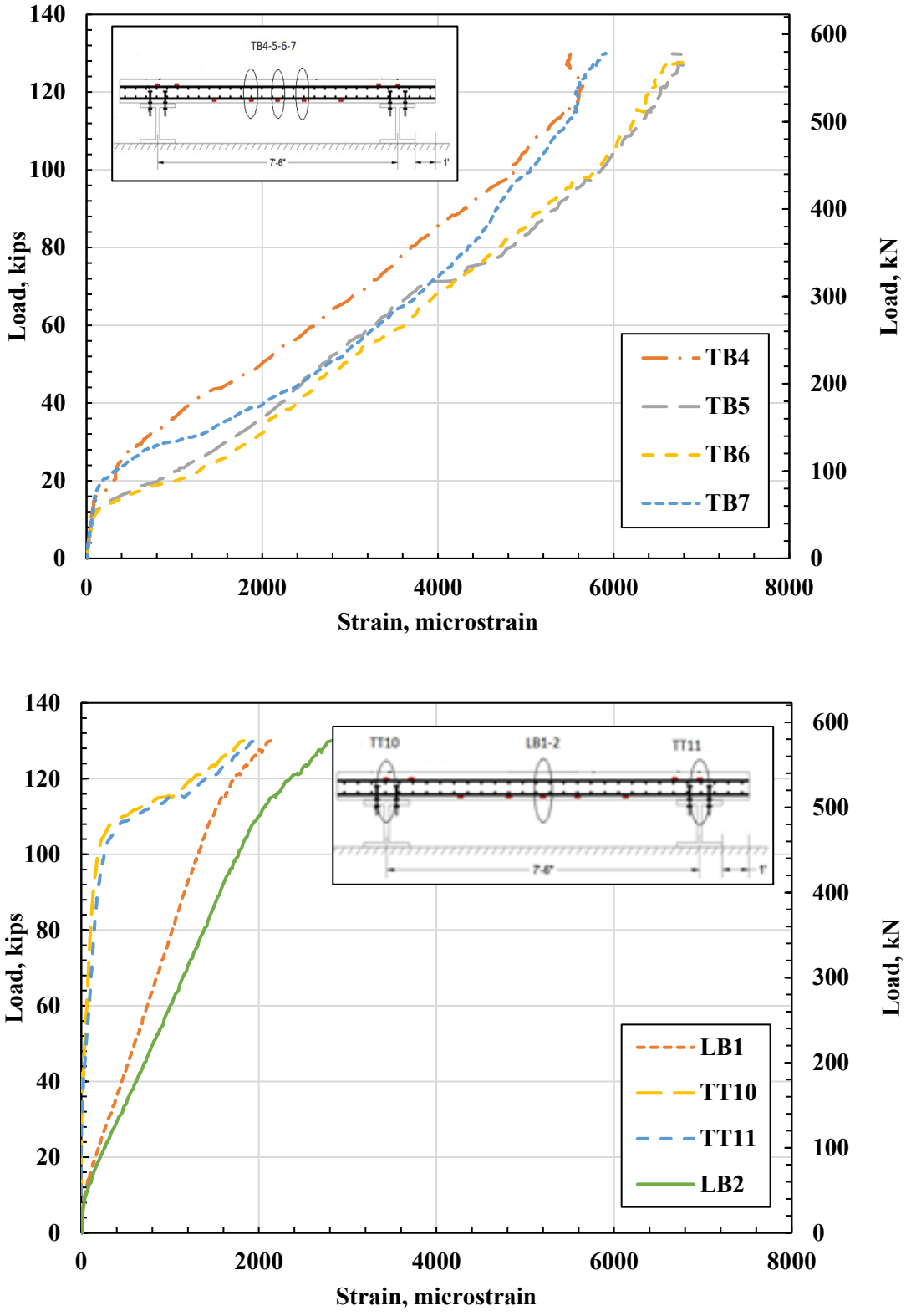

Figure 56: Load-strain curves of BFRP of bridge deck Prototype 1.

The strains in the concrete at the top of the midspan were measured using five strain gauges installed on the compression face of the concrete at the midspan. The strain measurements in the concrete were recorded by strain gauges C1, C2, C3, C4, and C5. The load-strain curves were plotted as shown in Figure 57. During testing, the maximum strain recorded in the concrete at the top of the midspan was a 1980 micro-strain. Figure 57 shows the concrete strain in compression and the strain in the BFRP in tension.

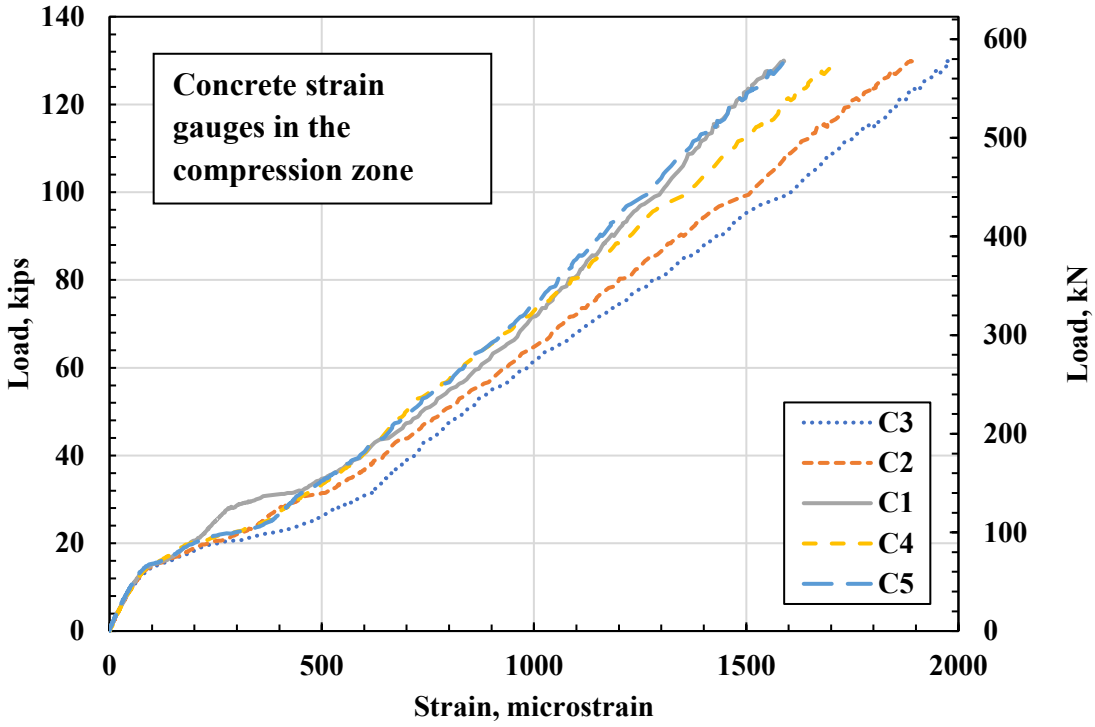

Figure 57: Load-strain curves of concrete at the midspan of bridge deck Prototype 1.

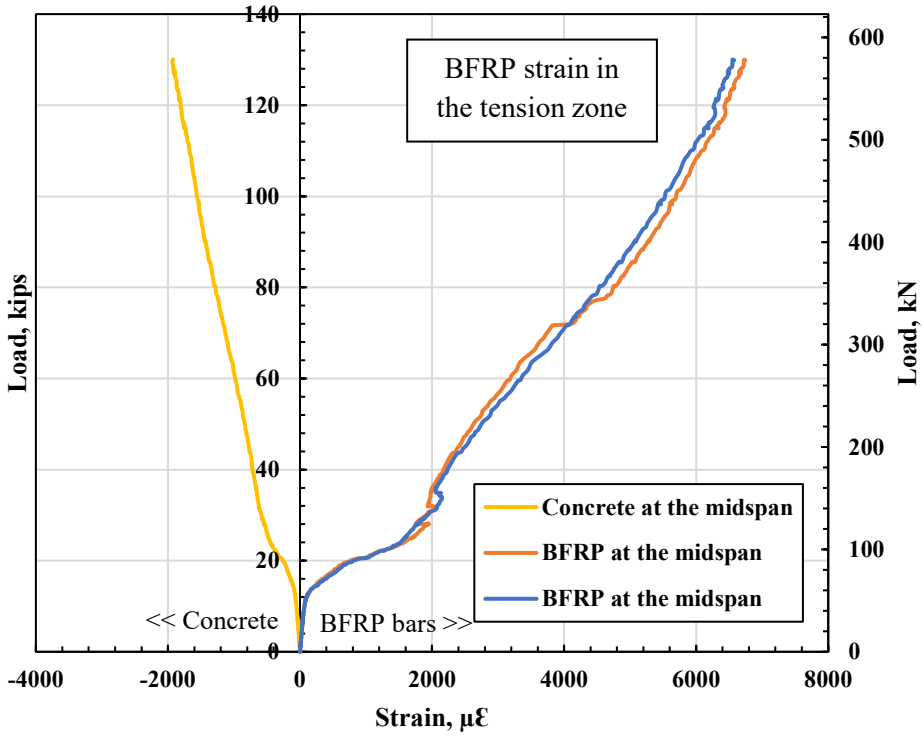

Figure 58: Load-strain curves in the concrete top surface and BFRP bars of bridge deck Prototype 1.

Figure 59: Failure mode of single-span Prototype 1.

4.1.1.4 Nonlinear Finite Element Analysis results

The single-span bridge deck test was simulated using ABAQUS to validate the finite element analysis. Figure 60 shows the single-span bridge deck assembly. During testing, the slab deflection at midspan was collected using LVDTs. In addition, the strain gauges were installed on the top surface of the concrete and on the bottom reinforcement.

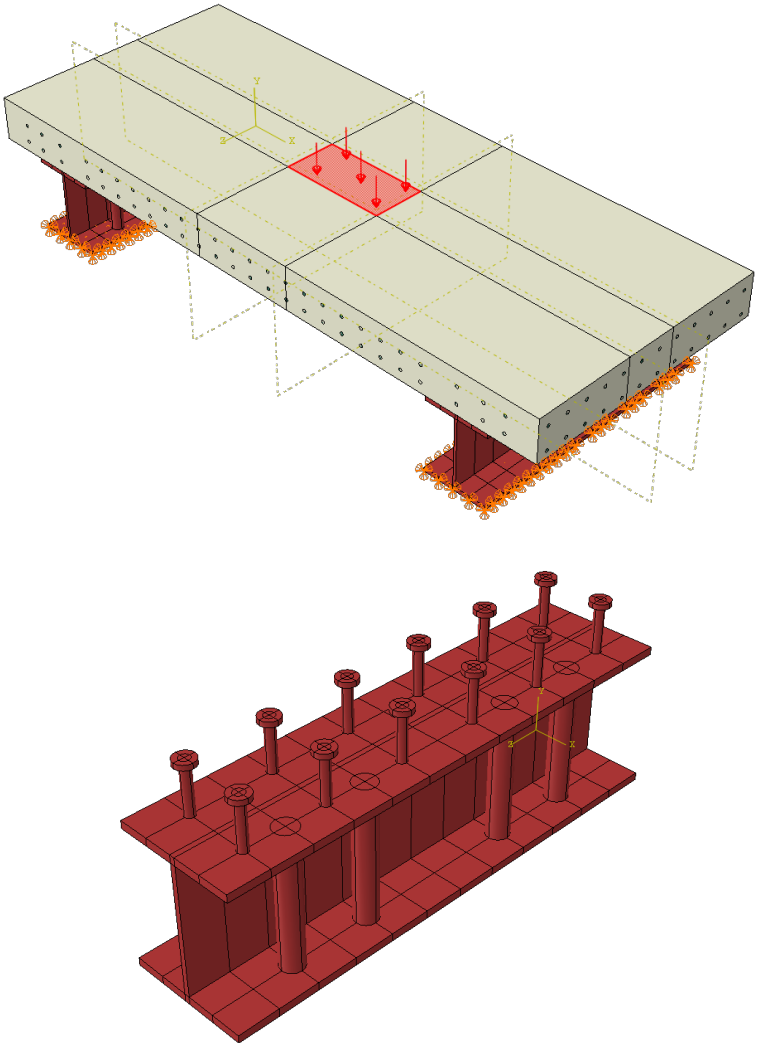

Figure 60: single span bridge deck assembly.

Figure 61 and 62 show plots of load-deflection and load-strain curves for concrete and reinforcement for experimental work and NLFEA at locations used in the experimental work. By visual inspection, there is an excellent agreement between the experimental results and the NLFEA. The finite element analysis predicted the bridge deck slab's ultimate strength capacity of 133 kips compared to an experimental capacity of 130 kips with a 2.5% error.

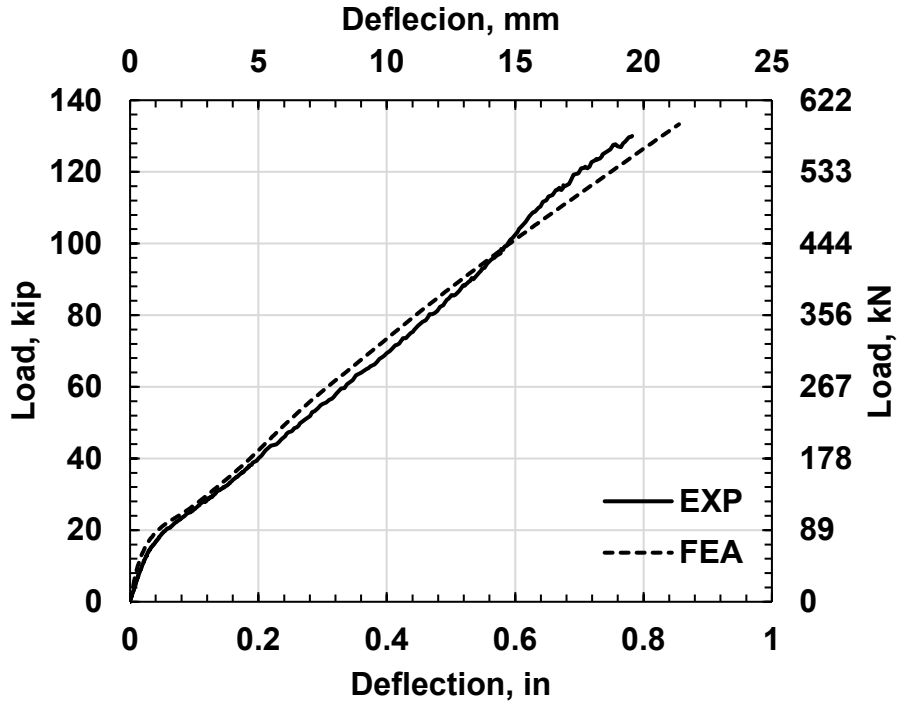

Figure 61: Load-deflection curves for single-span bridge deck slabs.

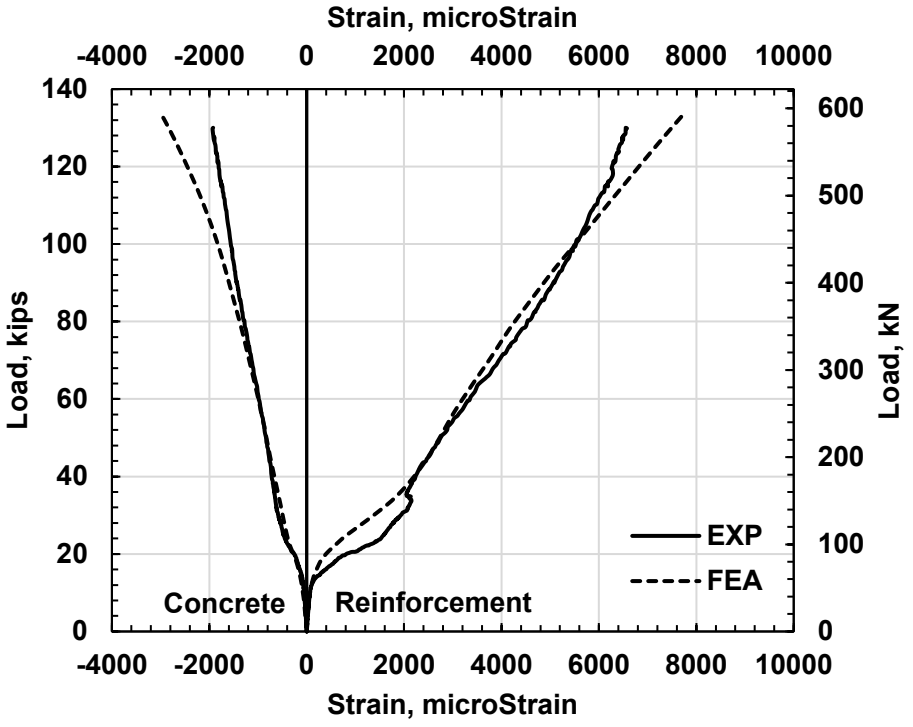

Figure 62: Load-strain curves for single-span bridge deck slabs.

4.1.2 Single-span bridge deck slab Prototype 2

The second simply-supported slab was cast successfully on September 24, 2021, as shown in Figure 64. BFRP #5 bar spaced at 6 inches was used at the top and bottom reinforcement mats in both directions. Figure 63 shows the reinforcement detailing with the strain gauge's locations. The same testing setup was used for both slabs 1 and 2. The concrete mix used in the second single-span slab is the same as the mix used for the single-span bridge deck slab Prototype 1 with a compressive strength of 6950 psi. The exact boundary condition was applied to the second and third simply-supported slabs. The mix proportions for the single-span bridge deck Prototype 2 and the two-span continuous bridge deck Prototype 1 are presented in Table 17.

Table 17: Concrete mix proportion for Prototype 2.

Material	Designation	Design Qty	Required	Batched
Coarse aggregate	22CM161HR	520 lb.	3644 lb.	3610 lb.
Coarse aggregate	22CM11BLJ	1360 lb.	9529 lb.	9470 lb.
Fine aggregate	27FM01OH	1250 lb.	9077 lb.	9080 lb.
Slag	SLG-SKY	190 lb.	1330 lb.	1325 lb.
Cement	CEM-HCMSG	330 lb.	6602310 lb.	2295 lb.
Water	WATER1	27.5 gal.	143.7 gal.	143.6 lb.
Air entrainment admixture	AE-DX2	3.0 oz.	21 oz.	21 oz.
Medium range water reducer	WRR-REC	2.0 /C	72.8 oz.	72 oz.
High range water reducer	HR-A575	2.0 /C	72.8 oz.	72 oz.

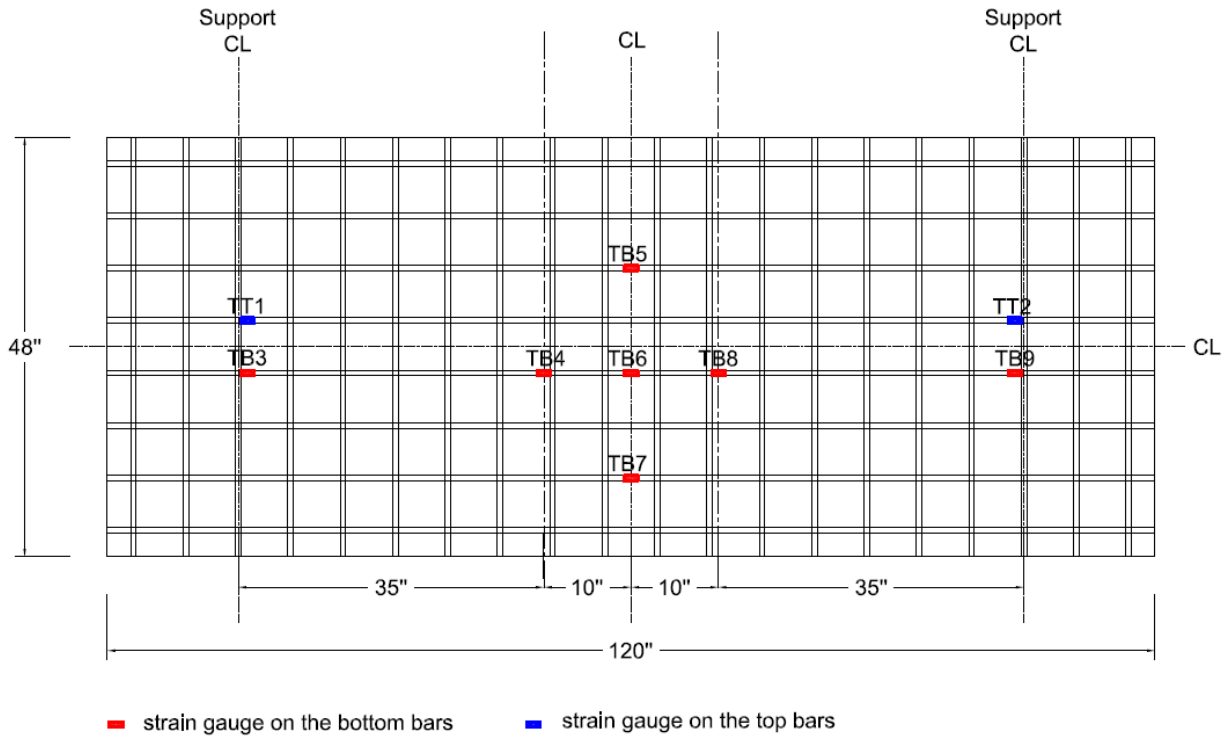

Figure 63: Reinforcement detailing of single-span bridge deck Prototype 2.


BFRP #5 bar spaced at 6 in.
Top and bottom

Figure 64: Single-span bridge deck Prototype 2 before and during the concrete pour.

The tested specimens were designed to simulate the commonly used slab-on-girder bridges. The slabs were casted in place, representing the bridge deck's actual behavior in the real bridges. Figure 65 shows the Load-Deflection curve of the tested simply supported slab with 6 in. reinforcement spacing and maintaining the same boundary conditions for both slabs (slab Prototype 2). The investigation of Figure 65 shows the higher capacity of slab Prototype 1 than slab Prototype 2 due to the more reinforcement in slab Prototype 1 with a constant concrete compressive strength and span length. The percentage increase in the reinforcement ratio is 33%, while this difference's effect on the ultimate strength is a 19% increase between the two slabs. The two slab Prototypes had the same mode of failure (compression shear failure), starting with the crash of the concrete in the compression zone at the bottom, followed by shear failure at an angle of approximately 45º.

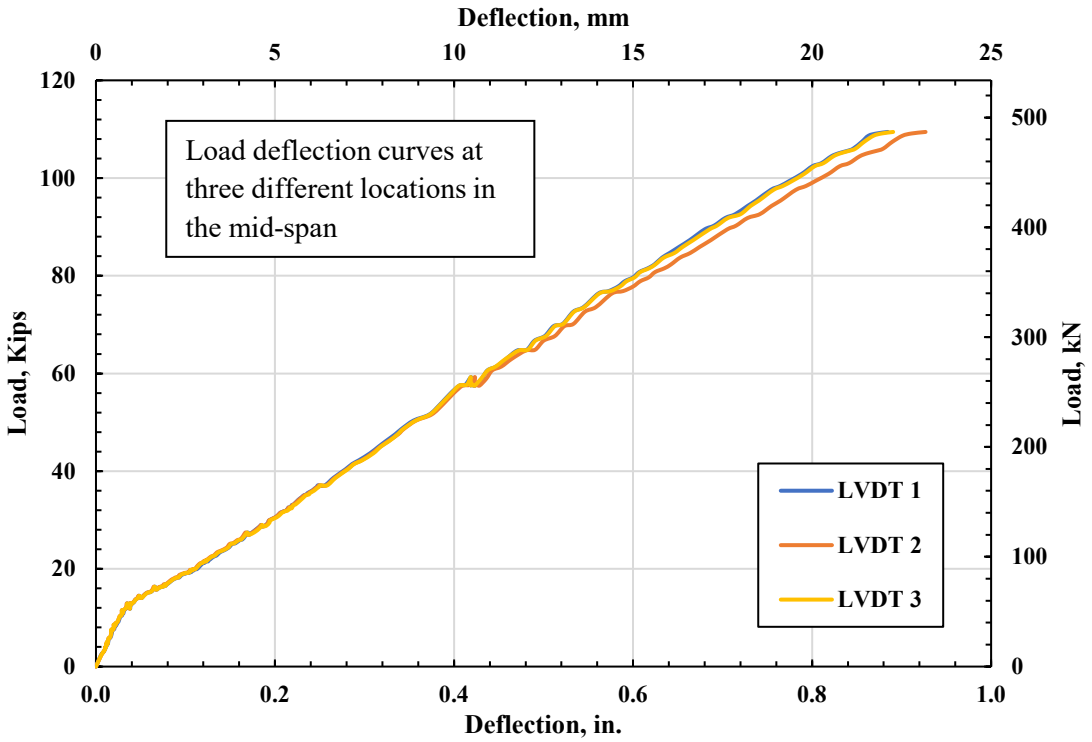

Figure 65: Load-deflection curves of bridge deck Prototype 2.

The two slab Prototypes had the same mode of failure (compression shear failure), starting with the crash of the concrete in the compression zone at the bottom, followed by shear failure at an angle of approximately 40º, as shown in Figure 66. The

bold lines represent the failure mode, and the cracks are presented with regular line size. The number at the crack lines in the figure represented the load when the crack was visible by naked eyes during testing. The investigation of the figure shows that the slab cracked at the midspan first, and other cracks started to appear at different locations due to the release of the stress from the midspan caused by the crack. Other cracks began to appear at the supports on both sides caused by the negative moment at the support. The failure mode was sudden, without any fracture in the BFRP bars.

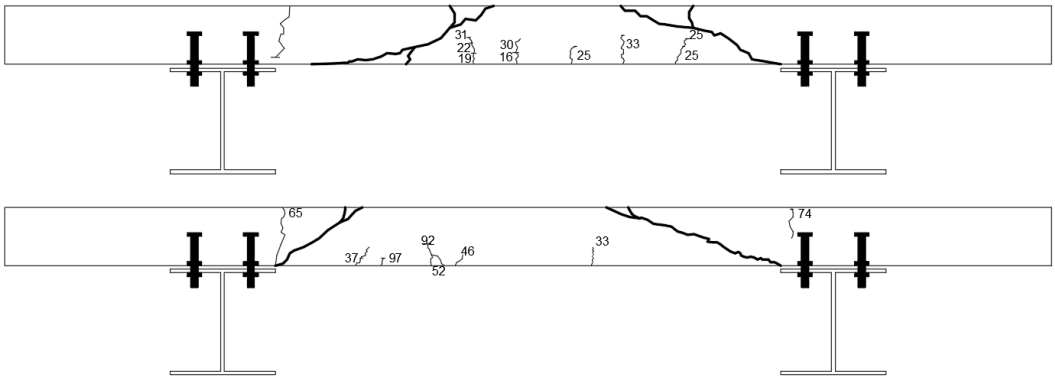

Figure 66: Crack mapping and failure mode of a single-span bridge deck Prototype 2.

The slab was designed as an over-reinforced to prevent any failure in the BFRP bars, unlike steel-reinforced concrete. The maximum strain in the BFRP bars recorded was 6729 and 7835 μƐ for slabs Prototype 1 and 2, respectively, which is estimated to be 28% and 32% of the ultimate strain of the bar. It is to be noted that the slab was able to sustain a load of 51 kips after failure in the concrete without any fracture or failure in the BFRP bars. The Load-Strain curve in the BFRP and concrete at the midspan of the two slab Prototypes are shown in Figure 67. The curves to the right represent the strain in the BFRP (tension), while the curves on the left represent the strain in the concrete surface at the midspan (compression). The load strain curve undergoes a linear relationship before cracking, followed by a jump in the strain caused by the cracking stage of the section, and continues approximately straight until failure. Slab Prototype 1 had higher ultimate strength and lower maximum strain in concrete and BFRP reinforcing bar than Prototype 2 predicted. Figure 68 shows the load versus maximum crack opening of slab Prototype 1.

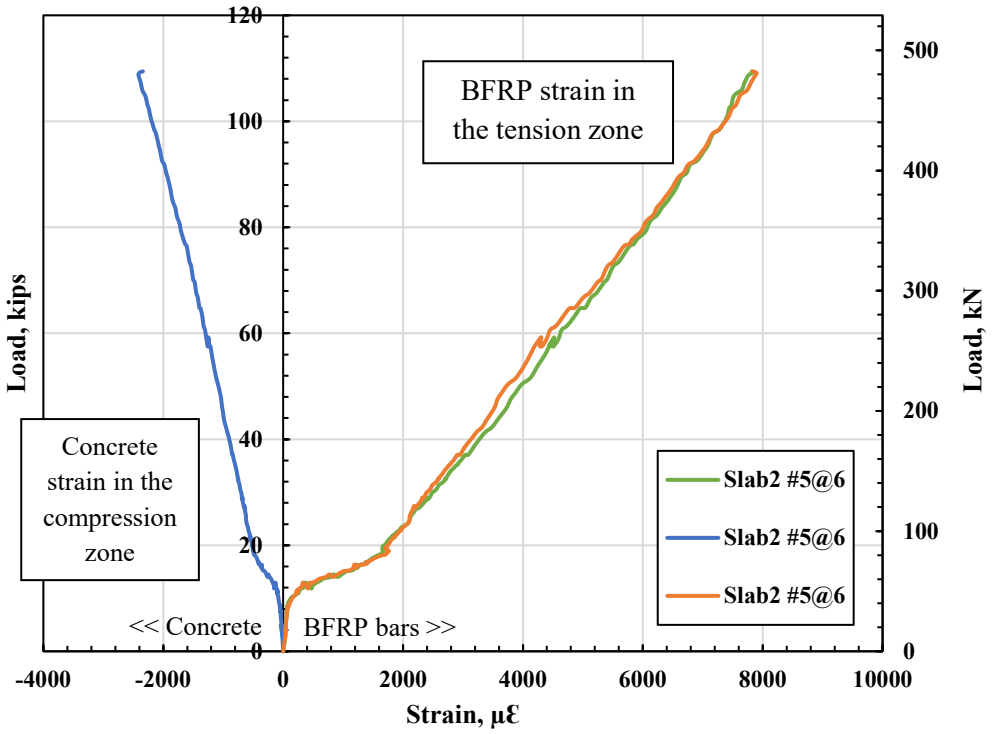

Figure 67: Load-strain curves in the concrete top surface and BFRP bars of bridge deck Prototype 2.

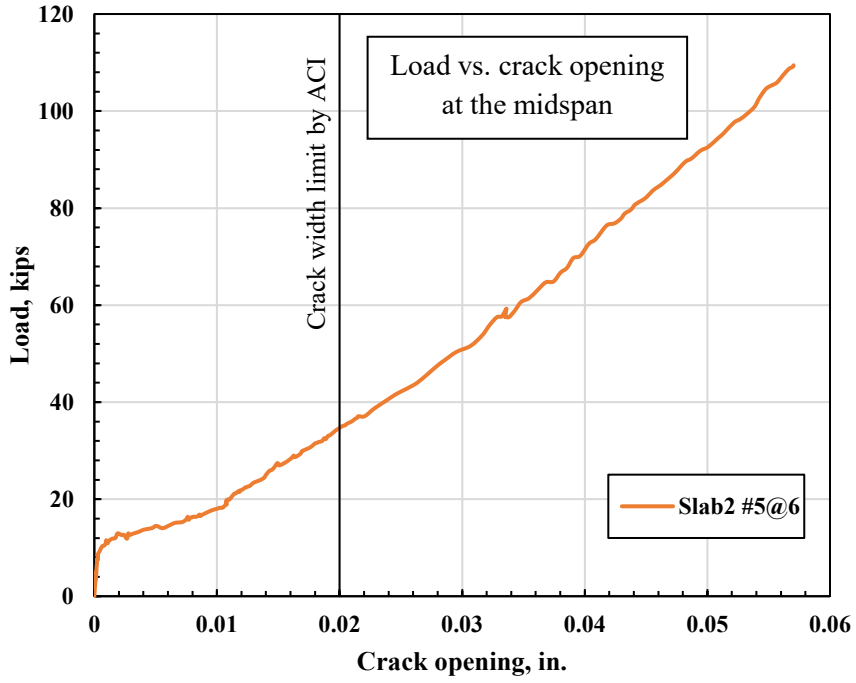

Figure 68: Load-crack width curve at the bottom midspan of bridge deck Prototype 2.


DELL
DELL

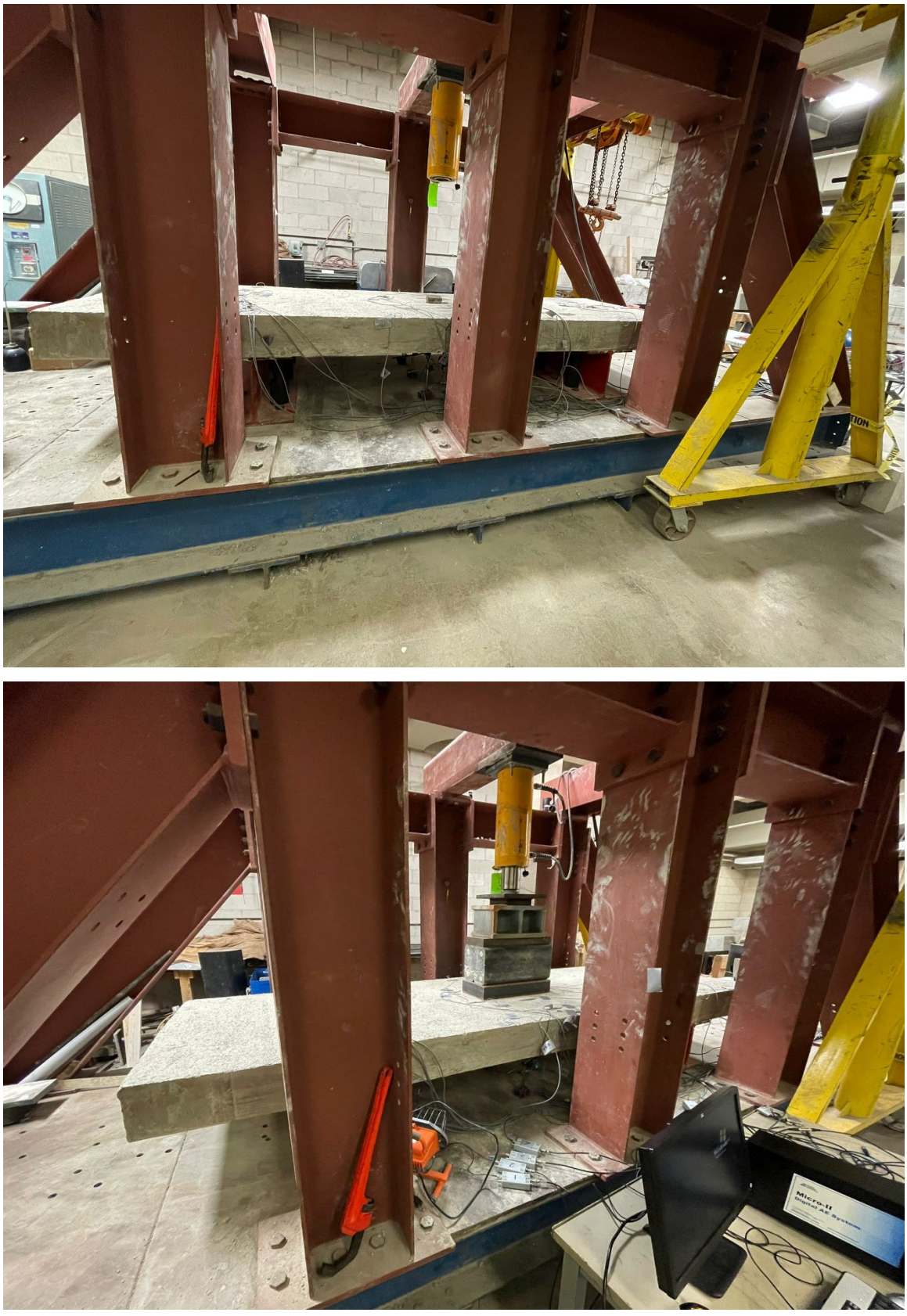

Figure 69: Testing setup of bridge deck Prototype 2.

Figure 70: Concrete strain gauges, LVDT, and crack-meters installed on bridge deck Prototype 2.

Figure 71: Failure mode of bridge deck Prototype 2.

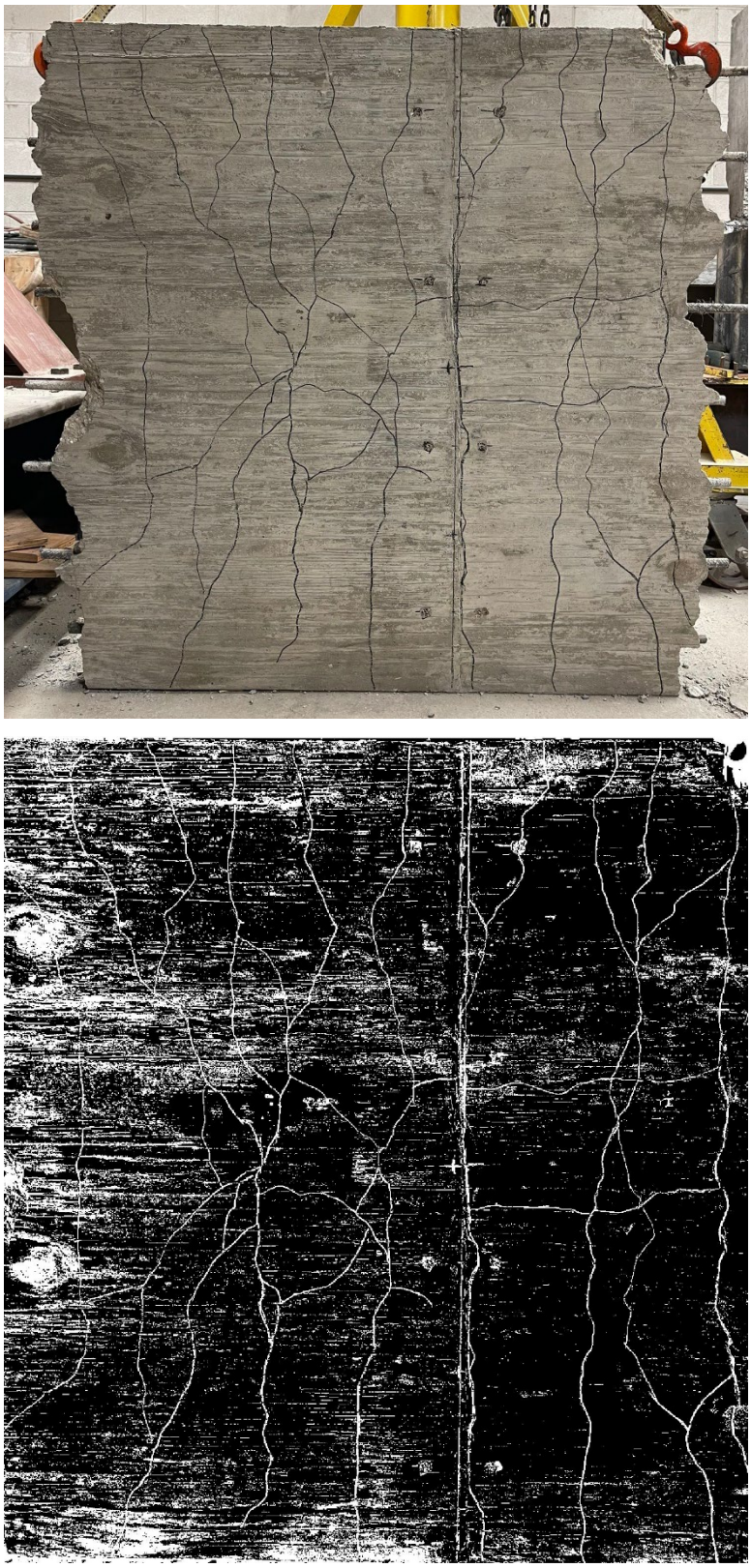

Figure 72: Crack mapping at the bottom midspan of bridge deck Prototype 2.

4.1.2.1 Nonlinear Finite Element Analysis results

Figure 73 shows the load-deflection curves of specimen SS2. It reveals that both the experimental and the numerical curves are bilinear. The NLFEA overestimated the cracking load. By visual inspection, there is a good agreement between the experimental results and the NLFEA. Figure 74 shows the load-strain curves of specimen SS2. The finite element analysis predicted the bridge deck slab's ultimate strength capacity of 120 kips compared to an experimental capacity of 109 kips with a 9.2% error.

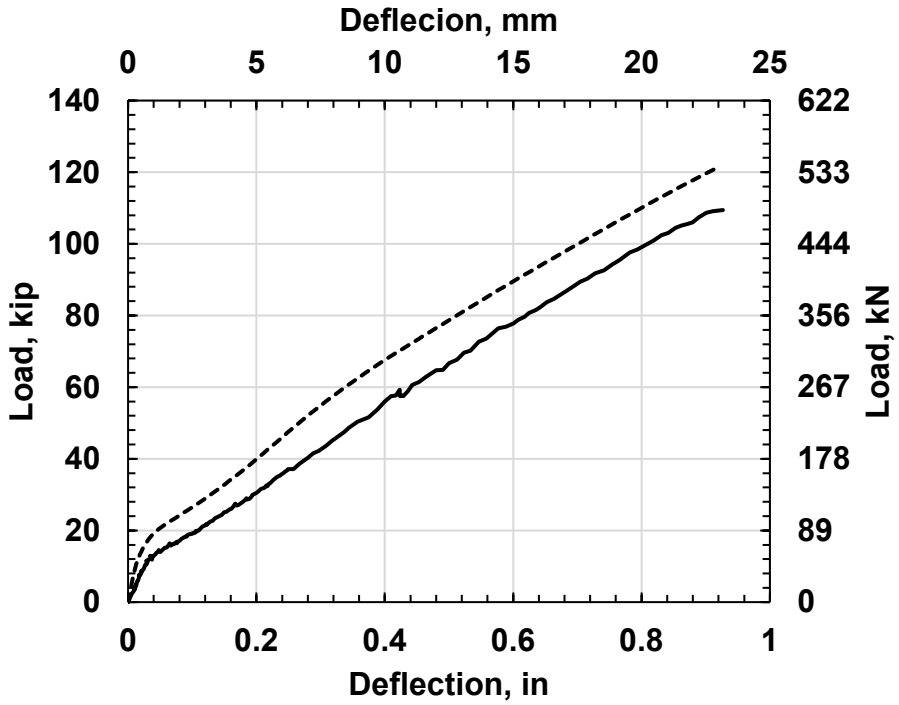

Figure 73: Load-deflection curves for single-span bridge deck slabs.

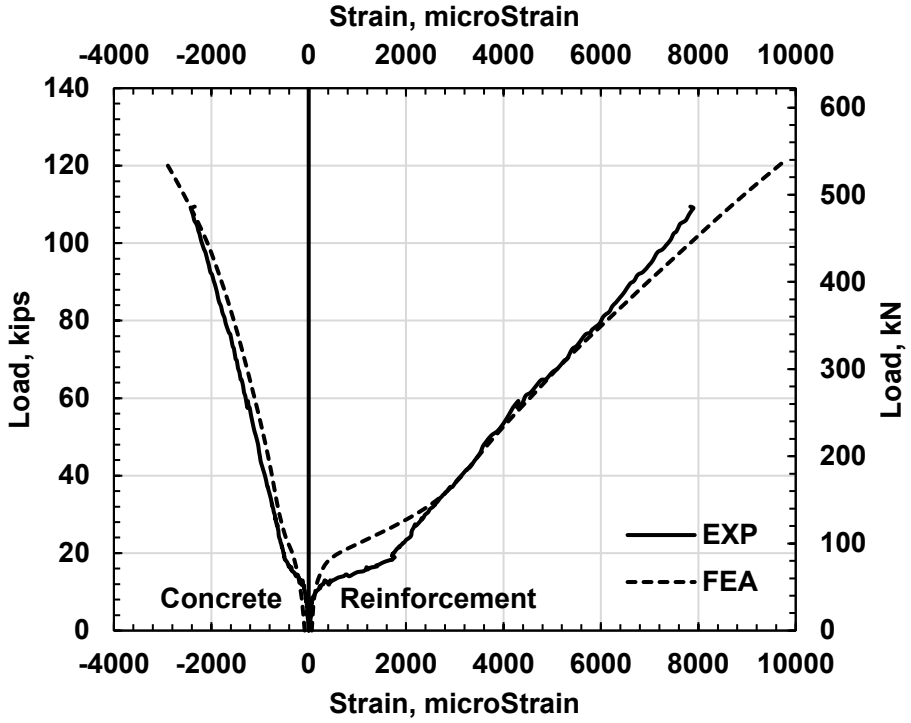

Figure 74: Load-strain curves for single-span bridge deck slabs.

4.1.3 Single-span bridge deck slab Prototype 3

Based on the test results of the bridge deck slabs, BFRP No. 6 bar spaced at 6 inches was used in the transverse direction for the top and bottom reinforcement mat. The reinforcement ratio of this slab is close to the reinforcement ratio in Prototype 1 and the effect of changing the bar size and spacing while keeping the same reinforcement ratio will be demonstrated. The total slab length of the slab is 10 ft. and the width 4 ft., and 8 in. thickness. BFRP #5 bars at 6 inches were also used in the longitudinal direction for the bottom and top longitudinal reinforcement. Using No. 6 bars spaced at 6 in is to study the effect of bar size on the behavior and ultimate strength of the slab. The supported span length of the slab is 7 ft. as in the previous Prototypes.

For this bridge deck slab Prototype, the formwork is shown in Figure 75. The slab construction preparation was finished as well as the concrete pouring. The Illinois Tollway concrete mix proportion for bridge decks was used for the slabs with a 6500 psi compressive strength. Moreover, the BFRP reinforcing bars are from the same source

as the bars used in the tested slabs. Figure 76 shows the reinforcement detailing with the strain gauge's locations. The same testing setup was used for both slabs 1 and 2.

Table 18: Concrete mix proportion for Prototype 3.

Material	Designation	Design Qty	Required	Batched
Coarse aggregate	22CM161HR	520 lb.	2346 lb.	2400 lb.
Coarse aggregate	22CM11BLJ	1360 lb.	6135 lb.	6090 lb.
Fine aggregate	27FM01OH	1250 lb.	5797 lb.	5740 lb.
Slag	SLG-SKY	190 lb.	855 lb.	860 lb.
Cement	CEM-HCMSG	330 lb.	1485 lb.	1495 lb.
Water	WATER1	27.5 gal.	100 gal.	100 lb.
Air entrainment admixture	AE-DX2	3.0 oz.	13.5 oz.	13.5 oz.
Medium range water reducer	WRR-REC	2.0 /C	46.8 oz.	46 oz.
High range water reducer	HR-A575	2.0 /C	46.8 oz.	45 oz.

Figure 75: Formwork and BFRP reinforcement mesh of bridge deck Prototype 3.

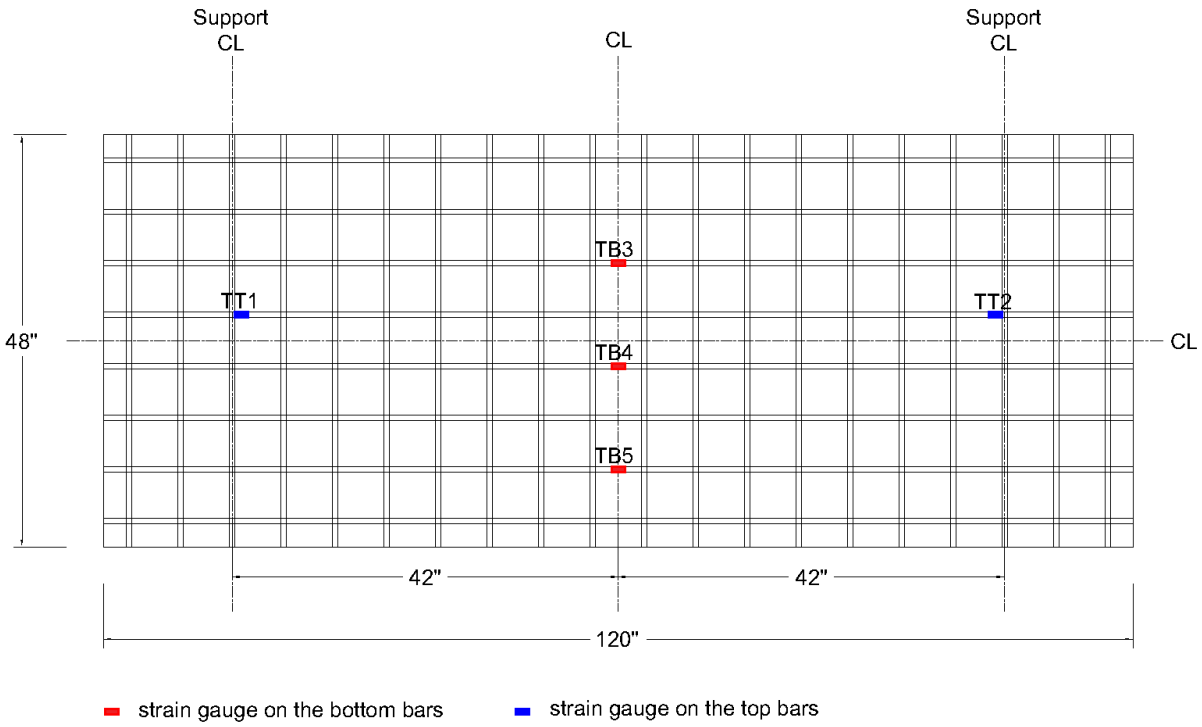

Figure 76: Location of strain gauges on reinforcement of bridge deck Prototype 3.

The tested specimens were designed to simulate the commonly used slab-on-girder bridges. The slabs were casted in place, representing the bridge deck's actual behavior in the real bridges. Figure 77 shows the Load-Deflection curve of the tested single span bridge deck slab with 6 in. reinforcement spacing and maintaining the same boundary conditions for both slabs (Prototypes 1 and 2). The investigation of Figure 77 shows the higher capacity of slab Prototypes 1 and 3 than slab Prototype 2 due to the more reinforcement in slab Prototype 1. The percentage increase in the reinforcement ratio is 33%, while this difference's effect on the ultimate strength is a 19% increase between the two slabs. The two slab Prototypes had the same mode of failure (compression shear failure), starting with the crash of the concrete in the compression zone at the bottom, followed by shear failure at an angle of approximately 45º.

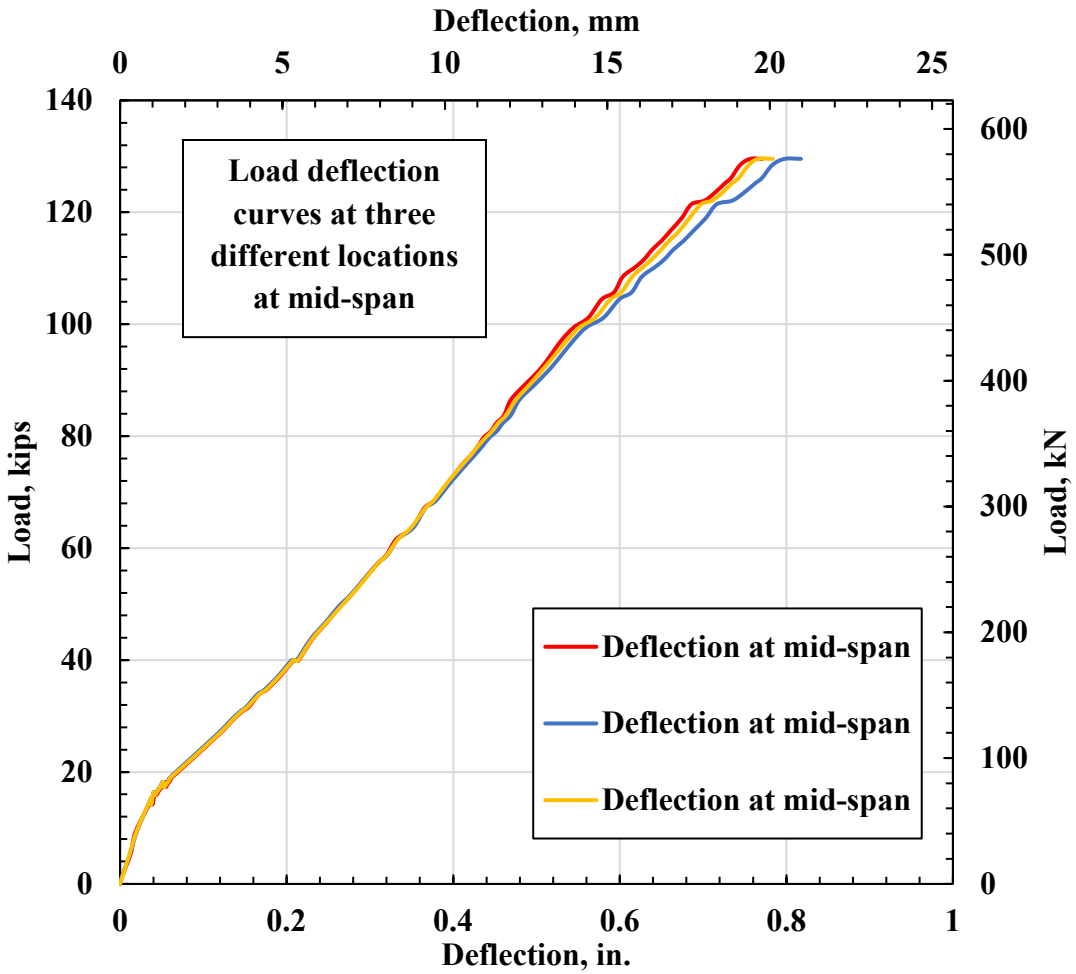

Figure 77: Load-deflection curves of bridge deck Prototype 3.

The failure mode of the three single-span bridge deck Prototypes 1, 2, and 3 had the same mode of failure (compression shear failure), starting with the crash of the concrete in the compression zone at the bottom, followed by shear failure at an angle of approximately 45º, as shown in Figure 81. The bold lines represent the failure mode, and the cracks are presented with regular line size. The investigation of the figure shows that the slab cracked at the midspan first, and other cracks started to appear at different locations due to the release of the stress from the midspan caused by the crack initiation. Other cracks began to appear at the supports on both sides caused by the negative moment at the support. The failure mode was sudden, without any fracture in the BFRP bars.

The slab was designed as an over-reinforced to prevent any failure in the BFRP bars, unlike steel-reinforced concrete. The maximum strain in the BFRP bars recorded was 6187 με for slabs Prototype 3, which is estimated to be 28% of the ultimate strain of the bar. It is to be noted that the slab was able to sustain at least a load of 55 kips after failure in the concrete without any fracture or failure in the BFRP bars. The Load-Strain curve in the BFRP and concrete at the midspan of the two slab Prototypes are shown in Figure 78. The curves to the right represent the strain in the BFRP (tension), while the curves on the left represent the strain in the concrete surface at the midspan (compression). The load strain curve undergoes a linear relationship before cracking, followed by a jump in the strain caused by the cracking stage of the section, and continues approximately straight until failure. Slab Prototype 1 and 3 had higher ultimate strength and lower maximum strain in concrete and BFRP reinforcing bar than Prototype 2 as predicted. Figure 79 shows the load versus maximum crack opening of slab Prototype 3.

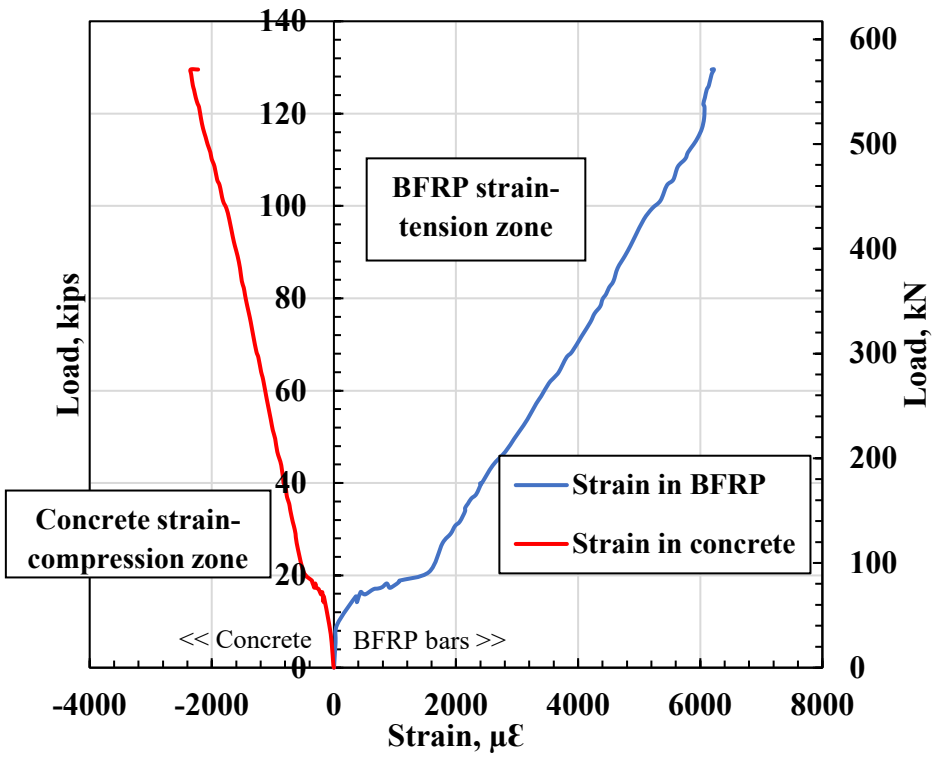

Figure 78: Load-strain curves in the concrete top surface and BFRP bars of bridge deck Prototype 3.

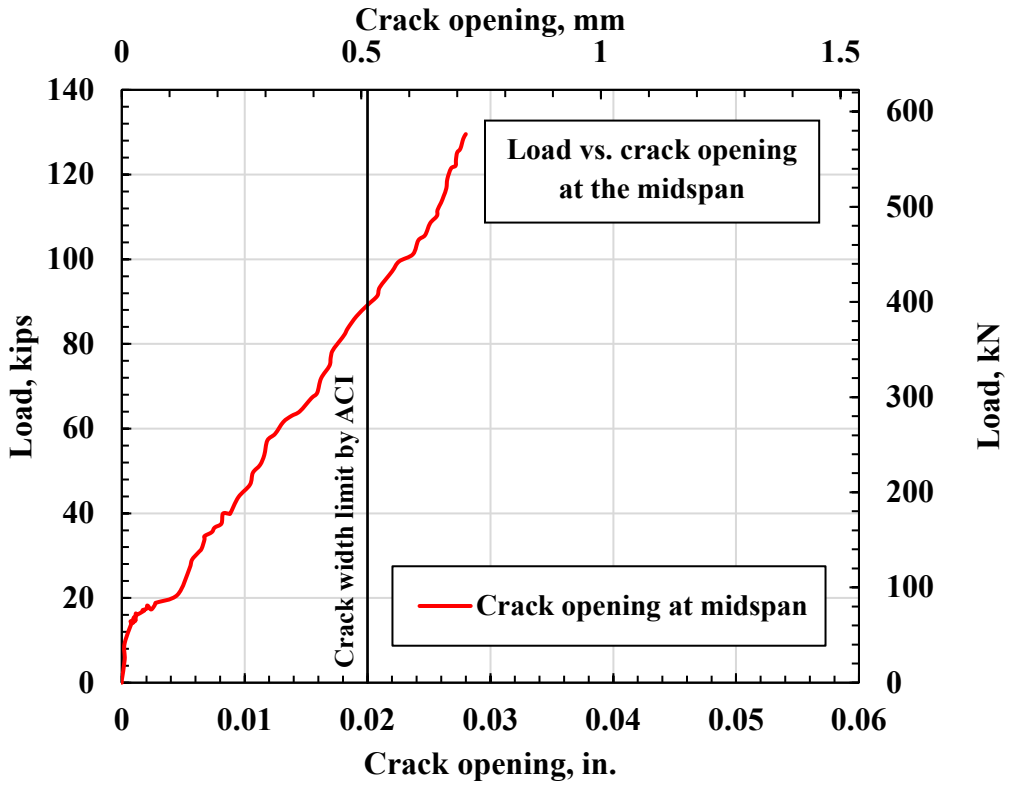

Figure 79: Load-crack opening curve of bridge deck Prototype 3.

Figure 80: Mode of failure of bridge deck Prototype 3.

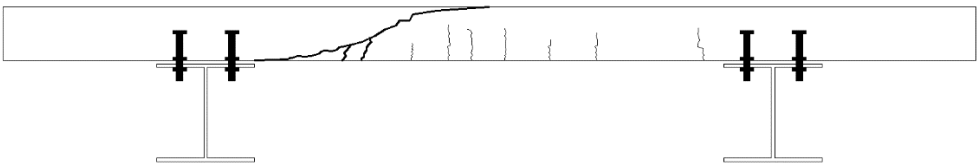

Figure 81: Crack mapping of bridge deck Prototype 3.

4.1.3.1 Nonlinear Finite Element Analysis results

Figure 82 and 83 show plots of load-deflection and load-strain curves for concrete and reinforcement for experimental work and NLFEA at locations used in the experimental work. By visual inspection, there is an excellent agreement between the experimental results and the NLFEA. The finite element analysis predicted the bridge deck slab's ultimate strength capacity of 133 kips compared to an experimental capacity of 129 kips with a 3.0% error.

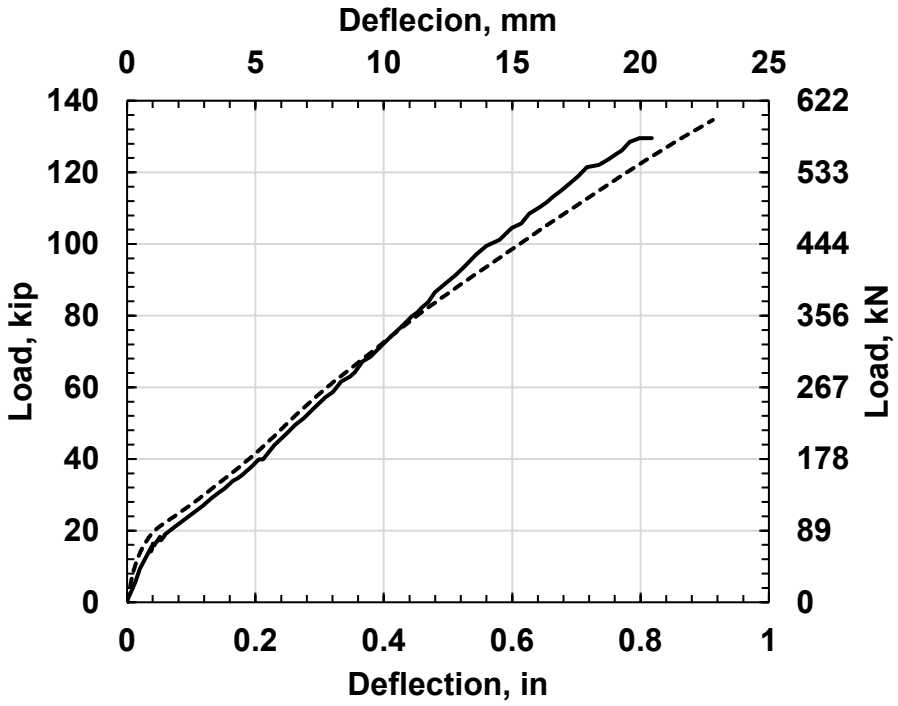

Figure 82: Load-deflection curves for single-span bridge deck slabs.

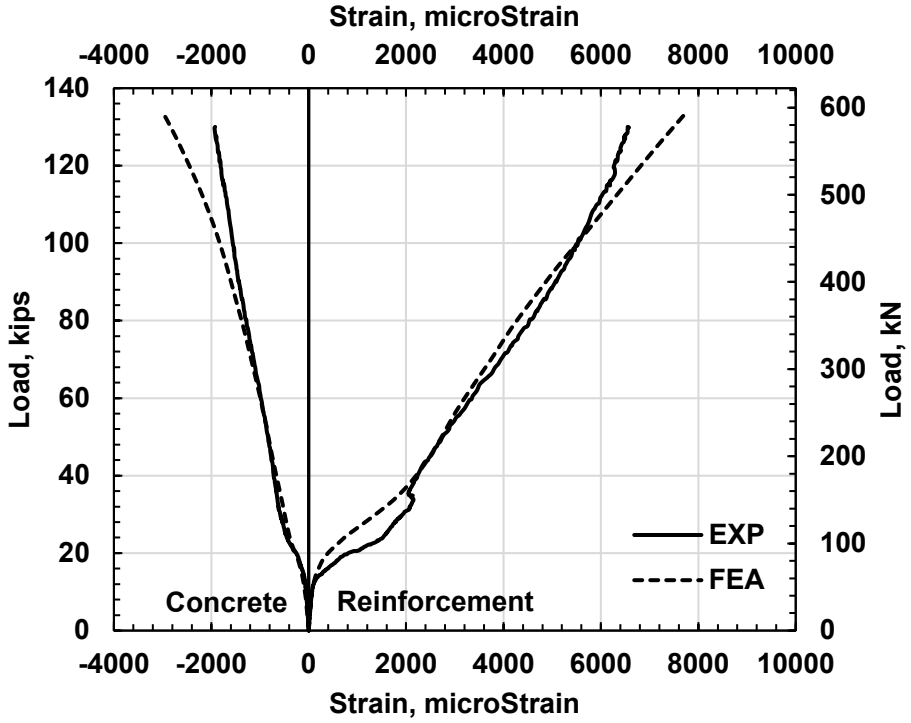

Figure 83: Load-strain curves for single-span bridge deck slabs.

4.1.4 Single-span bridge deck slab Prototype 4

Based on the tested bridge deck slabs results, BFRP No.5 sbar spaced at 8 in. was used in the transverse direction for the top and bottom reinforcement mat. The total slab length of the slab is 10 ft. and the width 4 ft. and an 8 in. thickness. Also, the same bar size was used in the longitudinal direction but with a spacing of 8 in. for the bottom and top longitudinal reinforcement. Using No. 5 bars at 8 in. is to study the effect of increasing the spacing to 8 inches on the slab behavior and the ultimate strength of the slab. The supported span length of the slab is 7 ft. as in the previous Prototypes.

The reason for testing an additional slab is the interest in this topic and to produce a valuable outcome from this research project and the promising results obtained from the complete, tested bridge deck slabs.

Figure 84 shows the formwork and the BFRP reinforcement. The slab construction preparation was finished, as well as the concrete pouring and the embedded strain gauges. The Illinois Tollway concrete mix proportion for bridge decks was used with a

compressive strength of 6350 psi. Moreover, the BFRP reinforcing bars are from the same source as the bars used in the tested slabs.

Table 19: Concrete mix proportion for Prototype 4.

Material	Designation	Design Qty	Required	Batched
Coarse aggregate	22CM161HR	520 lb.	2346 lb.	2400 lb.
Coarse aggregate	22CM11BLJ	1360 lb.	6135 lb.	6090 lb.
Fine aggregate	27FM01OH	1250 lb.	5797 lb.	5740 lb.
Slag	SLG-SKY	190 lb.	855 lb.	860 lb.
Cement	CEM-HCMSG	330 lb.	1485 lb.	1495 lb.
Water	WATER1	27.5 gal.	100 gal.	100 lb.
Air entrainment admixture	AE-DX2	3.0 oz.	13.5 oz.	13.5 oz.
Medium range water reducer	WRR-REC	2.0 /C	46.8 oz.	46 oz.
High range water reducer	HR-A575	2.0 /C	46.8 oz.	45 oz.

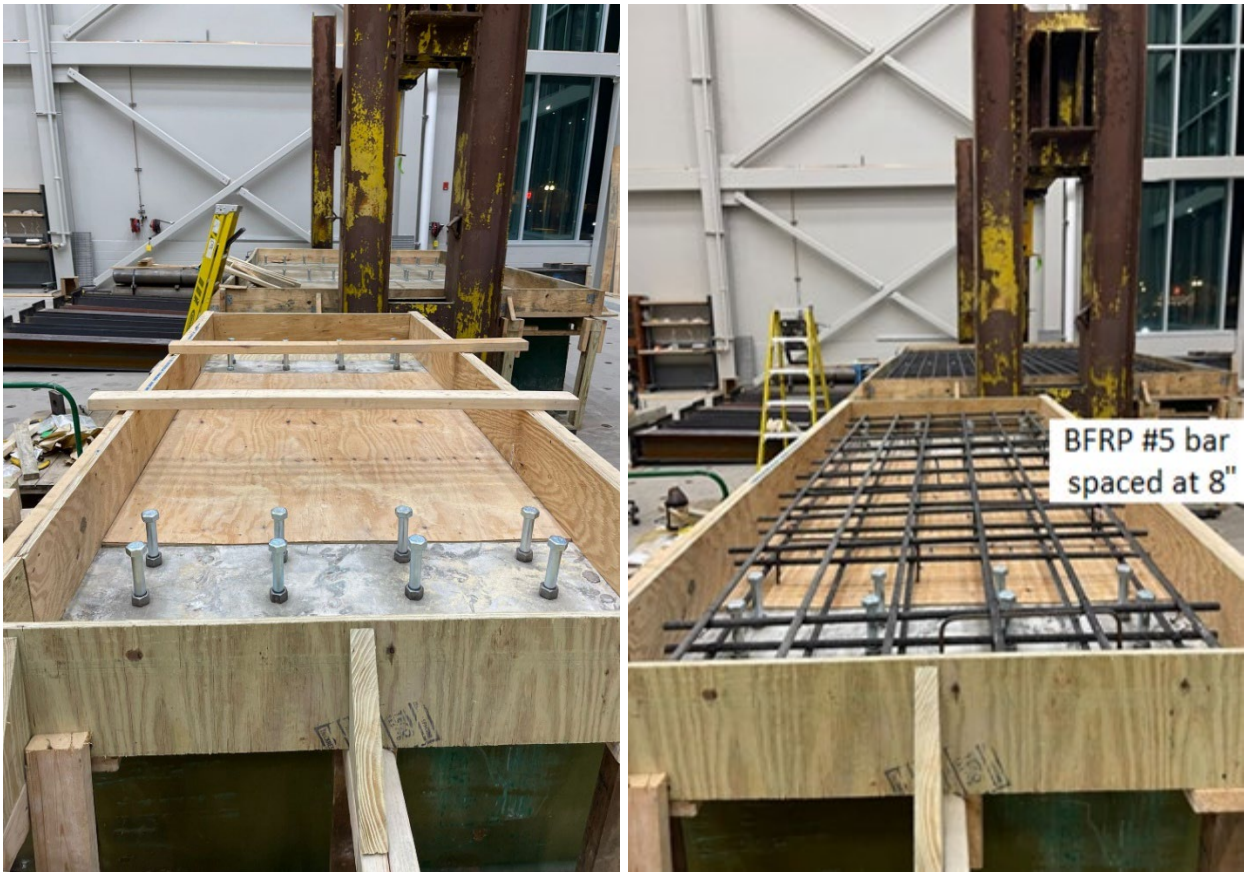

Figure 84: Formwork and BFRP reinforcement mesh of bridge deck Prototype 4.

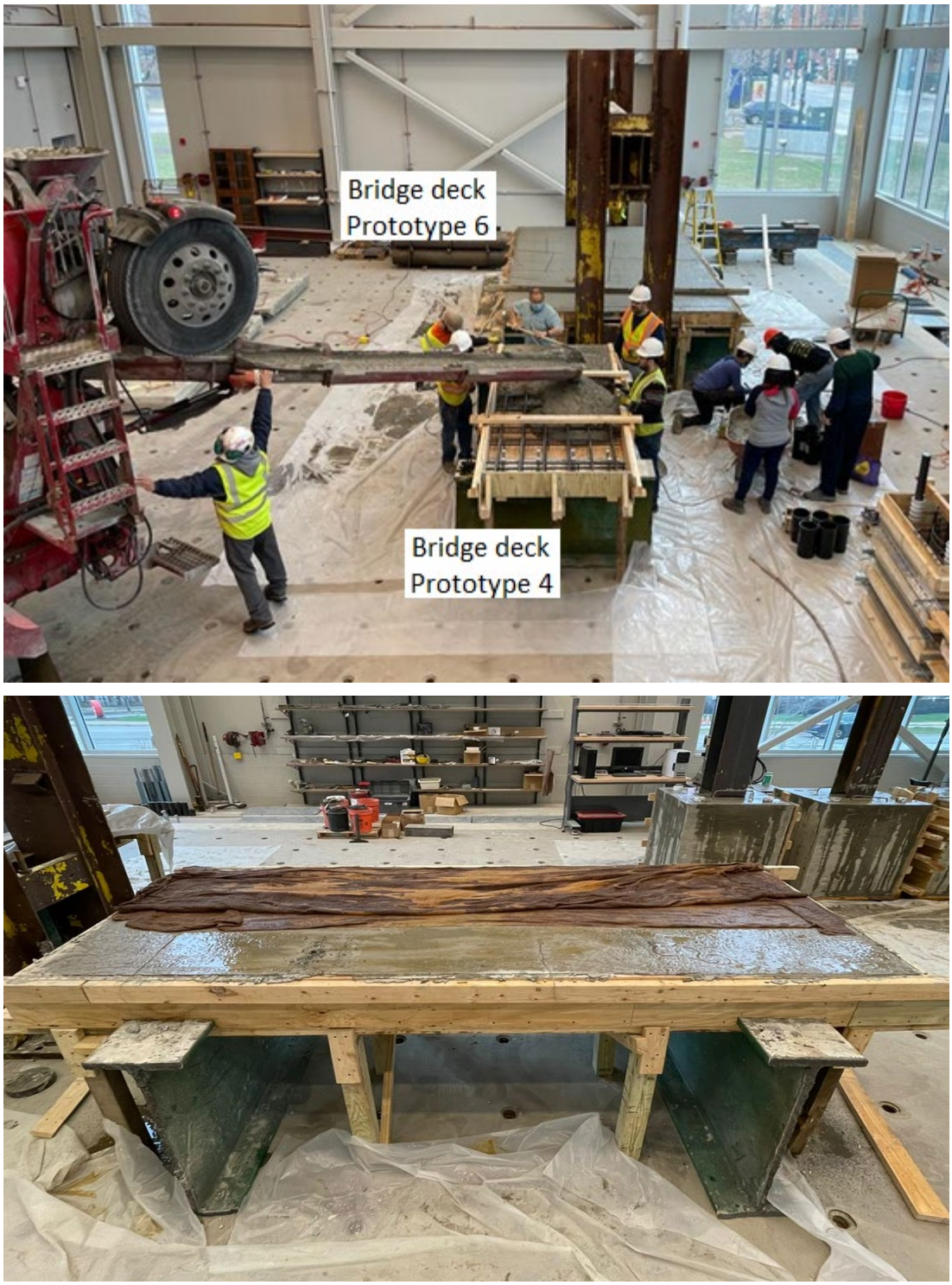

Figure 85: Concrete pouring of Single-span bridge deck Prototype 4.

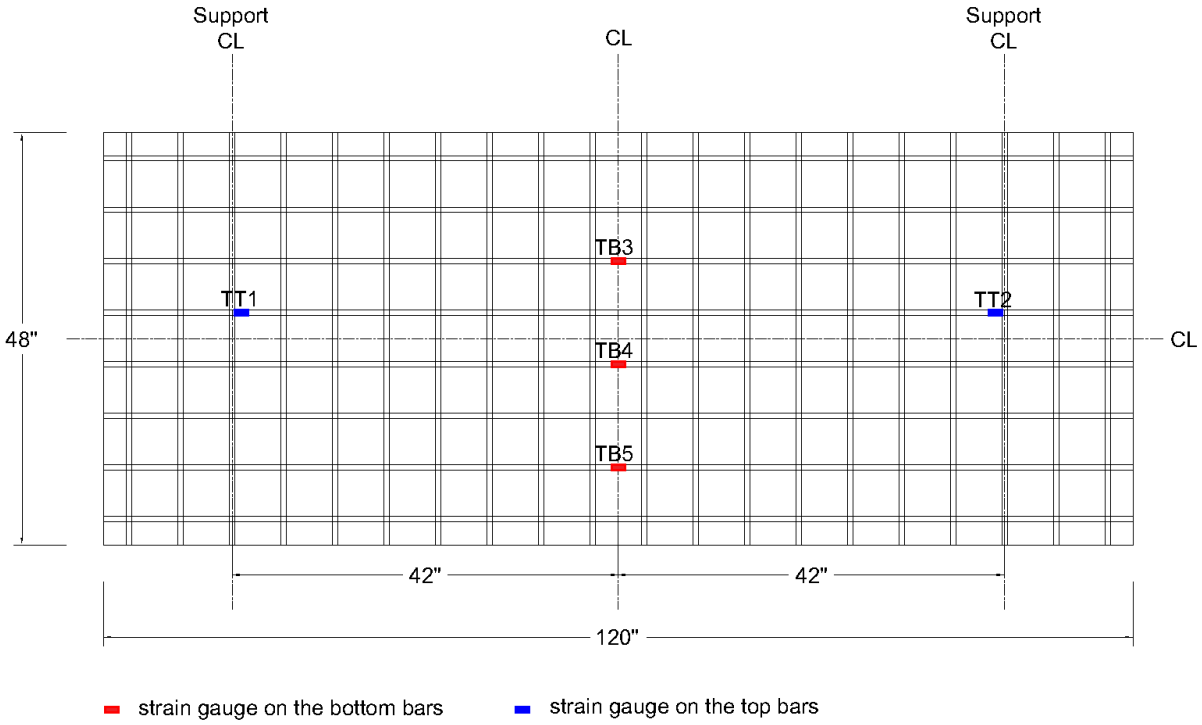

Figure 86: Locations of reinforcement and strain gauges of bridge deck Prototype 4.

The tested specimens were designed to simulate the commonly used slab-on-girder bridges. The slabs were casted in place, representing the bridge deck's actual behavior in the real bridges. Figure 87 shows the Load-Deflection curve of the tested single span bridge deck slab with 8 in. reinforcement spacing and maintaining the same boundary conditions for both slabs (Prototypes 1, 2, and 3). The four tested bridge deck slab Prototypes had the same mode of failure (compression shear failure), starting with the crash of the concrete in the compression zone at the bottom, followed by shear failure at an angle of approximately 45º.

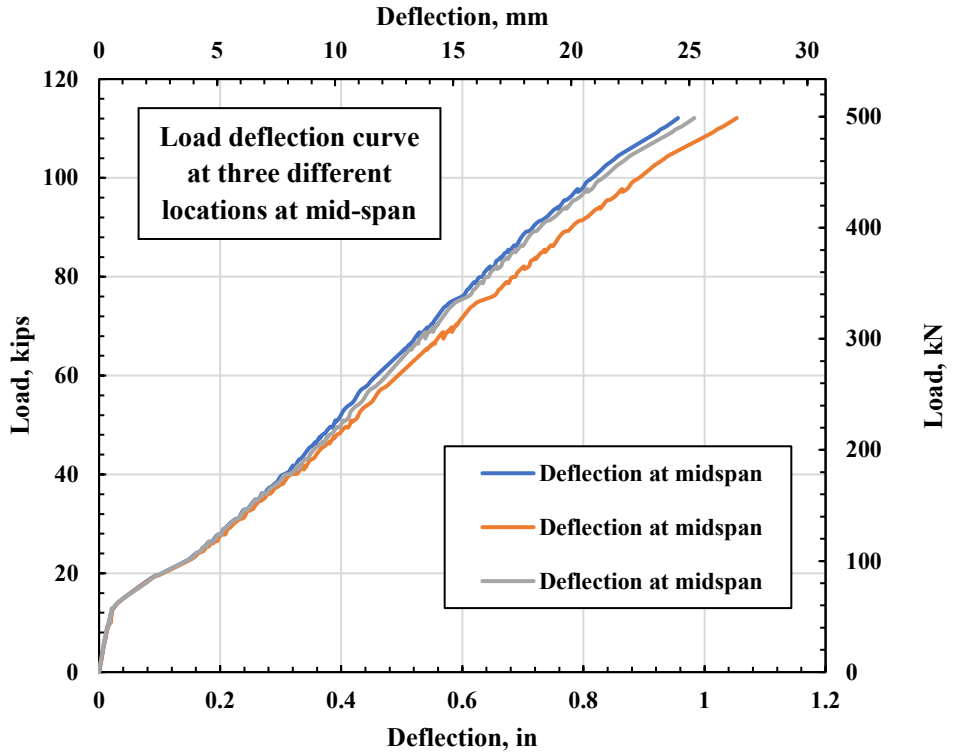

Figure 87: Load-deflection curves at the midspan of bridge deck Prototype 4.

The failure mode of the three single-span bridge deck Prototypes 1, 2, 3, and 4 had the same mode of failure (compression shear failure), starting with the crash of the concrete in the compression zone at the bottom, followed by shear failure at an angle of approximately 45º, as shown in Figure 91. The bold lines represent the failure mode, and the cracks are presented with regular line size. The investigation of the figure shows that the slab cracked at the midspan first, and other cracks started to appear at different locations due to the release of the stress from the midspan caused by the crack initiation. Other cracks began to appear at the supports on both sides caused by the negative moment at the support. The failure mode was sudden, without any fracture in the BFRP bars.

The slab was designed as an over-reinforced to prevent any failure in the BFRP bars, unlike steel-reinforced concrete. The maximum strain in the BFRP bars recorded was 10597 μƐ for slabs Prototype 4, which is estimated to be 48% of the ultimate strain of the bar. It is to be noted that the slab was able to sustain at least a load of 40 kips

after failure in the concrete without any fracture or failure in the BFRP bars. The Load-Strain curve in the BFRP and concrete at the midspan of the two slab Prototypes are shown in Figure 88. The curves to the right represent the strain in the BFRP (tension), while the curves on the left represent the strain in the concrete surface at the midspan (compression). The load strain curve undergoes a linear relationship before cracking, followed by a jump in the strain caused by the cracking stage of the section, and continues approximately straight until failure. Slab Prototype 1 and 3 had higher ultimate strength and lower maximum strain in concrete and BFRP reinforcing bar than Prototype 2 as predicted. Figure 89 shows the load versus maximum crack opening of slab Prototype 3.

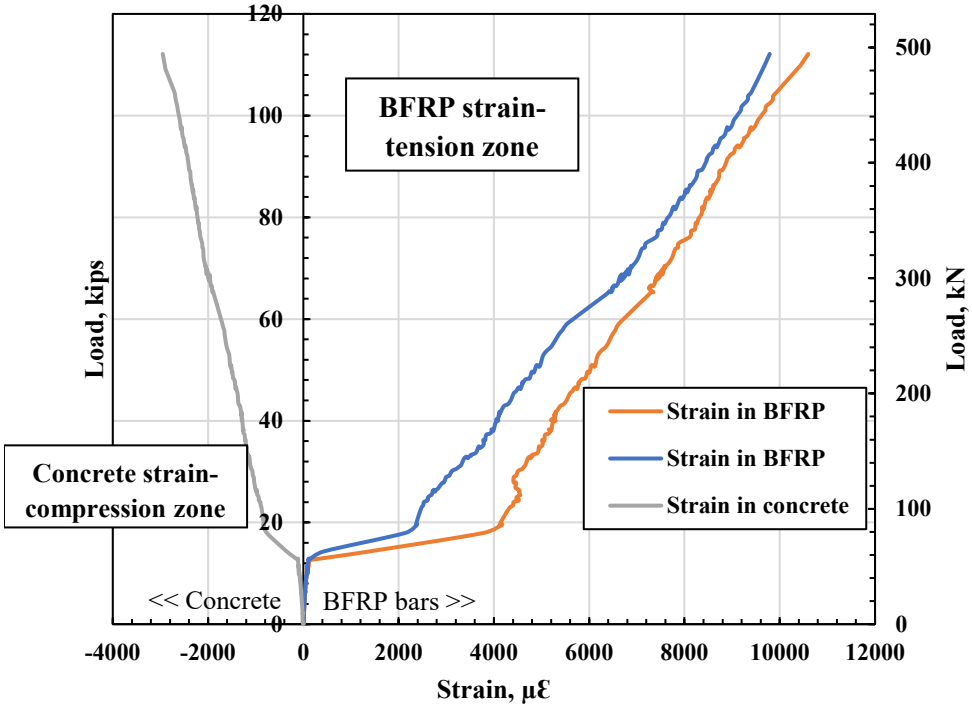

Figure 88: Load-strain curves in the concrete top surface and BFRP bars of bridge deck Prototype 4.

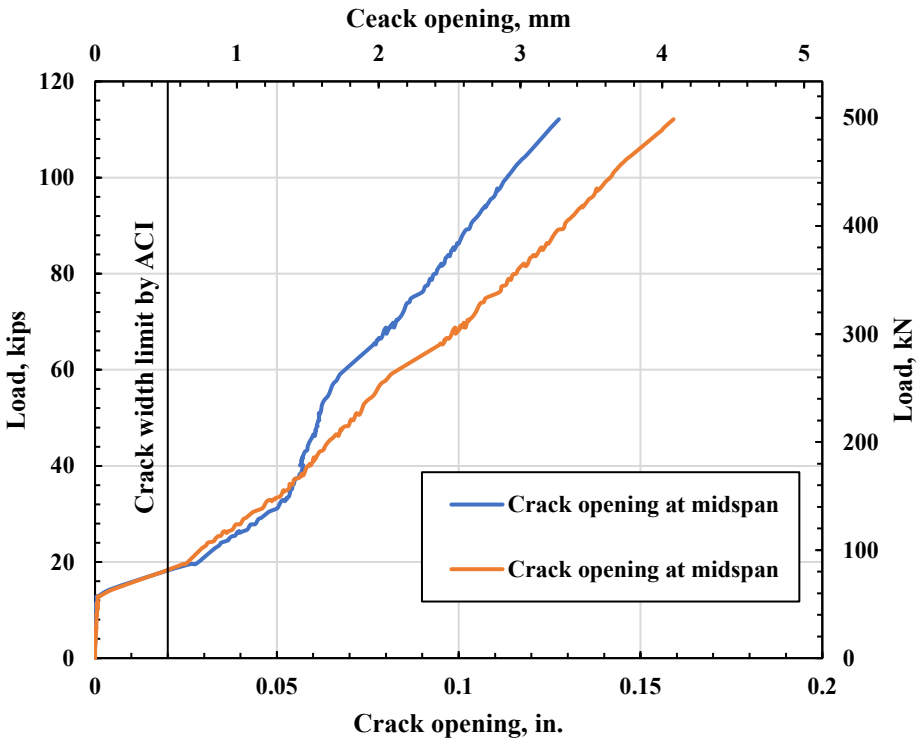

Figure 89: Load-crack width curves of bridge deck Prototype 4.

Figure 90: Mode of failure of bridge deck Prototype 4.

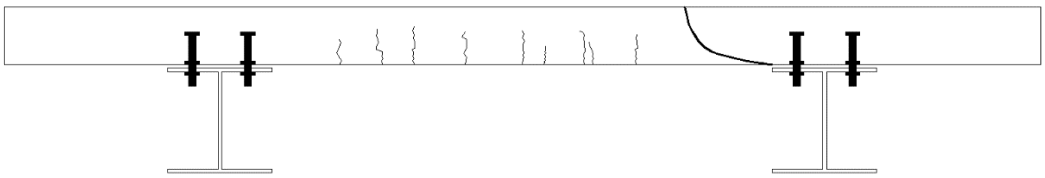

Figure 91: Crack mapping of bridge deck Prototype 4.

4.1.4.1 Nonlinear Finite Element Analysis results

Figure 92 shows the load-deflection curves of specimen SS2. It reveals that both the experimental and the numerical curves are bilinear. The NLFEA overestimated the cracking load. By visual inspection, there is a good agreement between the experimental results and the NLFEA. Figure 93 shows the load-strain curves of specimen SS2. The finite element analysis predicted the bridge deck slab's ultimate strength capacity of 114 kips compared to an experimental capacity of 112 kips with a 1.8% error. By visual inspection, there is a poor agreement between the experimental results and the NLFEA.

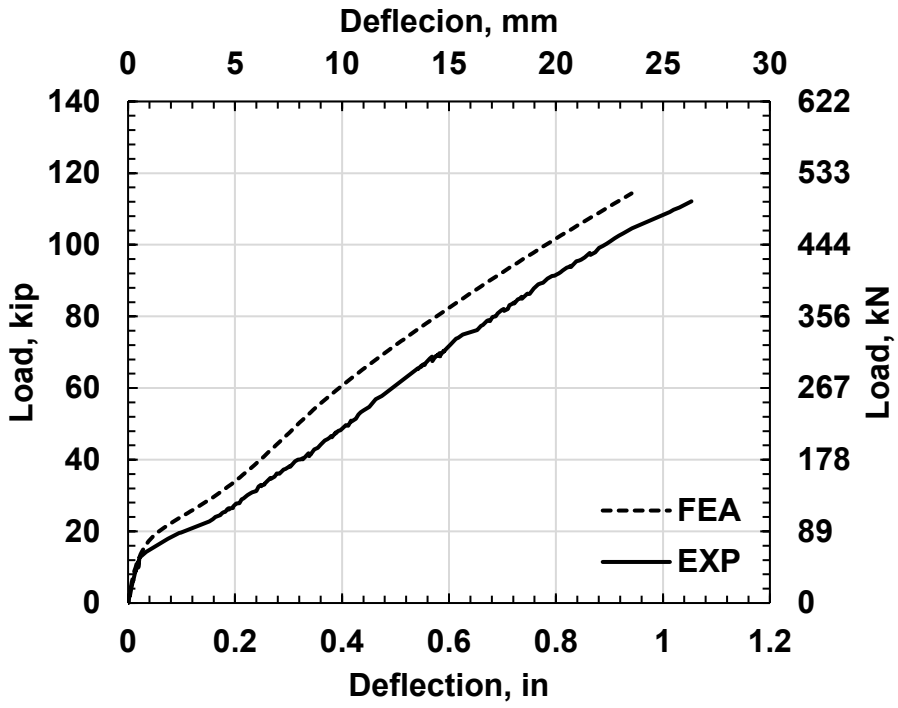

Figure 92: Load-deflection curves for single-span bridge deck slabs.

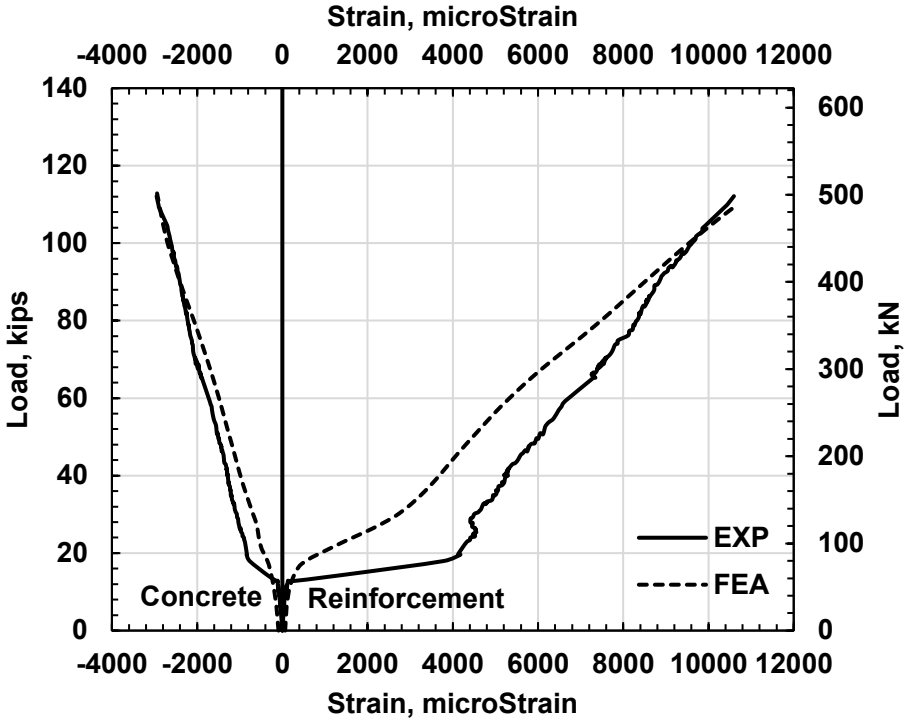

Figure 93: Load-strain curves for single-span bridge deck slabs.

4.2 Two-span continuous bridge deck slabs

4.2.1 Two-span continuous bridge slab Prototype 5

This test represents a bridge prototype of a two-span continuous bridge deck slab, 18 feet long, 10 feet wide, and 8 inches thick, reinforced with #5 BFRP bars spaced at 4 inches in the top and bottom transverse directions. BFRP #5 bars at 4 in. spacing are provided in the bottom longitudinal direction and at 6 in. in the top longitudinal direction. Figure 94 shows the W36x182 steel beams before and after removing the shear studs and cleaning the surface of the top flange for bolt placement (as recommended by three members of the technical review panel during their visit to the lab facility). Figure 95 shows the slab formwork, bolts, and the bottom layer of BFRP bars. The areas of interest in the continuous slab testing are the positive moment and the negative moment regions. A total of thirty-three embedded strain gauges were installed on the reinforcing bars to track the strain measurements in the BFRP bars. In addition, twelve more strain gauges were installed on the concrete surface to measure the strain readings in the concrete. Three LVDT devices were placed at each midspan to record the vertical deflection of the slab.

Furthermore, four LVDT devices were placed to measure the lateral displacement of the slab (two in the longitudinal direction and two in the transverse direction). Two-span continuous bridge deck slab Prototype 5 was cast on Sep 24, 2021, and the single-span bridge deck slab Prototype 2. The slabs were covered with wet burlap to maintain the curing conditions, and the burlap layer was covered with plastic sheets to keep them moist. The concrete cylinder and beam samples were taken during casting and were placed on the slabs to provide a similar curing condition. The slabs are checked daily for additional water if needed. The compressive strength of the concrete, based on the 6 x 12 in. cylinders testing, is 6950 psi.

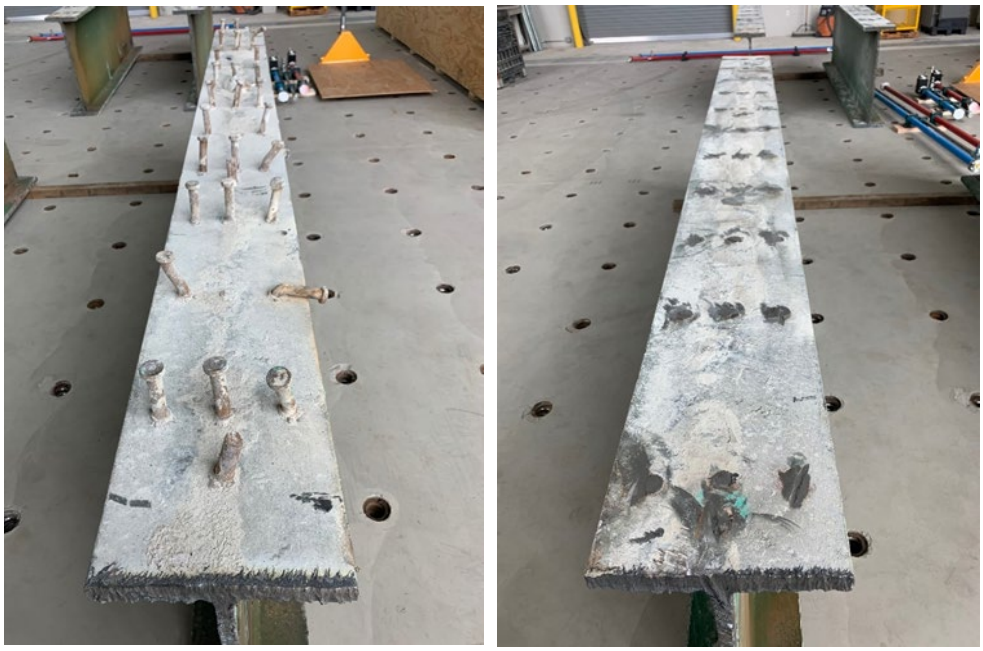

Figure 94: Steel beams before and after removal of shear studs.

Figure 95: Formwork of the slab with the bottom BFRP reinforcement of bridge deck Prototype 5.


OZINGA
OZINGA
1303
HYSTER


OZINGA
OZINGA


OZINGA
OZINGA
OZINGA

Figure 96: Continuous bridge deck Prototype 5 during and after concrete pouring.

The slab was tested until failure (two-wheel points at each midspan) represented the tandem loading in bridge decks. The distance between the two points of loading in the same midspan is 4 ft, representing the distance between the axle of a tandem. The tested specimens were designed to simulate the commonly used slab-on-girder bridges for two spans on three steel girders. The slabs were cast in place to represent the

actual behavior of the bridge deck. Figure 99 shows the Load-Deflection curve of the tested slab with reinforcement spacing of 4 in. on both directions for top and bottom mats. Figure 99 shows that the maximum applied load is 241 kips on each span (482 kips total applied load). The tested slab had the same mode of failure (flexural-shear failure), starting with crushing of the concrete in the compression zone at the bottom, followed by shear failure at an angle of approximately 45º as the two single-span decks. The bold lines in Figure 100 represent the mode of failure, and the cracks are shown with regular line size. The number at the crack lines in the figure represented the load when the crack was visible by the naked eye during testing. The investigation of the formation shows that the slab cracked at the midspans first, and the other cracks started to appear at different locations. Other cracks started to appear at the supports right after the cracks appeared in the midspan on both sides of the middle support generated at the negative moment region at the support. The mode of failure was a sudden failure without any fracture in the BFRP bars in the slab.

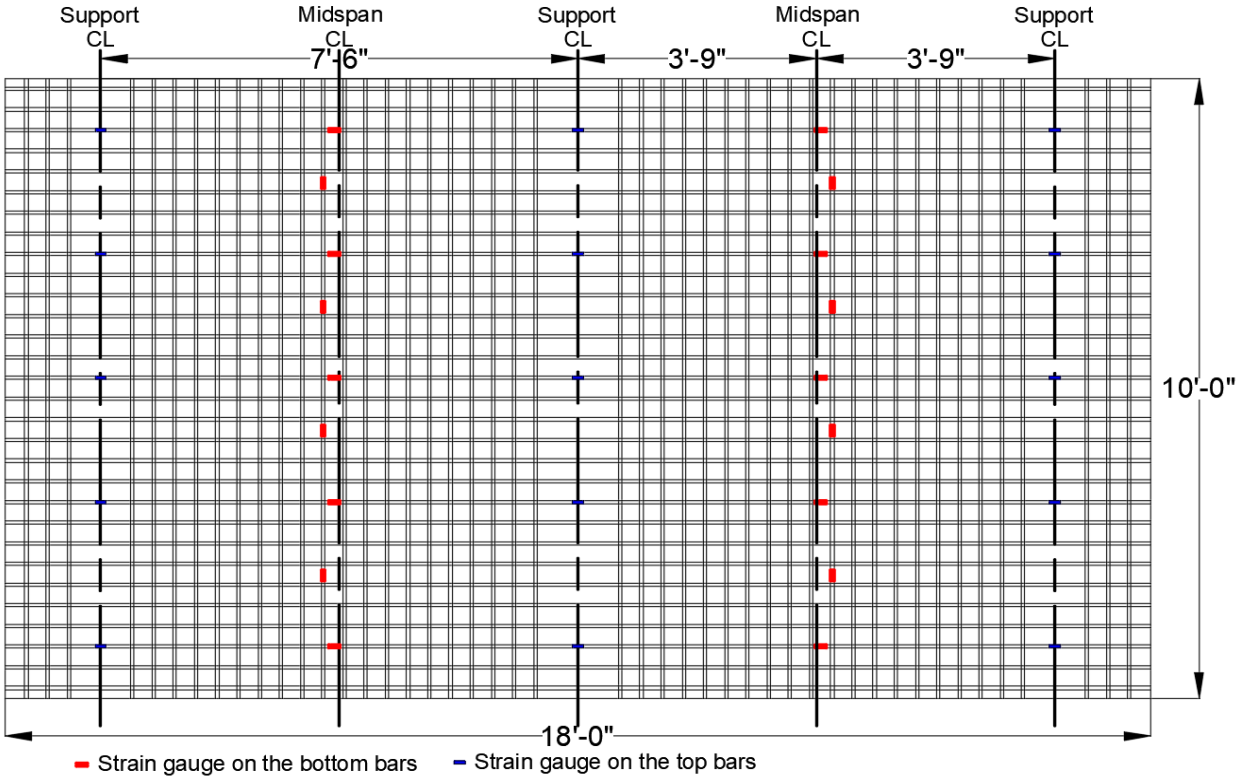

Figure 97: Strain gauges location on the top and bottom embedded BFRP bars.

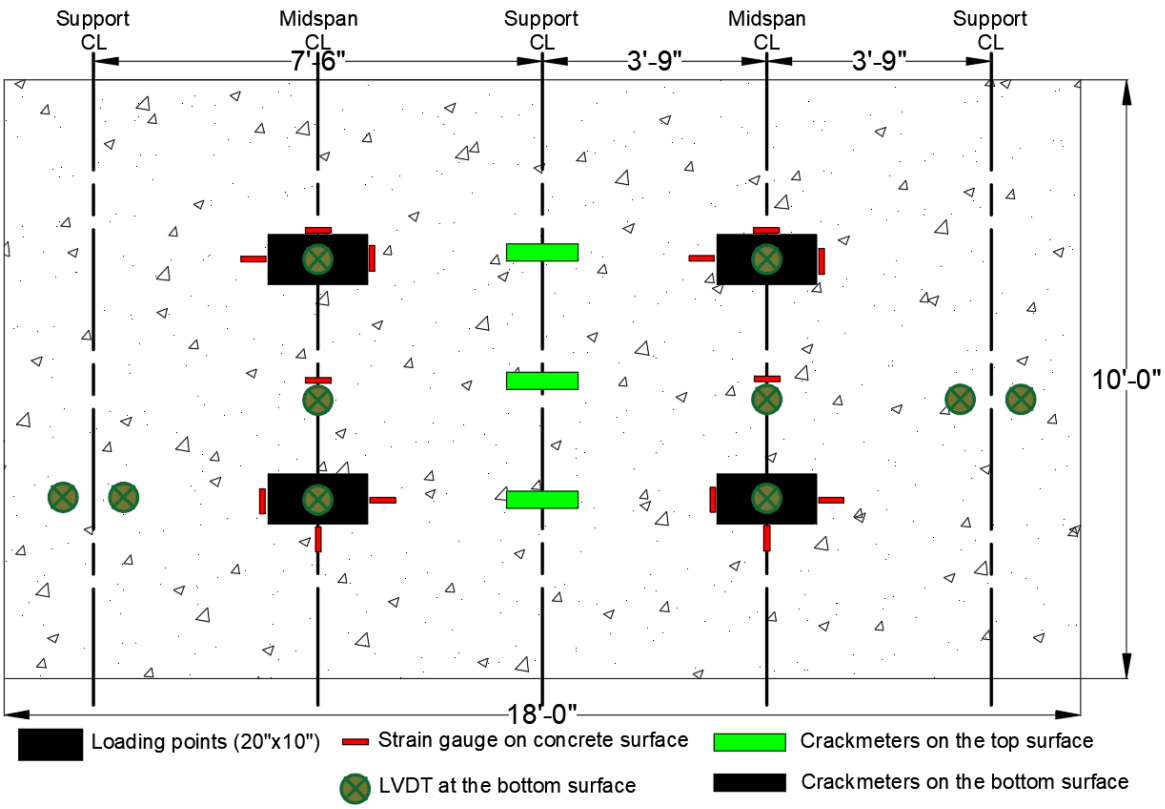

Figure 98: Instrumentation plan on the two-span Prototype 5.

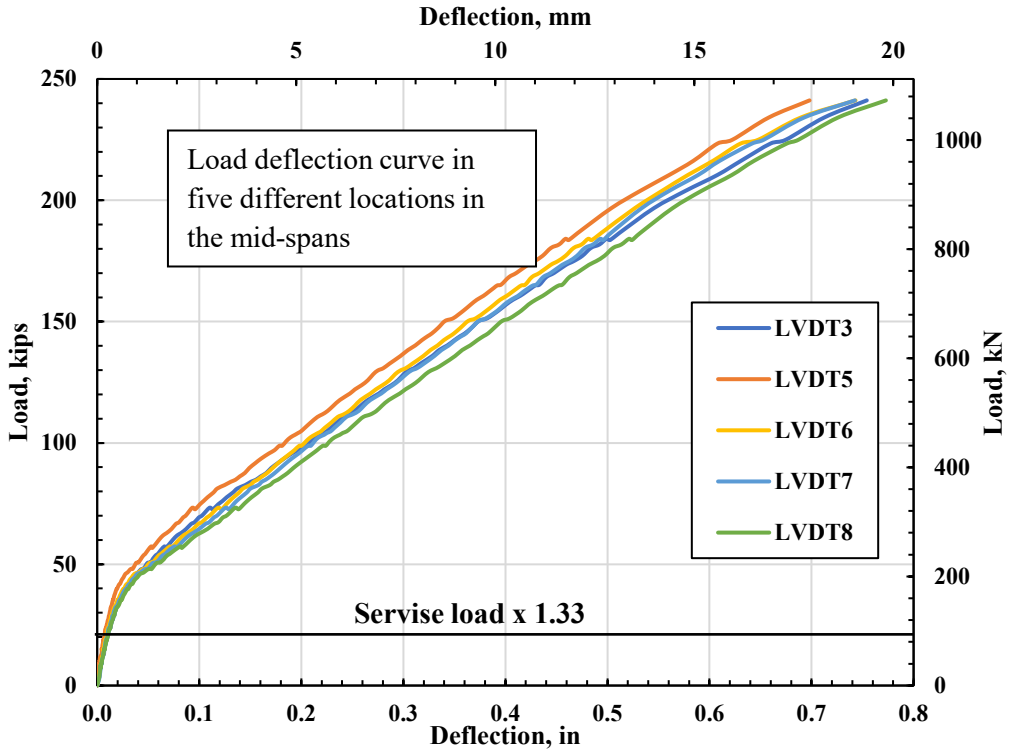

Figure 99: Load-deflection curves of the two-span Prototype 5.

The slab was designed as an over-reinforced section to prevent any failure in the BFRP bars, unlike steel-reinforced concrete. The maximum strain in the BFRP bars recorded was 6720 με at the midspan, which is estimated to be 28% of the ultimate strain of the bar. It is to be noted that the slab was able to sustain a load of 60 kips after failure in the concrete without any fracture or failure in the BFRP bars. The load-strain curves in the BFRP and concrete at the midspan are shown in Figure 100. The curves to the right represent strain readings in the BFRP (tension), while those on the left represent strain readings on the concrete surface at midspan (compression). The load strain curve undergoes a linear relationship before cracking, followed by a jump in the strain caused by the cracking of the concrete section, and continues approximately straight until failure. The cracks at the midspans were formed before the cracks at the negative moment regions (at supports), as shown in Figures 101 and 102, due to the shear studs that provide a partial fixation over the support. Even though the clear cover at the top mat is 2.25”, the maximum strain in the BFRP at the midspan is lower than the maximum strain at the support.

Crack width and serviceability are the BFRP design's primary concerns, and it always controls the design. The strength limit state is also the concern of the structural engineers, but with FRP materials, it is way higher than the designed load. Figures 103 and 104 show the crack width versus the applied load of the tested slab. CM2 is the crack meter placed in the midspan, and two major cracks passed through, which means this crack meter's reading is for two cracks. The ACI crack limit is also shown in Figure 102 (0.02 in).

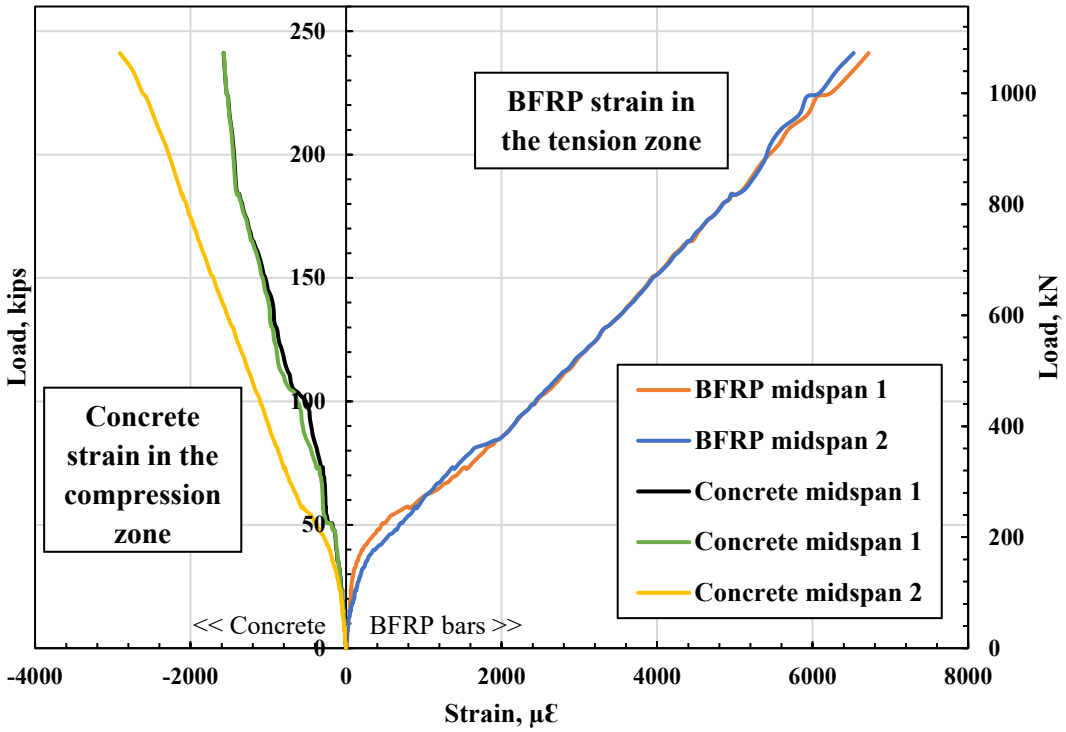

Figure 100: Load-strain curves at the concrete top surface and BFRP bars of bridge deck Prototype 5.

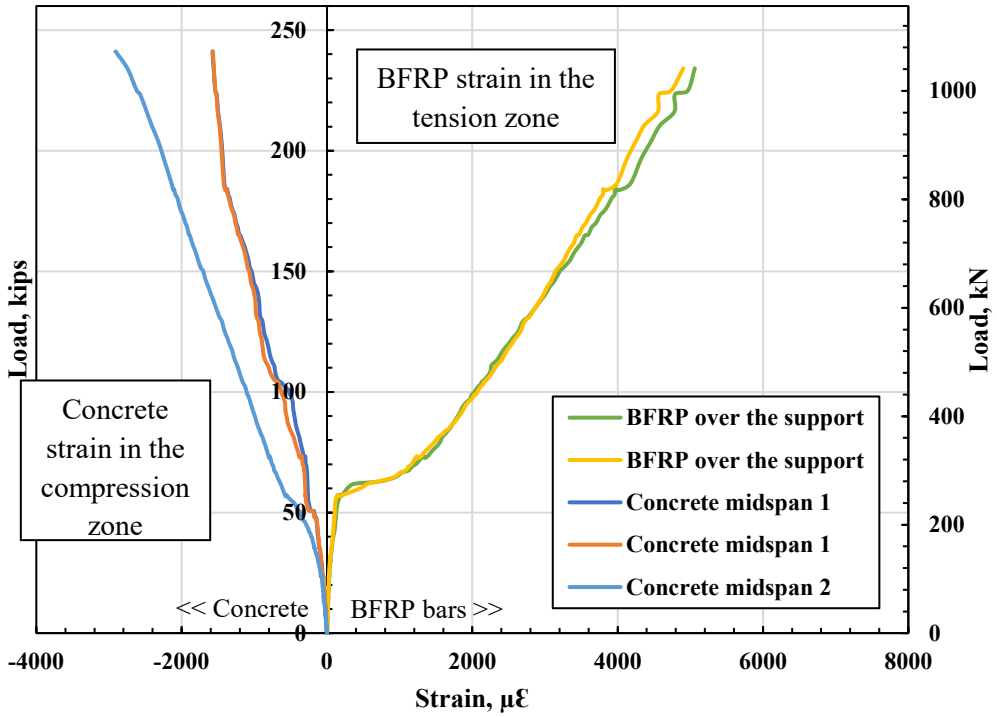

Figure 101: Load-strain curves in the BFRP at the support and concrete surface at the midspan.

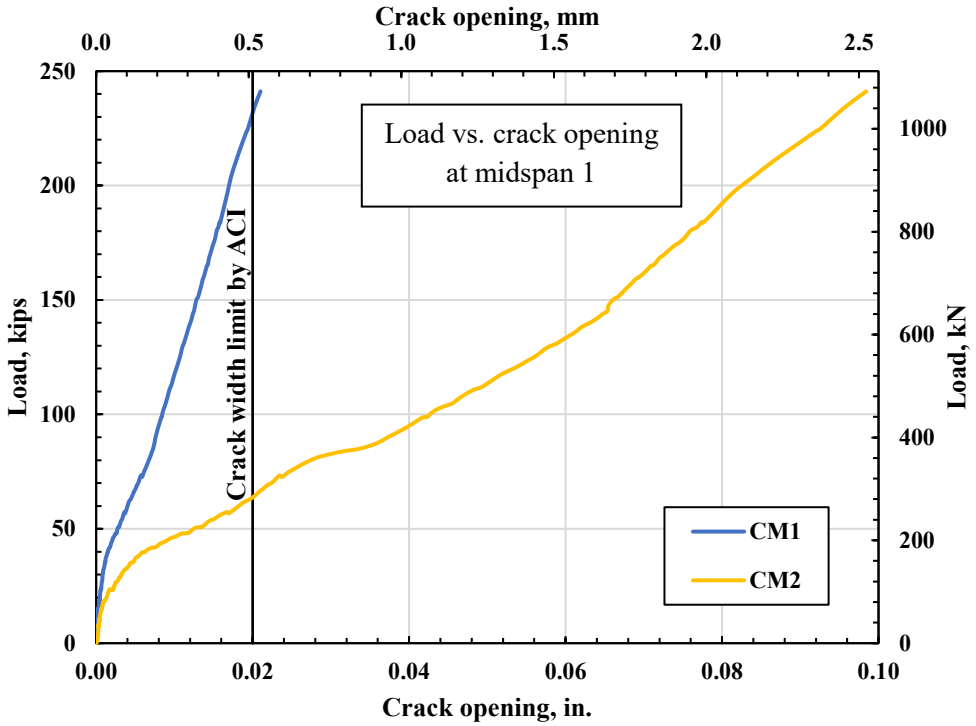

Figure 102: Load-crack width curves of two-span at the positive moment region of Prototype 5.

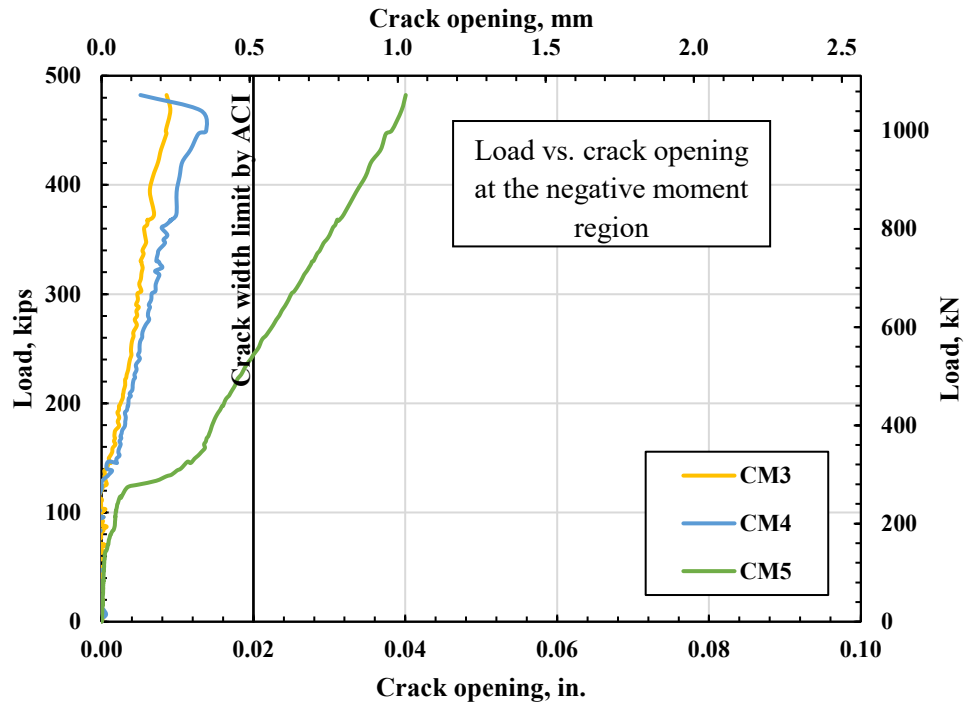

Figure 103: Load vs. crack width of two-span at the negative moment region of Prototype 5.

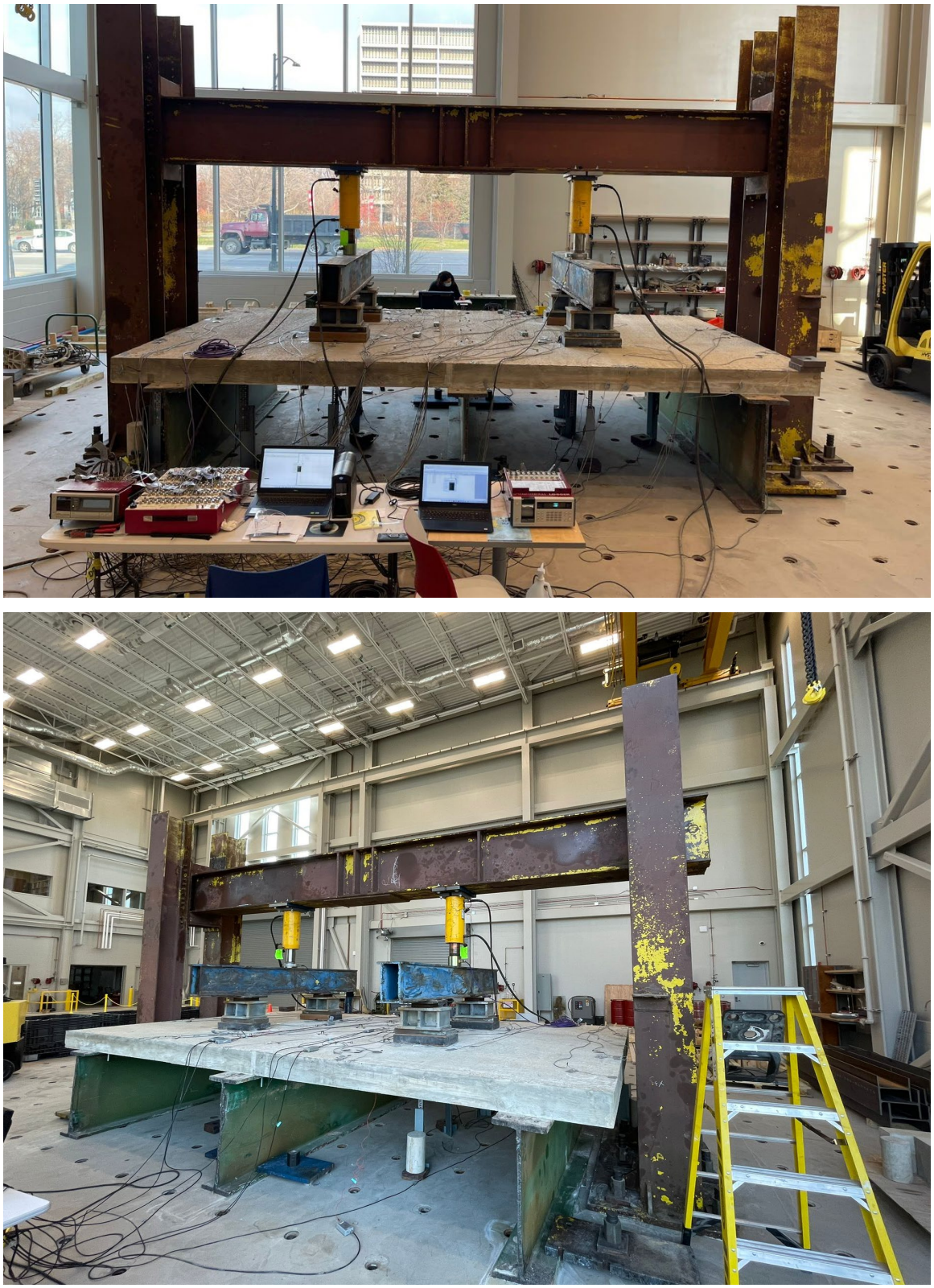

Figure 104: Testing setup of two-span continuous bridge deck slab Prototype 5.

Figure 105: Instrumentation at the bottom concrete surface of the two-span Prototype 5.

Figure 106: Failure mode of the two-span Prototype 5.

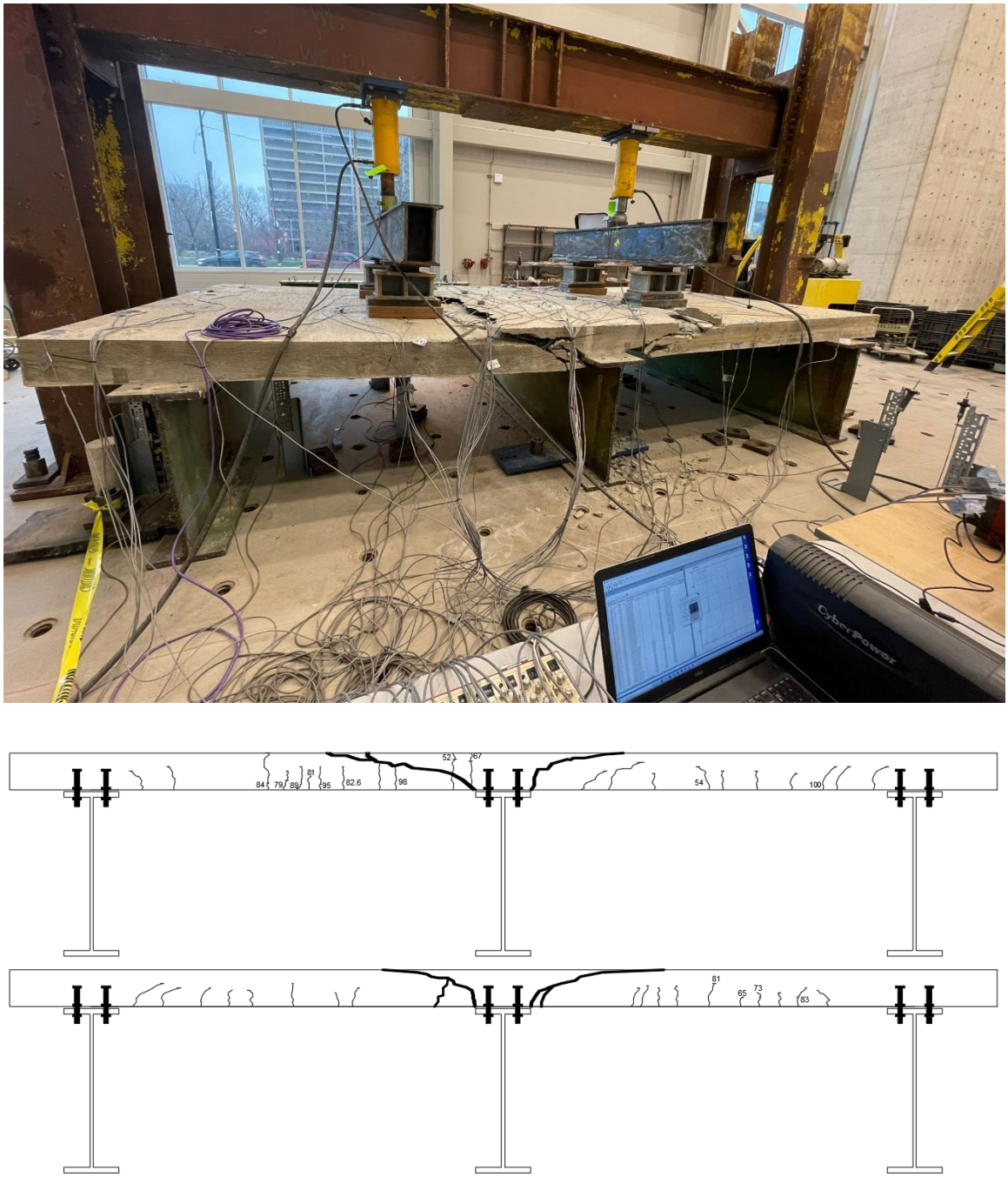

Figure 107: Crack and failure mapping of the two-span Prototype 5.

4.2.1.1 Nonlinear Finite Element Analysis results

Figure 108 and 109 show plots of load-deflection and load-strain curves for concrete and reinforcement for experimental work and NLFEA at locations used in the experimental work. By visual inspection, there is an excellent agreement between the experimental results and the NLFEA. The finite element analysis predicted the bridge deck slab's ultimate strength capacity of 267 kips compared to an experimental capacity of 241 kips with a 6.1% error.

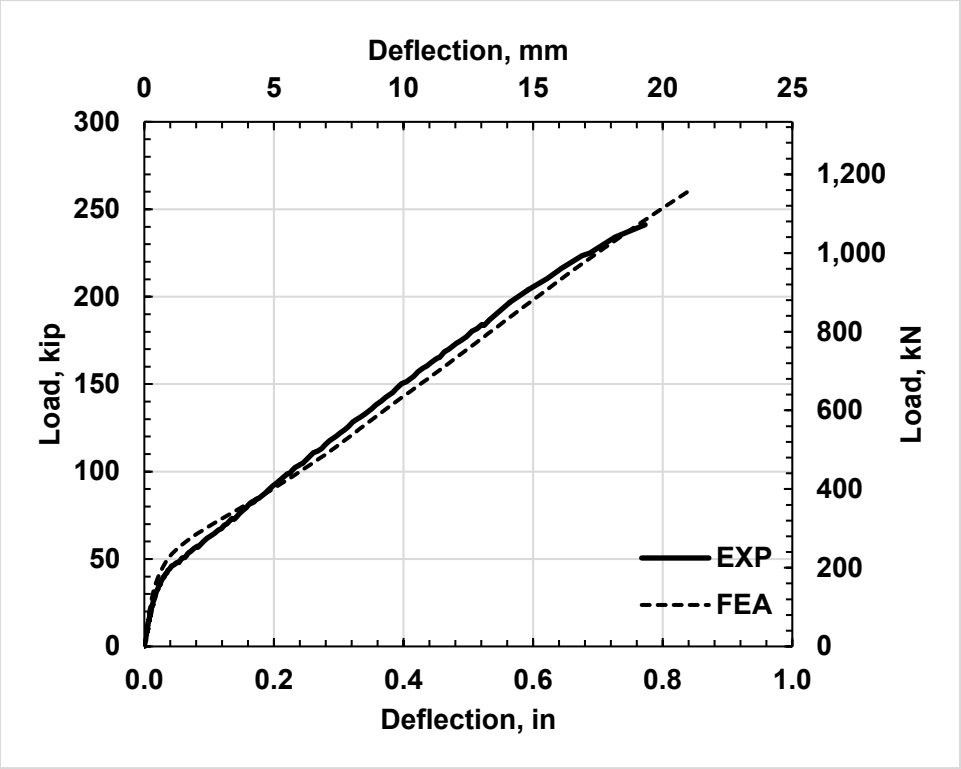

Figure 108: Load-deflection curves for single-span bridge deck slabs.

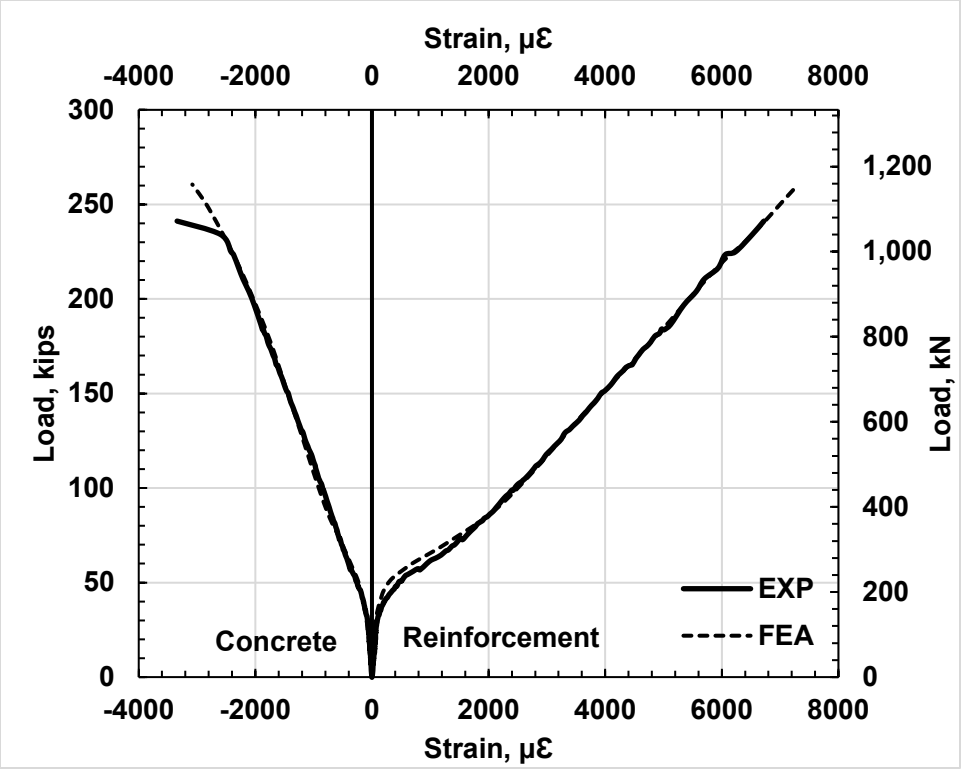

Figure 109: Load-strain curves for single-span bridge deck slabs.

4.2.2 Two-span continuous bridge slab Prototype 6

Based on the tested bridge deck slabs results, BFRP No.5 bars at 6 in. were used in the transverse direction for the top and bottom reinforcement mat. Also, No. 5 bars at 8 and 6 inches was used in the top and bottom longitudinal direction, respectively. Using No. 5 bar at 6 in is to study the effect of increasing the spacing up to 6 inches on the slab behavior and the ultimate strength of the slab. This test represents a bridge prototype of a two-span continuous bridge deck slab, 18 feet long, 10 feet wide, and 8 inches thick, reinforced with #5 BFRP bars. The areas of interest in the continuous slab testing are the positive moment and the negative moment regions. A total of thirty-three embedded strain gauges were installed on the reinforcing bars to track the strain measurements in the BFRP bars. In addition, twelve more strain gauges were installed on the concrete surface to measure the strain readings in the concrete. Three LVDT devices were placed at each midspan to record the vertical deflection of the slab.

The formwork for this slab Prototype is shown in Figures 110 and 111. The slab construction preparation is shown in Figure 111. Figure 112 shows the casted specimen. Illinois Tollway concrete mix proportion for bridge decks was also used for the slabs with the same properties. Moreover, the BFRP reinforcing bars are from the same source as the bars used in the previous tested slabs. The slabs were covered with wet burlap to maintain the curing conditions, and the burlap layer was covered with plastic sheets to keep them moist. The concrete cylinder and beam samples were taken during casting and were placed on the slabs to provide a similar curing condition. The slabs are checked daily for additional water if needed. The compressive strength of the concrete, based on the 6 x 12 in. cylinders testing, is 6500 psi.

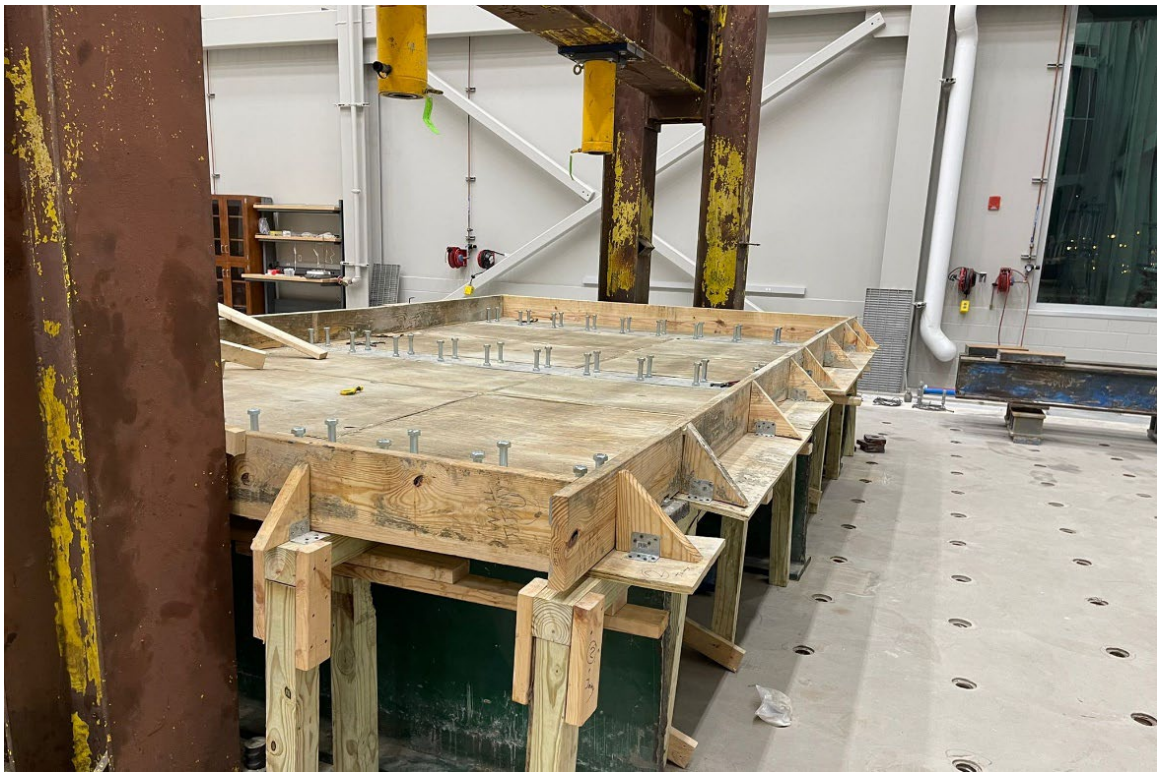

Figure 110: Formwork of two-span Prototype 6.

Figure 111: BFRP reinforcing bars in two-span Prototype 6.

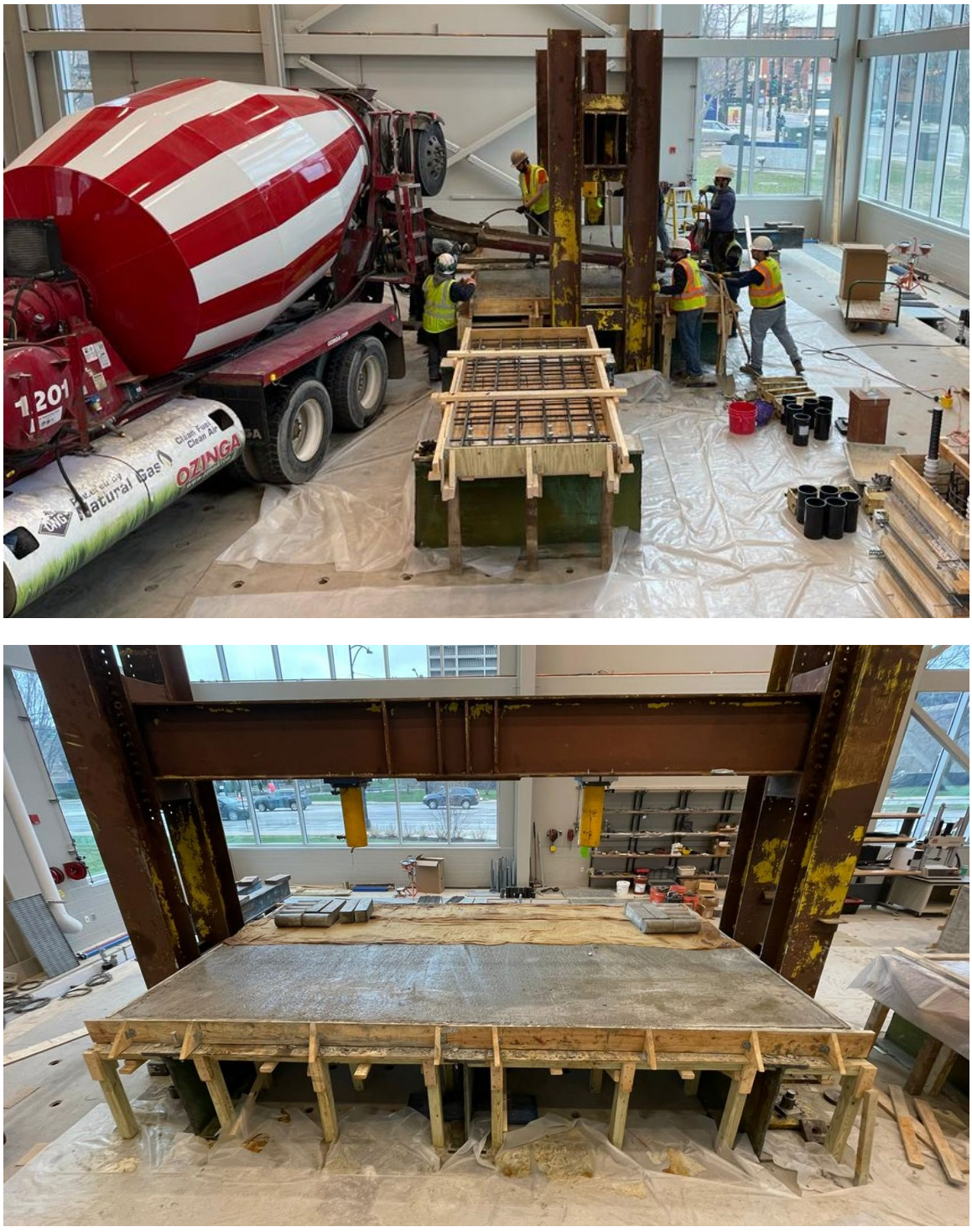

Figure 112: Cast of Concrete for the two-span bridge deck Prototype 6.

Table 20: Concrete mix design for bridge deck Prototype 6.

Material	Designation	Design Qty	Required	Batched
Coarse aggregate	22CM161HR	520 lb.	2346 lb.	2400 lb.
Coarse aggregate	22CM11BLJ	1360 lb.	6135 lb.	6090 lb.
Fine aggregate	27FM01OH	1250 lb.	5797 lb.	5740 lb.
Slag	SLG-SKY	190 lb.	855 lb.	860 lb.
Cement	CEM-HCMSG	330 lb.	1485 lb.	1495 lb.
Water	WATER1	27.5 gal.	100 gal.	100 lb.
Air entrainment admixture	AE-DX2	3.0 oz.	13.5 oz.	13.5 oz.
Medium range water reducer	WRR-REC	2.0 /C	46.8 oz.	46 oz.
High range water reducer	HR-A575	2.0 /C	46.8 oz.	45 oz.

The slab was tested until failure (two-wheel points at each midspan) represented the tandem loading in bridge decks. The distance between the two points of loading in the same midspan is 4 ft, representing the distance between the axle of a tandem. The tested specimens were designed to simulate the commonly used slab-on-girder bridges for two spans on three steel girders. The slabs were cast in place to represent the actual behavior of the bridge deck. Figure 115 shows the Load-Deflection curve of the tested slab with reinforcement spacing of 6 in. on both directions for top and bottom mats except for the top longitudinal reinforcement (8 in. spacing). Figure 115 shows that the maximum applied load is 181 kips on each span (362 kips total applied load). The tested slab had the same mode of failure (compression shear failure), starting with crushing of the concrete in the compression zone at the bottom, followed by shear failure at an angle of approximately 45º as the two single-span decks. The bold lines in Figure 117 represent the mode of failure, and the cracks are shown with regular line size. The number at the crack lines in the figure represented the load when the crack was visible by the naked eye during testing. The investigation of the formation shows that the slab cracked at the midspans first, and the other cracks started to appear at different locations. Other cracks started to appear at the supports right after the cracks appeared in the midspan on both sides of the middle support generated at the negative moment region at the support. The mode of failure was a sudden failure without any fracture in the BFRP bars in the slab.

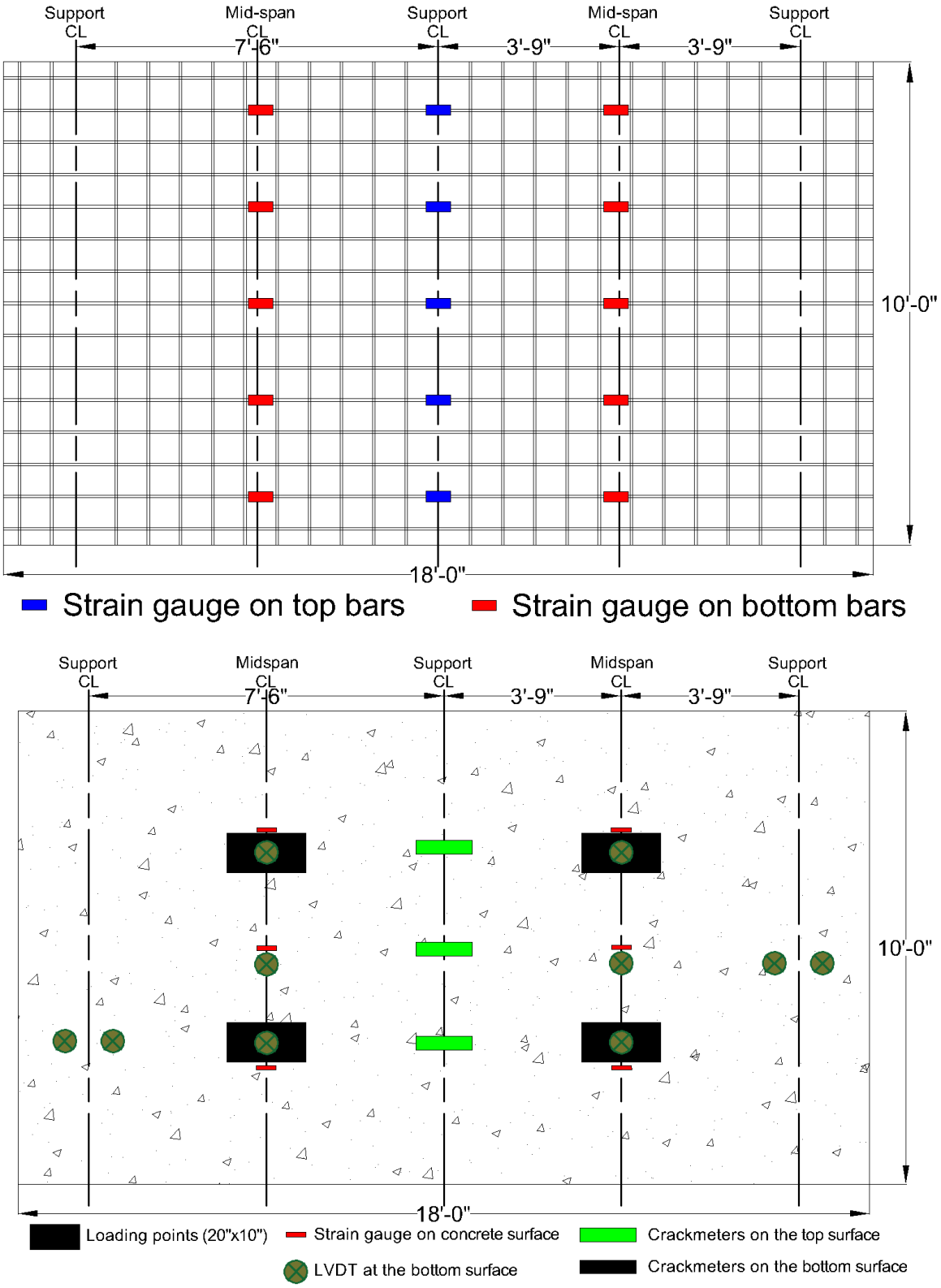

Figure 113: Instrumentation plan for bridge deck Prototype 6.

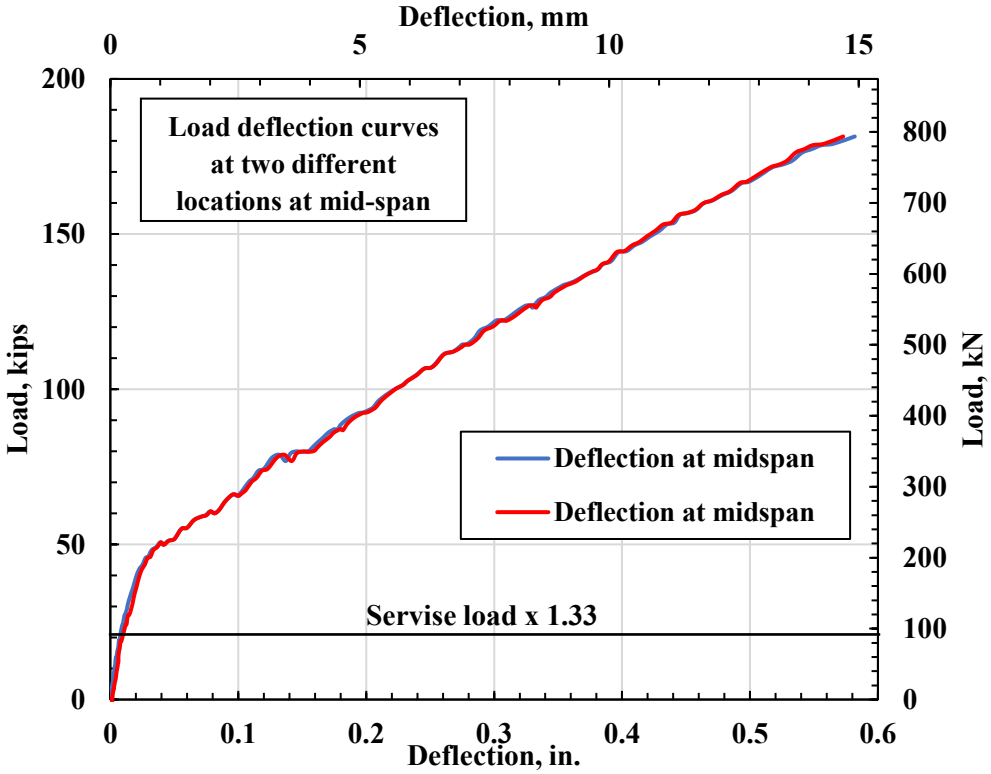

Figure 114: Load-deflection curves of bridge deck Prototype 6.

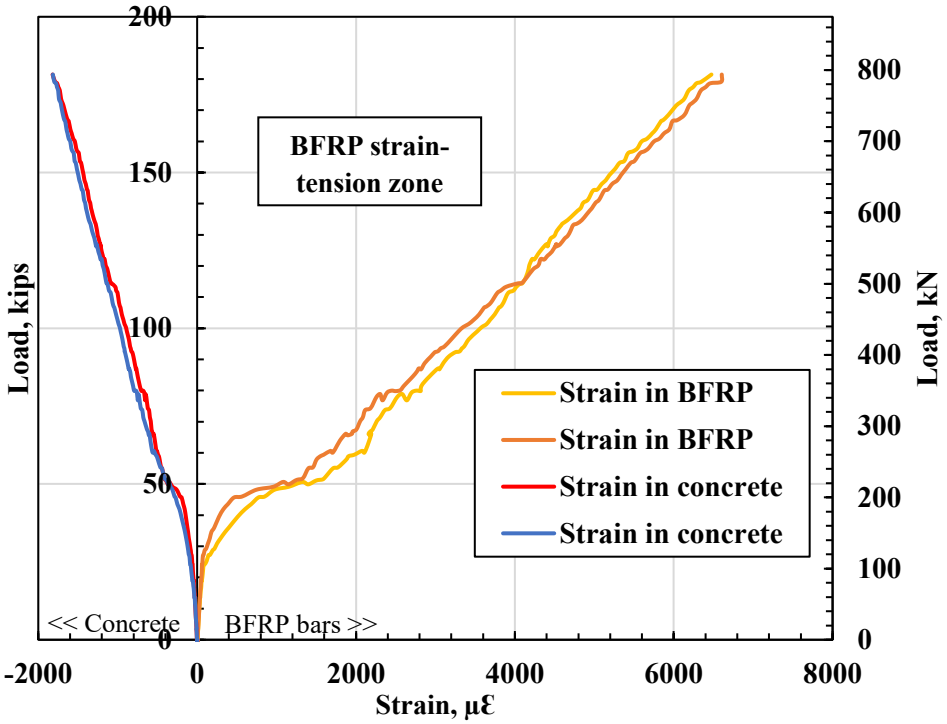

Figure 115: Load-strain curves in the concrete top surface and BFRP bars of bridge deck Prototype 6.

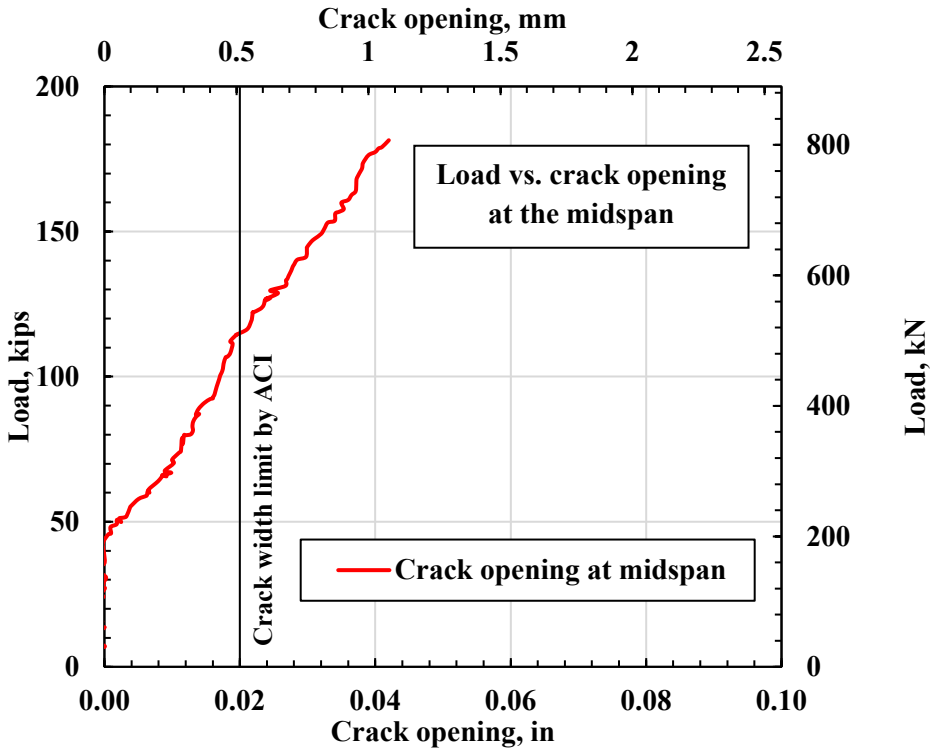

Figure 116: Load-crack opening curve of bridge deck Prototype 6.

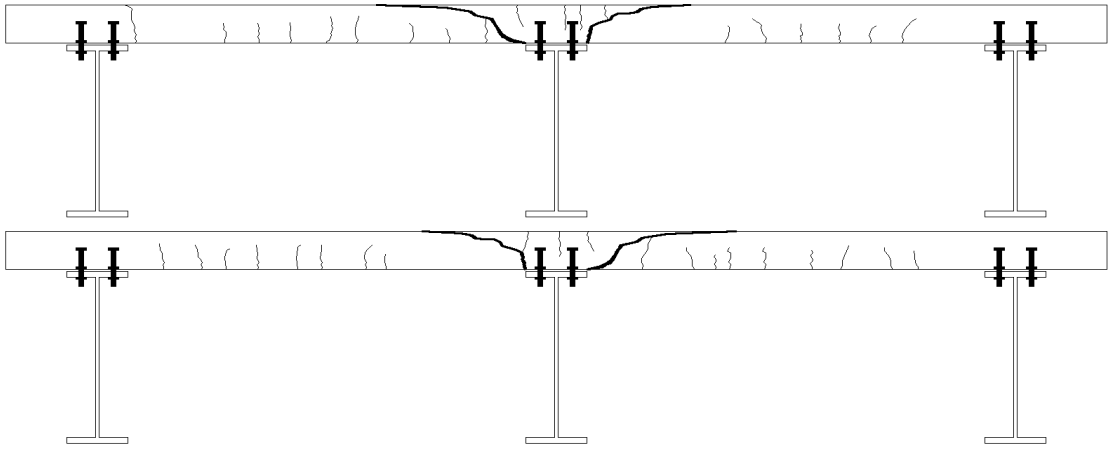

Figure 117: Crack mapping of bridge deck Prototype 6.

4.2.2.1 Nonlinear Finite Element Analysis results

Figure 118 and 119 show plots of load-deflection and load-strain curves for concrete and reinforcement for experimental work and NLFEA at locations used in the experimental work. By visual inspection, there is an excellent agreement between the experimental results and the NLFEA. The finite element analysis predicted the bridge deck slab's ultimate strength capacity of 183 kips compared to an experimental capacity of 182 kips with a 0.6% error.

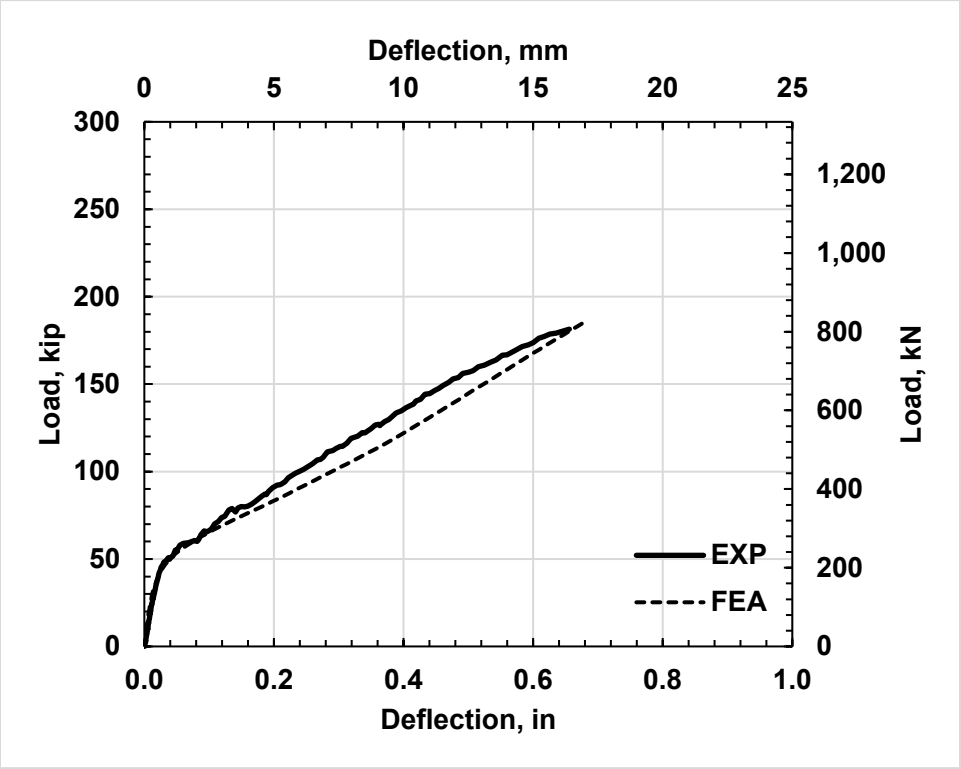

Figure 118: Load-deflection curves for single-span bridge deck slabs.

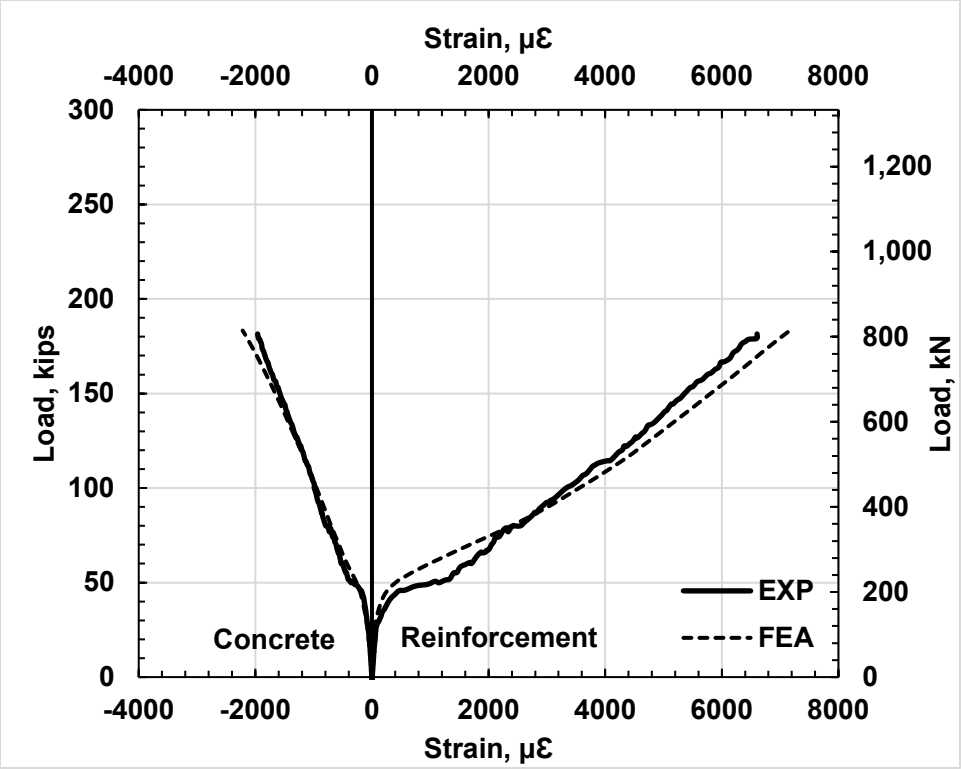

Figure 119: Load-strain curves for single-span bridge deck slabs.

4.3 Comparison between all tested bridge deck slabs

One of the most popular structural systems utilized in the United States highway bridges is the slab-on-girder superstructure. AASHTO LRFD specifications specify two methods for designing bridge decks: (1) the flexural design method and (approximate Method) (2) the empirical method. In the approximate method, a strip of the bridge deck is designed as a flexural member; top and bottom reinforcement at the positive and negative moments are required for design.

However, end-restrained deck slabs with a span ratio of less than 12 have been shown to react differently and fail in compression failure. An internal membrane force is developed under loading by the effect of the lateral restrained force caused by the fixation of the steel girder (Signe span bridge deck Prototypes 1 and 2) or by the continuity of the slab (Two-span bridge deck prototype). The restrained end causes a lateral restrain force that increases the capacity of the bridge deck compared to a non-restrained bridge deck slab (Hon et al., 2005).

In concrete design reinforced with steel bars, the reinforcement ratio has to be less than the balanced condition to prevent any failure in the concrete on compression and to maintain ductility for the structural element. Unlike steel, FRP material design requires the reinforcement ratio to be greater than the balanced condition to prevent any failure in the FRP rebars. The balanced reinforcement ratio is defined in ACI 440.1R-15 as follows Equation (16):

$$\rho_{fb} = 0.85\beta_1 \frac{f_c'}{f_{fu}} \frac{E_f \varepsilon_{cu}}{E_f \varepsilon_{cu} + f_{fu}} \qquad \text{Equation (16)}$$

Where β_1 is a factor taken as 0.85 for concrete strength less than or equal to 4000 psi, and it reduces continuously at a rate of 0.05 per each 1000 psi, but not taken less than 0.65. f_c' is the concrete compressive strength in psi; f_{fu} the design tensile stress of BFRP bar in psi; E_f is the design modulus of elasticity of the BFRP bars in psi; ε_{cu} is the design strain of concrete (0.003 in/in). The reinforcement ratio in the slab is the ratio of the reinforcement area over the effective depth between the top of the slab to the centroid of the bottom reinforcement multiplied by the one-foot width. According to ACI

440.1R-15, the balanced condition of the slab reinforced with FRP bars is way smaller than the balanced condition in regular concrete design due to the higher tensile strength of the reinforcement.

The slab thickness is assumed to be 8 inches thick as the most common bridge decks in North America, with a span to depth ratio of less than 12. The bridge deck is designed for flexural behavior and to resist dead and live load with the effect of impact. The slab will be designed with the strip width recommended by the AASHTO LRFD Table 4.6.2.1.3-1.

Testing results include crack width, deflection, strain in BFRP bars and concrete surface, ultimate load, and failure mode. Tables 21 and 22 summarize the testing results at cracking and at ultimate failure load for all tested slabs. All the graphs were shown per width of foot for the purpose of comparison.

Table 21: Testing results of the tested bridge deck slabs.

Slab Prototype	Cracking load, kip	Cracking load per foot, kip	Ultimate load, kip	Ultimate load per foot, kip
SS1 #5@4	13.50	**3.38**	130	**32.5**
SS2 #5@6	11.84	**2.96**	109	**27.4**
SS3 #6@6	14.18	**3.54**	129	**32.4**
SS4 #5@8	12.88	**3.22**	112	**28.0**
TS5 #5@4	33.05	**3.31**	241	**24.1**
TS6 #5@6	41.93	**4.19**	181	**18.1**

Table 22: Testing results of the tested bridge deck slabs.

Slab Prototype	Deflection at cracking load, in.	Maximum deflection at ultimate load, in	Strain in BFRP at cracking load, με	Maximum strain in BFRP at ultimate load, με	Strain in concrete at cracking load, με	Maximum strain in concrete at ultimate load, με	Maximum crack width at ultimate load, in.
SS1 #5@4	0.02677	0.78222	163	6549	87	1921	0.03963
SS2 #5@6	0.02948	0.92377	269	7835	109	2339	0.06742
SS3 #6@6	0.03740	0.81752	377	6187	168	2224	0.02801
SS4 #5@8	0.02146	1.0533	133	10597	112	2951	0.12756
TS5 #5@4	0.02106	0.77284	237	6720	92	1572	0.04001
TS6 #5@6	0.02283	0.65590	330	6604	143	1961	0.04334

4.3.1 Load-deflection behavior

The load versus deflection curves of the bridge deck slabs at the midspan per width of foot of all the tested slabs (Single-span and two-span) are shown in Figure 120. The recorded load and deflection don't account for the self-weight of the slabs. The bilinear curve starts with the linear uncracked elastic behavior (pre-cracking) using the full gross inertia of the section, followed by a second linear with lower stiffness representing the reduced inertia of the cracked section. All the tested slabs exhibit the same behavior before cracking since the elastic behavior is controlled by the concrete section only, with a negligible effect of the reinforcement.

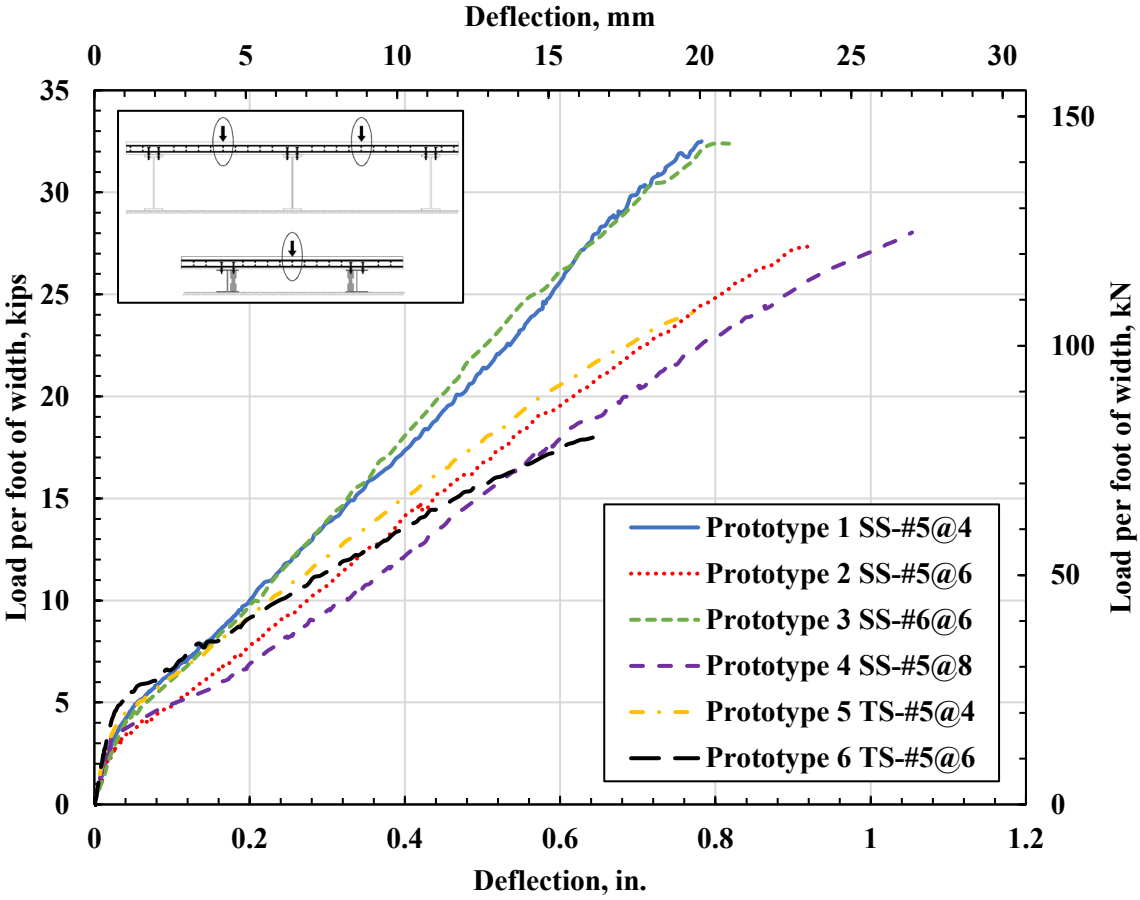

Figure 120: Load-deflection curves of the three tested slabs.

The investigation of Figure 120 reveals that all the tested slabs had a similar behavior after cracking with a difference in the elasticity of the section due to the

variation of reinforcement ratio and continuity between the slabs. This indicates that the reinforcement ratio has a significant effect on the ultimate flexural-shear strength of the bridge deck slabs. Prototypes 1 and 3 had similar behavior, ultimate load, and maximum deflection due to the negligible difference in the reinforcement ratio.

At the same load level (15 kips per foot of width), Prototypes 1, 2, and 4 (with a reinforcement ratio of 1.159, 0.773, and 0.579 respectively) had 0.335, 0.435, and 0.495 inches, respectively. This reveals the effect of the reinforcement ratio on the deflection behavior of the bridge deck slabs. The maximum deflections recorded for these slabs were 0.782, 0.924, and 1.05 inches, respectively. The decrease in the reinforcement ratio by 33% between Prototype 1 and 2, and by 25% between Prototype 2 and 4, results an increase in the maximum deflection by 18% and 13.6%, respectively.

4.3.2 Crack-width pattern

Mainly, the cracks formed was flexural cracks in the tension zones of all tested slabs with similar distribution. The crack formation started at the bottom face (directly under the loading area) of the midspan and shifted to the negative moment region in the two-span slabs. This crack is oriented in the longitudinal direction and parallel to the supporting beams. Fewer cracks were formed in the negative moment at the edge supports where the loading was close to failure load. The cracking load of the tested slabs ranged between 2.96 to 4.19 kips (per foot of width) and are shown in Table 21. The less reinforcement ratio, the more crack width was observed. No pre-existing cracks was recorded in the slabs in any direction due to the fact that the slabs were casted in place. Unlike conventional steel rebars, the cracks were uniformly distributed due to the fact that the BFRP bars were sand coated, which distribute the stress over longer length of the bar than steel, and the elastic behavior of the BFRP bars.

The load versus crack-width curves are shown in Figure 121. The curves start with an increase in the load without any crack recording. At the cracking load, the curve shifts, indicating the crack initiation at the midspan of the slabs. ACI440.1R limit the allowable crack width in FRP structures to be less than 0.02 inches, and it is shown in the load vs. crack-width figure. The maximum crack width recorded at failure was 0.127

inches in Prototype 4 where the lowest reinforcement ratio is used. At the same load level (15 kips per foot width), the crack width increased from 0.0183 to 0.071 when the reinforcement ratio is decreased by 50%, which reveals the high effect of reinforcement ratio on the crack-width behavior. Prototypes 1 and 3 with approximately the same reinforcement ratio had relatively similar crack width behavior. The two-span bridge deck slabs also exhibit the same crack-width behavior with approximately the same maximum crack width at failure (0.4 and 0.43 for Prototype 5 and 6, respectively) with different ultimate load and curve after cracking.

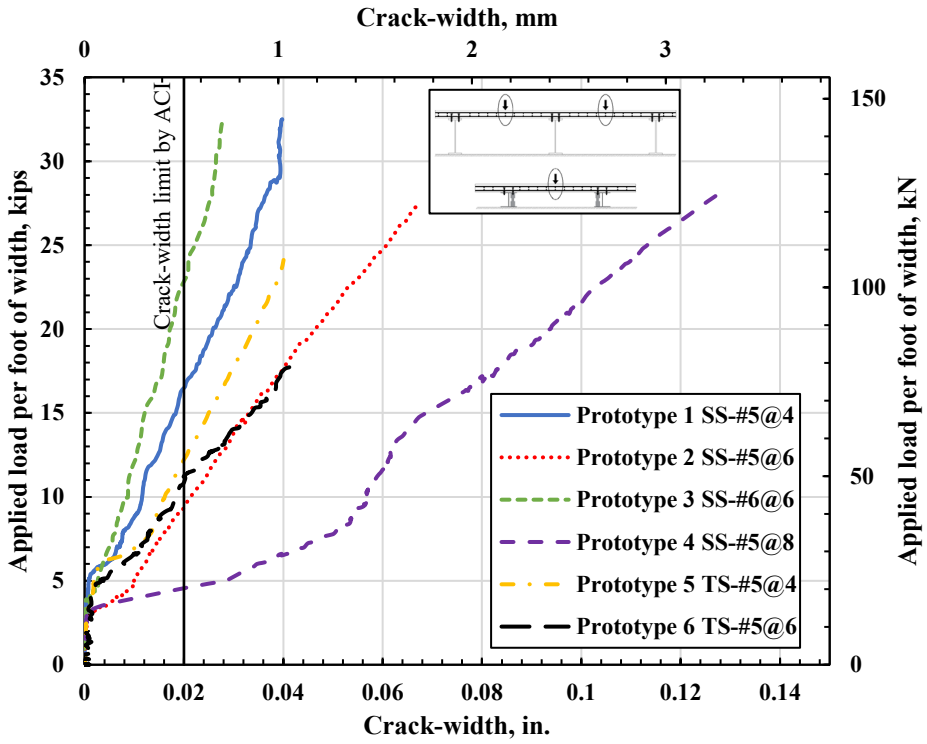

Figure 121: Load-crack opening curves at the midspan of the three tested bridge deck slabs.

4.3.3 Strain in BFRP and concrete

Figure 122 shows the load versus the strain in the transverse bottom mat of BFRP bars and concrete at midspan for the tested bridge deck prototypes. The strain in the BFRP bars and in the concrete varies linearly up to failure in the post-cracking stage. Tables 21 and 22 show the results of the concrete and BFRP bars strain at cracking load and at failure. The maximum strain in the BFRP bars recorded is 10597 με in bridge deck Prototype 3 where the lowest reinforcement ratio was used. This reveals

the effect of reinforcement ratio on the BFRP bar strain behavior that increases with the increase of the reinforcement ratio. At the same load level (15 kips per foot width), Prototypes 1, 2, 3, and 4 had a strain of 3025, 4610, 3450, and 6800 με, respectively. The strain in the BFRP bars increased by 52% and 47% when the reinforcement ratio decreased by 33% and 25%, respectively, between Prototypes 1 and 2, and Prototypes 2 and 4. Prototypes 1 and 3 had approximately similar behavior with a slight difference in the strain in the BFRP bars. Moreover, Prototypes 5 and 6 had a strain of 3930 and 5350 με, which is a 33% increase when the reinforcement ratio is decreased by 33%. The maximum strains obtained at failure range between 6187 and 10597 με, which represent 26 and 45% of the ultimate strain of the bar. It is worth noting that the single-span bridge deck slabs of four feet wide, were able to sustain 40 kips, and the two-span slab of ten feet wide to sustain 80 kips after failure, which is due to the flexibility of the BFRP bars in concrete.

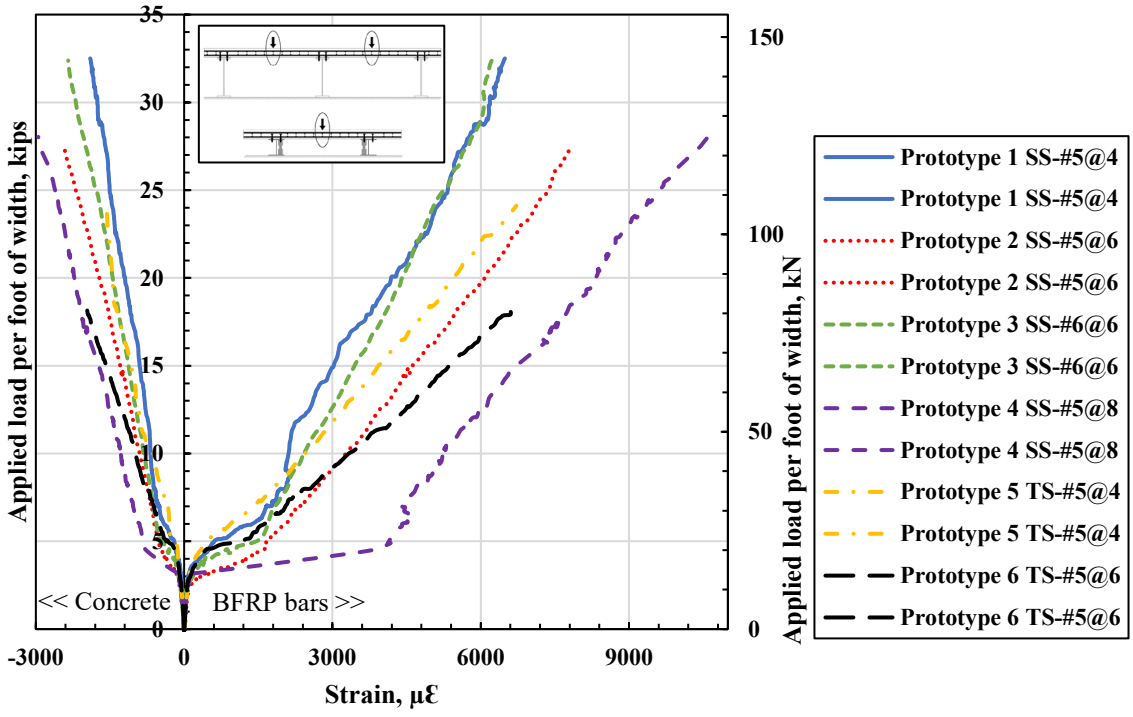

Figure 122: Load-strain curves on the concrete and BFRP bars at the midspan.

In addition, the maximum strain in the concrete recorded is 2951 με, which represents the failure strain of concrete in compression. The ratio between the strain in the BFRP and concrete can be useful to predict the position of the neutral axis at the

midspan. By assuming the linear triangular distribution of the stress along the section, the position of the neutral axis can be calculated. Figure 123 shows the stress distribution along the section and assuming the linear relationship between the stress and depth. The depth of the neutral axis can be calculated using Equation 17:

$$kd = \frac{\varepsilon_c}{\varepsilon_c + \varepsilon_f} \times d \qquad \text{Equation (17)}$$

Where ε_c is the strain in concrete, ε_f is the strain in the BFRP bars, and d is the effective depth.

By obtaining the ε_c and ε_f, the neutral axis location was computed for the six tested prototypes. The neutral axis location ranges between 1.27 and 1.75 in. for prototypes 5 and 3, respectively. This indicates that the crack depth from the bottom is between 6.25 to 6.75 in.

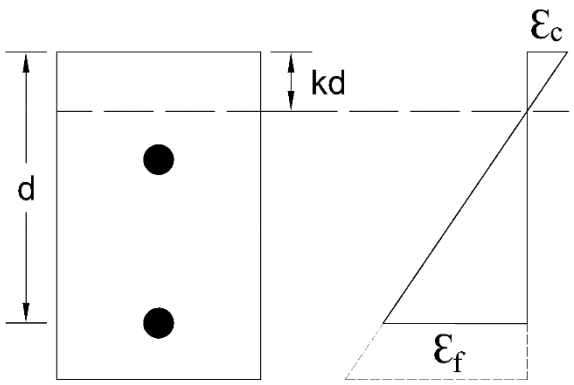

Figure 123: Neutral axis in the slab section.

4.3.4 Ultimate strength and failure mode

The failure mode of all the tested slabs is a flexural-shear failure, starting with the flexural cracks that reduces the compression zone, ending with a shear failure. This hypothesis can be proved by noticing the existence of the factor k to the shear strength equation in ACI440.1R-15, which represent the area of the compression zone in the section. The bottom surface of the slabs showed an acceptable number of cracks in the longitudinal direction parallel to the direction of the traffic flow. Figures 124 and 125 show the failure mode of tested single and two span bridge deck slabs. For better comparison, the ultimate load is recorded per foot width. As shown in Table 22, the

ultimate failure loads per foot width were 32.5, 27.4, 32.4, 28, 24.1, and 18.1 kips for Prototypes 1 to 6, respectively. The reinforcement ratio and the continuity condition affect the ultimate strength of the slab. For instance, Prototypes 1 and 3 with the same reinforcement ratio but different bar size and spacing had the same ultimate load capacity. Moreover, Prototypes 3 has a lower reinforcement ratio than Prototype 1 by 33%, which lowered the ultimate strength by 16%. Also Prototype 6 has 33% lower reinforcement ratio and the ultimate load is affected by 25%. This conclusion contradicts with the punching results obtained in Elgabbas research (Elgabbas et al.).

Figure 124: Typical mode of failure of single-span bridge deck Prototypes.

Figure 125: Typical mode of failure of two-span bridge deck Prototypes.

4.4 Flexural-shear capacity predictive model

Several predictive models have been generated to account for the punching shear capacity of bridge deck slab reinforced with FRP bars and none of these equations study the flexural-shear capacity (El-Gamal et al., 2005, El-Ghandour et al., 1999, Matthys and Taerwe et al., 2000, Ospina et al., 2003). Since bridge deck slabs has been designed as a flexural element, it's crucial to study the flexural shear capacity for better understanding of the behavior and easing the design of the bridge deck using FRP materials as a main reinforcement. The shear strength capacity of flexural members reinforced with FRP reinforcement as main reinforcement in ACI440.1R-15 includes the factor k to the equation. This factor represents the depth of the compression zone which reduces the shear section and also accounts for the reinforcement ratio in the section.

$$V_{c,ACI440.1R} = \frac{2}{5}\sqrt{f_c'}b_0kd \;;\; k = \sqrt{2\rho_f n_f + \left(\rho_f n_f\right)^2} - \rho_f n_f \qquad \text{Equation (18)}$$

Where Vc is the shear capacity, f'c is the concrete compressive strength, b0 is the critical parameter at 0.5d from the loading area, d is the flexural depth from the top concrete surface, ρ_f is the reinforcement ratio, and nf is the ratio of the modulus of elasticity of FRP reinforcement to the modulus of elasticity of concrete.

El-Gamal et al. predictive model is the only model that accounts for the slab continuity of the bridge deck. However, this model is a predictive model for the punching shear capacity of bridge deck slabs reinforced with FRP reinforcement.

4.4.1 Proposed design equation

A proposed design equation for the ultimate strength of bridge deck slabs reinforced with FRP reinforcement as main reinforcement was generated. This equation added a factor α to the existing equation in ACI440.1R-15. This factor alfa, after analyzing the test results in the literature, needs to include the effect of reinforcement ratio, concrete compressive strength, reinforcement modulus of elasticity, and the span length of the bridge deck slab. The British standard BS8110-1-97 includes the reinforcement ratio, concrete compressive strength in the punching shear equation. El-

Ghandour et al. introduced the value of the modulus of elasticity of FRP reinforcement to the modulus of elasticity of steel to the ACI 318-05 punching shear equation. Moreover, Matthys and Taerwe accounted for the same parameters but with different form of equation. Finally, Ospina et al. also included the reinforcement ratio, and modulus of elasticity of FRP to steel and the concrete compressive strength to their equation. None of the models accounted for the span length of the slab. Since the failure is a flexural-shear failure, the span length must be included in the equation based on the analysis of the literature data. The proposed equation in this research is as follows:

$$V_c = \frac{2}{5}\sqrt{f_c'}\, b_w kd\, \alpha\, (1.2)^N \qquad \text{Equation (19)}$$

Where N = 0 (for one span slab) N = 1 (for one end continuous slab)

$$\alpha = 10\left(\frac{1}{\rho}\right)^{0.415}\left(\frac{1}{S}\right)^{2.216}\left(\frac{1}{E_f}\right)^{0.261}\left(\frac{1}{f_c'}\right)^{0.122} \qquad \text{Equation (20)}$$

Where V_c is the predicted flexural-shear strength, MN, b_0 is the width of the tested slab in m, d is the structural depth if the reinforcement in m, ρ is the reinforcement ratio, S is the span length in m, E_f is the modulus of elasticity of the FRP reinforcement in GPa, f'_c is the concrete compressive strength in MPa.

This equation was validated with other research projects that tested slabs reinforced with FRP bars for the flexural-shear failure. Table 23 shows the input parameters of the present study as well as the other research in the literature. The average value of the experimental flexural-shear strength over the predicted strength is 1.00 with a coefficient of variation of 10%. Figure 126 shows the distribution of the experimental to predicted values around the identity line of equation y=x. the only red point is considered as an outlier which is the present testing (Prototype 6) which was expected to have higher strength.

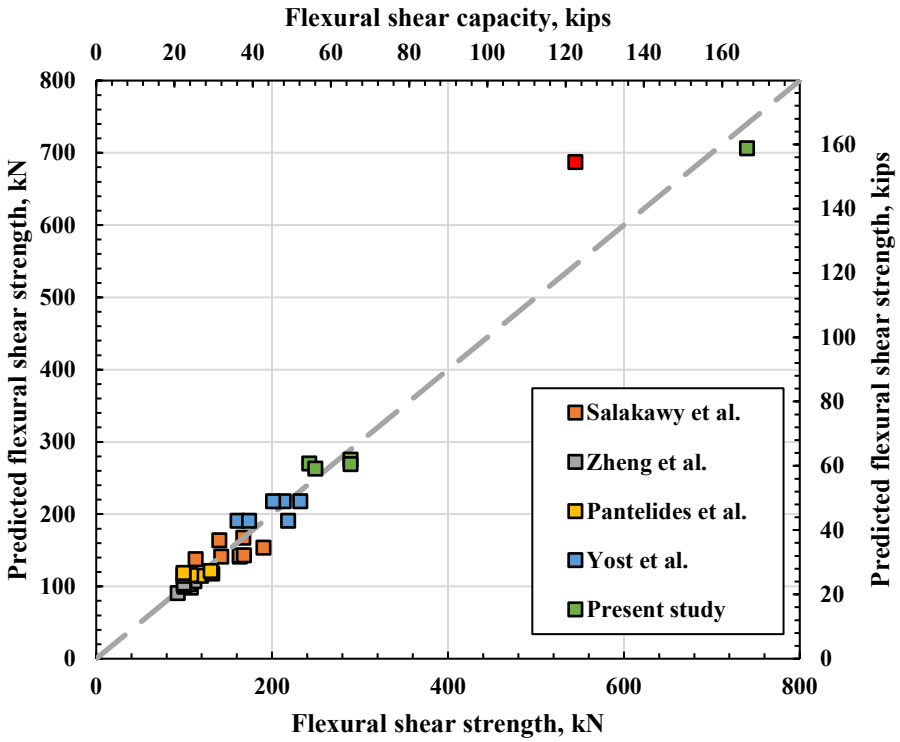

Figure 126: Experimental flexural-shear capacity versus predicted flexural-shear capacity.

Table 23: Comparison of theoretical and experimental results.

Reference		V_{test}	b_0, ft	d, in	f'c, ksi	ρ, %	Span, ft	Ef, ksi	N	ACI440.1R-15		Proposed equation	
										V_{theort}	V_{test}/V_{theort}	V_{theort}	V_{test}/V_{theort}
Salakawy et al.	S-C1	31.5	3.3	6.53	5.8	0.39	8.2	16534	0	14.5	2.10	36.8	0.86
	S-C2B	37.5	3.3	6.53	5.8	0.78	8.2	16534	0	20.4	1.84	37.7	1.00
	S-C3B	42.7	3.3	6.53	5.8	0.118	8.2	16534	0	8.6	4.99	34.6	1.24
	S-G1	25.4	3.3	6.53	5.8	0.86	8.2	5801	0	13.3	1.91	30.9	0.82
	S-G2	31.9	3.3	6.53	5.8	1.7	8.2	5801	0	18.1	1.76	31.8	1.00
	S-G2B	36.6	3.3	6.53	5.8	1.71	8.2	5801	0	18.2	2.01	31.8	1.15
	S-G3	36.6	3.3	6.53	5.8	2.44	8.2	5801	0	21.3	1.72	31.1	1.14
	S-G3B	37.8	3.3	6.53	5.8	2.63	8.2	5801	0	22	1.72	32.2	1.18
Zheng et al.	CG10	24.2	1.65	6.3	10.6	0.3	7	6469	0	4.8	5.02	22.1	1.09
	CG11	23.7	1.65	6.3	10.4	0.7	7	6469	0	7.17	3.31	23.2	1.02
	CG12	25.1	1.65	6.3	10.8	1.4	7	6469	0	10	2.51	24.1	1.04
	CG14	20.79	1.65	6.3	4.3	0.7	7	6469	0	5.6	3.68	20.4	1.02
	CG15	22.5	1.65	6.3	8.1	0.7	7	6469	0	6.7	3.35	22.4	1.00
	CG16	22.4	1.65	6.3	9.8	0.7	7	6469	0	7.1	3.17	23	0.97
	CG19	22.4	1.65	6.3	10.9	0.7	7	6469	0	7.3	3.08	23.4	0.96
Pantelides et al.	SP-1-NW	26.7	2	8	8.7	0.65	8	6280	0	10	2.67	25.8	1.04
	SP-2-NW	29.7	2	8	10.3	0.65	8	6280	0	10.5	2.83	26.5	1.12
	SP-3-NW	29.2	2	8	12.9	0.65	8	6280	0	11.1	2.63	27.3	1.07
	SP-4-LW	24.3	2	8	9.1	0.65	8	6280	0	10.2	2.39	26	0.93
	SP-5-LW	22.3	2	8	8.7	0.65	8	6280	0	10	2.22	25.8	0.86
	SP-6-LW	22.3	2	8	10.9	0.65	8	6280	0	10.6	2.09	26.7	0.83
Yost et al.	H1	49	4	6.97	4.8	2.26	8	5990	0	25.7	1.90	42.9	1.14
	H2	36.1	4	9.97	4.8	2.26	8	5990	0	25.7	1.40	42.9	0.84
	H3	39	4	6.97	4.8	2.26	8	5990	0	25.7	1.52	42.9	0.91
	C1	52.2	4	7.1	4.8	2.48	8	12328	0	36.8	1.42	48.9	1.07
	C2	47.9	4	7.1	4.8	2.48	8	12328	0	36.8	1.30	48.9	0.98
	C3	45.2	4	7.1	4.8	2.48	8	12328	0	36.8	1.23	48.9	0.92
Present study	P1	64.5	4	6.7	7.1	1.159	7	8673	0	24.2	2.69	61.9	1.05
	P2	54.5	4	6.7	6.95	0.773	7	8673	0	20	2.72	60.7	0.90
	P3	64.5	4	6.6	6.5	1.107	7	8803	0	23	2.82	60.6	1.07
	P4	61	4	6.7	6.35	0.579	7	8673	0	17.1	3.28	59.2	0.95
	P5	166.4	10	6.7	6.95	1.159	7.5	8673	1	60	2.77	158.8	1.04
	P6	122.5	10	6.7	6.5	0.73	7.5	8673	1	47.8	2.56	154.5	0.79
Average											2.50		**1.00**
SD											0.906		0.109
COV, %											36		**10.9**

5 Non-Linear Finite Element Analysis

A parametric study was conducted using non-linear finite element analysis on concrete bridge deck slabs reinforced with BFRP bars to assess its flexural behavior. The experimental testing program conducted at UIC was used for validating the finite element analysis. Then, the finite element analysis was extrapolated to study the effect of the following parameters:

1. Slab span lengths of 6, 8, 10, 12, and 14 ft.
2. Transverse bar sizes of #5 and #6.
3. Transverse bar spacing of 4, 6, and 8 in.
4. Longitudinal bar spacing of 6 and 12 in.
5. Concrete compressive strengths of 4 ksi, 6 ksi, and 8 ksi.

5.1.1 Description of NLFEA

The specimens were used in the simulations without considering any symmetry. The 8-noded hexahedral (brick) element, with reduced integration (C3D8R) to avoid the shear locking effect, was used for the concrete slab, FRP bars, and supports. Since no reinforcement slippage was reported in the considered experimental studies, a perfect bond between concrete and all types of reinforcement is assumed in this study. Therefore, the embedded method simulated the perfect bond between the concrete and the reinforcement. Restraints were introduced at the bottom of the support mimicking the experimental boundary conditions. The numerical study was conducted with the commercial FEA software ABAQUS.

5.1.2 Parametric Study

The design of bridge deck slabs includes determining their materials, dimensions, and reinforcement. Each parameter influences the slab behavior. Therefore, this parametric study aims to evaluate the behavior of BFRP-reinforced concrete bridge deck slabs. Table 24 illustrates the specimens' details of the parametric study.

Table 24: Specimens' details of parametric study.

Group	Specimen	Span Length, L	f'_c	Transverse bar size	Transverse bar spacing	Longitudinal bar size	Longitudinal bar spacing
		ft	ksi	#	in	#	in
Span length	S1	6	4	6	4	5	6
	S2	8	4	6	4	5	6
	S3	10	4	6	4	5	6
	S4	12	4	6	4	5	6
	S5	14	4	6	4	5	6
Trans. bar size	S1	6	4	6	4	5	6
	S6	6	4	5	4	5	6
Trans. bar spacing	S1	6	4	6	4	5	6
	S7	6	4	6	6	5	6
	S8	6	4	6	8	5	6
Long. bar	S1	6	4	6	4	5	6
	S9	6	4	6	4	5	12
Concrete strength	S1	6	4	6	4	5	6
	S10	6	6	6	6	5	6
	S11	6	8	6	8	5	6

Note:
S1: fc4-S6-T#6@4-L#5@6
S2: fc4-S8-T#6@4-L#5@6
S3: fc4-S10-T#6@4-L#5@6
S4: fc4-S12-T#6@4-L#5@6
S5: fc4-S14-T#6@4-L#5@6
S6: fc4-S6-T#5@4-L#5@6
S7: fc4-S6-T#6@6-L#5@6
S8: fc4-S6-T#6@8-L#5@6
S9: fc4-S6-T#6@4-L#5@12
S10: fc6-S6-T#6@4-L#5@6
S11: fc8-S6-T#6@4-L#5@6

5.1.2.1 Influence of Span Length

The supported span length is the center-to-center distance between the supporting beams. In this parametric study, six span lengths are considered 6ft, 8 ft, 10 ft, 12 ft, and 14 ft, respectively. Figures 127-128 show load-strain curves in the negative and positive regions. The cracking loads are 13.7 kip/ft, 9.7 kip/ft, 7.7 kip/ft, 5.8 kip/ft, and 5.5 kip/ft for specimens S1, S2, S3, S4, and S5, respectively. The nominal loads are 58.3 kip/ft, 45.3 kip/ft, 36.7 kip/ft, 30.8 kip/ft, and 26.2 kips, respectively. Figure 129 shows load-deflection curves.

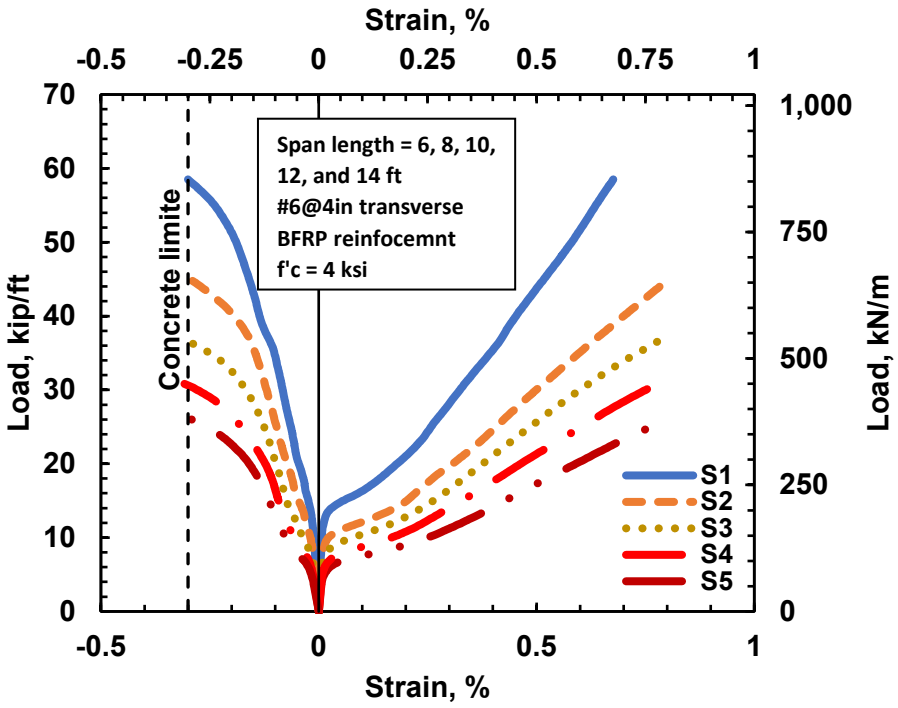

Figure 127: Load-strain curves in negative moment region.

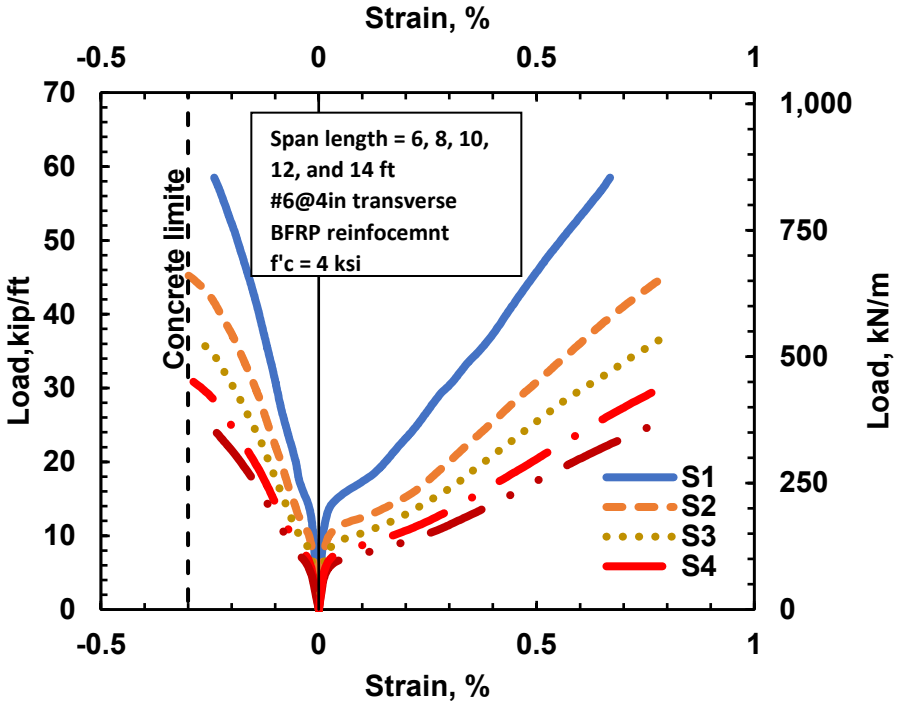

Figure 128: Load-strain curves in positive moment region.

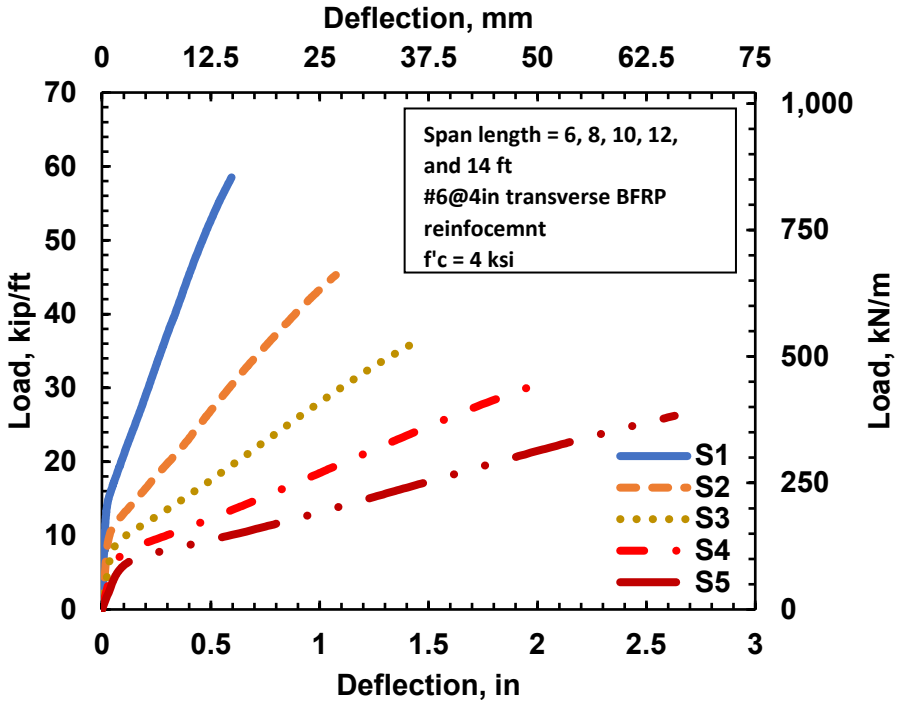

Figure 129: Load-deflection curves in positive moment region.

5.1.2.2 Influence of Transverse Bar Size

Transverse reinforcement is the main reinforcement in the bridge deck slabs since it spans between the supporting beams. The transverse bar size effect on the bridge deck behavior was examined in this group of specimens S1 and S6. Figures 130-131 show the load-strain curves in the negative and positive moment regions. The nominal loads are 58.5 kip/ft and 55.2 kip/ft for specimens S1 and S6. The strain in the BFRP bars at the nominal load is 0.0067 and 0.0088 for specimens S1 and S7. Load-deflection curves shown in Figure 132 illustrate the effect of transverse bar size on the slab deflection.

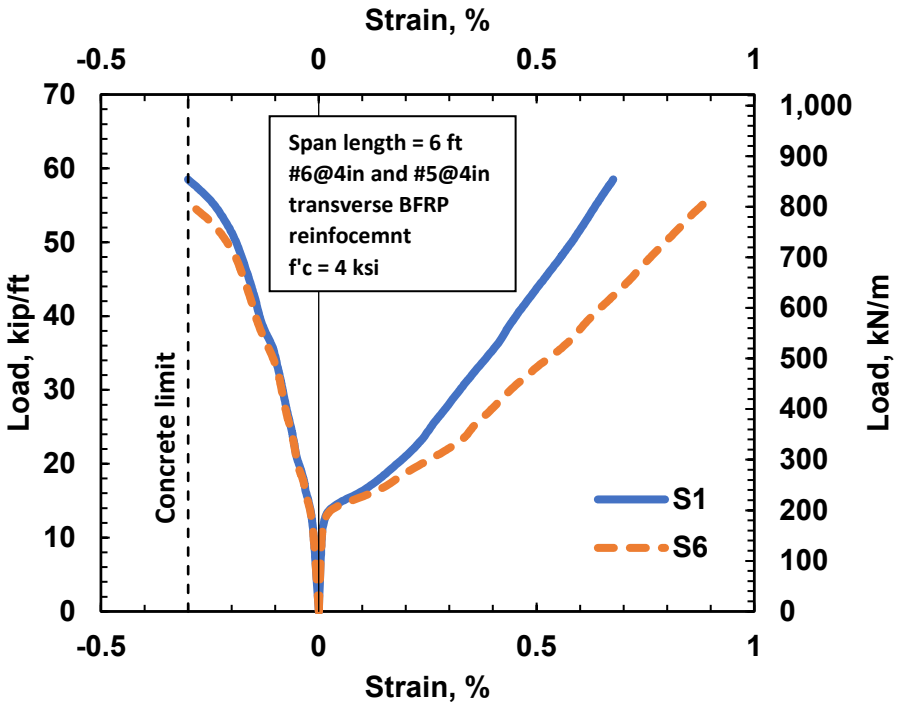

Figure 130: Load-strain curves in negative moment region.

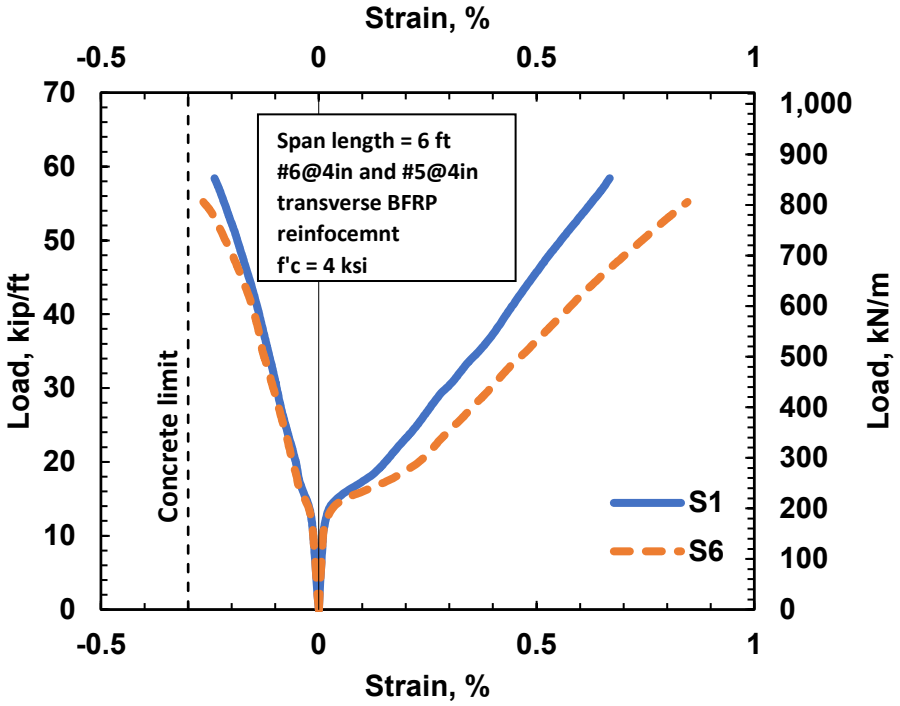

Figure 131: Load-strain curves in positive moment region.

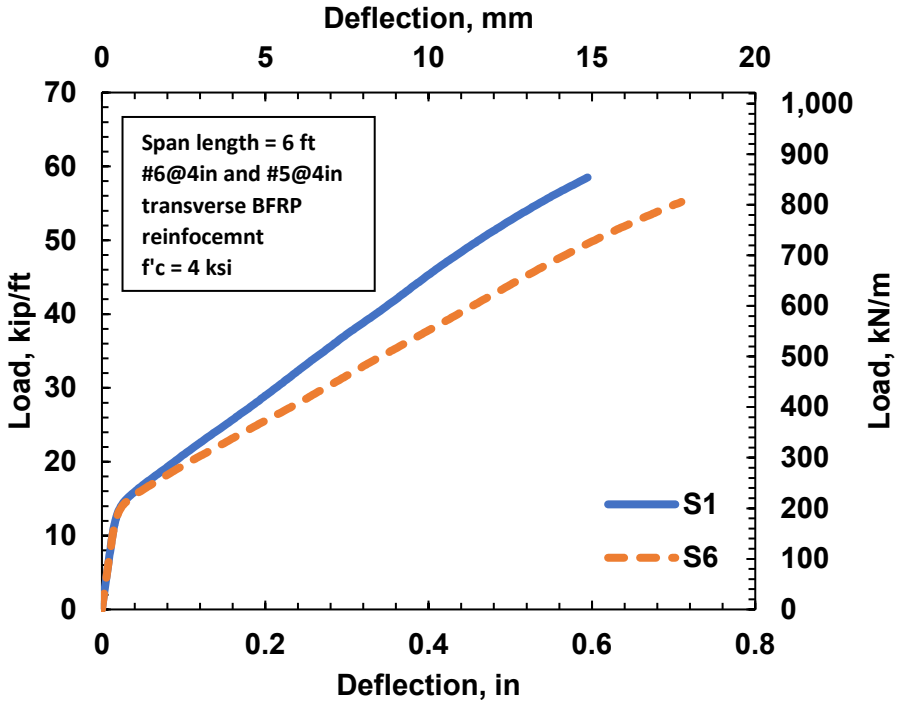

Figure 132: Load-deflection curves in positive moment region.

5.1.2.3 Influence of Transverse Bar Spacing

The transverse bar spacing effect on the bridge deck behavior was examined in this group of specimens S1, S7, and S8. Figures 133-134 show the load-strain curves in the negative and positive moment regions. The nominal loads are 58.5 kips, 52.0 kips, and 48.4 kips for specimens S1, S7, and S8. The strain in the BFRP bars at the nominal load is 0.0067, 0.0088, and 0.01 for specimens S1, S7, and S8. Load-deflection curves shown in Figure 135 illustrate the effect of transverse bar spacing on the slab deflection.

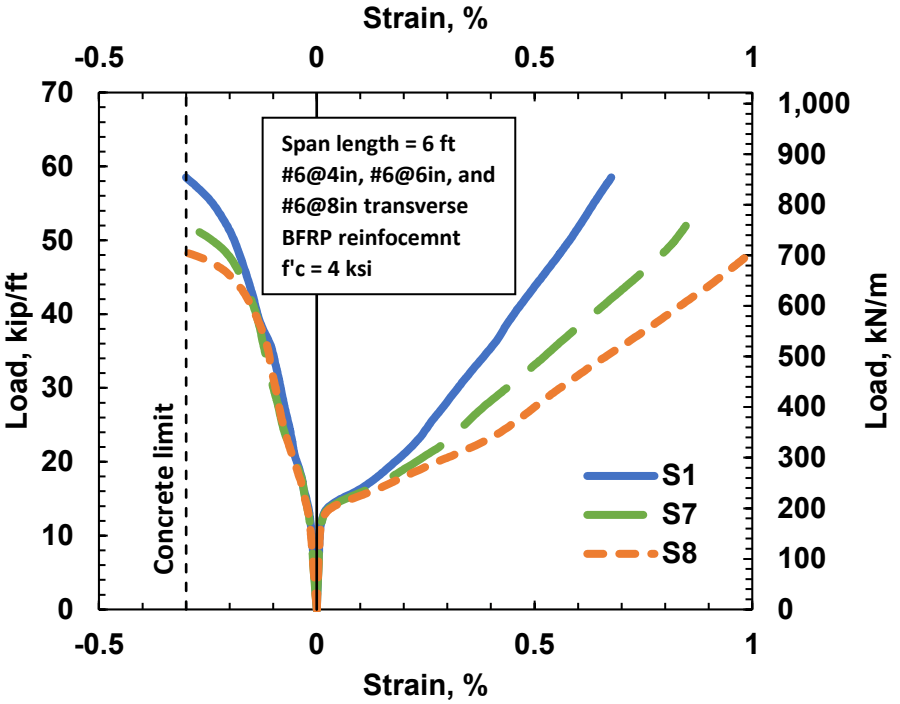

Figure 133: Load-strain curves in negative moment region.

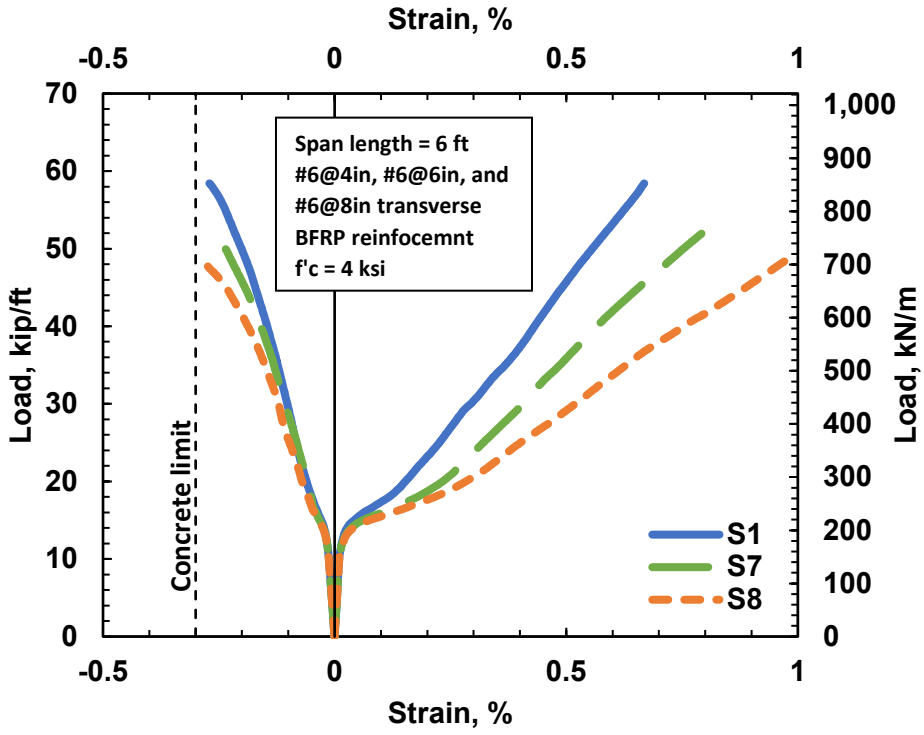

Figure 134: Load-strain curves in positive moment region.

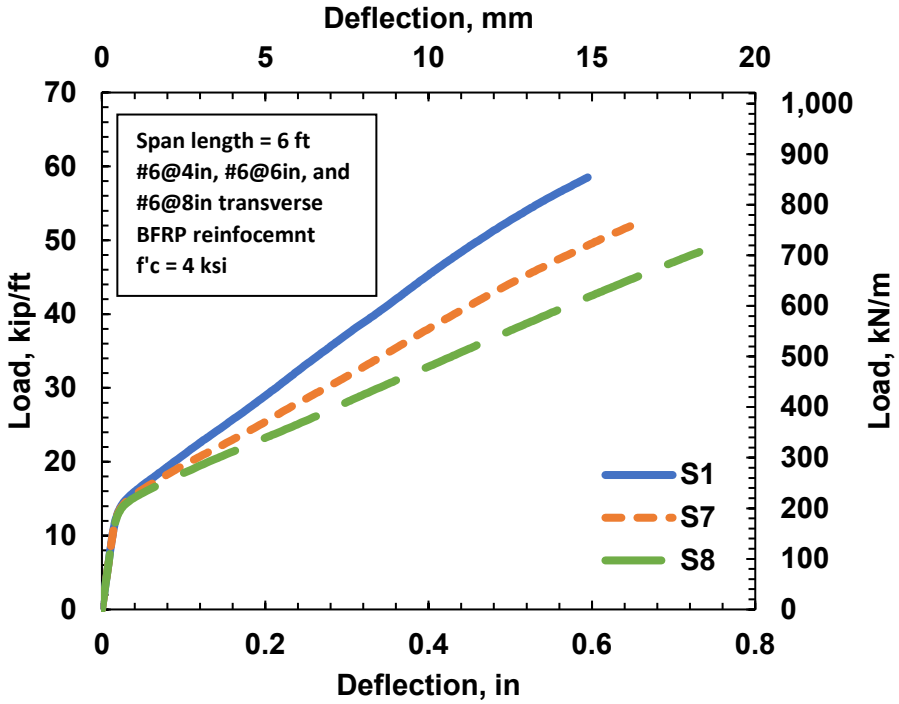

Figure 135: Load-deflection curves in positive moment region.

5.1.2.4 Influence of Longitudinal Bar Spacing

Longitudinal reinforcement in bridge deck slabs is not designed. The top longitudinal reinforcement needs to satisfy shrinkage and temperature requirements per Article 5.10.6 in AASHTO LRFD. The bottom longitudinal reinforcement is a percentage of the bottom transverse reinforcement per Article 9.7.3.2 AASHTO LRFD. This percentage is equal to 67% for all bridges with beam spacing within the limits of the standard deck design charts. The longitudinal bar effect on the bridge deck behavior was examined in this group of specimens S1 and S9. Figures 136-137 show load-strain curves in the negative and positive moment regions. The nominal loads are 58.5 kip/ft and 57.4 kip/ft for specimens S1 and S9. The BFRP strains at the nominal load are 0.0067 and 0.0064 for specimens S1 and S9. Figure 138 shows load-deflection curves. Load-strain and load-deflection curves reveal that the longitudinal bar does not affect bridge deck slab behavior.

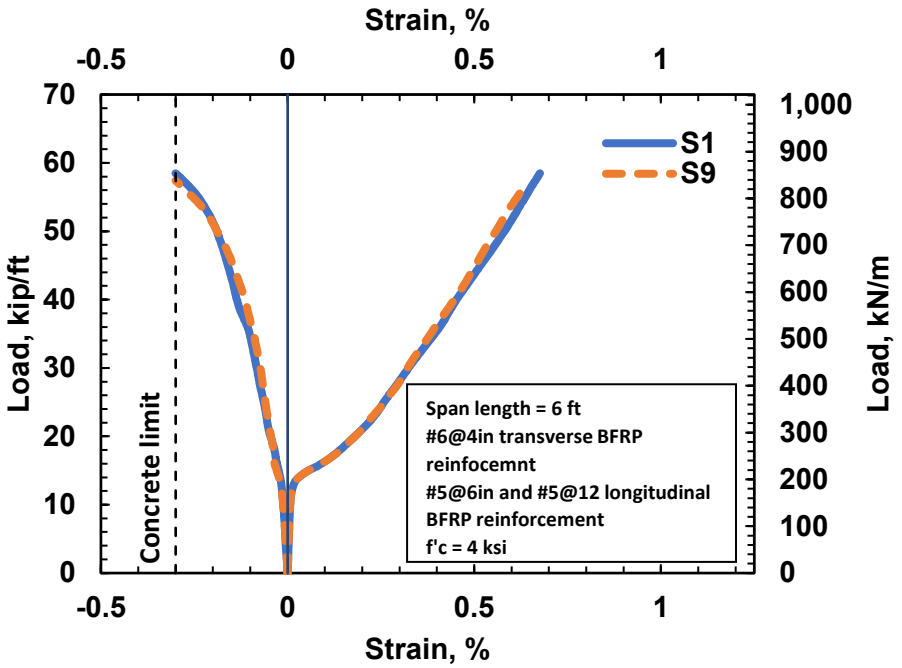

Figure 136: Load-strain curves in negative moment region.

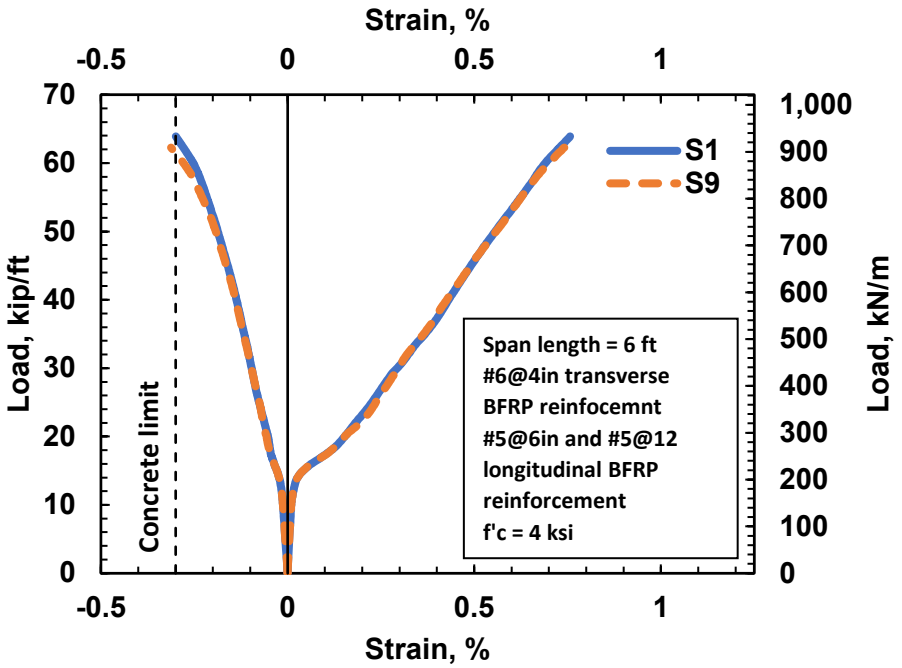

Figure 137: Load-strain curves in positive moment region.

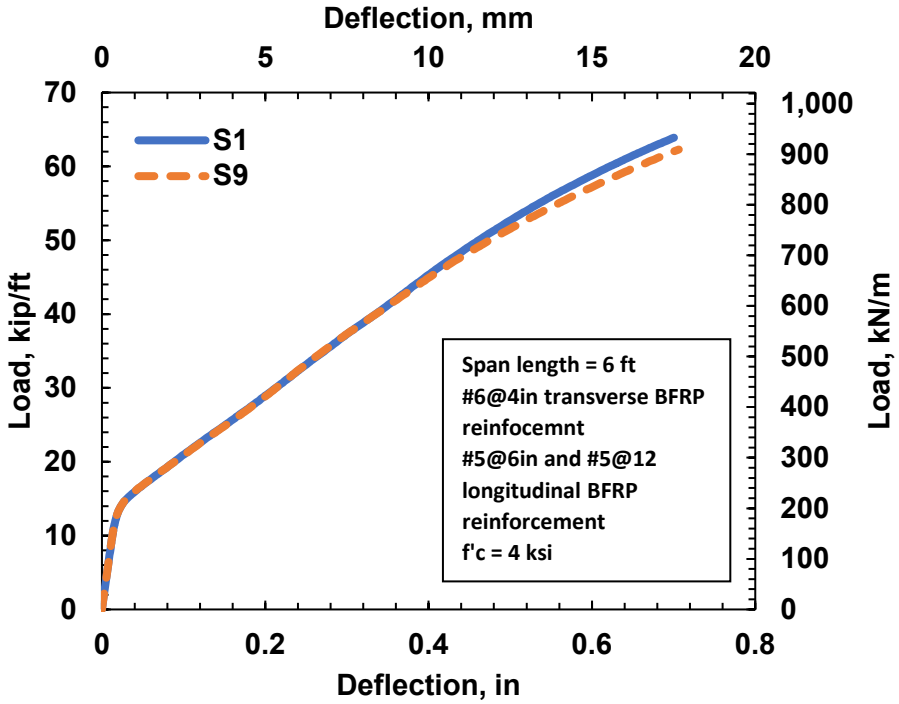

Figure 138: Load-deflection curves at positive moment region.

5.1.2.5 Influence of Concrete Compressive Strength

The concrete compressive strength effect on the bridge deck behavior was examined in this group; the concrete strength for specimens S1, S10, and S11 are 4 ksi, 6 ksi, and 8 ksi, respectively. Figures 139-140 show the load-strain curves in the negative and positive moment regions. The nominal loads are 58.5 kips, 69.2 kips, and 74.1 kips for specimens S1, S11, and S12. The strain in the BFRP bars at the nominal load is 0.0067, 0.0078, and 0.0082 for specimens S1, S10, and S11. Load-deflection curves shown in Figure 141 illustrate the effect of transverse bar spacing on the slab deflection.

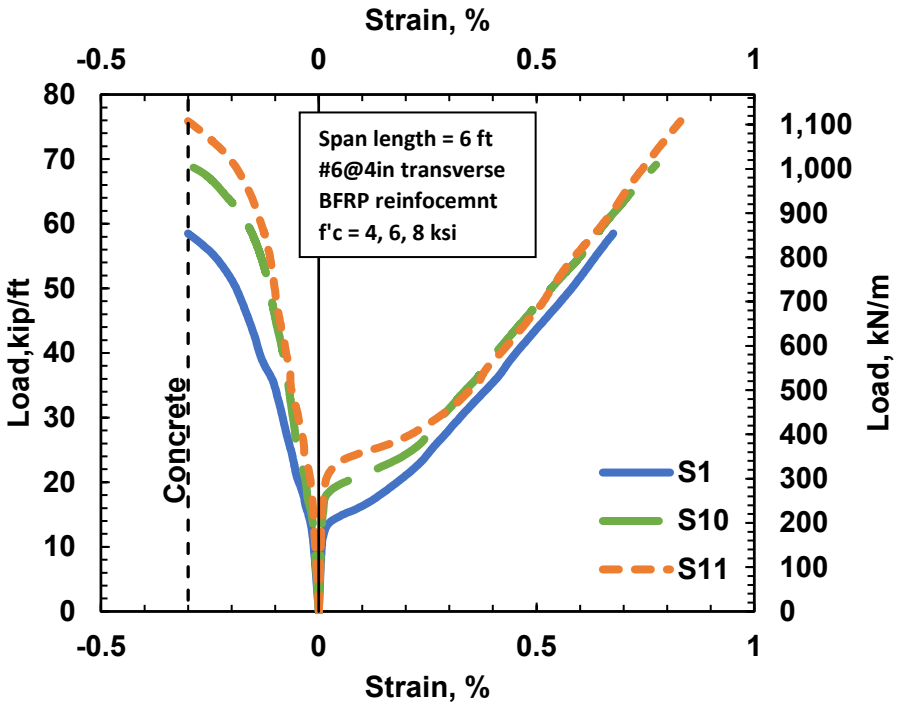

Figure 139: Load-strain curves at negative moment region.

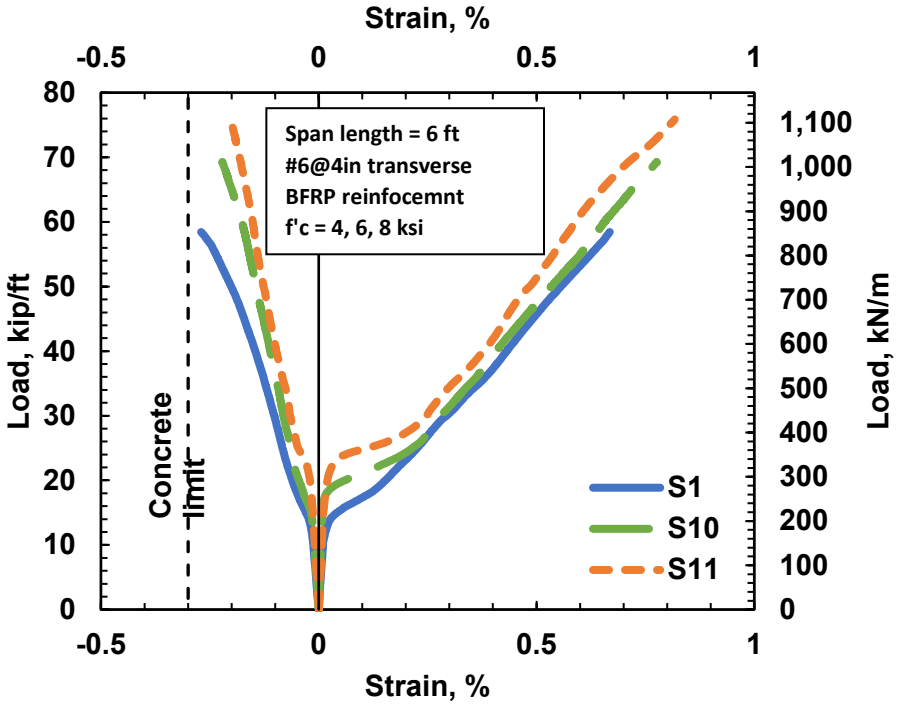

Figure 140: Load-strain curves at positive moment region.

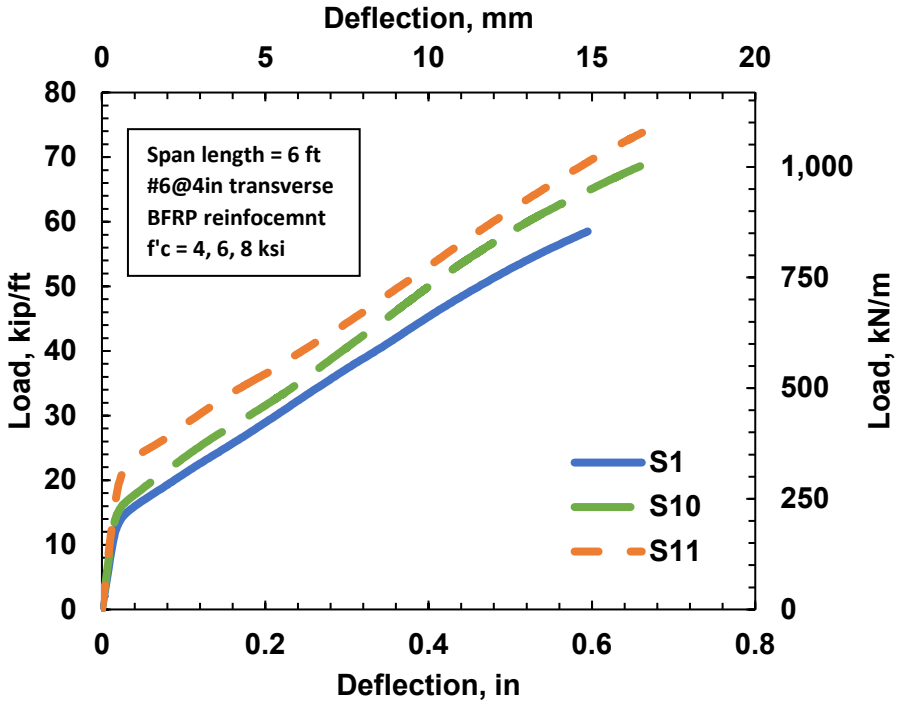

Figure 141: Load-deflection curves at positive moment region.

5.1.2.6 Summary

This parametric study assesses the flexural behavior of bridge deck slabs. Five parameters were evaluated: (1) span length, (2) transverse bar size, (3) transverse bar spacing, (4) longitudinal bar spacing, and (5) concrete compressive strength. The flexural behavior is evaluated based on the cracking load, nominal load, strain in BFRP bars at nominal load, and deflection of the concrete slab at nominal load. It is concluded that the cracking load is directly proportional to the span length and concrete compressive strength, while the nominal load is directly proportional to the span length, concrete compressive strength, and transverse bar size and spacing. Also, the strain in the BFRP bar at nominal load is directly proportional to the transverse bar size, transverse bar spacing, and concrete compressive strength. Finally, the longitudinal bar is the only parameter that does not significantly affect the slab serviceability and ultimate strength. A summary of the parametric study results has been summarized in Table 25.

Table 25: Summary of Parametric study.

Parameter	Span length ft	f'_c Ksi	Trans. Reinf.	Long. Reinf.	Slab Thick.	Cracking load Kip/ft	Nominal load Kip/ft	Strain in BFRP at nominal load	Deflection at Nominal in	Note
Span length	6	4	#6@4	#5@6	8	13.7	58.5	0.0067	0.59	Directly proportional to cracking load, nominal load, and deflection.
	8	4	#6@4	#5@6	8	9.7	45.3	0.0081	1.07	
	10	4	#6@4	#5@6	8	7.7	36.7	0.0076	1.47	
	12	4	#6@4	#5@6	8	5.8	30.8	0.0078	2.03	
	14	4	#6@4	#5@6	8	5.5	26.2	0.0081	2.63	
Transverse bar size	6	4	#6@4	#5@6	8	13.7	55.2	0.0088	0.71	directly proportional to, nominal load, strain in BFRP, and deflection.
	6	4	#5@4	#5@6	8	13.7	58.5	0.0067	0.59	
Transverse bar spacing	6	4	#6@4	#5@6	8	13.7	58.5	0.0067	0.59	directly proportional to, nominal load, strain in BFRP, and deflection.
	6	4	#6@6	#5@6	8	13.7	52.0	0.0085	0.65	
	6	4	#6@8	#5@6	8	13.7	48.4	0.0100	0.73	
Longitudinal bar	6	4	#6@4	#5@6	8	13.7	58.5	0.0067	0.59	Does not have any effect.
	6	4	#6@4	#5@12	8	13.7	57.4	0.0064	0.60	
Concrete compressive strength	6	4	#6@4	#5@6	8	13.7	58.5	0.0067	0.59	Directly proportional to cracking load, nominal load, strain in BFRP, and deflection.
	6	6	#6@4	#5@6	8	16.8	69.2	0.0078	0.66	
	6	8	#6@4	#5@6	8	20.4	74.1	0.0082	0.70	

6 Design Philosophy and Structural Performance

6.1 Design Philosophy

The design philosophy of AASHTO GFRP is based on limit state design principles. Based on AASHTO LRFD, a limit state is a "condition beyond which the bridge or component ceases to satisfy its designed provisions." Constructability, safety, and serviceability are achieved if the bridge and its components satisfy all the limit states. A limit state can be satisfied by checking a value such as but not limited to stress or deformation of a component under a given load combination with a limit specified in the code.

AASHTO GFRP considers five limit states for designing bridges reinforced with GFRP bars: (1) service limit state, (2) strength limit state, (3) creep rupture limit state, (4) fatigue limit state, and (5) extreme event limit state. These limit states, excluding extreme event limit state, will be used in this study due to the limited research and design guides for using BFRP bars in bridges and the similar behavior of these rebars.

6.1.1 Service Limit State

AASHTO GFRP provision 2.6.7, if the empirical design method is not used, the crack can be controlled by controlling the reinforcement distribution. Two checks are to be considered in this study: maximum spacing of the rebars and concrete cover thickness measured to the top of reinforcement for negative moment and the bottom of reinforcement for positive moment.

$$s \leq \min\left(1.15\frac{C_b E_f w}{f_{f,s}} - 2.5c_c\ ;\ 0.92\frac{C_b E_f w}{f_{f,s}}\right) \leq \min\left(1.5d, 18in\right) \qquad \text{AASHTO GFRP (2.6.7-1)}$$

Where

s = average spacing of reinforcement in layer closest to tension face (in).

E_f = tensile modulus of elasticity of Reinforcement (ksi).

$f_{f,s}$ = Calculated tensile stress in reinforcement at the service limit state (ksi).

c_c = Clear cover (in).

C_b = Reduction factor that accounts for the degree of bond between the

reinforcement and the surrounding concrete.

w = maximum concrete crack width limit in concrete components, which is set as 0.028 (in).

And

$$d_c \leq \frac{C_b E_f w}{2 f_{f,s} \zeta}$$ AASHTO GFRP (2.6.7-2)

Where:

$$\zeta = \frac{h - kd}{d - kd}$$

Excluding the stress at the service condition $f_{f,s}$, all the information needed for the service limit is geometrical and material properties.

6.1.2 Strength Limit State

As per AASHTO GFRP article 2.6.3.1, the stress in BFRP reinforcement f_f at nominal flexural resistance shall be less than or equal to the design tensile strength f_{fd}:

$$f_f = \sqrt{\frac{(E_f * \varepsilon_{cu})^2}{4} + \frac{0.85\beta_1 * f'_c}{\rho_f} E_f * \varepsilon_{cu}} - 0.5 E_f * \varepsilon_{cu} \leq f_{fd}$$ AASHTO GFRP (2.6.3.1-1)

Where

E_f = tensile modulus of elasticity of Reinforcement (ksi)

ε_{cu} = ultimate strain in concrete, is not greater than 0.003

β_1 = factor dependent on concrete strength.

f'_c = specified compressive strength of concrete (ksi)

ρ_f = BFRP reinforcement ratio.

f_{fd} = design tensile strength of BFRP reinforcing bars considering the Environmental Reduction Factor, C_E.

As per Article 2.6.3.2, the factored flexural resistance, M_r, shall be greater than or equal to the applied moment calculated using Strength I load combination shall

satisfy:

$$M_r \geq M_{Strength\ I}$$

Where:

$$M_r = \emptyset M_n \qquad \text{AASHTO GFRP (2.6.3.2.1-1)}$$

And

M_n = nominal flexural resistance (kip-in).

$\emptyset$ = resistance factor.

In which:

$$\emptyset = \begin{cases} 0.55 & for \quad \varepsilon_{ft} = \varepsilon_{fd} \\ 1.55 - \dfrac{\varepsilon_{ft}}{\varepsilon_{fd}} & for \quad 0.80\varepsilon_{fd} < \varepsilon_{ft} < \varepsilon_{fd} \\ 0.75 & for \quad \varepsilon_{ft} < 0.80\varepsilon_{fd} \end{cases}$$

And

ε_{fd} = design tensile strain of GFRP reinforcing bars (AASHTO GFRP Eq. 2.4.2.1-1).

ε_{ft} = tensile strain in extreme tension GFRP at nominal resistance.

6.1.3 Creep Rupture Limit State

As per Article 2.5.3, the tensile stress f_f of the rebars under the Service I load combination, where the live load factor is reduced to 0.2, shall satisfy:

$$f_{f,f} \leq C_c * f_{fd} \qquad \text{AASHTO GFRP (2.5.4-1)}$$

Where:

$$f_{f,f} = \frac{n_f * d * (1-k)}{I_{cr}} * M_{Creep} \qquad \text{AASHTO GFRP (2.5.4-2)}$$

And

C_c = creep reduction factor

n_f = modular ratio

d = distance from extreme compression fiber to centroid of tensile

reinforcement (in)

k = ratio of depth of neutral axis to reinforcement depth.

I_{cr} = moment of inertia of transformed cracked section (in4).

M_{Creep} = moment due to dead loads and sustained portion of live loads included in Service I load combination (kip-in).

In which:

$$k = \sqrt{2\rho_f * n_f + (\rho_f * n_f)^2} - \rho_f * n_f \qquad \text{AASHTO GFRP (2.5.3-4)}$$

$$I_{cr} = \frac{b * d^3}{3} k^3 + n_f * A_f * (d - k * d) \qquad \text{AASHTO GFRP (2.5.3-3)}$$

6.1.4 Fatigue Limit State

As per AASHTO GFRP provision 2.5.4, Fatigue does not need to be investigated for multi-girder applications. However, if required, the tensile stress f_f of the rebars under the Fatigue I load combination shall not be greater than 25% of the design strength of the rebar f_{fd}.

6.2 Structural Behavior

The bridge deck slab structural behavior is judged using the design philosophy of AASHTO GFRP. The nominal capacity of the slab is achieved when the compressive strain in concrete reaches its ultimate value of 0.003 or when the strain in the BFRP bar reaches its design strain. The ultimate capacity of the slab is calculated by multiplying the nominal capacity by the resistance factor. Then, all the limit states are checked at the critical locations (Negative and positive moment regions). In this section, Specimen S1 will be used to illustrate the structural behavior of the bridge deck slabs. Figure 142 shows the damaged areas at the nominal slab load.

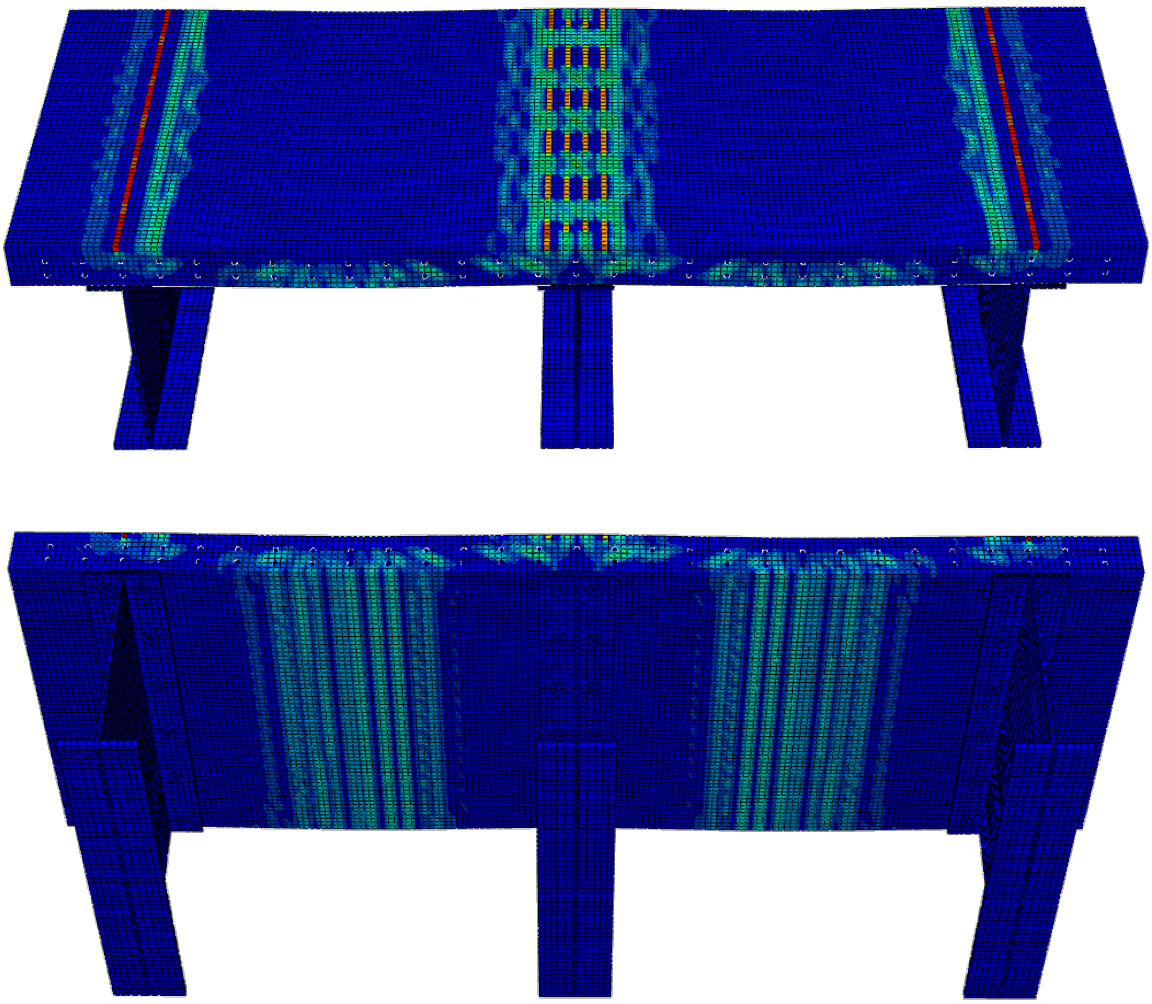

Figure 142: Slab damaged areas at the nominal capacity.

6.2.1 Negative Moment Region

The negative moment region over the middle support is the critical region for Specimen S1. Figure 143 shows the strain contour of specimen S1. Figure 144 shows the load-strain curves at the negative moment region, revealing that the nominal and ultimate capacities are equal to 58.5 kip/ft and 43.9 kip/ft, respectively. Also, the strain in the BFRP bar is 0.0066, which is 41% of its design strain of 0.016. The design strain is the ultimate rebar strain multiplied by the Environmental Redaction Factor.

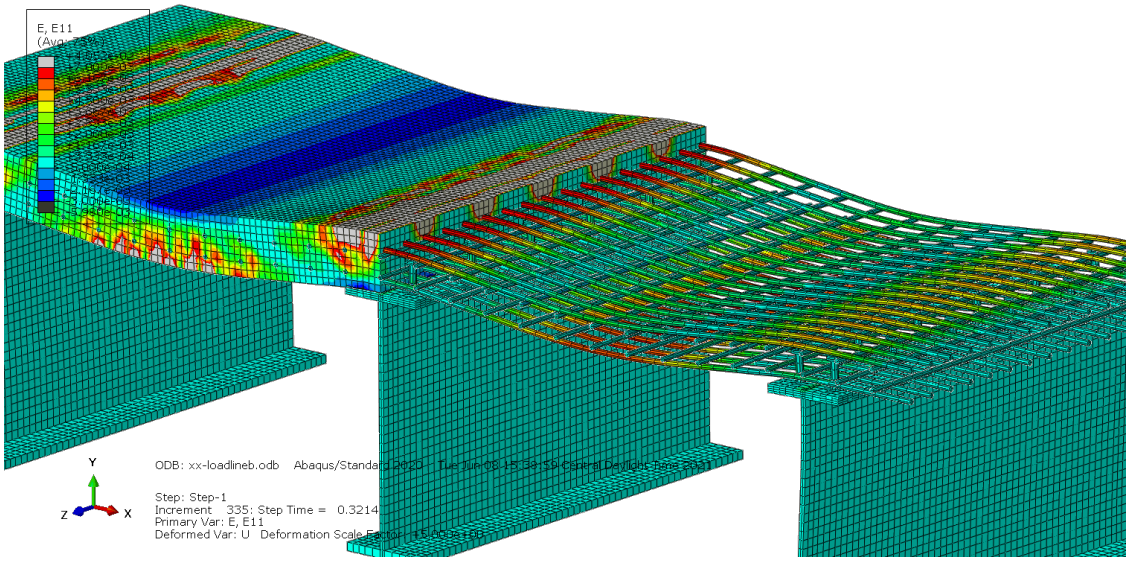

Figure 143: Strain contour of specimen S1.

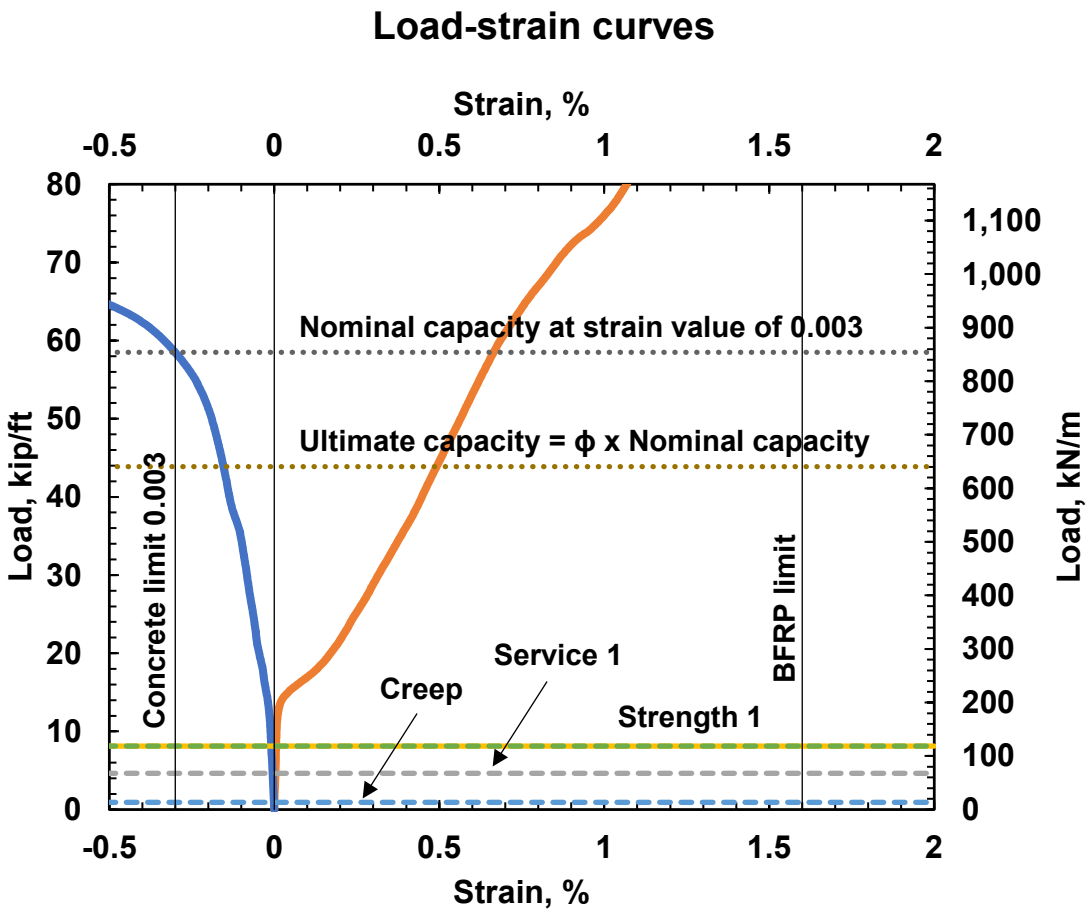

Figure 144: load-strain curves for negative moment region of Specimen S1.

In addition, All the load combinations are less than the cracking load of 13.7 kip/ft. Table 26 illustrates the limit states checks. It can be observed that the strain values are minimal since all the load combinations are less than the cracking load.

Table 26: Limit states checks at negative region of specimen S1.

Criteria	Limit	Limit value	Strain
BFRP	f_{fd}	0.016	0.0066
Concrete	Ultimate Strain	0.003	0.003
Service limit	Spacing	18 in	4 in
Strength limit	f_{fd}	0.016	0.0000914
Creep rupture limit	$0.2 \times f_{fd}$	0.0032	0.0000093
Fatigue limit	$0.25 \times f_{fd}$	0.004	0.0000914

6.2.2 Positive Moment Region

Figure 145 shows the strain contour of Specimen S1. Figure 146 shows the load-strain curves at the positive moment region. It reveals that the crushing of the concrete determines the capacity, and the nominal and ultimate capacities are 63.9 kip/ft and 47.9 kip/ft, respectively.

Also, the strain in the BFRP bar is 0.0075, which is 46% of its design strain of 0.016. In addition, All the load combinations are less than the cracking load of 8.9 kip/ft. Table 27 illustrates the limit states checks. It can be observed that the strain values are minimal since all the load combinations are less than the cracking load.

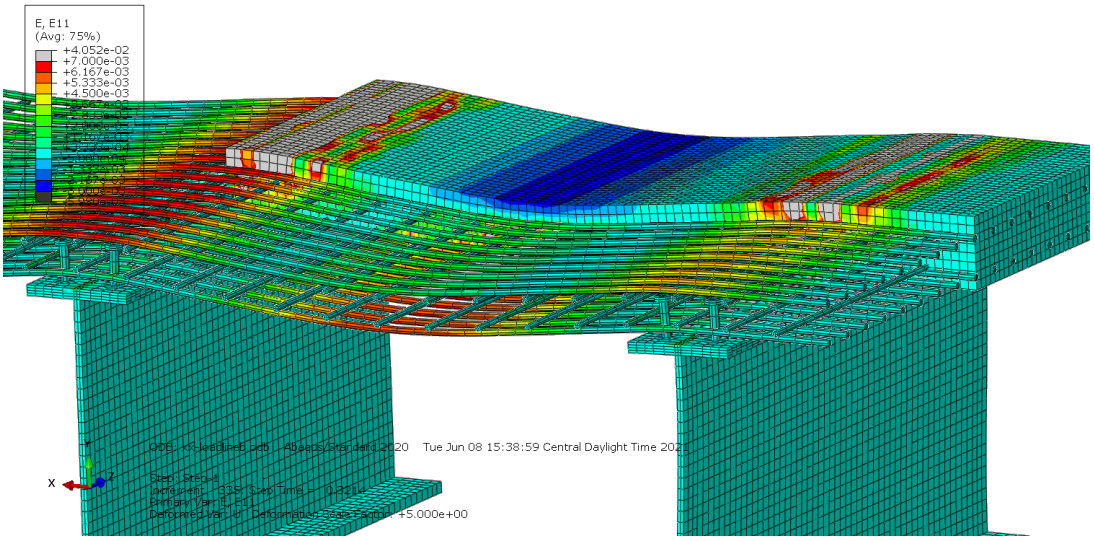

Figure 145: Strain contour of specimen S1.

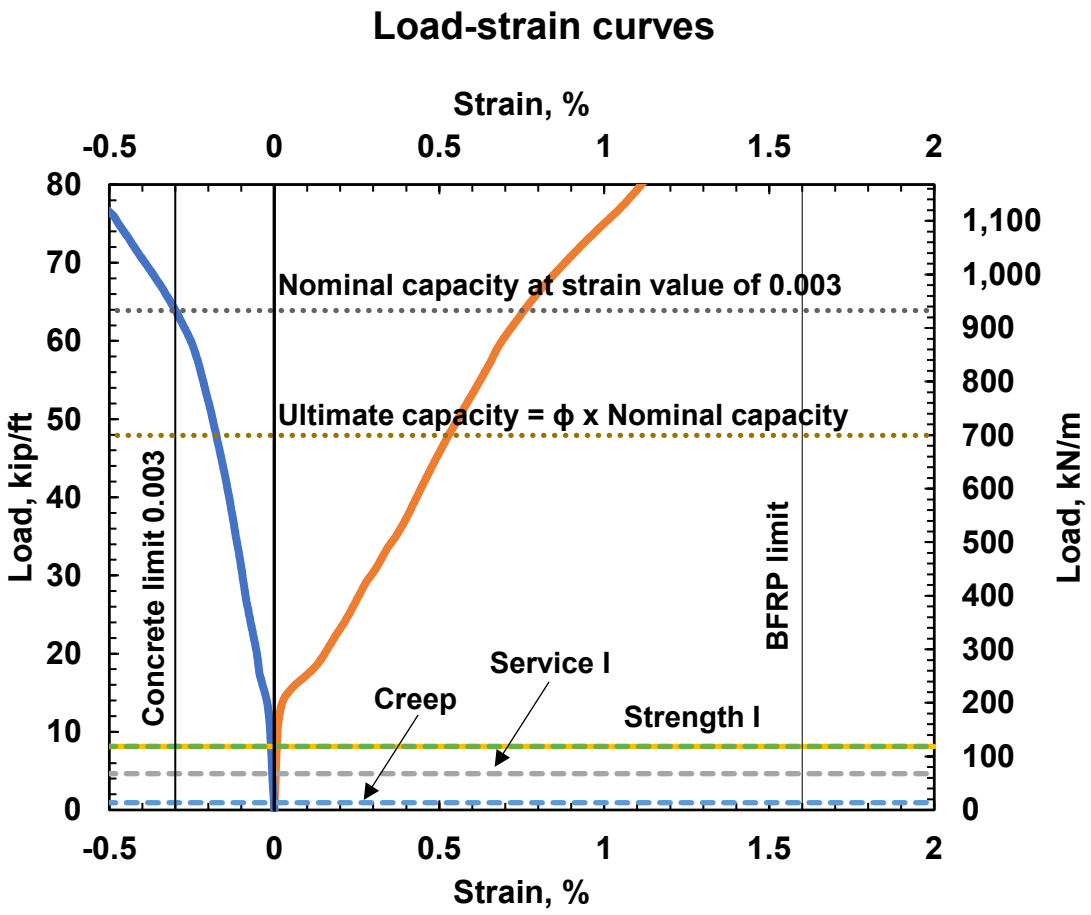

Figure 146: Load-strain curves for positive moment region of specimen S1.

Table 27: Limit states checks at positive region of specimen S1.

Criteria	Limit	Limit value	Strain
BFRP	f_{fd}	0.016	0.0075
Concrete	Ultimate Strain	0.003	0.003
Service limit	Spacing	18 in	4 in
Strength limit	f_{fd}	0.016	0.0000787
Creep rupture limit	$0.2 \times f_{fd}$	0.0032	0.000009
Fatigue limit	$0.25 \times f_{fd}$	0.004	0.0000787

6.2.3 Deflection

Figure 147 shows the deflection contour at the ultimate load. The load-deflection curve of Specimen S1 is presented in Figure 148. The deflection values are 0.006 in, 0.011 in, and 0.38 in at a wheel load of 2.9 kip/ft, cracking load of 8.9 kip/ft, and ultimate load of 43.9 kip/ft, respectively.

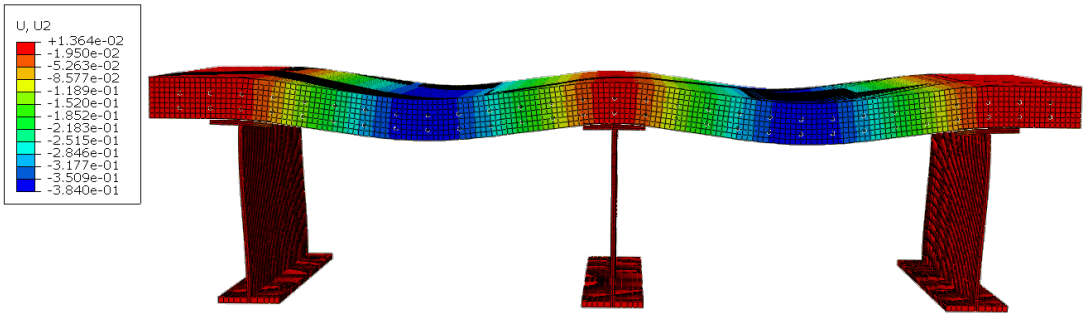

Figure 147: Deflection contours of Specimen S1.

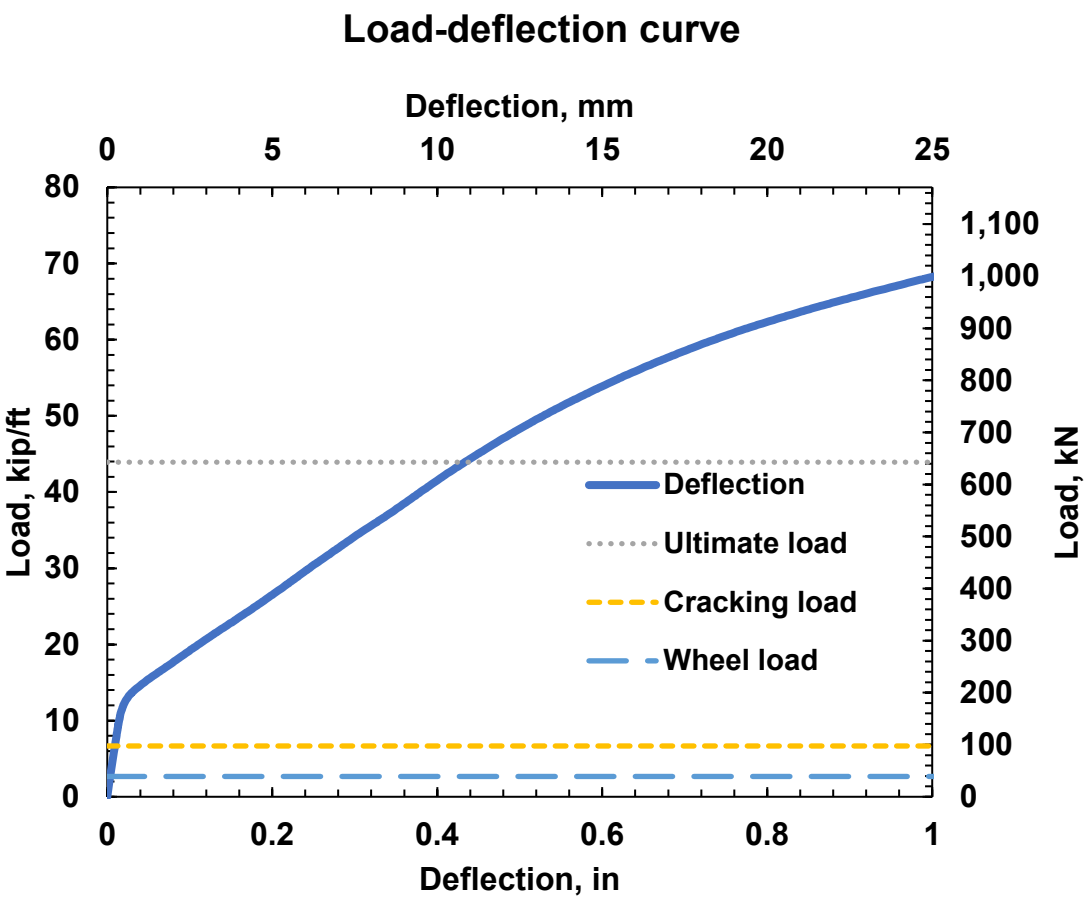

Figure 148: Load-deflection curve of specimen S1.

7 Statistical Evaluation of Flexural Capacity

The empirical equations were derived based on the parameters listed in Table 28 and the numerical results. The parametric study considers the specimen's span length, concrete compressive strength, and reinforcement amount. The parametric study results for each specimen include cracking load, nominal capacity, strain in BFRP, and deflection. The log-log linear regression method was used on the parametric study results to describe the effect of each parameter is discussed in the following sections.

7.1 Cracking Load

An empirical equation for predicting BFRP-bridge deck slabs cracking load is presented in Equation 1. Table 28 shows the details of the specimens, cracking load, and estimated cracking load. It reveals that Equation 21 can predict the specimen cracking load with a margin of error equal to 7% and an average ratio of FEA/Estimated cracking load equal to 1.00. Figure 149 shows the slab predicted cracking load against the FEA cracking load.

$$P_{cr} = 42.78\left(\frac{1}{L}\right)^{1.128}(f'_c)^{0.574}(\rho)^{-0.01928} \qquad \text{Equation (21)}$$

Table 28: Numerical and estimated values of cracking load.

Specimen	Span Length, L	f'_c	Trans. bar size	Trans. bar spacing	Long. bar size	Long. bar spacing	FEA Cracking load	Estimated cracking load	FEA/ Estimated
	ft	ksi	#	in	#	in	Kip/ft	Kip/ft	-
S1	6	4	6	4	5	6	13.7	13.6	0.99
S2	8	4	6	4	5	6	9.7	9.8	1.01
S3	10	4	6	4	5	6	7.7	7.6	0.99
S4	12	4	6	4	5	6	5.8	6.2	1.07
S5	14	4	6	4	5	6	5.5	5.2	0.95
S6	6	4	5	4	5	6	13.7	13.7	1.00
S7	6	4	6	6	5	6	13.7	13.7	1.00
S8	6	4	6	8	5	6	13.7	13.7	1.00
S9	6	4	6	4	5	12	13.7	13.6	0.99
S10	6	6	6	4	5	6	16.8	17.1	1.02
S11	6	8	6	4	5	6	20.4	20.2	0.99

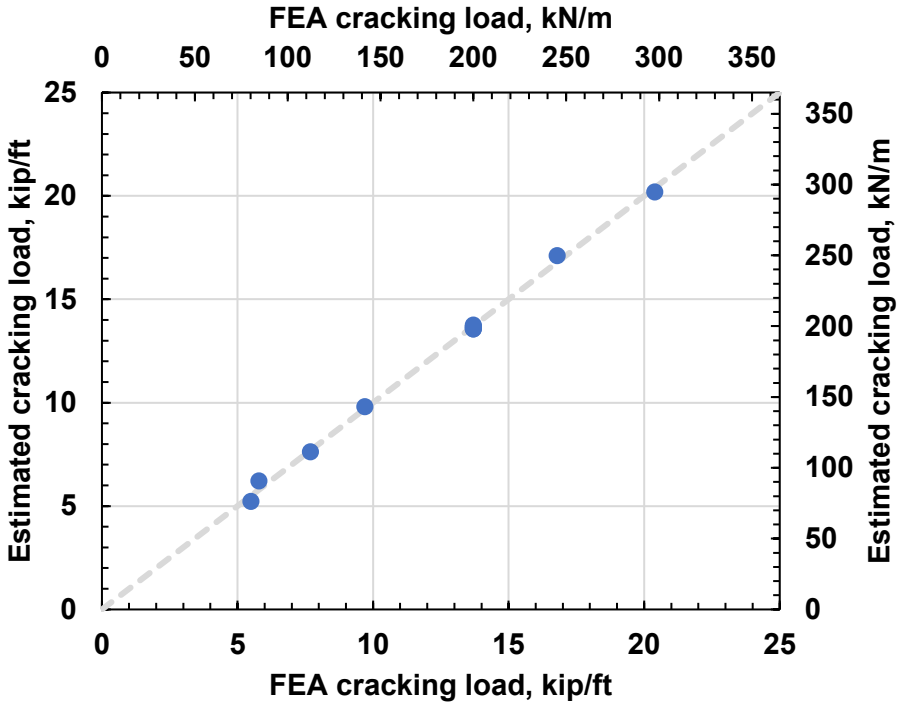

Figure 149: Predicted cracking load against FEA cracking load.

7.2 Nominal Capacity

An empirical equation for predicting BFRP-bridge deck slabs' nominal capacity is shown in Equation 22. Table 29 shows the specimen's details, nominal capacity, and estimated nominal capacity. It reveals that Equation 22 can predict the specimen's nominal capacity with a margin of error equal to 4% and an average ratio of FEA/Estimated nominal capacity equal to 1.00. Figure 150 shows the slab predicted nominal capacity against the FEA nominal capacity.

$$P_n = 552..55\left(\frac{1}{L}\right)^{0.940}(f'_c)^{0.351}(\rho)^{0.265} \qquad \text{Equation (22)}$$

Table 29: Numerical and estimated values of Nominal capacity.

Specimen	Span Length, L	f'_c	Trans. Bar size	Trans. Bar spacing	Long. Bar size	Long. Bar spacing	FEA nominal capacity	Estimated nominal capacity	FEA/ Estimated
	ft	ksi	#	in	#	in	Kip/ft	Kip/ft	-
S1	6	4	6	4	5	6	58.5	58.8	1.01
S2	8	4	6	4	5	6	45.3	44.9	0.99
S3	10	4	6	4	5	6	36.7	36.4	0.99
S4	12	4	6	4	5	6	30.8	30.7	1.00
S5	14	4	6	4	5	6	26.2	26.5	1.01
S6	6	4	5	4	5	6	55.2	53.2	0.96
S7	6	4	6	6	5	6	52	52.8	1.02
S8	6	4	6	8	5	6	48.4	48.9	1.01
S9	6	4	6	4	5	12	57.4	58.8	1.02
S10	6	6	6	4	5	6	69.2	67.8	0.98
S11	6	8	6	4	5	6	74.1	75.0	1.01

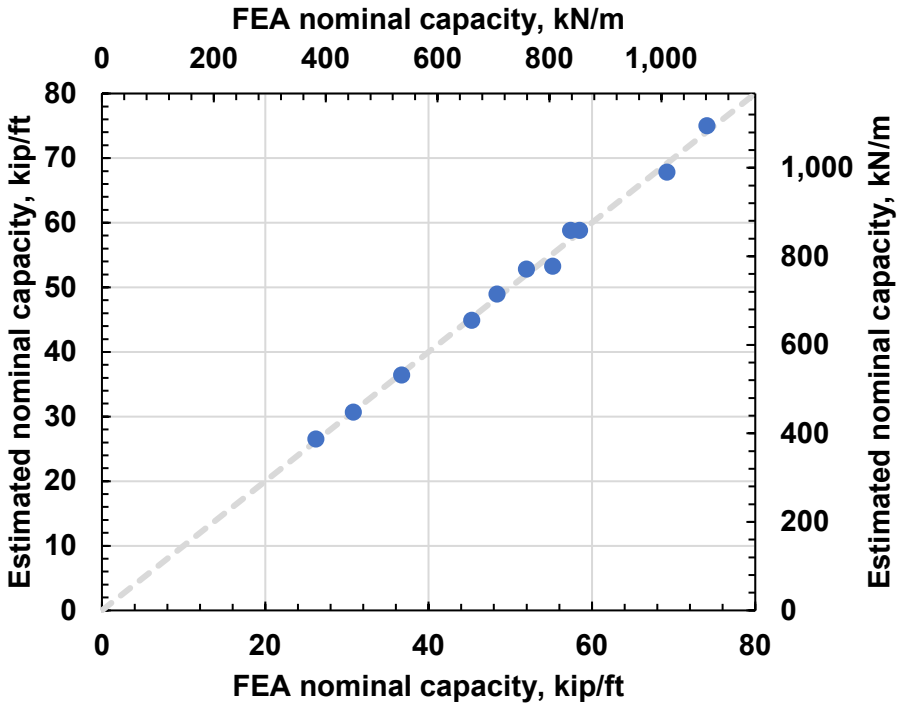

Figure 150: Predicted cracking load against FEA nominal capacity.

7.3 Nominal Moment Capacity

The nominal capacity of the slabs is calculated using the stress values in the BFRP reinforcement. The nominal moment capacity is calculated as follows:

$$M_n = A_f f_f * (d - \frac{a}{2})$$ AASHTO GFRP (2.6.3.2.2-1)

In which:

$$a = \frac{A_f f_f}{0.85 f'_c b}$$

Where

A_f = area of BFRP reinforcement.

f_f = stress in BFRP reinforcement obtained from the FEA modeling.

d = distance from extreme compression fiber to centroid of tensile reinforcement.

f'_c = specified compressive strength of concrete.

An empirical equation for predicting BFRP-bridge deck slabs' nominal moment capacity is presented in Equation 23. Table 30 shows the specimens' details, nominal moment capacity, and estimated nominal moment capacity. It reveals that Equation 23 can predict the specimen's nominal moment capacity with a margin of error equal to 8% and an average ratio of FEA/Estimated nominal capacity equal to 1.00. Figure 151 shows the predicted nominal moment capacity against the FEA nominal moment capacity.

$$M_n = 50.61 \left(\frac{1}{L}\right)^{0.170} (f'_c)^{0.379} (\rho)^{0.356}$$ Equation (23)

Table 30: Numerical and estimated values of nominal moment capacity.

Specimen	Span Length, L	f'_c	Trans. Bar size	Trans. Bar spacing	Long. Bar size	Long. Bar spacing	FEA M_n	Estimated M_n	FEA/ Estimated
	ft	ksi	#	in	#	in	Kip × ft/ft	Kip × ft/ft	-
S1	6	4	6	4	5	6	28.15	28.69	1.02
S2	8	4	6	4	5	6	32.73	30.13	0.92
S3	10	4	6	4	5	6	31.14	31.29	1.00
S4	12	4	6	4	5	6	31.78	32.28	1.02
S5	14	4	6	4	5	6	32.73	33.14	1.01
S6	6	4	5	4	5	6	26.42	25.10	0.95
S7	6	4	6	6	5	6	24.48	24.83	1.01
S8	6	4	6	8	5	6	21.98	22.41	1.02
S9	6	4	6	4	5	12	27.11	28.69	1.06
S10	6	6	6	4	5	6	34.11	33.46	0.98
S11	6	8	6	4	5	6	36.89	37.32	1.01

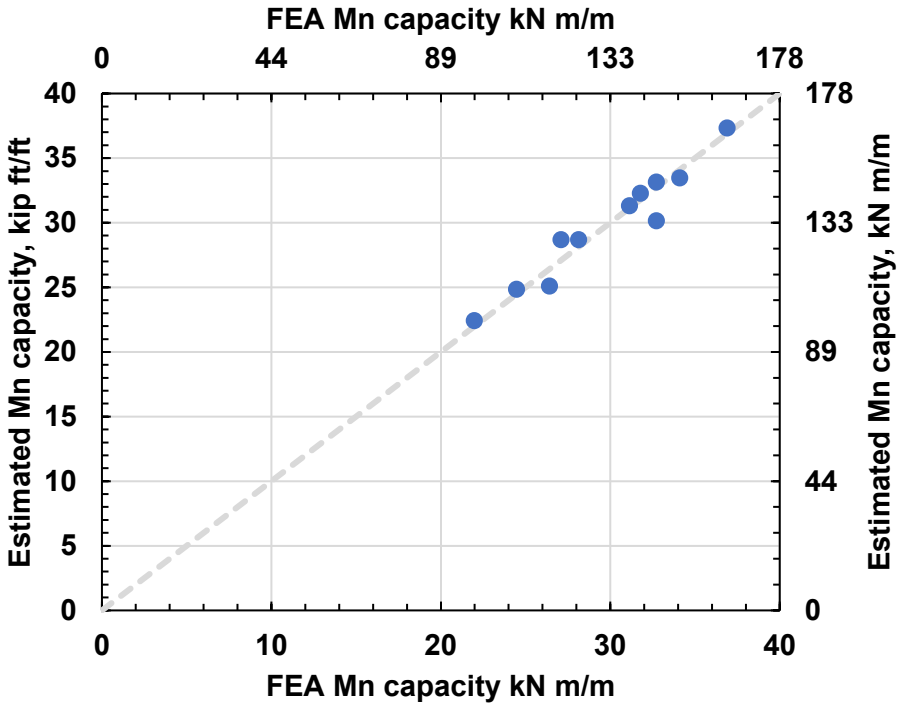

Figure 151: Predicted cracking load against FEA nominal moment capacity.

7.4 Strain in BFRP at Nominal Load

An empirical equation for predicting BFRP-bridge deck slabs strain in BFRP is presented in Equation 24. Table 31 shows the specimens details, strain in BFRP, and estimated strain in BFRP. It reveals that the equation can predict the specimen's strain in BFRP at nominal capacity with a margin of error equal to 10% and with an average ratio of FEA/Estimated equal to 1.00. Figure 152 shows the predicted strain against the FEA strain.

$$\varepsilon_f = 0.00033\left(\frac{1}{L}\right)^{-0.220}(f'_c)^{0.280}(\rho)^{-0.570} \qquad \text{Equation (24)}$$

Table 31: Numerical and estimated values of strain in BFRP at nominal load.

Specimen	Span Length, L	f'_c	Trans. Bar size	Trans. Bar spacing	Long. Bar size	Long. Bar spacing	FEA Strain in BFRP	Estimated Strain in BFRP	FEA/ Estimated
	ft	ksi	#	in	#	in	-	-	-
S1	6	4	6	4	5	6	0.0067	0.0068	1.02
S2	8	4	6	4	5	6	0.0081	0.0073	0.90
S3	10	4	6	4	5	6	0.0076	0.0076	1.01
S4	12	4	6	4	5	6	0.0078	0.0080	1.02
S5	14	4	6	4	5	6	0.0081	0.0082	1.02
S6	6	4	5	4	5	6	0.0088	0.0085	0.96
S7	6	4	6	6	5	6	0.0085	0.0086	1.01
S8	6	4	6	8	5	6	0.0100	0.0101	1.01
S9	6	4	6	4	5	12	0.0064	0.0068	1.07
S10	6	6	6	4	5	6	0.0078	0.0077	0.98
S11	6	8	6	4	5	6	0.0082	0.0083	1.01

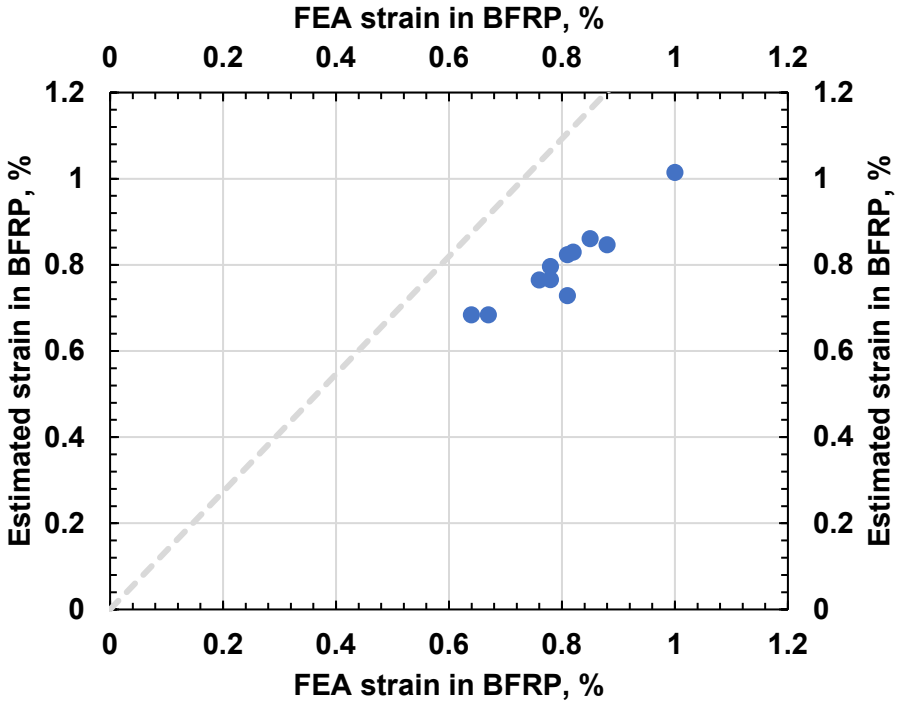

Figure 152: Predicted cracking load against FEA strain in BFRP.

7.5 Load at Maximum allowable crack width (Service Limit)

An empirical equation for predicting BFRP-bridge deck slabs load at maximum allowable crack is presented in Equation 25. Table 32. Shows the specimens details, Load and estimated load at maximum allowable crack width. It reveals that Equation 25 can predict the load at maximum allowable crack width with a margin of error equal to 8% and with an average ratio of FEA/Estimated nominal capacity equal to 1.00. Figure 153 shows the predicted loads against the FEA strain.

$$P_{ac} = 1685.6\left(\frac{1}{L}\right)^{1.041}(f'_c)^{0.311}(\rho)^{0.702} \qquad \text{Equation (25)}$$

Table 32: Numerical and estimated values of Load at Maximum allowable crack width.

Specimen	Span Length, L	f'_c	Trans. bar size	Trans. bar spacing	Long. bar size	Long. bar spacing	Service Limit Load	Estimated Service Limit Load	FEA/ Estimated
	ft	ksi	#	in	#	in	-	-	-
S1	6	4	6	4	5	6	26.5	26.3	0.99
S2	8	4	6	4	5	6	18.8	19.5	1.04
S3	10	4	6	4	5	6	15.7	15.4	0.98
S4	12	4	6	4	5	6	13.2	12.8	0.97
S5	14	4	6	4	5	6	10.6	10.9	1.03
S6	6	4	5	4	5	6	21.3	20.2	0.95
S7	6	4	6	6	5	6	18.3	19.8	1.08
S8	6	4	6	8	5	6	16.4	16.1	0.98
S9	6	4	6	4	5	12	26.5	26.3	0.99
S10	6	6	6	4	5	6	29.8	29.8	1.00
S11	6	8	6	4	5	6	32.5	32.6	1.00

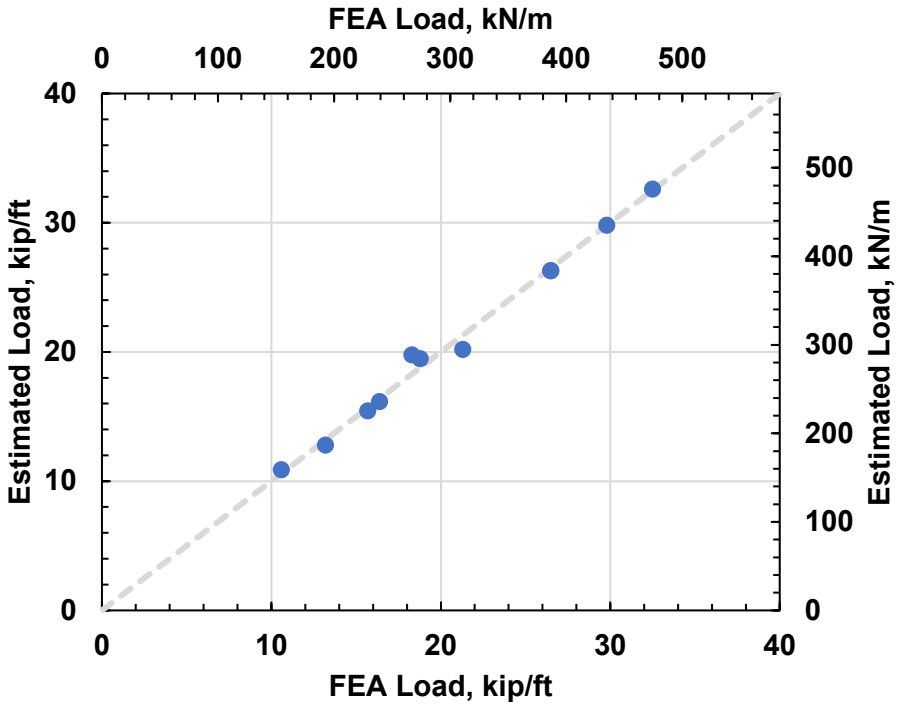

Figure 153: Predicted load at maximum allowable crack width against FEA results.

7.6 Load at Creep Rupture Stress Limit

An empirical equation for predicting BFRP-bridge deck slabs Load at creep rupture stress limit is presented in Equation 26. Table 33. shows the specimens details, load and load estimated load at creep rupture stress limit. It reveals that Equation 26 can predict the load at creep limit with a margin of error equal to 4% and with an average ratio of FEA/Estimated nominal capacity equal to 1.00. Figure 154 shows the predicted strain against the FEA strain.

$$\varepsilon_f = 0.00033\left(\frac{1}{L}\right)^{-0.220}(f'_c)^{0.280}(\rho)^{-0.570} \qquad \text{Equation (26)}$$

Table 33: Numerical and estimated values of load at creep rupture stress limit.

Specimen	Span Length, L	f'_c	Trans. bar size	Trans. bar spacing	Long. bar size	Long. bar spacing	Load Creep Rupture	Estimated	FEA/ Estimated
	ft	ksi	#	in	#	in	-	-	-
S1	6	4	6	4	5	6	-	56.1	-
S2	8	4	6	4	5	6	40.3	42.0	0.96
S3	10	4	6	4	5	6	34.0	33.5	1.02
S4	12	4	6	4	5	6	28.6	27.8	1.03
S5	14	4	6	4	5	6	23.4	23.8	0.98
S6	6	4	5	4	5	6	44.4	44.2	1.01
S7	6	4	6	6	5	6	43.5	43.3	1.00
S8	6	4	6	8	5	6	35.9	36.0	1.00
S9	6	4	6	4	5	12	-	56.1	-
S10	6	6	6	4	5	6	63.8	65.0	1.03
S11	6	8	6	4	5	6	65.5	66.6	0.98

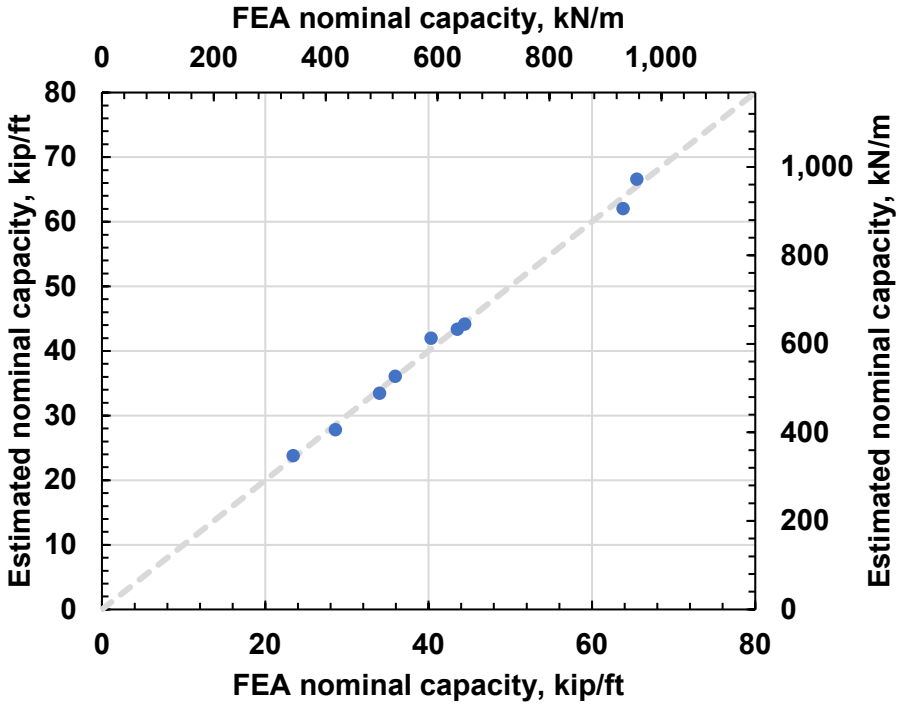

Figure 154: Predicted loads against the FEA strain in BFRP.

7.7 Deflection

An empirical equation for predicting BFRP-bridge deck slabs deflection is presented in Equation 27. Table 34 shows the specimens details, deflection, and estimated deflection. It reveals that Equation 27 can predict the specimen's deflection at nominal capacity with a margin of error equal to 10% and with an average ratio of FEA/Estimated deflection equal to 1.00. Figure 155 shows the predicted strain against the FEA strain.

$$\Delta = 0.007\left(\frac{1}{L}\right)^{-1.743}(f'_c)^{0.202}(\rho)^{-0.269} \qquad \text{Equation (27)}$$

Table 34: Numerical and estimated values of deflection.

Specimen	Span Length, L	f'_c	Trans. bar size	Trans. bar spacing	Long. bar size	Long. bar spacing	FEA deflection	Estimated Deflection	FEA/ Estimated
	ft	ksi	#	in	#	in	in	in	-
S1	6	4	6	4	5	6	0.59	0.61	1.03
S2	8	4	6	4	5	6	1.07	1.00	0.94
S3	10	4	6	4	5	6	1.47	1.48	1.01
S4	12	4	6	4	5	6	2.03	2.04	1.00
S5	14	4	6	4	5	6	2.63	2.67	1.01
S6	6	4	5	4	5	6	0.71	0.67	0.95
S7	6	4	6	6	5	6	0.65	0.68	1.04
S8	6	4	6	8	5	6	0.73	0.73	1.00
S9	6	4	6	4	5	12	0.60	0.61	1.01
S10	6	6	6	4	5	6	0.66	0.66	1.00
S11	6	8	6	4	5	6	0.70	0.70	1.00

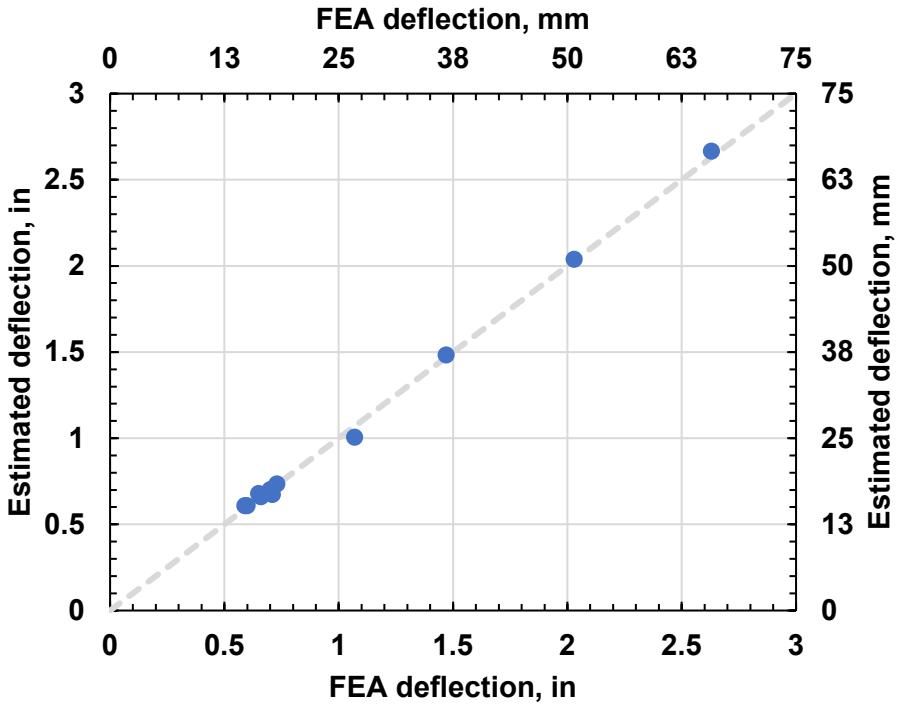

Figure 155: Predicted cracking load against FEA deflection.

8 Design Aids Based on AASHTO Table A4-1

Design aids are generated to ease designing standard FRP-reinforced bridge deck slabs based on AASHTO LRFD Bridge Design Guide Specifications for GFRP-Reinforced Concrete. The standard deck is defined as a deck slab on longitudinal beams with main reinforcement placed perpendicular to traffic. The design procedure is based on limit state design principles where structural components shall be proportioned to satisfy the requirements at all appropriate service, fatigue and creep rupture, strength, and extreme event limit states. The Traditional Design Method for deck slabs is based on flexure as outlined in Article 3.7.3 in AASHTO GFRP. The traditional Design Method permits the approximate elastic and refined analysis methods specified in Articles 4.6.2.1 and 4.6.3.2 of the AASHTO LRFD.

In a standard deck, two components are designed. Positive moment (bottom of slab transverse) reinforcement and negative moment (top of slab transverse) reinforcement are designed for the approximate method. These moments are calculated using the Approximate Elastic or "Strip" Method as applied to concrete slabs supported on parallel supports. Table A4-1 in APPENDIX A4 of AASHTO LRFD is used to generate the design aids. Longitudinal reinforcement in the standard slab is not designed. The top longitudinal reinforcement needs only satisfy the shrinkage and temperature requirements (5.10.6). The bottom longitudinal area is a percentage of the bottom transverse reinforcement (9.7.3.2). The maximum percentage is 67% for all bridges with beam spacing within the limits of the standard deck design charts.

In this chapter, the generated design aids are based on parameter values illustrated in the Table 35:

Table 35 Parameter's value used in design aids.

Parameter	Value
Slab Thickness	8 in
Concrete Compressive strength	4000 psi
Bar Modulus of Elasticity	8500 ksi
Bar Size	#5
Reinforcement Bottom Clear Cover	1in
Reinforcement Top Clear Cover	2.25in

8.1 Applied Loads

The applied moment on the standard bridge deck is due to the slab self-weight, slab future wearing and utilities, and HL93 truck loading. The applied moment due to slab self-weight and future wearing surface are calculated based on the IDOT bridge manual as follows:

$$M_{DC1} = \frac{1}{10} w_{DC1} L^2$$

$$M_{DW} = \frac{1}{10} w_{DW} L^2$$

Where:

w_{DC} = dead load of structural components (DC1) and non-structural attachments (DC2). Standard deck slabs are not designed for DC2 loading.

w_{DW} = dead load of future wearing surface, taken as 50 psf for IDOT bridge deck design.

L = center to center beam spacing for positive moment calculation. For negative moment calculation, L is taken as that defined in Bridge Manual Figure 3.2.1-2, which is shown below in Figure 156.

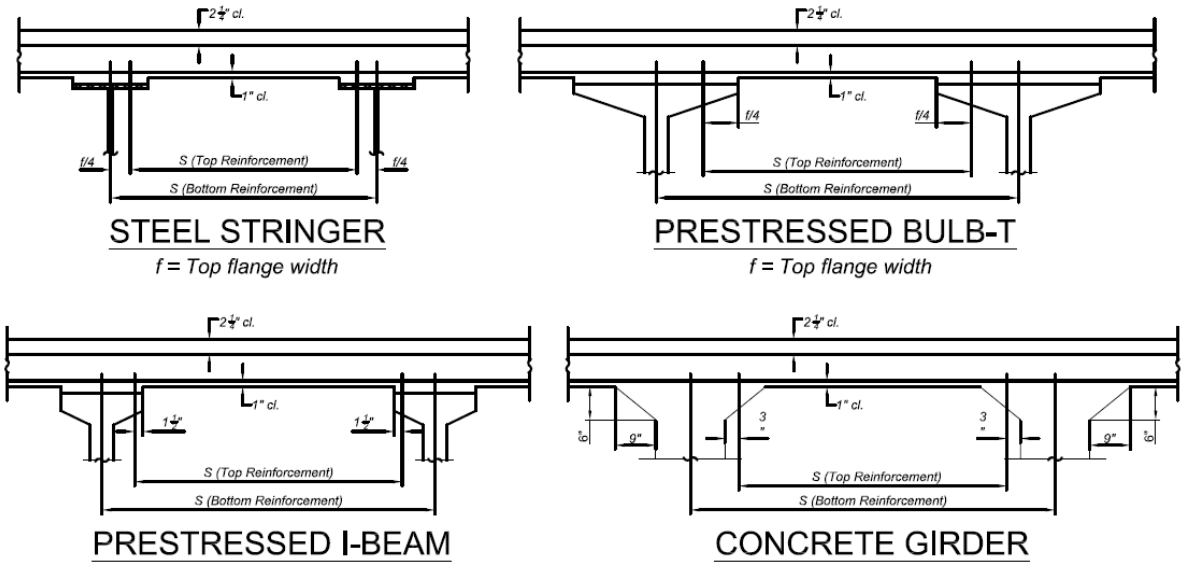

Figure 156: Design span definitions for LRFD slab design (Bridge Manual).

HL 93 truck loading is calculated using Table A4-1 from AASHTO LRFD:

Table A4-1 Maximum Live Load Moment per Unit Width, kip-ft/ft

S	Positive Moment	Negative Moment						
		Distance from CL of Girder to Design Section for Negative Moment						
		0.0 in.	3 in.	6 in.	9 in.	12 in.	18 in.	24 in.
4 ft -0 in.	4.68	2.68	2.07	1.74	1.60	1.50	1.34	1.25
4 ft -3 in.	4.66	2.73	2.25	1.95	1.74	1.57	1.33	1.20
4 ft -6 in.	4.63	3.00	2.58	2.19	1.90	1.65	1.32	1.18
4 ft -9 in.	4.64	3.38	2.90	2.43	2.07	1.74	1.29	1.20
5 ft -0 in.	4.65	3.74	3.20	2.66	2.24	1.83	1.26	1.12
5 ft -3 in.	4.67	4.06	3.47	2.89	2.41	1.95	1.28	0.98
5 ft -6 in.	4.71	4.36	3.73	3.11	2.58	2.07	1.30	0.99
5 ft -9 in.	4.77	4.63	3.97	3.31	2.73	2.19	1.32	1.02
6 ft -0 in.	4.83	4.88	4.19	3.50	2.88	2.31	1.39	1.07
6 ft -3 in.	4.91	5.10	4.39	3.68	3.02	2.42	1.45	1.13
6 ft -6 in.	5.00	5.31	4.57	3.84	3.15	2.53	1.50	1.20
6 ft -9 in.	5.10	5.50	4.74	3.99	3.27	2.64	1.58	1.28
7 ft -0 in.	5.21	5.98	5.17	4.36	3.56	2.84	1.63	1.37
7 ft -3 in.	5.32	6.13	5.31	4.49	3.68	2.96	1.65	1.51
7 ft -6 in.	5.44	6.26	5.43	4.61	3.78	3.15	1.88	1.72
7 ft -9 in.	5.56	6.38	5.54	4.71	3.88	3.30	2.21	1.94
8 ft -0 in.	5.69	6.48	5.65	4.81	3.98	3.43	2.49	2.16
8 ft -3 in.	5.83	6.58	5.74	4.90	4.06	3.53	2.74	2.37
8 ft -6 in.	5.99	6.66	5.82	4.98	4.14	3.61	2.96	2.58
8 ft -9 in.	6.14	6.74	5.90	5.06	4.22	3.67	3.15	2.79
9 ft -0 in.	6.29	6.81	5.97	5.13	4.28	3.71	3.31	3.00
9 ft -3 in.	6.44	6.87	6.03	5.19	4.40	3.82	3.47	3.20
9 ft -6 in.	6.59	7.15	6.31	5.46	4.66	4.04	3.68	3.39
9 ft -9 in.	6.74	7.51	6.65	5.80	4.94	4.21	3.89	3.58
10 ft -0 in.	6.89	7.85	6.99	6.13	5.26	4.41	4.09	3.77
10 ft -3 in.	7.03	8.19	7.32	6.45	5.58	4.71	4.29	3.96
10 ft -6 in.	7.17	8.52	7.64	6.77	5.89	5.02	4.48	4.15
10 ft -9 in.	7.32	8.83	7.95	7.08	6.20	5.32	4.68	4.34
11 ft -0 in.	7.46	9.14	8.26	7.38	6.50	5.62	4.86	4.52
11 ft -3 in.	7.60	9.44	8.55	7.67	6.79	5.91	5.04	4.70
11 ft -6 in.	7.74	9.72	8.84	7.96	7.07	6.19	5.22	4.87
11 ft -9 in.	7.88	10.01	9.12	8.24	7.36	6.47	5.40	5.05
12 ft -0 in.	8.01	10.28	9.40	8.51	7.63	6.74	5.56	5.21
12 ft -3 in.	8.15	10.55	9.67	8.78	7.90	7.02	5.75	5.38
12 ft -6 in.	8.28	10.81	9.93	9.04	8.16	7.28	5.97	5.54
12 ft -9 in.	8.41	11.06	10.18	9.30	8.42	7.54	6.18	5.70
13 ft -0 in.	8.54	11.31	10.43	9.55	8.67	7.79	6.38	5.86
13 ft -3 in.	8.66	11.55	10.67	9.80	8.92	8.04	6.59	6.01
13 ft -6 in.	8.78	11.79	10.91	10.03	9.16	8.28	6.79	6.16
13 ft -9 in.	8.90	12.02	11.14	10.27	9.40	8.52	6.99	6.30
14 ft -0 in.	9.02	12.24	11.37	10.50	9.63	8.76	7.18	6.45
14 ft -3 in.	9.14	12.46	11.59	10.72	9.85	8.99	7.38	6.58
14 ft -6 in.	9.25	12.67	11.81	10.94	10.08	9.21	7.57	6.72
14 ft -9 in.	9.36	12.88	12.02	11.16	10.30	9.44	7.76	6.86
15 ft -0 in.	9.47	13.09	12.23	11.37	10.51	9.65	7.94	7.02

8.2 Service Limit State

Then, Service I load combination is defined as:

$$M_{ServiceI} = 1.00M_{DC} + 1.00M_{DW} + 1.00M_{LL+IM}$$ AASHTO LRFD (Table 3.4.1-1)

The strain in FRP reinforcement due to Service I load combination is calculated as:

$$f_{f,s} = \frac{n_f * d * (1-k)}{I_{cr}} * M_{ServiceI}$$ AASHTO GFRP (2.5.4-2)

As per AASHTO GFRP Article 2.6.3.2, the slab design should satisfy:

$$s \leq \min\left(1.15\frac{C_b E_f w}{f_{f,s}} - 2.5c_c\ ;\ 0.92\frac{C_b E_f w}{f_{f,s}}\right) \leq \min\left(1.5d, 18in\right)$$ AASHTO GFRP (2.6.7-1)

Where

s = average spacing of reinforcement in layer closest to tension face (in).

E_f = tensile modulus of elasticity of Reinforcement (ksi).

$f_{f,s}$ = Calculated tensile stress in reinforcement at the service limit state (ksi).

c_c = Clear cover (in).

C_b = Reduction factor that accounts for the degree of bond between the reinforcement and the surrounding concrete.

w = maximum concrete crack width limit in concrete components, which is set as 0.028 (in).

Then, a design aid is generated and shown in Figure 157. The x-axis represents span length, and the y-axis represents the maximum spacing of #5 BFRP bars.

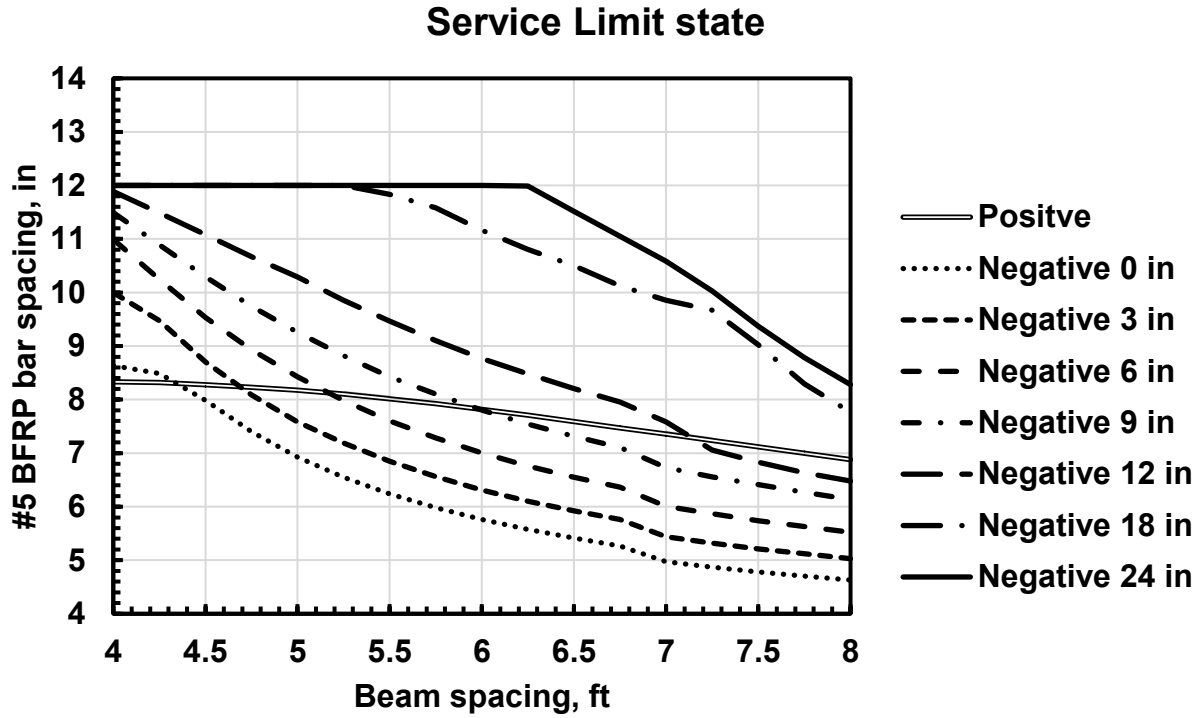

Figure 157: Service limit state design aids of #5 BFRP bar using Table A4-1 of AASHTO cade.

8.3 Strength Limit State

As per AASHTO GFRP Article 2.6.3.2, the slab design should satisfy:

$$\emptyset M_n \geq M_u$$

In which:

M_n = nominal flexural resistance

$\emptyset$ = resistance factor

M_u = applied moment calculated using Strength I load combination

The nominal flexural strength M_n of BFRP-reinforced bridge deck slabs is calculated based on force equilibrium and strain compatibility consideration.

$$M_n = A_f f_f (d - \frac{a}{2})$$ AASHTO GFRP (2.6.3.1-1)

Then, Strength I load combination is defined as:

$$M_{StrengthI} = \gamma_p M_{DC} + \gamma_p M_{DW} + 1.75 M_{LL+IM}$$ AASHTO LRFD (Table 3.4.1-1)

Where γ_p equals to 1.25 for M_{DC} and 1.5 for M_{DW}.

After equating $\emptyset M_n$ to $M_{StrengthI}$, a chart is developed for designing the BFRP-bridge deck slabs. The strength limit state design chart is shown in Figure 158. The x-axis represents span length, and the y-axis represents the maximum spacing of #5 BFRP bars.

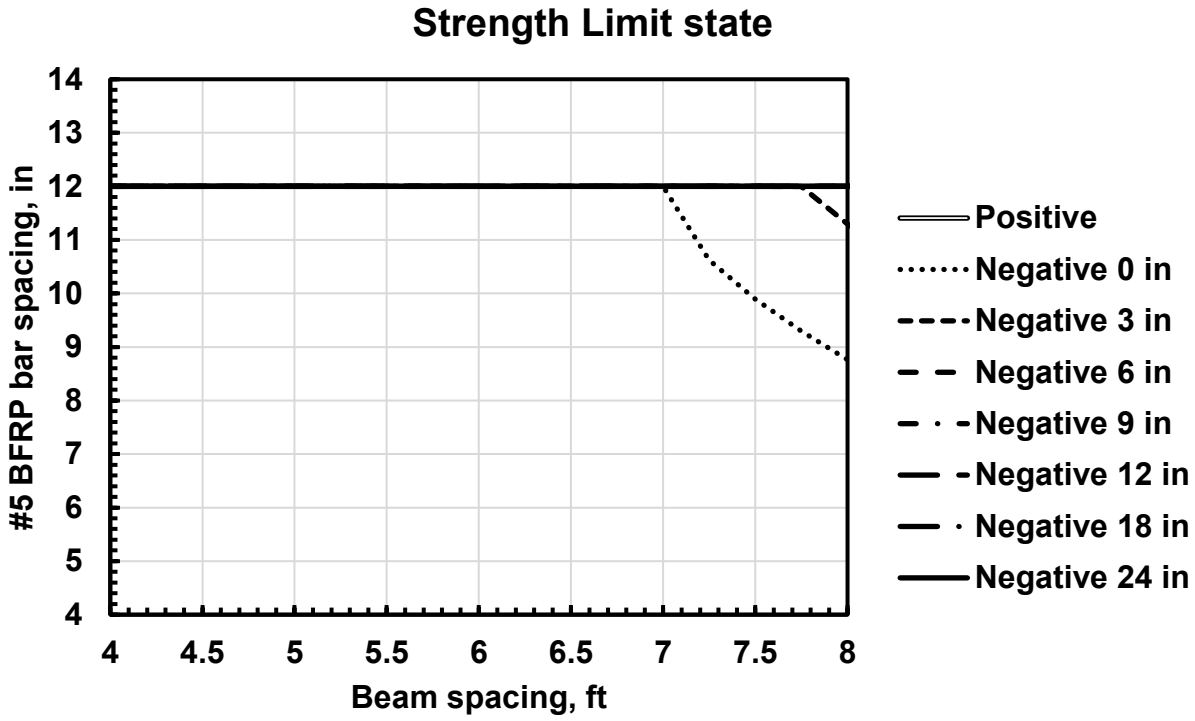

Figure 158: Strength limit design aid of #5 BFRP bar using Table A4-1 from AASHTO cade.

8.4 Creep Rupture Limit State

Then, Service I load combination is defined as:

$$M_{Creep-Rupture} = 1.00 M_{DC} + 1.00 M_{DW} + 0.20 M_{LL+IM}$$

The strain in FRP reinforcement due to Service I load combination is calculated as:

$$f_{f,c} = \frac{n_f * d * (1-k)}{I_{cr}} * M_{Creep-Rupture}$$ AASHTO GFRP (2.5.4-2)

Where:

C_c = creep reduction factor

n_f = modular ratio

d = distance from extreme compression fiber to centroid of tensile reinforcement (in)

k = ratio of depth of neutral axis to reinforcement depth.

I_{cr} = moment of inertia of transformed cracked section (in4).

M_{Creep} = moment due to dead loads and sustained portion of live loads included in Service I load combination (kip-in).

In which:

$$k = \sqrt{2\rho_f * n_f + (\rho_f * n_f)^2} - \rho_f * n_f$$ AASHTO GFRP (2.5.3-4)

$$I_{cr} = \frac{b * d^3}{3} k^3 + n_f * A_f * (d - k * d)$$ AASHTO GFRP (2.5.3-3)

As per AASHTO GFRP Article 2.6.3.2, the slab design should satisfy:

$$f_{f,f} \leq C_c * f_{fd}$$ AASHTO GFRP (2.5.4-1)

Then, a design aid is generated and shown in Figure 159. The x-axis represents span length, and the y-axis represents the maximum spacing of #5 BFRP bars.

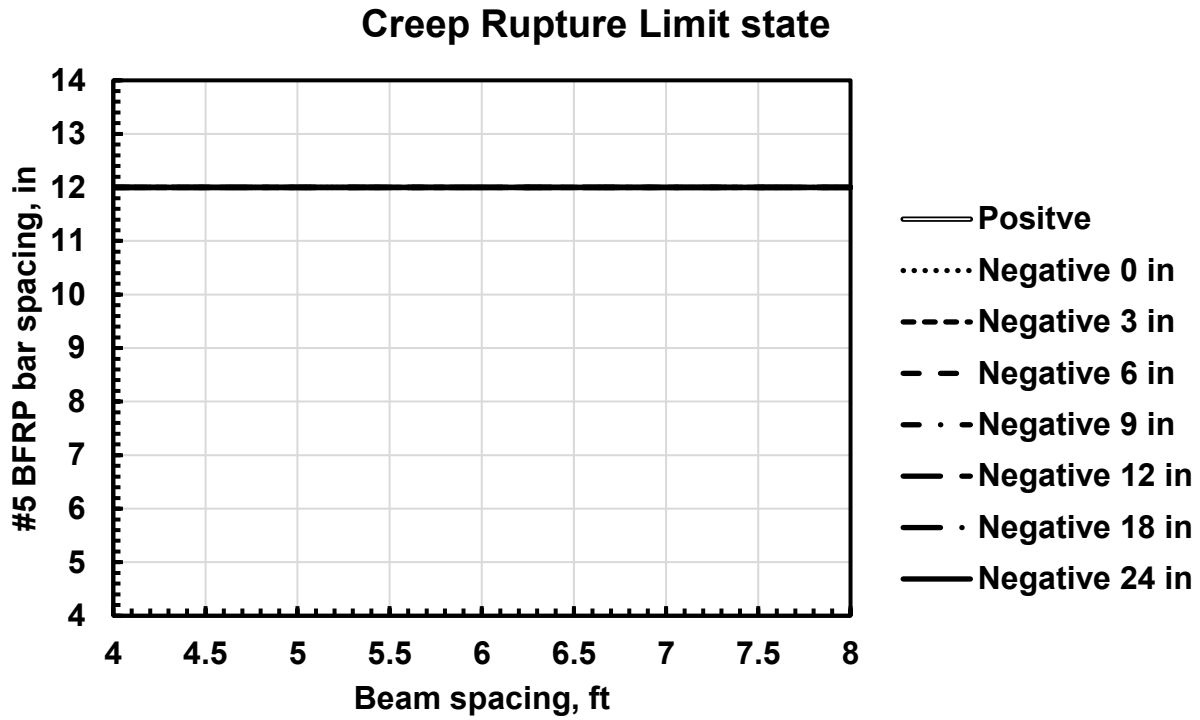

Figure 159: Creep rupture limit design aid of #5 BFRP bar using Table A4-1 from AASHTO cade.

8.5 Conclusions

The design aids for BFRP for designing reinforced concrete bridge deck slab were generated to satisfy the service, strength, and creep rupture limit states. The service limit state governed the design of the standard slab reinforced with the design parameters considered in this study. The maximum spacing controlled the strength limit state for span lengths between 4 ft to 7 ft. The Creep rupture limit state was controlled by the maximum spacing for any span length.

9 Design Aids Based on Numerical Analysis

AASHTO GFRP (2018) allows two design processes: Empirical design and Traditional design. The Empirical design is based on a complex internal membrane stress state referred to as internal arching while the traditional design process is based on the flexure. The Traditional design method allows determining the live load force effect based on the approximate method (AASHTO LRFD Article 4.6.2.1) or the refined methods (AASHTO LRFD Article 4.6.3.2). The finite element analysis of the FRP-reinforced concrete bridge deck slabs in Chapter 5 is an acceptable method of analysis since it satisfies the requirements of equilibrium and compatibility and utilizes stress-strain diagrams for the proposed materials. Therefore, the results from the numerical evaluation of the flexural capacity are utilized to generate design aids based on the limit states.

9.1 Service Limit State

As mentioned in Section 7.5 from this document, the load at maximum allowable crack width is defined
as:

$$P_{ac} = 1685.6\left(\frac{1}{L}\right)^{1.041}(f'_c)^{0.311}(\rho)^{0.702}$$

As per AASHTO GFRP Article 2.6.3.2, the slab design should satisfy:

$$P_{ServiceI} = 1.00P_{DC} + 1.00P_{DW} + 1.00P_{LL+IM}$$ AASHTO LRFD (Table 3.4.1-1)

Then, a design aid is generated and shown in Figure 160. The x-axis represents span length, and the y-axis represents the maximum spacing of #5 BFRP bars.

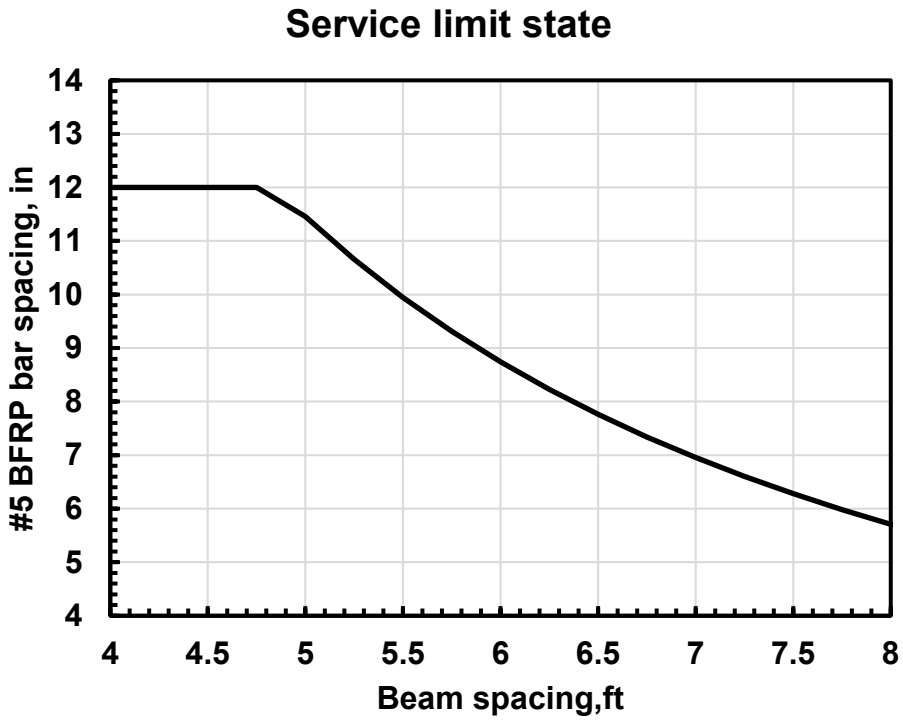

Figure 160: Service limit design aid of #5 BFRP bar using NLFEA.

9.2 Strength Limit State

The nominal flexural strength M_n of BFRP-reinforced bridge deck slabs is calculated based on nonlinear finite element analysis.

$$M_n = 50.61\left(\frac{1}{L}\right)^{0.170}(f'_c)^{0.379}(\rho)^{0.356}$$ AASHTO LRFD (Table 3.4.1-1)

Then, Strength I load combination is defined as:

$$M_{StrengthI} = \gamma_p M_{DC} + \gamma_p M_{DW} + 1.75M_{LL+IM}$$ AASHTO LRFD (Table 3.4.1-1)

Where γ_p equals to 1.25 for M_{DC} and 1.5 for M_{DW}.

Then, a design aid is generated and shown in Figure 161. The x-axis represents span length, and the y-axis represents the maximum spacing of #5 BFRP bars.

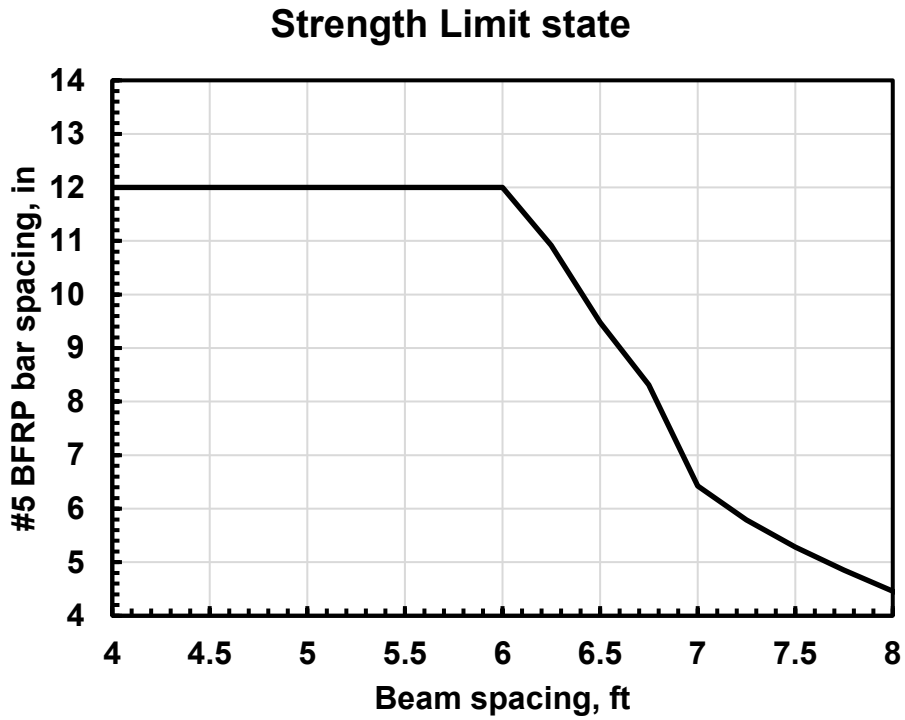

Figure 161: Strength limit design aid of #5 BFRP bar using NLFEA.

9.3 Creep Rupture Limit State

As mentioned in Section 7.6 from this document, the load at Creep Rupture Limit is defined
as:

$$P_{ac} = 1685.6\left(\frac{1}{L}\right)^{1.041}(f'_c)^{0.311}(\rho)^{0.702}$$

As per AASHTO GFRP Article 2.6.3.2, the slab design should satisfy:

$$P_{ServiceI} = 1.00P_{DC} + 1.00P_{DW} + 0.2P_{LL+IM}$$

Then, a design aid is generated and shown in Figure 162. The x-axis represents span length, and the y-axis represents the maximum spacing of #5 BFRP bars.

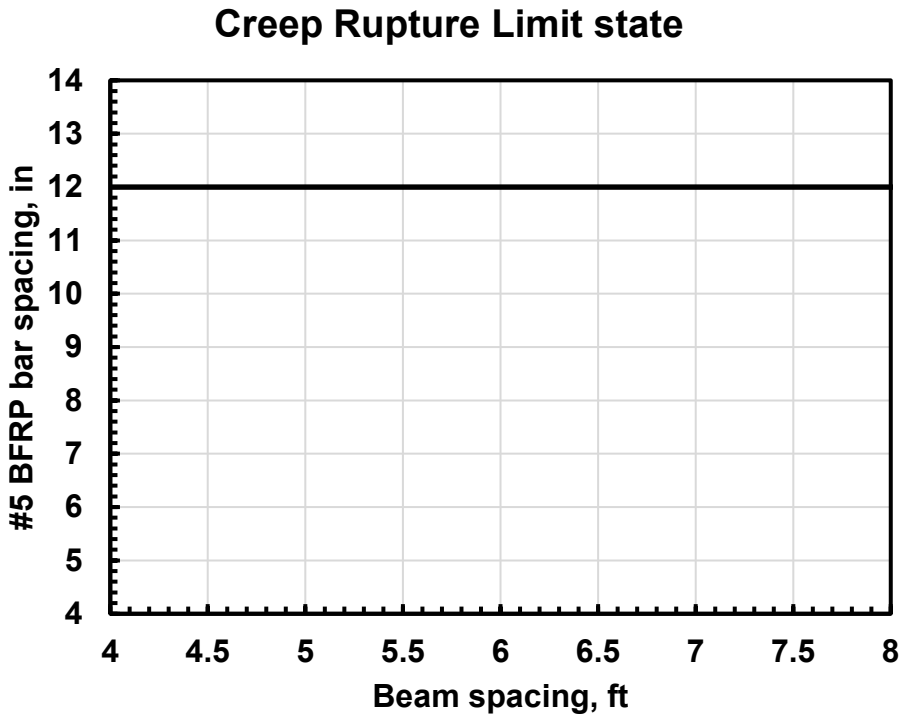

Figure 162: Creep rupture limit design aid of #5 BFRP bar using NLFEA.

9.4 Conclusion

The design aids for BFRP-reinforced concrete bridge deck slabs were generated based on the parametric study to satisfy the Service, Strength, and Creep rupture limit states. The service limit state was mostly governing the design of the standard slab reinforced with #5 BFRP bar especially for small beam spacing. In some cases, the strength limit state governed the design in long span regions.

The Creep rupture limit state was controlled by the maximum spacing for any span length. The minimum spacing of all considered limit states was plotted in Figure 163 for concrete strength of 4ksi, 5ksi, 6ksi, 7ksi, and 8ksi.

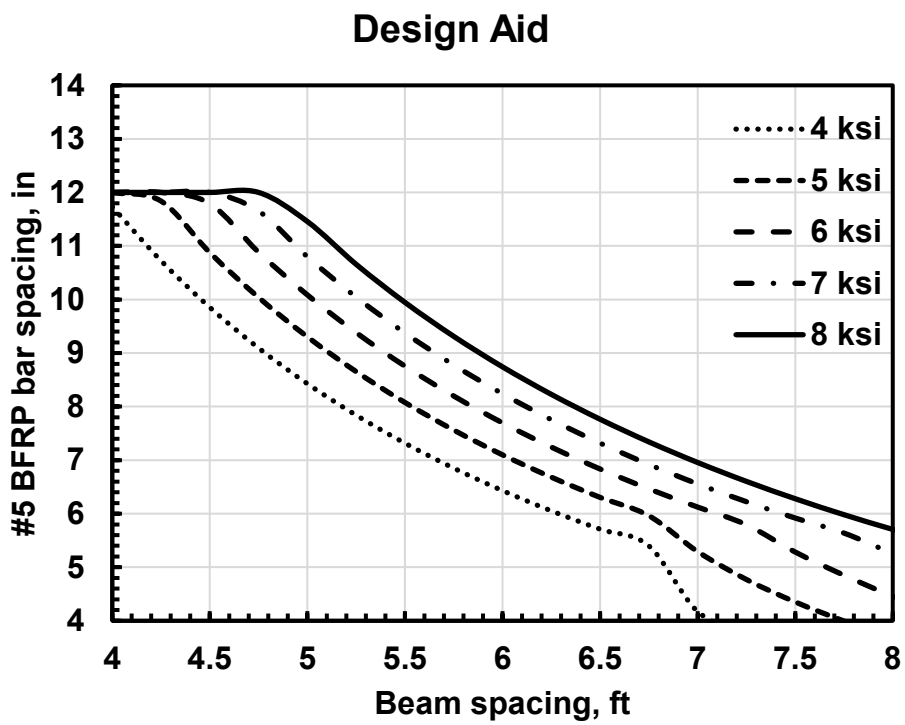

Figure 163: Creep rupture limit state design aid of #5 BFRP bars using NLFEA.

10 Life-Cycle Cost Analysis

Life-cycle cost analysis is used to study the cost efficiency of different alternatives in a certain project. In bridge construction projects, life-cycle cost analysis includes initial construction, inspection, maintenance, demolition, replacements, and user costs. Life-cycle cost analysis procedure is summarized as follows:

1. Define the project objectives.
2. Identify the project alternatives that satisfy the project objectives.
3. Estimate the cost and timing for all the activities that occur over the life cycle of the project.
4. Compute the project life-cycle costs of all alternatives.
5. Selection of the best alternative.

In this research study, BFRP bars are used as an alternative to regular mild steel reinforcement. A specific bridge construction project shall be selected to run the life cycle cost analysis. In order to run the analysis, full project information is required which includes the following: (1) description of the selected project, (2) traffic data, (3) schedule of initial construction activities of each alternative, (3) prices of initial construction activities of each alternative, (4) activity timing for Inspection, maintenance, and rehabilitation of the bridge of each alternative, and (5) activity costs for Inspection, maintenance, and rehabilitation of the bridge for each alternative. A higher initial construction cost for a bridge deck reinforced with BFRP bars is expected. However, due to the noncorrosive nature of the BFRP bars, less maintenance and rehabilitation activities are expected through the life cycle of the bridge deck. Therefore, it is expected that the life-cycle cost for the BFRP deck reinforcement alternative to be lower than the steel reinforcement alternative.

Since the cost of the bridge activities over its life cycle vary widely based on the project location, time, and size, determining the cost and time schedules of bridge activities over its life-cycle can be a challenge. Illinois department of transportation (IDOT) has a Transportation Bulletin Archive that contains a collection of transportation bulletins posted by IDOT since 2005. The archive contains final bidders list, corrected tabulation of bids, plans, proposals, and unit price tabulation of each bid. After selecting

a project by UIC and the peer review committee, the cost data is not available to run the bridge life-cycle cost analysis. The cost information of the BFRP bars could not be obtained due to the lack of the BFRP material cost from the manufacture.

11 Summary and Conclusions

This report documents the investigation of the mechanical properties of basalt fiber-reinforced polymer (BFRP) bars, finite element analysis, and fabrication and testing of single-span and two-span continuous bridge deck slabs. The tests were conducted according to ASTM standard test methods. Based on the test results, the following conclusions can be drawn:

1. The maximum tensile stress of BFRP increases with the decrease of BFRP bar size, while the modulus of elasticity increases with the increase of the BFRP bar size.
2. The maximum bond stress of BFRP bars obtained from the hinged beam did not show an effect of the bar size, while the pullout test reveals that the effect of bar size on the bond stress decreases with the increase of the bar size. This difference in the bond strength is due to the applied tensile load's misalignment after the beam starts to deflect.
3. The average transverse shear of the BFRP bar is 30 ksi, about 15% of the tensile strength with no effect of the bar size.
4. Freeze and thaw cycles have no significant effect on the tensile strength of BFRP bars.
5. Accelerated alkaline solution reveals a significant loss in the tensile strength of #5 bars, and a minor loss in #6 bar. The effect of aqueous solution decreases with the increase of bar size.
6. The predicted residual strength after the real exposure to harsh environmental aqueous solution for bars #5 and #6 are 53 and 87%, respectively.
7. The flexural-shear was the failure of the single-span and two-span bridge deck slabs.
8. After failure, the tested slabs were able to sustain a load of 40 kips and 80 kips for single-span and two-span bridge deck prototypes, respectively. No degradation was observed on the BFRP bars. The strains registered on the BFRP bars were about 20-30% of the ultimate strains.

9. The reinforcement ratio in the transverse direction at the top and bottom of the bridge deck slabs significantly affects the ultimate flexural-shear capacity of the bridge deck slab.
10. Deflection, crack-width, and strain in the BFRP reinforcement is also affected by the reinforcement ratio. The higher the reinforcement ratio, the less deflection, crack-width, and strain generated in the BFRP main reinforcement.
11. The slab continuity affects the slab ultimate capacity and increases its flexural-shear strength.
12. The proposed equation for predicting the ultimate strength capacity of the bridge deck slab yielded good results.
13. The experimental testing of the single-span and two-span continuous bridge deck slabs shows very good promising results for the use of BFRP bars as internal reinforcement in bridge decks.
14. The finite element analysis using ABAQUS shows very good promising results. The validation is done on limited number of tested specimens. The final validation was fully executed with a good correlation with the experimental results.
15. Design aids using BFRP bars in bridge decks based on the approximate method and the finite element analysis were developed based on #5 and #6 bars. The design aids are based on the service and ultimate limit states.
16. A MathCad document was developed for the design of standard bridge deck slabs reinforced with BFRP bars.
17. As a rule of thumb, the design is based on a maximum span to depth ratio less than or equal to 12 ($\ell/h \leq 12$).
    a. For #5 and #6 bars, the maximum spacing in the transverse direction at the positive moment region less than or equal to 6 and 8 inches, respectively.
    b. For #5 and #6 bars, the maximum spacing in the transverse direction at the negative moment region less than or equal to 5 and 6 inches, respectively.

c. For the distribution reinforcement, the amount of BFRP reinforcement is limited to two-thirds of the positive reinforcement.
d. The temperature and shrinkage reinforcement is limited to #5 at 12 inches.

12 Design Recommendations

After conducting an intensive experimental research program on bridge deck slabs reinforced with BFRP bars, development of design aids for bridge deck slabs using #5 and #6 BFRP bars and studying the AASHTO LRFD Bridge Design Guide Specifications for GFRP-Reinforced Concrete, the following design guidelines are summarized in Table 36.

Table 36: Design recommendations for BFRP-reinforced concrete bridge deck slabs

Span Length	Negative Moment Region		Positive Moment Region	
	#5 BFRP bars	#6 BFRP bars	#5 BFRP bars	#6 BFRP bars
4.0 ft.	10 in	12 in	8 in	10 in
4.5 ft.	8 in	10 in	8 in	10 in
5.0 ft.	7 in	9 in	8 in	10 in
5.5 ft.	6 in	8 in	8 in	9 in
6.0 ft.	6 in	8 in	7 in	9 in
6.5 ft.	6 in	7 in	7 in	9 in
7.0 ft.	5 in	6 in	7 in	9 in
7.5 ft	5 in	6 in	7 in	8 in
8.0 ft	5 in	6 in	6 in	8 in

As a rule of thumb, the design is based on a maximum span to depth ratio less than or equal to 12 ($\ell/h \leq 12$), the following bar spacings are recommended for bridge deck slabs reinforced with BFRP bars:

For bridge deck slab reinforced with #5 BFRP bars:

1. For negative moment region, maximum BFRP bar spacing of 5in in the transverse direction at the top of the bridge deck slab (#5 @ 5in or #6 @ 6in)
2. For positive moment region, maximum BFRP bar spacing of 6in in the transverse direction at the bottom of the bridge deck slab.
3. For distribution reinforcement (longitudinal bottom reinforcement), maximum BFRP bar spacing of 9in in the longitudinal direction at the bottom of the bridge deck slab.
4. For temperature and shrinkage reinforcement (longitudinal top reinforcement), maximum BFRP bar spacing of 18in in the longitudinal direction at the top of the bridge deck slab.

References

AASHTO. (2009). *American Association of State Highway and Transportation.*

Achillides, Z. (1998). *Bond behaviour of FRP bars in concrete.* University of Sheffield.

ACI 440.1R-15. (2015). American Concrete Institute.

Adhikari, S. (2009). *Mechanical properties and flexural applications of basalt fiber reinforced polymer (BFRP) bars.* University of Akron.

Atutis, E., Atutis, M., Budvytis, M., & Valivonis, J. (2017). Serviceability and Shear Response of RC Beams Prestressed with a Various Types of FRP Bars. *Procedia Engineering*. doi:10.1016/j.proeng.2017.02.017

Bakht, B., Al-Bazi, G., Banthia, N., Cheung, M., Erki, Mari, A., Faoro, M., . . . Tadros, G. (2000). Canadian Bridge Design Code provisions for fiber-reinforced structures. *Journal of Composites for Construction*. doi:10.1061/(ASCE)1090-0268(2000)4:1(3)

Banibayat, P., & Patnaik, A. (2015). Creep Rupture Performance of Basalt Fiber-Reinforced Polymer Bars. *Journal of Aerospace Engineering, 28*(3). doi:10.1061/(asce)as.1943-5525.0000391

Bank, L. (2007). *Composites for Construction: Structural Design with FRP Materials.* Composites for Construction: Structural Design with FRP Materials. doi:10.1002/9780470121429

Benmokrane, B., Tighiouart, B., & Chaallal, O. (1996). Bond strength and load distribution of composite GFRP reinforcing bars in concrete. *ACI Materials Journal*. doi:10.14359/9810

Bouguerra, K., Ahmed, E. A., El-Gamal, S., & Benmokrane, B. (2011). Testing of full-scale concrete bridge deck slabs reinforced with fiber-reinforced polymer (FRP) bars. *Construction and Building Materials*. doi:10.1016/j.conbuildmat.2011.04.028

Bradberry, T. (2001). Concrete bridge decks reinforced with fiber-reinforced polymer bars. *Transportation Research Record*. doi:10.3141/1770-13

Bradley, S. W., Puckett, P. M., Bradley, W. L., & Sue, H. J. (1998). Viscoelastic Creep Characteristics of Neat Thermosets and Thermosets Reinforced with E-Glass. *Journal of Composites Technology and Research*. doi:10.1520/ctr10500j

Brik, V. B. (2003). *Advanced Concept Concrete Using Basalt Fiber / BF Composite Rebar Reinforcement.*

Castro, P. F., & Carino, N. J. (1998). Tensile and nondestructive testing of FRP bars. *Journal of Composites for Construction*. doi:10.1061/(asce)1090-0268(1998)2:1(17)

de Larrard, F., Schaller, I., & Fuchs, J. (1993). Effect of bar diameter on the bond strength of passive reinforcement in high-performance concrete. *ACI Materials Journal*. doi:10.14359/3888

Ehlen, M. A. (1997). Life-cycle costs of new construction materials. *Journal of Infrastructure Systems*. doi:10.1061/(ASCE)1076-0342(1997)3:4(129)

Ehsani, M. R., Saadatmanesh, H., & Tao, S. (1996). Design recommendations for bond of GFRP rebars to concrete. *Journal of Structural Engineering*. doi:10.1061/(ASCE)0733-9445(1996)122:3(247)

El Refai, A., Ammar, M.-A., & Masmoudi, R. (2015). Bond Performance of Basalt Fiber-Reinforced Polymer Bars to Concrete. *Journal of Composites for Construction*. doi:10.1061/(asce)cc.1943-5614.0000487

Elgabbas , F., Ahmed, E. A., & Benmokrane, B. (2015). Physical and mechanical characteristics of new basalt-FRP bars for reinforcing concrete structures. *Construction and Building Materials*. doi:10.1016/j.conbuildmat.2015.07.036

Elgabbas, F., Ahmed, E. A., & Benmokrane, B. (2016). Experimental Testing of Concrete Bridge-Deck Slabs Reinforced with Basalt-FRP Reinforcing Bars under Concentrated Loads. *Journal of Bridge Engineering*. doi:10.1061/(ASCE)BE.1943-5592.0000892

Elgabbas, F., Ahmed, E., & Benmokrane, B. (2013). Basalt FRP reinforcing bars for concrete structures.

Elgabbas, F., Vincent, P., Ahmed, E. A., & Benmokrane, B. (2016). Experimental testing of basalt-fiber-reinforced polymer bars in concrete beams. *Composites Part B: Engineering*. doi:10.1016/j.compositesb.2016.01.045

El-Gamal, S., El-Salakawy, E., & Benmokrane, B. (2005). Behavior of concrete bridge deck slabs reinforced with fiber-reinforced polymer bars under concentrated loads. *ACI Structural Journal*. doi:10.14359/14668

El-Ragaby, A., El-Salakawy, E., & Benmokrane, B. (2007). Fatigue analysis of concrete bridge deck slabs reinforced with E-glass/vinyl ester FRP reinforcing bars. *Composites Part B: Engineering*. doi:10.1016/j.compositesb.2006.07.012

El-Salakawy, E., Benmokrane, B., & Desgagné, G. (2003). Fibre-reinforced polymer composite bars for the concrete deck slab of Wotton Bridge. *Canadian Journal of Civil Engineering*. doi:10.1139/l03-055

El-Salakawy, E., Benmokrane, B., Masmoudi, R., Brière, F., & Breaumier, É. (2003). Concrete Bridge Barriers Reinforced with Glass Fiber-Reinforced Polymer Composite Bars. *ACI Structural Journal*. doi:10.14359/12848

Estes, A. C., & Frangopol, D. M. (2001). Minimum expected cost-oriented optimal maintenance planning for deteriorating structures: Application to concrete bridge decks. *Reliability Engineering and System Safety*. doi:10.1016/S0951-8320(01)00044-8

Fatih Kara, I., Alpaslan Koroglu, M., & Ashour, A. F. (2017). Tests of continuous concrete slabs reinforced with basalt fiber-reinforced plastic bars. *ACI Structural Journal*. doi:10.14359/51689784

Faza, S. S., & GangaRao, H. (1993). *Glass FRP reinforcing bars for concrete.*

Fenwick, R., & Pauley, T. (1968). Mechanism of Shear resistance of Concrete Beams. *Journal of the Structural Division*.

Grace, N. F., Soliman, A. K., Abdel-Sayed, G., & Saleh, K. R. (1998). Behavior and ductility of simple and continuous FRP reinforced beams. *Journal of Composites for Construction*. doi:10.1061/(ASCE)1090-0268(1998)2:4(186)

Gribniak, V., Arnautov, A. K., Kaklauskas, G., Tamulenas, V., Timinskas, E., & Sokolov, A. (2015). Investigation on application of basalt materials as reinforcement for flexural elements of concrete bridges. *Baltic Journal of Road and Bridge Engineering*. doi:10.3846/bjrbe.2015.25

Haramis, J. (2003). *Freeze-thaw durability of polymeric composite materials for use in civil infrastructure.*

Hartmann, A., Neitzel, M., & Mitschang, P. (2000). Life cycle cost modelling of continuous fibre reinforced thermoplastics. *International SAMPE Symposium and Exhibition*.

Hassan, T. K., & Rizkalla, S. H. (2004). Bond mechanism of near-surface-mounted fiber-reinforced polymer bars for flexural strengthening of concrete structures. *ACI Structural Journal*. doi:10.14359/13458

Hollaway, L., & Head. (2001). *Chapter 2-Advanced polymer composite materials and their components.*

Hong, T., Han, S., & Lee, S. (2007). Simulation-based determination of optimal life-cycle cost for FRP bridge deck panels. *Automation in Construction*. doi:10.1016/j.autcon.2006.01.001

Huckelbridge, A., & Eitel, A. (2003). Preliminary Performance Observations for an FRP Reinforced Concrete Bridge Deck.

Huo, W., Zhang, Z., Wang, M., Li, M., & Sun, Z. (2007). Experimental study on acid and alkali resistance of basalt fiber used for composites. *Fuhe Cailiao Xuebao/Acta Materiae Compositae Sinica*.

Karbhari, V. M. (2003). Durability of FRP composites for civil infrastructure - Myth, mystery and reality. *Advances in Structural Engineering*. doi:10.1260/136943303322419250

Karbhari, V. M., & Pope, G. (1994). Impact and flexure properties of glass/vinyl ester composites in cold regions. *Journal of Cold Regions Engineering*. doi:10.1061/(ASCE)0887-381X(1994)8:1(1)

Karbhari, V. M., Rivera, J., & Zhang, J. (2002). Low-temperature hygrothermal degradation of ambient cured E-glass/vinylester composites. *Journal of Applied Polymer Science*. doi:10.1002/app.11205

Karbhari, V. M., Seible, F., Burgueño, R., Davol, A., Wernli, M., & Zhao, L. (2000). Structural characterization of fiber-reinforced composite short- and medium-span bridge systems. *Applied Composite Materials*. doi:10.1023/A:1008974804077

Kocaoz, S., Samaranayake, V. A., & Nanni, A. (2005). Tensile characterization of glass FRP bars. *Composites Part B: Engineering*. doi:10.1016/j.compositesb.2004.05.004

Li, H., Xian, G., Ma, M., & Wu, J. (2012). Durability and fatigue performances of basalt fiber / epoxy reinforcing bars. *Proceedings of the 6th International Conference on FRP Composites in Civil Engineering, CICE 2012*.

Lin, Z., Fakharifar, M., Wu , C., Chen, G., Bevans, W., Gunasekaran, A., & Sedigh, S. (2013). *Design, construction and load testing of the Pat Daly Road Bridge in Washington County, MO, with internal glass fiber reinforced polymers reinforcement.*

Liu, Q., Shaw, , M. T., Parnas, R. S., & McDonnell, A. (2006). Investigation of Basalt Fiber composite mechanical properties for applications in Transportation. *Polymer Composites*. doi:10.1002/pc.20162

Lord, H. W., & Dutta, P. K. (1988). On the Design of Polymeric Composite Structures for Cold Regions Applications. *Journal of Reinforced Plastics and Composites*. doi:10.1177/073168448800700503

Mkarand, H., TaoHoon, H., & Daniel , H. (2004). Constructability, Maintainability, and Operability of Fiber Reinforced Polymer (FRP) Bridge Deck Panels. *Purdue Civil Engineering Joint Transportation Research Program*. doi:FHWA/IN/JTRP-2004/15, SPR-2778

Nanni , A. (1993). Flexural behavior and design of RC members using FRP reinforcement. *Journal of Structural Engineering (United States)*. doi:10.1061/(ASCE)0733-9445(1993)119:11(3344)

Nanni, A., & Faza, S. (2002). Design and construction of concrete reinforced with FRP bars: an emerging technology. *Concrete international*.

Nathan, T. R., & Onyemelukwe, O. U. (2000). Comparison of bridge deck alternatives using life cycle costs., (p. 6).

Nystrom, H. E., Watkins, S. E., Nanni, A., & Murray, S. (2003). Financial viability of fiber-reinforced polymer (FRP) bridges. *Journal of Management in Engineering*. doi:10.1061/(ASCE)0742-597X(2003)19:1(2)

Ovitigala, T., & Issa, M. A. (2013). Mechanical and bond strength of basalt fiber reinforced polymer (BFRP) bars for concrete structures.

Ovitigala, T., Ibrahim, M. A., & Issa, M. A. (2016). Serviceability and ultimate load behavior of concrete beams reinforced with basalt fiber-reinforced polymer bars. *ACI Structural Journal*. doi:10.14359/51688752

Plaseied, A., & Fatemi, A. (2009). Tensile creep and deformation modeling of vinyl ester polymer and its nanocomposite. *Journal of Reinforced Plastics and Composites*. doi:10.1177/0731684408090378

Rivera, J., & Karbhari, V. M. (2002). Cold-temperature and simultaneous aqueous environment related degradation of carbon/vinylester composites. *Composites Part B:Engineering*. doi:10.1016/S1359-8368(01)00058-0

Schaefer, B. C. (2002). Thermal and environmental effects on fiber-reinforced polymer reinforcing bars and reinforced concrete elements. *OAKTrust*. Retrieved from http://hdl.handle.net/1969.1/ETD-TAMU-2002-THESIS-S33

Scott, D. W., Lai, J. S., & Zureick, A. (1995). Creep Behavior of Fiber-Reinforced Polymeric Composites: A Review of the Technical Literature. *Journal of Reinforced Plastics and Composites*. doi:10.1177/073168449501400603

Shi, J., Wang, X., Wu, Z., & Zhu, Z. (2015). Creep behavior enhancement of a basalt fiber-reinforced polymer tendon. *Construction and Building Materials*. doi:10.1016/j.conbuildmat.2015.07.118

Sim, J., Park, C., & Moon, D. (2005). Characteristics of basalt fiber as a strengthening material for concrete structures. *Composites Part B: Engineering*. doi:10.1016/j.compositesb.2005.02.002

Singhvi, A., & Mirmiran, A. (2002). Creep and durability of environmentally conditioned FRP-RC beams using fiber optic sensors. *Journal of Reinforced Plastics and Composites*. doi:10.1177/0731684402021004254

Stone, D., Nanni, A., & Myers, J. (2001). Field and Laboratory Performance of FRP Bridge Panels. *Composites in Construction*.

Tepfers, R. (2006). Bond clause proposals for FRP bars/rods in concrete based on CEB/FIP Model Code 90. Part 1: Design bond stress for FRP reinforcing bars. *Structural Concrete*. doi:10.1680/stco.2006.7.2.47

Vincent, T., & Vincent, T. (2013). Influence of fiber orientation and specimen end condition on axial compressive behavior of FRP-confined concrete. *Construction and Building Materials*. doi:10.1016/j.conbuildmat.2013.05.085

Wang, X., Shi, J., Liu, J., Yang, L., & Wu, Z. (2014). Creep behavior of basalt fiber reinforced polymer tendons for prestressing application. *Materials and Design*. doi:10.1016/j.matdes.2014.03.009

Wu, G., Sun, G., Wu, Z., & Luo, Y. (2012). Mechanical properties of steel-FRP composite bars (SFCBs) and performance of SFCB reinforced concrete structures. *Advances in Structural Engineering*. doi:10.1260/1369-4332.15.4.625

Zhang, X., & Ou, J. (2007). Durability experimental research on resistance of acidic, alkali, salt solutions and freeze-thaw properties of FRP bar.

Zheng, Y., Yu, G., & Pan, Y. (2012). Investigation of ultimate strengths of concrete bridge deck slabs reinforced with GFRP bars. *Construction and Building Materials*. doi:10.1016/j.conbuildmat.2011.09.002

Appendix A

LRFD Deck Slab Design Example: 7 ft. Beam Spacing, Positive Moment Reinforcement

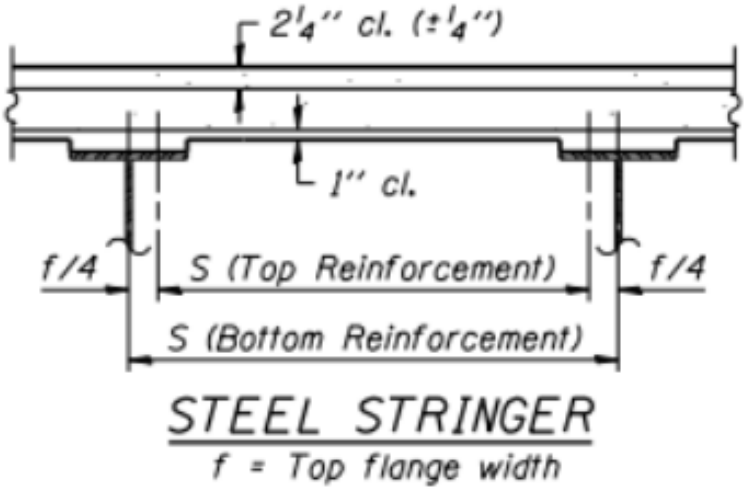

Design Stresses

$f_{fu} = 200ksi$	Tensile strength for product certification as reported by BFRP manufacturers.
$C_E = 0.8$	Environment reduction factors. Assumed 0.8 for BFRP.
$f_d = C_E f_{fu} = 160ksi$	Design tensile strength of BFRP reinforcing bars considering reductions for service environment calculated as per Article 2.4.2.1 of AASHTO GFRP.
$E_f = 8500ksi$	Tensile modulus of elasticity of GFRP reinforcement.
$f'_c = 4ksi$	Compressive strength of concrete for use in design

Design Thickness

Standard eight inch slab thickness.

The IDOT standard slab thickness us 8 in. for all girder spacing less than or equal to 9ft - 6in. For girder spacing exceeding 9ft – 6 in., the standard design charts in the IDOT bridge manual are not applicable.

Initial Reinforcement Trial

#5 BFRP bar @ 6in.

D**etermine Maximum Factored Loading**

<u>Unfactored Loads and Moments</u>

$w_{DC1} = \left(\frac{0.150k}{ft^3}\right)(0.667ft)(1ft) = 0.100\frac{k}{ft}$

Dead load of structural components (DC1). Standard deck slabs are not designed for non-structural attachments (DC2).

$w_{DW} = \left(\frac{0.050k}{ft^2}\right)(1ft) = 0.050\frac{k}{ft}$

Dead load of future wearing surface taken as 50 psf for IDOT bridge deck designs.

$M_{DC1} = \frac{1}{10}\left(0.100\frac{k}{ft}\right)(7ft)^2 = 0.490k - ft$

Applied moment due to Dead load of structural components (DC1).

$M_{DW} = \frac{1}{10}\left(0.050\frac{k}{ft}\right)(7ft)^2 = 0.245k - ft$

Applied moment due to future wearing surface (DW)

$M_{LL+IM} = 5.21k - ft$ — Applied moment due to vehicular live load (LL) with dynamic load allowance (IM). It is taken from AASHTO LRFD Table A4-1.

Factored Moments

When designing deck slabs, three load combinations are considered:

$$M_{STRENGTH\ I} = \eta_i[1.25M_{DC1} + 1.50M_{DW} + 1.75M_{LL+IM}]$$
$$= 1.00[1.25(0.490k - ft) + 1.50(0.245k - ft) + 1.75(5.21k - ft)]$$
$$= 10.10k - ft\left(\frac{12in}{ft}\right)$$
$$= 121.17k - in$$

$$M_{SERVICE\ I} = \eta_i[1.00M_{DC1} + 1.00M_{DW} + 1.00M_{LL+IM}]$$
$$= 1.00[1.00(0.490k - ft) + 1.00(0.245k - ft) + 1.00(5.21k - ft)]$$
$$= 5.95k - ft\left(\frac{12in}{ft}\right)$$
$$= 71.34k - in$$

$$M_{Creep\ Rupture} = \eta_i[1.00M_{DC1} + 1.00M_{DW} + 0.20M_{LL+IM}]$$
$$= 1.00[1.00(0.490k - ft) + 1.00(0.245k - ft) + 0.20(5.21k - ft)]$$
$$= 1.78k - ft\left(\frac{12in}{ft}\right)$$
$$= 21.36k - in$$

Cracked section properties

The moment of inertia of transformed cracked section is calculated as following:

$b = 12in$ Strip width

$d = 8in - 1in\ clear - 0.5(0.625in\ )$ Distance from extreme compression fiber to centroid of tensile reinforcement.

$E_c = 120000k_1 {w_c}^2 {f'_c}^{0.33}$ Modulus of elasticity of concrete as per AASHTO GFRP Article 2.4.1.

$= 120000(1.0)(0.145kcf)^2(4ksi)^{0.33}$

$= 3987ksi$

$n_f = \frac{8500ksi}{3987ksi} = 2.132$ Modular ratio = E_f/E_c as per AASHTO GFRP Article 2.5.3.

$\rho_f = \frac{A_{\#5}}{S\ d}$ BFRP reinforcement ratio as per AASHTO GFRP Article 2.5.3.

$= \frac{0.31in^2}{6in(6.69in)} = 0.0077$

$k = \sqrt{2\rho_f n_f + \left(\rho_f n_f\right)^2} - \rho_f n_f$ Ratio of depth of neutral axis to depth of flexural reinforcement as per AASHTO GFRP Article 2.5.3.

$= \sqrt{2(0.0077)(2.132) + ((0.0077)(2.132))^2} - (0.0077)(2.132)$

$= 0.165$

$I_{cr} = \frac{1}{3}b(kd)^3 + n_f A_{\#5}\left(\frac{b}{S}\right)(d - kd)^2$ Moment of inertia of transformed cracked section as per AASHTO GFRP Article 2.5.3.

$= \frac{1}{3}(12in)\left(0.165(6.69in)\right)^3 + 2.132(0.31in^2)\left(\frac{12in}{6in}\right)(6.69in - 0.165(6.69in))^2$

$= 46.63in^4$

Check Service Limit State

$$f_{f,s} = \frac{n_f d(1-k)}{I_{cr}} M_{SERVICE\ I}$$

$$= \frac{2.132(6.69in)(1-0.165)}{46.63in^4} 71.34k-in$$

$$= 18.22ksi$$

Calculated tensile stress in BFRP reinforcement at the service limit state as per AASHTO GFRP Articles 2.5.3 and 2.6.7.

$$s_{max1} = 1.15\frac{C_b E_f w}{f_{f,s}} - 2.5C_c$$

$$= 1.15\frac{0.83(8500ksi)(0.028in)}{18.22ksi} - 2.5(1in)$$

$$= 9.97\ in$$

Maximum spacing allowed for controlling crack width.

$$s_{max2} = 0.92\frac{C_b E_f w}{f_{f,s}}$$

$$= 0.92\frac{0.83(8500ksi)(0.028in)}{18.22ksi}$$

$$= 9.98\ in$$

Maximum spacing allowed for controlling crack width.

#5 BFRP bar @ 6 in satisfies Service Limit State.

Check Service Limit State Using Design Aid

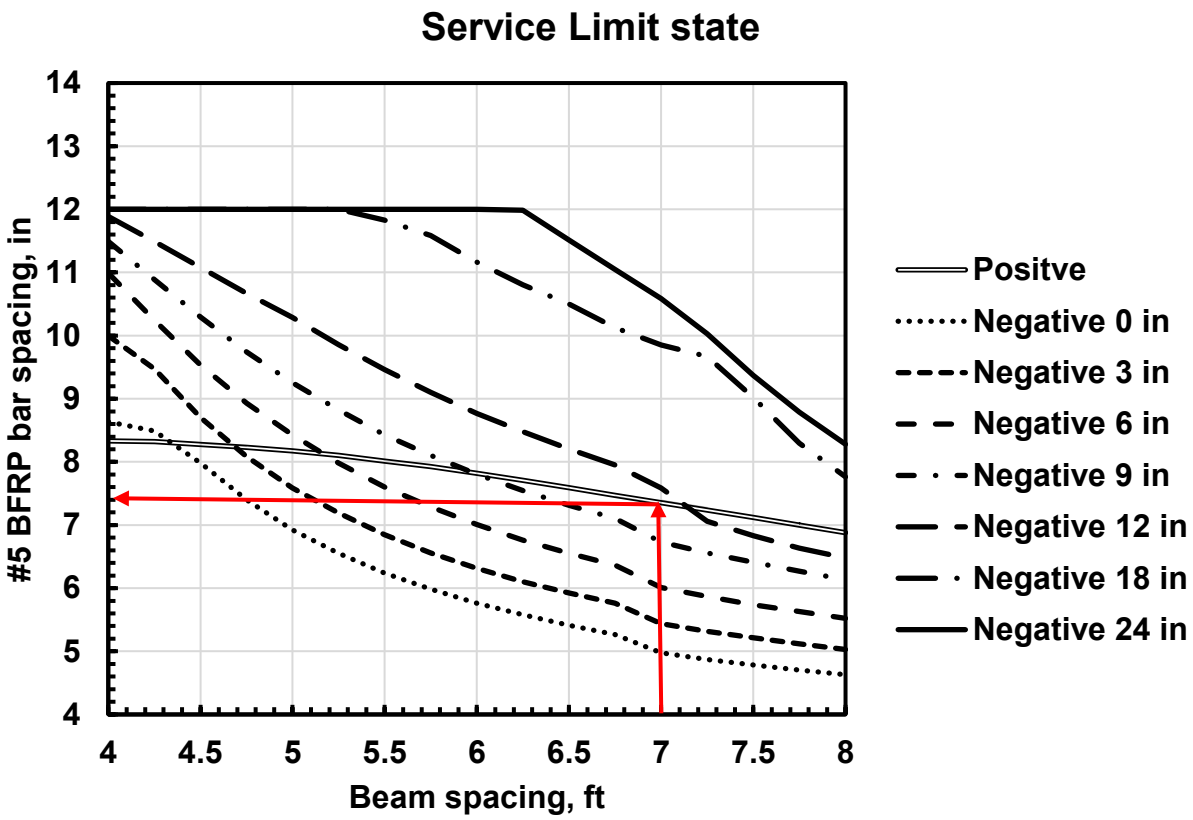

- The maximum allowable #5 BFRP bar spacing to satisfy the Service Limit State is 7.4 in.
- #5 BFRP bar @ 6 in satisfies Service Limit State.

Check Strength Limit State

$$M_r = \phi M_n = \phi \left[A_f f_f \left(d - \frac{a}{2} \right) \right] \geq M_{STRENGTH\ I}$$

Where

$$f_f = \sqrt{\frac{(E_f \varepsilon_{cu})^2}{4} + \frac{0.85\beta_1 f'_c}{\rho_f} E_f \varepsilon_{cu}} - 0.5 E_f \varepsilon_{cu}$$

Effective strength in BFRP reinforcement at the strength and extreme event limit state as per AASHTO GFRP Article 2.6.3.1.

$$= \sqrt{\frac{(8500ksi(0.003))^2}{4} + \frac{0.85(0.85)(4ksi)}{0.0077} 8500ksi(0.003)} - 0.5(8500)(0.003)$$

$$= 85.9ksi$$

$$a = \frac{A_{\#5} f_f}{0.85 * f'_c S}$$

$$= \frac{0.31in^2(85.9ksi)}{0.85(4ksi)(6in)}$$

$$= 1.31in$$

Depth of equivalent rectangular stress block as per AASHTO GFRP Article 2.6.3.2.2.

$$M_n = 0.31in^2 \left(\frac{12in}{6in} \right) (85.9ksi) \left(6.69in - \frac{1.31in}{2} \right)$$

$$= 321.4k - in$$

Nominal flexural resistance as per AASHTO GFRP Article 2.6.3.2.1.

$$\varepsilon_f = \frac{f_f}{E_f}$$

$$= \frac{85.9ksi}{8500ksi}$$

$$= 0.01$$

Longitudinal tensile strain in the section at the centroid of the BFRP tension reinforcement as per AASHTO GFRP Article 2.7.3.6.2.

$$\varepsilon_{fd} = \frac{f_{fd}}{E_f}$$

$$= \frac{160ksi}{8500ksi}$$

$$= 0.02$$

Design tensile strain at rupture of GFRP reinforcing bars considering reduction for service environment as per AASHTO GFRP Article 2.4.2.1.

$$\phi = \begin{cases} 0.55 & for \quad \varepsilon_f = \varepsilon_{fd} \\ 1.55 - \frac{\varepsilon_f}{\varepsilon_{fd}} & for \quad 0.80\varepsilon_{fd} < \varepsilon_f < \varepsilon_{fd} \\ 0.75 & for \quad \varepsilon_f \leq 0.80\varepsilon_{fd} \end{cases}$$

$$= 0.75$$

Resistance factor as per AASHTO GFRP Article 2.5.5.2.

$$M_r = 0.75(321.4k - in)$$

$$M_r = 241.1k - in \geq 121.17k - in$$

Factored flexural resistance as per AASHTO GFRP Article 2.6.3.2.1.

Check Strength Limit State Using Design Aid

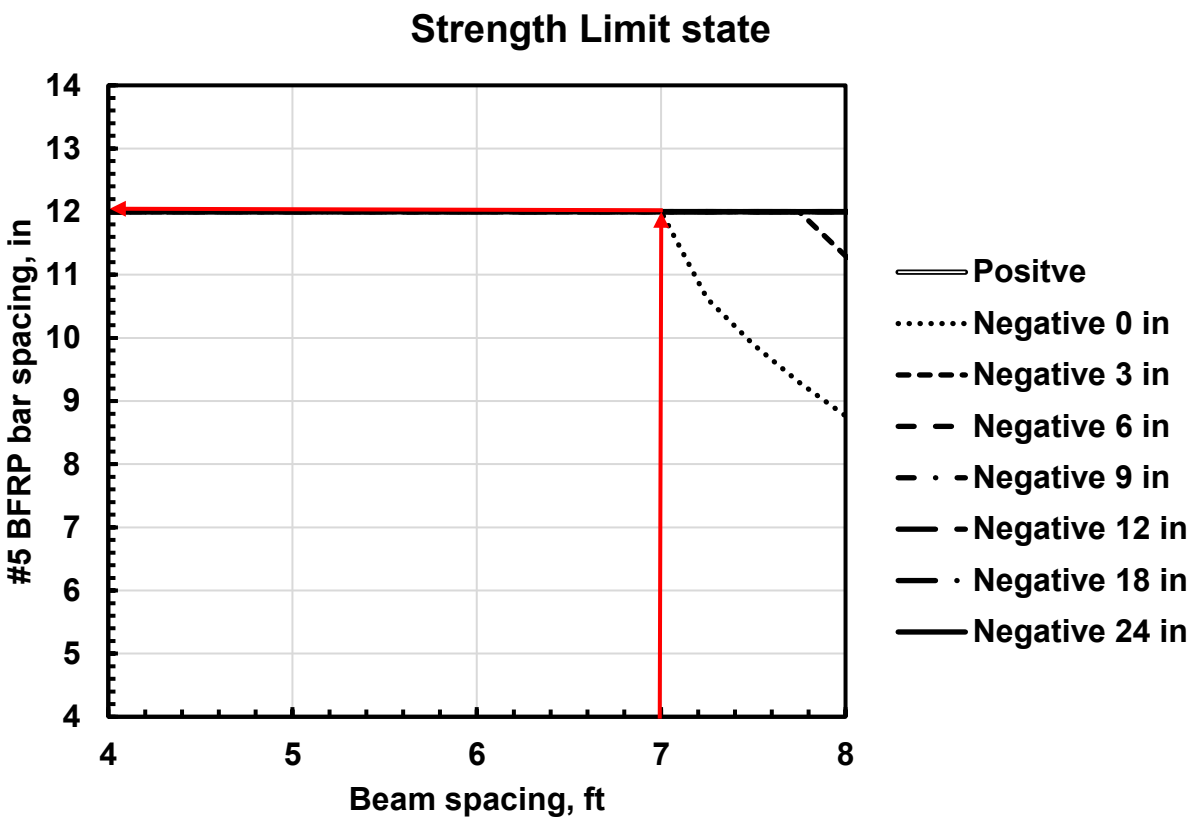

- The maximum allowable #5 BFRP bar spacing to satisfy the Strength Limit State is 12 in.
- #5 BFRP bar @ 6 in satisfies Strength Limit State.

Check Creep Rupture Limit State

$$f_f \leq C_c f_{fd}$$

Where

$$f_{f,c} = \frac{n_f d(1-k)}{I_{cr}} M_{Creep\ Rupture}$$

$$= \frac{2.132(6.69in)(1-0.165)}{46.63in^4} 21.36k-in$$

$$= 5.46ksi$$

Calculated tensile stress in GFRP reinforcement at creep rupture limit state as per AASHTO GFRP Article 2.5.3

$$C_c = 0.3$$

Creep rupture reduction factor as per AASHTO GFRP Article 2.5.3.

$$C_c f_{fd} = 0.3(160ksi)$$

$$5.46ksi \leq 48ksi$$

Check Creep Rupture Limit State using Design Aid

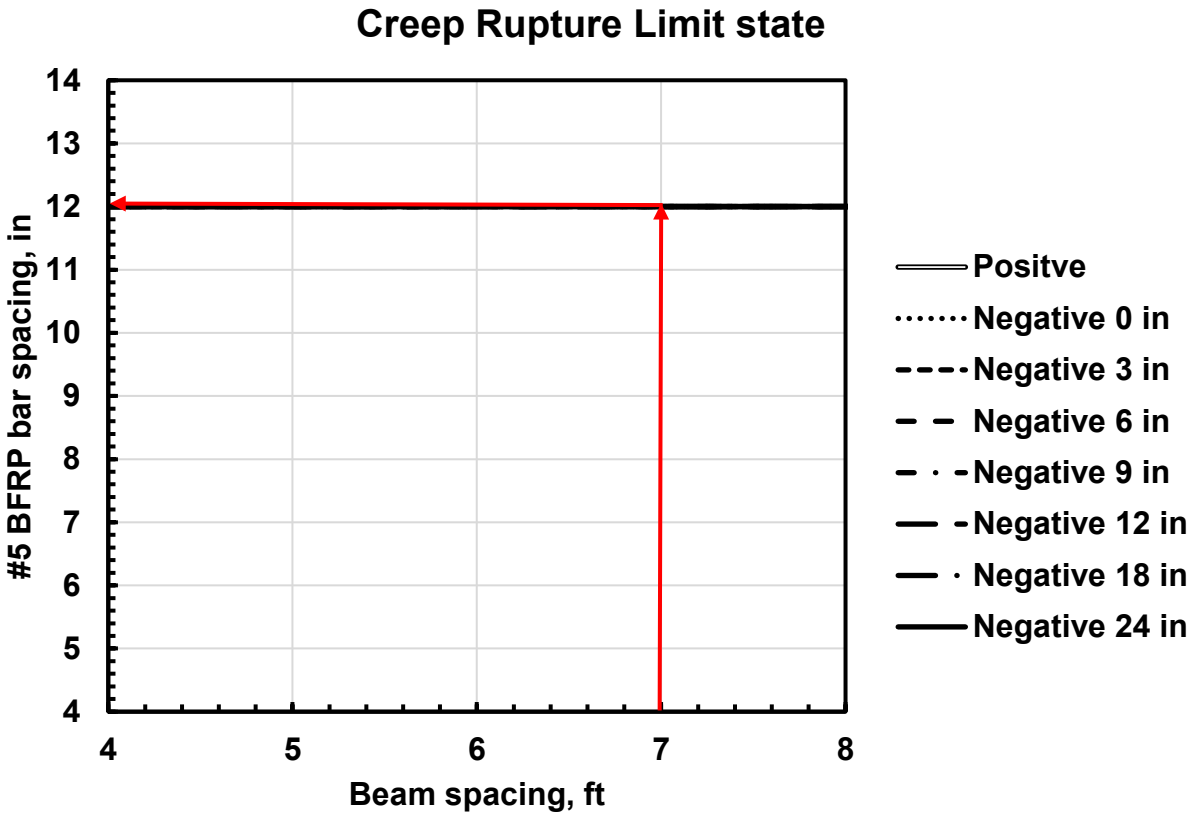

- The maximum allowable #5 BFRP bar spacing to satisfy the Creep Rupture Limit State is 12 in.
- #5 BFRP bar @ 6 in satisfies Strength Limit State.

LRFD Deck Slab Design Example: 7 ft. Beam Spacing, Negative Moment Reinforcement

Design Stresses

$f_{fu} = 200ksi$	Tensile strength for product certification as reported by BFRP manufacturers.
$C_E = 0.8$	Environment reduction factors. Assumed 0.8 for BFRP.
$f_d = C_E f_{fu} = 160ksi$	Design tensile strength of BFRP reinforcing bars considering reductions for service environment calculated as per Article 2.4.2.1 of AASHTO GFRP.
$E_f = 8500ksi$	Tensile modulus of elasticity of GFRP reinforcement.
$f'_c = 4ksi$	Compressive strength of concrete for use in design

Design Thickness

Standard eight inch slab thickness.

The IDOT standard slab thickness us 8 in. for all girder spacing less than or equal to 9ft - 6in. For girder spacing exceeding 9ft – 6 in., the standard design charts in the IDOT bridge manual are not applicable.

Initial Reinforcement Trial

#5 BFRP bar @ 6in.

Determine Maximum Factored Loading

Unfactored Loads and Moments

$$w_{DC1} = \left(\frac{0.150k}{ft^3}\right)(0.667ft)(1ft) = 0.100\frac{k}{ft}$$

Dead load of structural components (DC1). Standard deck slabs are not designed for non-structural attachments (DC2).

$$w_{DW} = \left(\frac{0.050k}{ft^2}\right)(1ft) = 0.050\frac{k}{ft}$$

Dead load of future wearing surface taken as 50 psf for IDOT bridge deck designs.

$$M_{DC1} = \frac{1}{10}\left(0.100\frac{k}{ft}\right)(7ft)^2 = 0.490k - ft$$

Applied moment due to Dead load of structural components (DC1).

$$M_{DW} = \frac{1}{10}\left(0.050\frac{k}{ft}\right)(7ft)^2 = 0.245k - ft$$

Applied moment due to future wearing surface (DW)

$$M_{LL+IM} = 5.17k - ft$$

Applied moment due to vehicular live load (LL) with dynamic load allowance (IM). It is taken from AASHTO LRFD Table A4-1.

Factored Moments

When designing deck slabs, three load combinations are considered:

$$M_{STRENGTH\ I} = \eta_i[1.25M_{DC1} + 1.50M_{DW} + 1.75M_{LL+IM}]$$

$$= 1.00[1.25(0.490k - ft) + 1.50(0.245k - ft) + 1.75(5.17k - ft)]$$

$$= 10.03k - ft\left(\frac{12in}{ft}\right)$$

$$= 120.33k - in$$

$$M_{SERVICE\ I} = \eta_i[1.00M_{DC1} + 1.00M_{DW} + 1.00M_{LL+IM}]$$
$$= 1.00[1.00(0.490k - ft) + 1.00(0.245k - ft) + 1.00(5.17k - ft)]$$
$$= 5.905k - ft\left(\frac{12in}{ft}\right)$$
$$= 70.86k - in$$

$$M_{Creep\ Rupture} = \eta_i[1.00M_{DC1} + 1.00M_{DW} + 0.20M_{LL+IM}]$$
$$= 1.00[1.00(0.490k - ft) + 1.00(0.245k - ft) + 0.20(5.17k - ft)]$$
$$= 1.77k - ft\left(\frac{12in}{ft}\right)$$
$$= 21.23k - in$$

Cracked section properties

The moment of inertia of transformed cracked section is calculated as following:

$b = 12in$ — Strip width

$d = 8in - 2.25in\ clear - 0.5(0.625in) = 5.44in$ — Distance from extreme compression fiber to centroid of tensile reinforcement.

$E_c = 120000k_1{w_c}^2{f'_c}^{0.33}$
$= 120000(1.0)(0.145kcf)^2(4ksi)^{0.33}$
$= 3987ksi$

Modulus of elasticity of concrete as per AASHTO GFRP Article 2.4.1.

$n_f = \frac{8500ksi}{3987ksi} = 2.132$ — Modular ratio = E_f/E_c as per AASHTO GFRP Article 2.5.3.

$$\rho_f = \frac{A_{\#5}}{S\,d}$$

$$= \frac{0.31in^2}{6in(5.44in)} = 0.0095$$

BFRP reinforcement ratio as per AASHTO GFRP Article 2.5.3.

$$k = \sqrt{2\rho_f n_f + \left(\rho_f n_f\right)^2} - \rho_f n_f$$

$$= \sqrt{2(0.0095)(2.132) + ((0.0095)(2.132))^2} - (0.0095)(2.132)$$

$$= 0.182$$

Ratio of depth of neutral axis to depth of flexural reinforcement as per AASHTO GFRP Article 2.5.3.

$$I_{cr} = \frac{1}{3}b(kd)^3 + n_f A_{\#5}\left(\frac{b}{S}\right)(d - kd)^2$$

Moment of inertia of transfomed cracked section as per AASHTO GFRP Article 2.5.3.

$$= \frac{1}{3}(12in)\big(0.182(5.44in)\big)^3 + 2.132(0.31in^2)\left(\frac{12in}{6in}\right)(5.44in - 0.182(5.44in))^2$$

$$= 30.06in^4$$

Check Service Limit State

$$f_{f,s} = \frac{n_f d(1-k)}{I_{cr}} M_{SERVICE\ I}$$

$$= \frac{2.132(5.44in)(1 - 0.182)}{30.06in^4} 70.86k - in$$

$$= 22.36ksi$$

Calculated tensile stress in BFRP reinforcement at the service limit state as per AASHTO GFRP Articles 2.5.3 and 2.6.7.

$$s_{max1} = 1.15\frac{C_b E_f w}{f_{f,s}} - 2.5C_c$$

$$= 1.15\frac{0.83(8500ksi)(0.028in)}{22.364ksi} - 2.5(2.25in)$$

$$= 4.54\ in$$

Maximum spacing allowed for controlling crack width.

$$s_{max2} = 0.92\frac{C_b E_f w}{f_{f,s}}$$

Maximum spacing allowed for controlling crack width.

$$= 0.92\frac{0.83(8500ksi)(0.028in)}{22.36ksi}$$

$$= 8.13\ in$$

❖ Service limit is not satisfied.

Check Service Limit State Using Design Aid

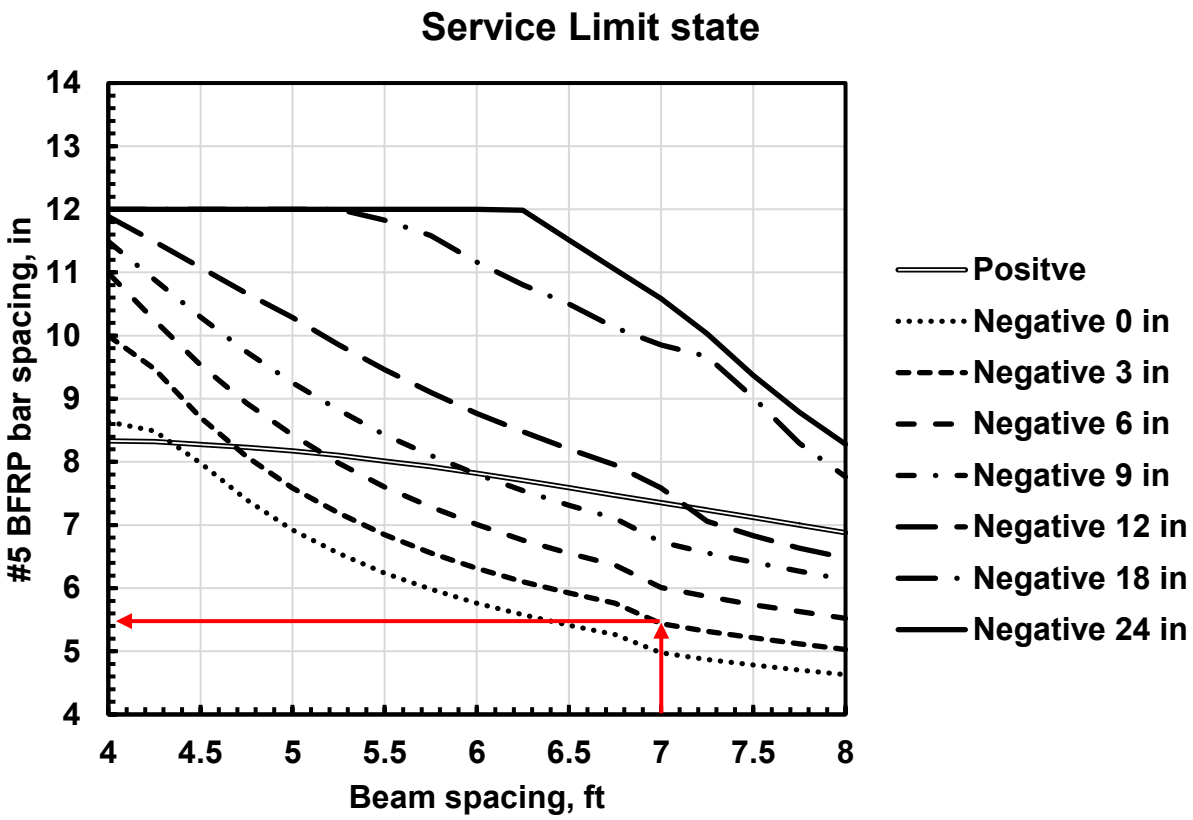

- The maximum allowable #5 BFRP bar spacing to satisfy the Service Limit State is 5.44 in.
- #5 BFRP bar @ 6 in does not satisfy Service Limit State.

Second Reinforcement Trial

#5 BFRP bar ($E_f = 8500ksi, f_d = 160ksi$) @ 5in.

Cracked section properties

The moment of inertia of transformed cracked section is calculated as following:

$b = 12in$ — Strip width

$d = 8in - 1in\ clear - 0.5(0.625in)$ — Distance from extreme compression fiber to centroid of tensile reinforcement.

$E_c = 120000k_1{w_c}^2{f'_c}^{0.33}$
$= 120000(1.0)(0.145kcf)^2(4ksi)^{0.33}$
$= 3987ksi$ — Modulus of elasticity of concrete as per AASHTO GFRP Article 2.4.1.

$n_f = \frac{8500ksi}{3987ksi} = 2.132$ — Modular ratio = E_f/E_c as per AASHTO GFRP Article 2.5.3.

$\rho_f = \frac{A_{\#5}}{S\ d}$
$= \frac{0.31in^2}{5in(5.44in)} = 0.0114$ — BFRP reinforcement ratio as per AASHTO GFRP Article 2.5.3.

$k = \sqrt{2\rho_f n_f + (\rho_f n_f)^2} - \rho_f n_f$
$= \sqrt{(2(0.0114)(2.132) + ((0.0114)(2.132))\text{^}2\ ) - (0.0114)(2.132)}$
$= 0.20$ — Ratio of depth of neutral axis to depth of flexural reinforcement as per AASHTO GFRP Article 2.5.3.

$$I_{cr} = \frac{1}{3}b(kd)^3 + n_f A_{\#5}\left(\frac{b}{S}\right)(d - kd)^2$$

Moment of inertia of transfomed cracked section as per AASHTO GFRP Article 2.5.3.

$$= \frac{1}{3}(12in)\big(0.2(5.44in)\big)^3 + 2.132(0.31in^2)\left(\frac{12in}{5in}\right)(5.44in - 0.2(5.44in))^2$$

$$= 35.19in^4$$

Check Service Limit State

$$f_{f,s} = \frac{n_f d(1-k)}{I_{cr}} M_{SERVICE\ I}$$

$$= \frac{2.132(5.44in)(1 - 0.182)}{35.19in^4}70.86k - in$$

$$= 19.10ksi$$

Calculated tensile stress in BFRP reinforcement at the service limit state as per AASHTO GFRP Articles 2.5.3 and 2.6.7.

$$s_{max1} = 1.15\frac{C_b E_f w}{f_{f,s}} - 2.5C_c$$

$$= 1.15\frac{0.83(8500ksi)(0.028in)}{19.10ksi} - 2.5(2.25in)$$

$$= 6.27\ in$$

Maximum spacing allowed for controlling crack width.

$$s_{max2} = 0.92\frac{C_b E_f w}{f_{f,s}}$$

$$= 0.92\frac{0.83(8500ksi)(0.028in)}{19.10ksi}$$

Maximum spacing allowed for controlling crack width.

$= 9.51\ in$

Check Service Limit State Using Design Aid

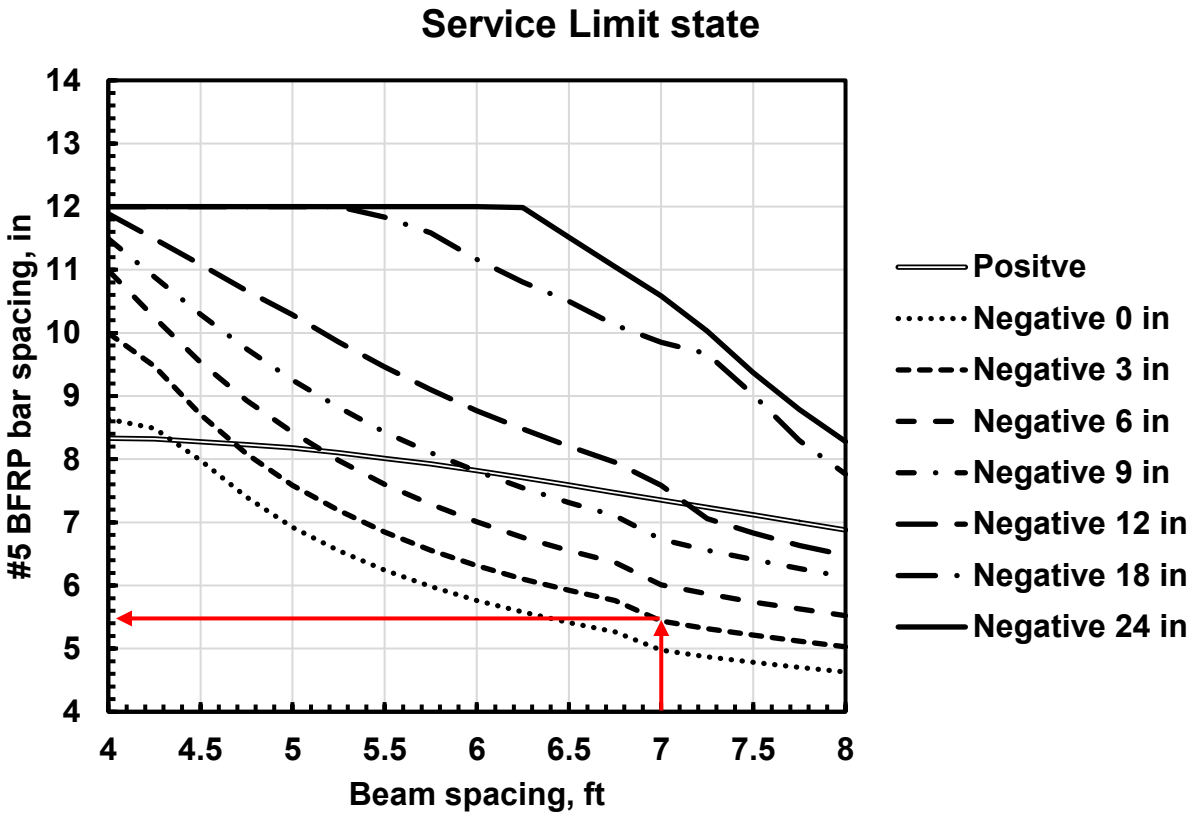

- The maximum allowable #5 BFRP bar spacing to satisfy the Service Limit State is 5.44 in.
- #5 BFRP bar @ 5 in satisfies Service Limit State.

Check Strength Limit State

$$M_r = \phi M_n = \phi \left[A_f f_f \left(d - \frac{a}{2} \right) \right] \geq M_{STRENGTH\ I}$$

Where

$$f_f = \sqrt{\frac{(E_f \varepsilon_{cu})^2}{4} + \frac{0.85\beta_1 f'_c}{\rho_f} E_f \varepsilon_{cu}} - 0.5 E_f \varepsilon_{cu}$$

Effective strength in BFRP reinforcement at the strength and extreme event limit state as per AASHTO GFRP Article 2.6.3.1.

$$= \sqrt{\frac{(8500ksi(0.003))^2}{4} + \frac{0.85(0.85)(4ksi)}{0.0114} 8500ksi(0.003)} - 0.5(8500)(0.003)$$

$$= 68.66ksi$$

$$a = \frac{A_{\#5} f_f}{0.85 * f'_c S}$$

Depth of equivalent rectangular stress block as per AASHTO GFRP Article 2.6.3.2.2.

$$= \frac{0.31in^2(68.66ksi)}{0.85(4ksi)(5in)}$$

$$= 1.252in$$

$$M_n = 0.31in^2 \left(\frac{12in}{5in} \right) (68.66ksi) \left(6.69in - \frac{1.252in}{2} \right)$$

Nominal flexural resistance as per AASHTO GFRP Article 2.6.3.2.1.

$$= 310k - in$$

$$\varepsilon_f = \frac{f_f}{E_f}$$

Longitudinal tensile strain in the section at the centroid of the BFRP tension reinforcement as per AASHTO GFRP Article 2.7.3.6.2.

$$= \frac{68.66ksi}{8500ksi}$$

$$= 0.008$$

$$\varepsilon_{fd} = \frac{f_{fd}}{E_f}$$

$$= \frac{160ksi}{8500ksi}$$

$$= 0.02$$

Design tensile strain at rupture of GFRP reinforcing bars considering reduction for service environment as per AASHTO GFRP Article 2.4.2.1.

$$\phi = \begin{cases} 0.55 & for \quad \varepsilon_f = \varepsilon_{fd} \\ 1.55 - \frac{\varepsilon_f}{\varepsilon_{fd}} & for \quad 0.80\varepsilon_{fd} < \varepsilon_f < \varepsilon_{fd} \\ 0.75 & for \quad \varepsilon_f \leq 0.80\varepsilon_{fd} \end{cases}$$

$$= 0.75$$

Resistance factor as per AASHTO GFRP Article 2.5.5.2.

Check Strength Limit State Using Design Aid

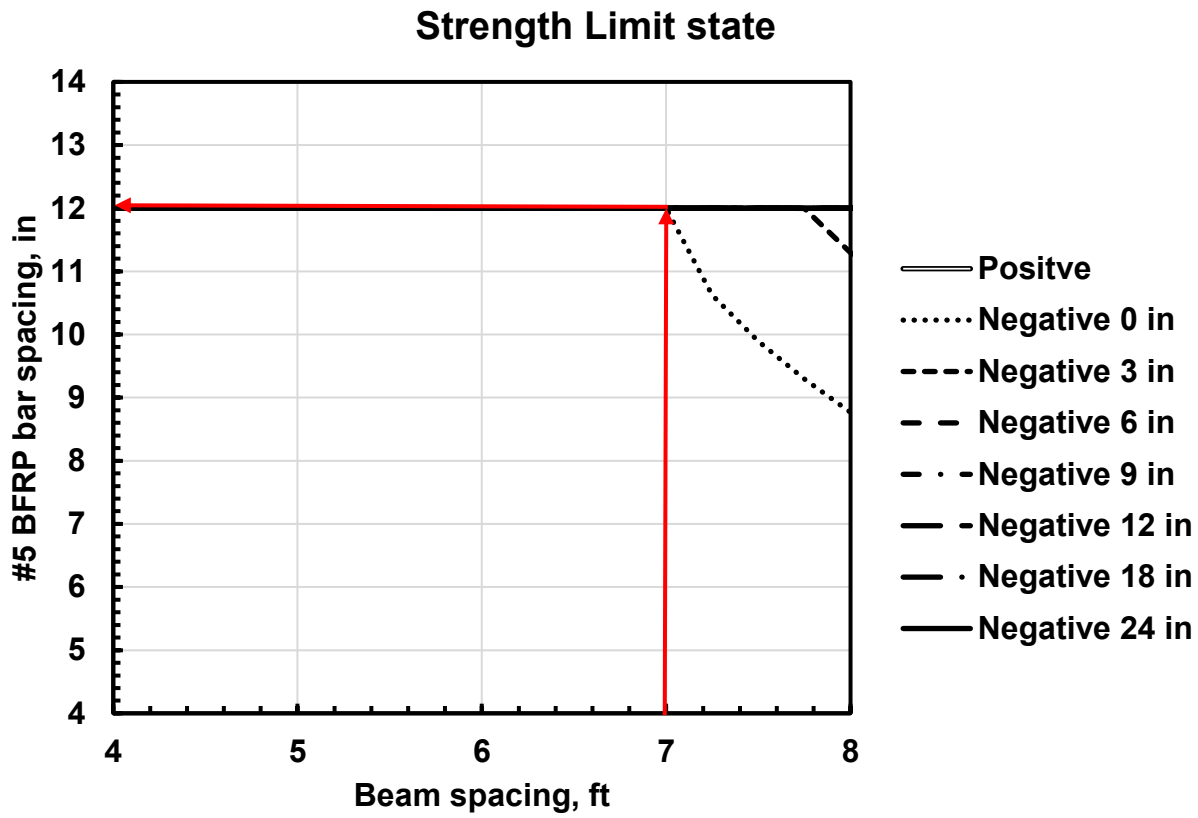

- The maximum allowable #5 BFRP bar spacing to satisfy the Strength Limit State is 12 in.
- #5 BFRP bar @ 5 in satisfies Strength Limit State.

Check Creep Rupture Limit State

$$f_f \leq C_c f_{fd}$$

Where

$f_{f,c} = \frac{n_f d(1-k)}{I_{cr}} M_{Creep\ Rupture}$

$= \frac{2.132(5.44in)(1-0.182)}{35.19in^4} 21.23k-in$

$= 5.73ksi$

Calculated tensile stress in GFRP reinforcement at creep rupture limit state as per AASHTO GFRP Article 2.5.3

$C_c = 0.3$

Creep rupture reduction factor as per AASHTO GFRP Article 2.5.3.

$C_c f_{fd} = 0.3(160ksi)$

$5.73ksi \leq 48ksi$

Check Creep Rupture Limit State using Design Aid

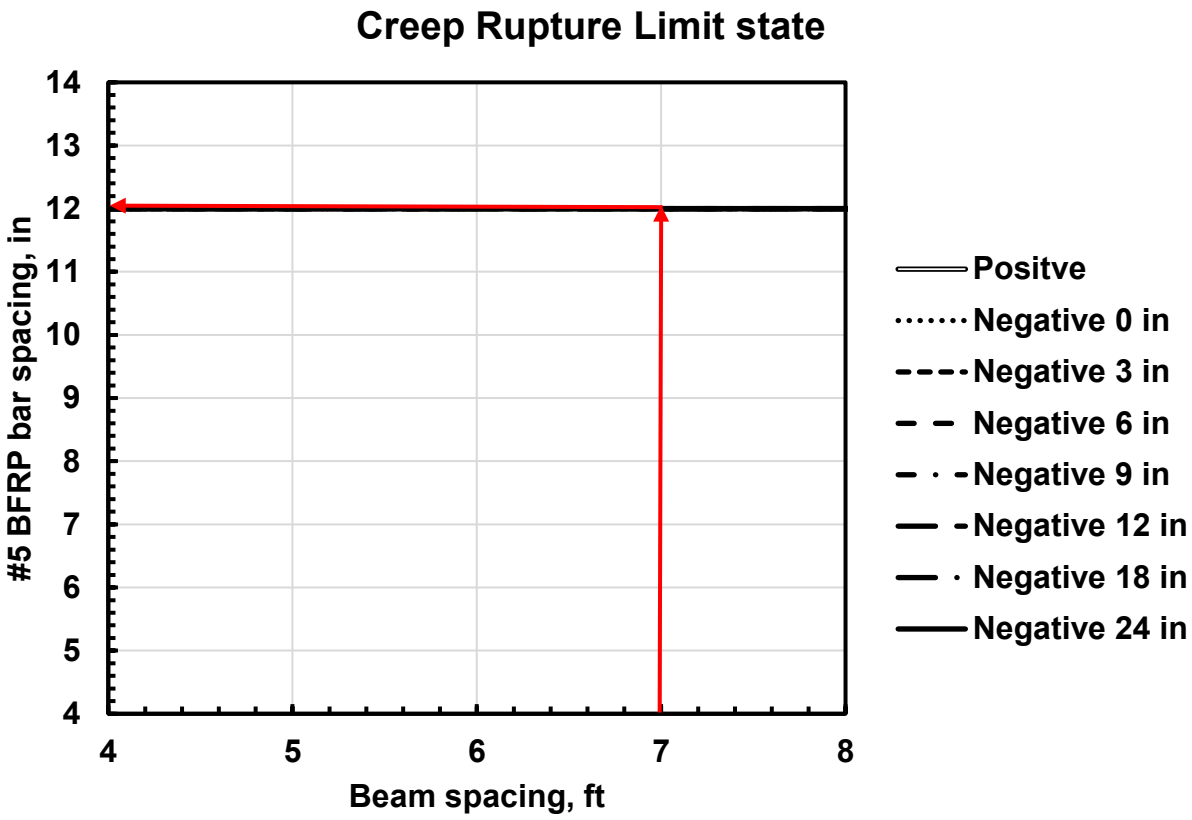

- The maximum allowable #5 BFRP bar spacing to satisfy the Creep Rupture Limit State is 12 in.
- #5 BFRP bar @ 5 in satisfies Strength Limit State.